

TU UB  
Die approbierte Originalversion dieser  
Dissertation ist in der Hauptbibliothek der  
Technischen Universität Wien aufgestellt und  
zugänglich.  
http://www.ub.tuwien.ac.at  
TU UB  
WIEN  
The approved original version of this thesis is  
available at the main library of the Vienna  
University of Technology.  
http://www.ub.tuwien.ac.at/eng

Diese Dissertation haben begutachtet:

TECHNISCHE  
UNIVERSITÄT  
WIEN  
Vienna University of Technology

*Carl T. Ill. J. J. M. M.*

**HINWEISE FÜR DIE ABFASSUNG DER 1. SEITE DER DISSERTATION**

DISSERTATION

Electrochemical Interference  
Thema

Ausgeführt zum Zwecke der Erlangung des akademischen Grades einer/eines Doktorin/Doktors der  
technischen Wissenschaften/der Naturwissenschaften/der Sozial- und Wirtschaftswissenschaften  
unter der Leitung von

(Betreuung)

Robert Stadler  
Name  
E 136  
Institutsnummer  
Dipl. - Ing. Dr. techn.  
Institutsbezeichnung

eingereicht an der Technischen Universität Wien

Faculty of physics  
Fakultät

von

(VerfasserInn)

Xin Zhao  
Name  
1476120  
Matrikelnummer  
Wiedner Hauptstr. 8, 1040, Wien  
Anschrift

Wien, am

29. 08. 2018

eigenhändige Unterschrift

*X. Zhao*

934.094 II

---

## Preface

---

This thesis is submitted in candidacy for the PhD degree from the Technical University of Vienna (TU Wien). The work is carried out in the institute of Theoretical Physics, faculty of Physics at TU Wien from February 2015 to July 2018 under the supervision of Dipl.-Ing. Dr. Robert Stadler. The financial support was provided by Austrian Science Fund (FWF).

I would like to thank my supervisor Robert Stadler for giving me the chance to do this interesting and prospective project, thanks for the helpful and productive discussions along these years. I have learned how to settle and analyze problems, inquire myself why problems come and what could be the solutions, I have learned how to think independently and arrange time and efforts for different tasks.

I would like to thank my families, especially my mother and uncle for their understandings and supports. Thanks to my friends both in China and in Vienna (10th floor in Freihaus is always a delightful place for me), with them I enjoy life here much more. Special thanks to Valerie Smejkal and Isabella Floss for their help and concerns in both scientific and personal life.

I want to thank my best friend Fan for her spiritual support and helpful conversations during the last stressful period, with her I have more courage to keep go on.

Vienna, August 24. 2018

Xin Zhao



---

List of included papers:

**Xin Zhao**, Victor Geskin and Robert Stadler

Destructive quantum interference in electron transport: A reconciliation of the molecular orbital and the atomic orbital perspective

*The Journal of Chemical Physics*, **146**, 092308 (2017)

**Xin Zhao**, Georg Kastlunger and Robert Stadler

Quantum interference in coherent tunneling through branched molecular junctions containing ferrocene centers

*Physical Review B* **96**, 085421 (2017)

**Xin Zhao**, Robert Stadler

Electron transport study in coherent tunneling through cyclic Ru/Os(PPh<sub>2</sub>)<sub>8</sub>(C<sub>2</sub>H<sub>4</sub>)<sub>4</sub> bis(pyridylacetylide) complexes

in preparation (2018)

**Xin Zhao**, Robert Stadler

Adsorption configuration prediction for Ferrocene compounds with different anchor groups in single-molecule junctions

in submission (2018)

---

## Abstract

---

This thesis is mainly focusing on the theoretical modeling of electron transport through molecules containing transition metals (Fe, Ru, Os), where the main contributions are,

i) electron transport in the coherent tunneling scheme where two models are evaluated in different perspective of orbital basis for understanding destructive quantum interference (DQI): one is the graphical rules which based on visually inspecting the connectivity of the carbon sites in conjugated  $\pi$  systems in an atomic orbital (AO) basis; the other focuses on the amplitudes and signs of the frontier molecular orbitals (MOs). We clarify the reconciliation between both models in terms of the zeroth order Green's function and compare their usability of predictions for a variety of systems. The conclusion we draw is that for a correct description of DQI from a MO perspective, it is necessary to include the contributions from all MOs rather than just those from the frontier orbitals, while graphical rules are applicable for all the systems we tested in this work while frontier MOs approximation fails to predict some cases properly. The graphical scheme in this sense has more general applicability.

ii) Double-branched molecules containing ferrocene moieties are of interest due to the fact that Fe(II) can be oxidized where asymmetry can be induced by oxidizing just one of the redox centers. If the symmetry of the two branches for electrons passing through is broken, DQI is supposed to occur. In these type of molecules, neither the graphical AO scheme nor the frontier orbital approximation can be applied to predict DQI since the ferrocene moiety is not part of the planar  $\pi$ -conjugated backbone. Hence we developed an atomic orbital (AO) fragment orbital (FO) scheme to illustrate the potential parameters causing DQI for these molecules containing ferrocene. We find that

---

the through-space coupling between left and right anchor groups is the decisive parameter that causes DQI appearing in the interesting region closer to the Fermi level regardless of the number of branches. We studied the charging effect by putting a counter charge chlorine in the junction and closer to one of the branches on the conductance, where we find that the charging effect rigidly shifted the transmission curves upward in the energy region but has no impact on the DQI feature we observed in the corresponding uncharged cases.

iii) When there are more spacer groups embedded in double-branched molecules, the decisive parameter through-space coupling we identified for the ferrocene molecules is vanishing due to the increased molecular length. We therefore want to see what is the impact of the expanded size on the conductance and more interestingly, will the vanishing through-space coupling enable the occurrence of DQI. Ru/Os(PPh<sub>2</sub>)<sub>8</sub>(C<sub>2</sub>H<sub>4</sub>)<sub>4</sub> bis(pyridylacetylde) compounds are investigated for this purpose.

iv) With the junction length increasing, the hopping process through the Ru/Os(PPh<sub>2</sub>)<sub>8</sub>(C<sub>2</sub>H<sub>4</sub>)<sub>4</sub> bis(pyridylacetylde) cyclic molecules in its respective symmetric (neutral) and asymmetric (charged) cases is intriguing. Within the Marcus theory framework we attempt to calculate the parameters for calculating hopping conductance for these cyclic molecules containing transition metals (Fe, Ru, Os). For the charged systems, spin-polarization is required for understanding the energy shift of the singly occupied orbital, since its energetic position defines the driving force, which is one of the key parameters in the Marcus theory.

v) We investigate the electrical transport properties of two type of molecular wires containing ferrocene moiety with same and different anchoring groups, 1,1'-bis(thiophenol-4-ethynyl)ferrocene and 1-(3-pyridylethynyl)-1'-(thiophenol-4-ethynyl)ferrocene, respectively, where a ferrocene moiety can be oxidized and in electron transport play a role as a switch between two redox states (Fe II/ Fe III), i.e. it allows for redox-gated control of the electron population at the ferrocene moiety as a switching mechanism between two redox states. It is interesting to see the influence on the conductance of the molecule containing different anchoring sites (pyridyl on one side and thiol on the other side) versus the same anchoring sites (thiol on each side) adsorbed to a STM-tip and a surface for forming a junction. The potential configurations formed in the

---

junctions and the trends of conductance variation for the two type of molecules are emphasized.

In the coherent transport scheme, destructive quantum interference is addressed, tight-binding (TB) methods and Larsson's formula are introduced for interpreting the reasons for DQI occurrence. The description of electronic structures and properties for single molecular junctions is based on the density functional theory (DFT) combined with the non-equilibrium Green's function formalism (NEGF). In this thesis both transport regimes are investigated, namely phase-coherent transport and two-step electron hopping. For the former a Landauer-Büttiker formalism is used, while for the latter three key parameters, namely the reorganization energy, the driving force and the transfer integral are needed for calculating the conductance within the framework of the semi-classical Marcus-Hush theory.

---

---

## Zusammenfassung

---

Diese Arbeit beschäftigt sich mit der theoretischer Modellierung des Elektronentransports durch Moleküle, die Übergangsmetalle (Fe, Ru, Os) enthalten. Deren Hauptbeiträge sind:

i) Elektronentransport im kohärenten Tunnelschema, für das zwei Modelle mit unterschiedlicher Orbitalbasis ausgewertet werden, um die destruktive Quanteninterferenz (DQI) zu verstehen: Zum einen die graphischen Regeln für  $\pi$ -Systeme auf einer Atomorbital (AO)-Basis, die auf der visuellen Überprüfung der Konnektivität der Kohlenstoffstellen im konjugierten Raum beruhen; der andere Modell konzentriert sich auf die Amplituden und Vorzeichen der Grenzorbitalorbitale (MOs). Wir erklären die Verbindung zwischen beiden Modellen durch Analyse der Green's Funktion 0-ter Ordnung und vergleichen ihre Verwendbarkeit für Vorhersagen für eine Vielzahl von Systemen. Die Schlussfolgerung die wir ziehen ist, dass für eine korrekte Beschreibung von DQI aus einer MO-Perspektive die Beiträge aller MOs und nicht nur die der Grenzorbitale einbezogen werden müssen. Während für alle Systeme, die wir in dieser Arbeit getestet haben, grafische Regeln gelten, die Näherung basierend auf Grenz-MOs einige Fälle kann nicht richtig vorhersagen. In diesem Sinne hat Das graphische Schema eine allgemeinere Anwendbarkeit.

ii) Doppelt verzweigt Moleküle, die Ferroceneinheiten enthalten, sind von Interesse, da nur eines der Redoxzentren Fe (II) oxidiert werden kann, wodurch Asymmetrie induziert werden kann. Wenn die Symmetrie der beiden Zweige für durchlaufende Elektronen gebrochen ist, sollte DQI auftreten. In diesem Typ von Molekülen kann weder das graphische AO-Schema noch die Grenzorbitalapproximation zur Vorhersage von DQI angewendet werden, da die Ferroceneinheit nicht Teil des planaren  $\pi$ -konjugierten Rückgrats ist. Daher haben wir ein

---

Atomorbital (AO) Fragment Orbital (FO) Schema entwickelt, um die entscheidenden Parameter zu finden, die DQI für diese Ferrocen enthaltenden Moleküle verursachen. Wir identifizieren Through-Space-Kopplung zwischen linken und rechten Ankergruppen als der entscheidenden Parameter, der bewirkt, dass DQI in der interessierenden Region unabhängig von der Anzahl der Verzweigungen näher an der Fermi-Ebene erscheint. Wir untersuchen den Ladungseffekt, indem wir eine Gegenladung Chlor in die Verbindung und näher zu einem der Zweige setzen. Wir finden, dass der Ladeeffekt verschiebt die Transmissionskurven im Energiebereich stark hat, aber keinen Einfluss auf die DQI. Die Ferrocen-Moleküle identifizierte entscheidende Parameter der Through-Space-Kopplung aufgrund der erhöhten Moleküllänge. Wir würden daher gerne sehen, was der Einfluss der expandierten Größe auf die Leitfähigkeit ist, und interessanterweise wird die verschwindende Through-Space-Kopplung das Auftreten von DQI ermöglichen. Zu diesem Zweck werden Ru/Os(PPh<sub>2</sub>)<sub>8</sub>(C<sub>2</sub>H<sub>4</sub>)<sub>4</sub> bis(pyridylacetylid) -Verbindungen untersucht.

iii) Wenn in doppelt verzweigt Molekülen mehr Spacer-Gruppen eingebettet sind, verschwindet der für die Ferrocen-Moleküle identifizierte entscheidende Parameter der Through-Space-Kopplung aufgrund der erhöhten Moleküllänge. Wir untersuchen daher, was der Einfluss die Moleküle Länge auf die Leitfähigkeit ist. Interessanterweise ermöglicht die verschwindende Through-Space-Kopplung das Auftreten von DQI. Zu diesem Zweck werden Ru/Os(PPh<sub>2</sub>)<sub>8</sub>(C<sub>2</sub>H<sub>4</sub>)<sub>4</sub> bis(pyridylacetylid) -Verbindungen untersucht.

iv) Mit steigender Verbindungslänge ist der Hopping-Prozess durch die Ru/Os(PPh<sub>2</sub>)<sub>8</sub>(C<sub>2</sub>H<sub>4</sub>)<sub>4</sub> bis(pyridylacetylid) zyclische Moleküle in ihren jeweiligen symmetrischen (neutralen) und asymmetrischen (geladenen) Zustand interessant. Im Rahmen der Marcus-Theorie versuchen wir, die Parameter für die Berechnung der Sprungleitfähigkeit für diese cyclischen Moleküle zu berechnen, die Übergangsmetalle (Fe, Ru, Os) enthalten. Für die geladenen Systeme ist eine Spinpolarisation erforderlich, um die Energieverschiebung eines einfach besetzten Orbitale zu verstehen, als die energetische Position des Orbital ist ein Schlüsselparameter der Marcus-Theorie.

v) Wir untersuchen die elektrischen Transporteigenschaften von zwei Arten von molekularen Drähten, die eine Ferroceneinheit mit gleichen und unter-

---

schiedlichen Ankergruppen enthalten, 1,1'-bis(thiophenol-4-ethynyl)ferrocene und 1-(3-pyridylethynyl)-1'-(thiophenol-4-ethynyl)ferrocene. Dort kann ein Ferrocenrest oxidiert werden und bei Elektronentransport die Rolle als Schalter zwischen zwei Redoxzuständen spielen (Fe II/Fe III), dh er erlaubt Redox-gesteuerte Kontrolle der Elektronenpopulation bei der Ferroceneinheit als Schaltmechanismus zwischen zwei Redoxzuständen agieren. Wir untersuchen den Einfluss von Molekülen mit verschiedenen Verankerungsstellen (Pyridyl auf der einen Seite und Thiol auf der anderen Seite) gegenüber der selben Verankerungsstelle (Thiol auf jeder Seite) an einer STM Spitze und einer Oberfläche auf die Leitfähigkeit.

In dem kohärenten Transportschema wird die destruktive Quanteninterferenz behandelt, Tight-Binding (TB) -Methoden und Larssons Formel werden eingeführt um die Gründe für das DQI-Auftreten zu interpretieren. Die Beschreibung elektronischer Strukturen und Eigenschaften für einzelne molekulare Verbindungen basiert auf der Dichtefunktionaltheorie (DFT) in Kombination mit dem Nicht-Gleichgewichts-Green's funktionformalismus (NEGF). In dieser Arbeit untersuchen wir sowohl phasenkohärente Transport und Elektronen hopping. Für ersteres benutzen wir den Landauer-Büttiker -Formalismus, während für die Berechnung des hopping Leitfähigkeit, semi-klassische Marcus-Hush-Theorie mit den drei Schlüsselparameter, nämlich die Reorganisationsenergie, die "driving force" und das Transferintegral verwenden.



---

---

## Contents

---

<b>Contents</b>	<b>13</b>
<b>1 Introduction</b>	<b>15</b>
<b>2 Density Functional Theory (DFT)</b>	<b>19</b>
2.1 The many-body problem . . . . .	19
2.1.1 The Hohenberg-Kohn Theorems . . . . .	20
2.1.2 The Kohn-Sham Equations . . . . .	21
2.1.3 The Local-Density Approximation (LDA) . . . . .	23
2.1.4 The Generalized Gradient Approximation(GGA) . . . . .	24
2.2 The Projector Augmented Wave (PAW) method . . . . .	24
<b>3 Non-Equilibrium Green's Function (NEGF) Formalism</b>	<b>29</b>
3.1 Landauer Büttiker Theory . . . . .	31
<b>4 Destructive Quantum Interference in Electron Transport</b>	<b>35</b>
4.1 Motivation . . . . .	35
4.2 Pairing Theorem and Frontier Orbital Approximation . . . . .	37
4.2.1 Larsson's Formula . . . . .	39

## CONTENTS

---

4.2.2	Numerical Studies . . . . .	41
4.2.3	Graphical Scheme . . . . .	42
<b>5</b>	<b>Quantum Interference for Branched Molecules Containing Ferrocene in the Junctions</b>	<b>47</b>
5.1	Motivation . . . . .	47
5.2	Theoretical/Computational methods . . . . .	48
5.3	QI Feature in Transmission Functions . . . . .	51
5.4	Computational Tools Used for the Interpretation of Destructive Quantum Interference Effects . . . . .	56
5.4.1	Localized Basis Representation . . . . .	56
5.4.2	Fragment Orbitals and Effective Coupling Model . . . . .	58
5.5	Atomic Orbital (AO) Analysis . . . . .	64
5.5.1	Identifying the Sources for Destructive Quantum Interference (DQI) . . . . .	68
5.5.2	Simplified Hamiltonian for Analyzing the Source of DQI from a Mathematical Point of View . . . . .	69
5.6	Charging effect . . . . .	73
<b>6</b>	<b>Electron Transport Study in Coherent Tunneling Through Cyclic Ruthenium / Osmium Complexes</b>	<b>83</b>
6.1	Motivation . . . . .	83
6.2	Computational details for the NEGF-DFT calculations . . . . .	85
6.3	Results and discussion . . . . .	86
6.3.1	Comparison of a simplified $3 \times 3$ Hamiltonian for single branch Ferrocene, Ruthenium molecules . . . . .	90
		12

---

6.3.2	Conclusions from the TB analysis . . . . .	96
6.4	Effect of Charging . . . . .	97
6.5	Summary . . . . .	102
<b>7</b>	<b>Electron Hopping (Incoherent Electron Transport)</b>	<b>103</b>
7.1	Motivation . . . . .	103
7.2	Marcus-Hush Theory . . . . .	104
7.3	The Influence of Charging . . . . .	110
<b>8</b>	<b>Configuration Prediction for Ferrocene Compounds with Different Anchor Groups in Single-Molecule Junctions</b>	<b>115</b>
8.1	Motivation . . . . .	115
8.2	Geometry Adoption/Choice of geometries . . . . .	117
8.3	Theoretical/Computational methods . . . . .	122
8.4	Voltage and structure dependence of the conductance . . . . .	123
8.4.1	Analysis of the Dependence of the Conductance on the Junction Length in Terms of Fermi Level Alignment . . . . .	125
8.5	Summary . . . . .	131

CONTENTS

---

# CHAPTER 1

---

## Introduction

---

Single transistor (size of 100 nm scale) devices were first produced by researchers in the early 2000s [1], the present standard smallest commercial transistor components (around 67 silicon atoms) in a microprocessor is available from *Intel*. In 2017, IBM revealed that they had created silicon chips scaling down to 5 nm. For microprocessors with transistors smaller than 7nm the quantum mechanical wave nature cannot be ignored, and the quantum tunneling through its logic gates has a strong influence on device operation, e.g. conductance. This makes nano-scale systems fundamentally differ from the macroscopic device where classic models like Ohm's law [2, 3, 4, 5] does not apply.

The field of molecular electronics has been active for more than 40 years since Aviram and Ratner originally proposed a single molecule as a device, namely a molecular rectifier [6]. Since mid 1990s experimental advances helps the electronic characterization [7, 8, 9, 10], and then promotes the molecular electronics field. Single molecule electronics is a field which aims at maintaining a continuous rise in performance of digital devices even once the lower threshold for miniaturization faced by the semiconductor industry has been reached (where the current threshold for device operation is a key limiting condition for designing parameters since it determines the heating of the device). Molecules can self-organize when absorbed to electrodes, which is an essential advantage for overcoming the the technology difficulties.

Branched molecules containing a redox active center in each of their two branches might open up intriguing new possibilities also independent on

the respective electron transport regimes. For phase coherent electron tunneling, wave-like interference effects might be induced due to an asymmetry caused by the use of different metals in the two branches or by charging one of the branches, which might be an enabling tool for device design. In the hopping regime on the other hand a local gating effect might be achieved, because the charge on the metal in one branch possibly has an influence on the electron transport through the other, thereby offering a route towards chemical sensors. Within this thesis both possibilities will be investigated with theoretical simulations based on density functional theory for a series of target molecules. The semiclassical Marcus theory will be involved for describing electron hopping and a non-equilibrium Greens function approach for the description of phase coherent tunneling. There are two setups in experiments for forming single molecule junctions, namely Scanning Tunneling Microscope (STM) [10, 11, 12] and Mechanically Controlled Break Junctions (MCBJs) [13, 14, 15, 16, 17]. In STM method a conducting STM tip approaches the nearest atom on the sample and drags an atomic chain up during the withdrawing process. The idea of the MCBJ technique is to fabricate nanocontacts by pulling a ductile metal wire until it narrows down and eventually breaks and then let the ends of the contact approach each other again, where single molecule can be trapped in the process.

The main goal of this thesis is a theoretical characterization of the electron transport of single molecule junctions under electrochemical conditions in which the molecules are attached to two gold leads, where for both transport regimes a big challenge lies in the independent adjustment of the oxidation state of the two redox-active centers in the investigated molecules. The investigated molecules differ in various structural aspects from each other such as anchoring sites and chemical nature of the metal center which result in markedly different transport characteristics. This work will aim at an explanation of distinctive properties found for individual molecules. Acknowledging that the synthesis of larger metal-organic complexes is a formidable challenge for organic chemists, the theoretical screening of the properties of similar compounds with potentially decisive differences in their electronic properties with respect to electron transport is also meant to provide guidelines in terms of which compounds should be aimed for regarding particular applications. The fundamental question in the field of molecular electronics is: when electrons move through a

single molecule, how does an organic complex play a role in the perspective of structure and metallic property for transmission? How to interpret the electron as wave-particle duality? This question actually can be addressed by using non-equilibrium Green's function techniques (NEGF). NEGF techniques for electron transport problems on the molecular scale are used by different groups, and the agreement between simulations and experiments has improved considerably in recent years [18], [19].

Quantum interference (QI) effects have been found to significantly reduce the conductance in some single molecule junctions containing conjugated  $\pi$  systems where graphical rules could be derived to predict their occurrence from the molecular structure [20, 21]. QI effects could be applied for logical gates [22] and data storage [23] in single molecule electronics, and have been suggested as a general tool for the implementation of various type of single molecule devices.

This thesis is organized as follows: The next two chapters 2, 3 I will talk about density functional theory and non-equilibrium Green's function, based on which we conduct all the calculations. The fourth chapter 4 is about destructive quantum interference (DQI) for various type of molecules, and I focus on the topic under which condition DQI occurs. Chapters 5 and 6 of this thesis are the analysis of DQI on particular double-branched cyclic molecules from a size range of 8 Å to 21 Å. Chapter 7 is about electron hopping, within the framework of Marcus-Hush theory [24, 25, 26]. For cyclic molecules when its length increases, hopping regime as one of the electron transport mechanisms will play an important role for conductance, this process will be influenced by temperature as well as the oxidation states of the metal complex. We came up with two charging schemes, namely external charge and chlorine induced charge where the latter creates an asymmetry by manually putting chlorine atom closer to one of the branches, hence it would be interesting to see how the charge accommodates respectively on two branches after one of the metal centers is oxidized. The last chapter 8 is about the prediction for molecular geometries in the junction, the investigation of the conductance dependence on configurations through ferrocene compounds with different anchor groups in single-molecule junctions can be used for predicting the experimental measurements. In this work, I put emphasis on predicting the potential junction



geometries, the impact of molecular and interface dipole moments are considered and charge distribution over each molecule and metal surface when they form a junction is calculated to illustrate their interaction in the interface.

All the calculations are done with the GPAW code and the atomic simulation interface (ASE), which is based on density functional theory (DFT) and use the projector-augment wave (PAW) method, in this thesis linear combination of atomic orbitals(LCAO) basis set for the wave functions is used.

## CHAPTER 2

---

### Density Functional Theory (DFT)

---

#### 2.1 The many-body problem

The electronic many-body problem consists of finding the solutions of the Schrödinger equation for a system of  $N$  interacting non-relativistic electrons,

$$\hat{H}\Psi_i(\mathbf{r}_1\sigma_1, \dots, \mathbf{r}_N\sigma_N) = E_i\Psi_i(\mathbf{r}_1\sigma_1, \dots, \mathbf{r}_N\sigma_N) \quad (2.1)$$

considering the spin  $\sigma_i$ , where the wave function  $\Psi_i$  tells us the quantum state of the system, in most cases  $\hat{H}$  is the operator corresponding to the total energy of the system. Solving the full many-body Eq. 2.1 is a tough numerical problem, since the number of parameters required to establish a reasonably accurate  $\Psi$  grows exponentially when the number of electrons increase. In general the many-electron wave function  $(\mathbf{r}_1\sigma_1, \dots, \mathbf{r}_N\sigma_N)$  for a system of  $N$  electrons is not a legitimate scientific concept when  $N \geq 10^3$  (Kohn, 1999). Within the Born-Oppenheimer approximation due to the large difference of masses between nuclei and electrons ( $M_I / m_e \approx 10^3$ ), the electrons are considered as moving in a field of fixed nuclei, and the nuclei are affected by an effective potential generated by the electrons, so the movement of electrons and nuclei can be considered to be decoupled and the Hamiltonian of the  $N$ -electron system then can be reduced to,

$$\hat{H} = -\sum_{i=1}^N \frac{1}{2} \nabla_i^2 - \sum_i^N \sum_I^M \frac{Z_I}{|\mathbf{r}_i - \mathbf{R}_I|} + \frac{1}{2} \sum_{i \neq j} \frac{1}{|\mathbf{r}_i - \mathbf{r}_j|} = T + \hat{V}_{ext} + \hat{V}_{ee} \quad (2.2)$$

where  $\hat{V}_{ee}$  is the two-body interaction operator. There are several schemes, Hartree-Fock, DFT used for mapping it into an effective single particle potential.

### 2.1.1 The Hohenberg-Kohn Theorems

The variational principle in quantum mechanics states that the expectation energy computed from an unknown wave function  $\Psi$  is an upper bound to the true ground-state energy  $E_0$ . Full minimization of the functional  $E[\Psi]$  with respect to all allowed  $N$ -electrons wave functions will give the true ground state  $\Psi$  and its energy  $E_0$ ,

$$E_0 = \min_{\Psi \rightarrow N} \langle \Psi | T + \hat{V}_{ext} + \hat{V}_{ee} | \Psi \rangle \quad (2.3)$$

**The First Hohenberg-Kohn (HK) theorem** is to separate Eq. 2.3 into two parts where the first term is the universal term which is independent of the system,

$$F^{HK} = \min_{\Psi \rightarrow N} \langle \Psi | T + \hat{V}_{ee} | \Psi \rangle \quad (2.4)$$

the second term in Eq. 2.3 is a functional of merely the electronic density  $\int d\mathbf{r} n(\mathbf{r}) V_{ext}(\mathbf{r})$  where  $n(\mathbf{r})$  is the electron density which is defined as the probability to find electrons in the volume  $\int d\mathbf{r}$ . Since  $F^{HK}$  is universal (independent of the system), the minimum  $E_0$  only depends on the density, meaning that from the ground state density  $n_0(\mathbf{r})$ , the external potential can then be determined uniquely, Hamiltonian and other properties of the system can be defined such as, the energy as functional  $E[n_0(\mathbf{r})]$ , the kinetic energy as  $T[n_0(\mathbf{r})]$ , and the electron-electron interaction as  $\hat{V}_{ee}[n_0(\mathbf{r})]$ . Physical observables are then obtained from expectation values, which are functionals of  $n_0(\mathbf{r})$  as well.

**The second HK theorem** states that  $F^{HK}$  delivers the lowest energy if the input density is the true ground state density.  $\hat{V}_{ee}(\mathbf{r})$  can be divided into two parts where the first part is the classic coulomb term  $\hat{V}_H[n_0(\mathbf{r})] = \frac{1}{2} \int \int \frac{n(\mathbf{r})n(\mathbf{r}')}{|\mathbf{r} - \mathbf{r}'|} d\mathbf{r}d\mathbf{r}'$  (atomic units are used through out this thesis), the second part contains non-classic electron-electron interactions: such as exchange and correlation. While the explicit form of the non-classic part of functional  $F^{HK}$  is a major challenge of DFT.

### 2.1.2 The Kohn-Sham Equations

In 1965 Kohn and Sham [27] proposed an approach to overcome the problem of inaccurate approximations for the kinetic energy functional in  $F^{HK}$  with Thomas-Fermi model and Orbital-free DFT, where the assumption is that for an interacting  $N$  electrons system with non-uniform ground-state density  $n_0(\mathbf{r})$ , there is an equivalent non-interacting electron system with the same ground state density as the interacting system. For an interacting system the electrons are interacting with each other so the Hamiltonian operates on all electrons, Schrödinger equation (SE) is constructed and needs to be solved to obtain exact wavefunction for all interacting electrons. While for a non-interacting system one electron is moving in an "average" potential caused by the rest of the electrons in the system (for Kohn-Sham non-interacting electrons this potential is caused by the electrons under the Kohn-Sham assumption), SE is constructed for one electron, to obtain approximate wavefunction for all electrons one combines many one-electron wavefunctions. It is more accurate to do DFT calculations for the non-interacting system since its kinetic energy expression  $T_{non} = -\frac{1}{2}\nabla^2$  is exact (no needs for approximation). From the universal functional  $F^{HK}$ , the unknown expressions are the kinetic energy  $T[n_0(\mathbf{r})]$  and the electron-electron interaction term (non-classic contribution). We firstly consider a non-interacting system by omitting  $\hat{V}_{ee}$ , where by applying the Hohenberg-Kohn theorem, the Hamiltonian can be written as,

$$H_{non} = T + \hat{V}_{ext} = T[n] + \int d^3r n(\mathbf{r}) \hat{V}_{ext}(\mathbf{r}) \quad (2.5)$$

for such a non-interacting many-body ground-state, the wave function is a single Slater determinant, where single particle orbitals  $\Psi_i(\mathbf{r})$  are obtained solving the Schrödinger equation. The corresponding ground-state density is then obtained from  $n_0(\mathbf{r}) = \sum_i^N |\Psi_i(\mathbf{r})|^2$ . Within an effective single particle picture, one can then rewrite the energy functional as,

$$E_{n, \hat{V}_{ext}}^{HK} = \sum_i \langle \Psi_i | -\frac{1}{2} \nabla^2 + \hat{V}_{ext} | \Psi_i \rangle + \hat{V}_H[n] + E_{xc}[n] \quad (2.6)$$

where  $\hat{V}_H[n] = \int \frac{n(\mathbf{r}')}{|\mathbf{r} - \mathbf{r}'|} d\mathbf{r}'$  is the Hartree potential (Coulomb term), and the remaining contributions exchange-correlation energy  $E_{xc}[n]$  as,

$$E_{xc}[n] = T[n] - T_{non}[n] + \hat{V}_{ee}[n] - \hat{V}_H[n] \quad (2.7)$$

Now we define:

$$\hat{V}_{eff}[n] = \hat{V}_{ext}[n] + \hat{V}_H[n] + \hat{V}_{xc}[n] \quad (2.8)$$

where  $\hat{V}_{xc}[n] = \frac{\partial E_{xc}[n]}{\partial n}$  and the single particle Schrödinger equation for solving the ground-state density of interaction system becomes,

$$\left(-\frac{1}{2}\nabla^2 + \hat{V}_{eff}[n]\right)\Psi_i(\mathbf{r}) = \varepsilon_i\Psi_i(\mathbf{r}) \quad (2.9)$$

In kohn-Sham approach one needs firstly to find a  $\hat{V}_{eff}[n]$  which is equal to kohn-Sham potential so that the  $n_0[\mathbf{r}]$  of the system is equal to the kohn-Sham ground-state density, then obtain the wavefunction with Slater determinant for the kohn-Sham non-interacting electrons and build the density  $n_0[\mathbf{r}]$  so as the ground state energy  $E_0[\mathbf{r}]$ . Once we know 2.8 and 2.9 one can insert  $\hat{V}_{eff}$  into the one-particle equation, which in turn determine the orbitals and the ground-state density so as the energy in Eq. 2.6 which is written as the sum of the kinetic energy part in terms of a functional of the molecular orbitals and functionals of the density for the rest of energy contributions. The Kohn-Sham equations have to be solved iteratively.

The exchange and correlation (xc) energy functional in density functional theory is undefined (in exact analytical) terms but important functional of  $n_0$  in Kohn-Sham DFT, the crucial approximation is the relation between the interacting system and the non-interacting system under kohn-Sham assumption. The exchange-correlation term describes the effects of the Pauli principle and the coulomb potential beyond a pure electrostatic interaction of the electrons, if one would know the exact exchange-correlation potential then we would solve the many-body problem exactly, a sufficiently accurate and computationally conventional approximation is needed. The xc-energy can be viewed as the energy resulting from the interaction between an electron and its exchange-correlation hole [28], the separation of electrostatic and exchange-correlation energies can be viewed as an approximate separation of the consequences of long- and short-range effects of the coulomb interaction. We can then expect that the total interaction energy will be less sensitive to the changes in density for the long-range part, which can be calculated exactly. Hence only local contributions (short-range effect) is accounted in  $E_{xc}[n]$ , which means it must be possible to define the exchange-correlation energy by local or nearly local approximations. Most functional approximations are based on The local density (LD) and local spin density (LSD) approximations.

### 2.1.3 The Local-Density Approximation (LDA)

The Local-Density approximation (LDA) is originally proposed by Kohn and Sham in 1965 [27] as the first and simplest approximate exchange-correlation functionals and was rationalized by using a reasonable slowly varying spatial density. Here the exchange-correlation energy is expressed as,

$$E_{xc}^{LDA}[n] = \int n(\mathbf{r})\epsilon_{xc}[n(\mathbf{r})]d\mathbf{r} \quad (2.10)$$

where  $\epsilon_{xc}[n(\mathbf{r})]$  is the exchange-correlation (xc) energy per particle of a homogeneous electron gas and the xc potential  $V_{xc}$  then can be expressed as,

$$V_{xc}^{LDA}[n] = \frac{\partial E_{xc}^{LDA}[n]}{\partial n} \quad (2.11)$$

where the energy density  $\epsilon_{xc}[n(\mathbf{r})]$  can be separated further into exchange and correlation contributions,

$$\epsilon_{xc}[n(\mathbf{r})] = \epsilon_x[n(\mathbf{r})] + \epsilon_c[n(\mathbf{r})] \quad (2.12)$$

As was originally derived by Dirac [29], in a system where the density is not homogeneous the exchange-energy is obtained by applying the homogeneous electron gas results pointwise resulting in,

$$\epsilon_x[n(\mathbf{r})] = -\frac{3}{4}\left(\frac{3n(\mathbf{r})}{\pi}\right)^{1/3} \quad (2.13)$$

The LDA actually is based on a real physical system so that the exact conditions should be considered such as sum rules (an electron present at the point  $\mathbf{r}$  reduces the probability of finding one at  $\mathbf{r}+\mathbf{fl}$ , i.e. xc-hole contains one electron) and other constraints on the xc hole. In praxis, the LDA is implemented in a more general spin-polarized form (LSDA) with,

$$E_{xc}^{LSDA} = \int d\mathbf{r}n(\mathbf{r})\epsilon_{xc}^{LDA}(n_{\uparrow}(\mathbf{r}), n_{\downarrow}(\mathbf{r})) \quad (2.14)$$

due to the fact that it is not free of self-interaction, LDA has a wrong asymptotic trend of exchange-correlation potential. The respective errors in exchange and correlation energy tend to partially canceled within LDA. In praxis, covalent bonds, metallic bonds and ionic bonds are generally well described, while the accuracy of LDA is not sufficient for most applications, for example, binding energies of molecules and cohesive energies of solids are usually overestimated. In strongly correlated systems such as insulating 3 *d*-transition metal oxides, local spin density approximation predicts them wrongly as metallic properties.

### 2.1.4 The Generalized Gradient Approximation(GGA)

The idea of the generalized gradient approximation(GGA) is to construct xc functionals which do not only depend on the local density but also on its gradient  $\nabla n(\mathbf{r})$ , which is a better approximation accounting also for non-homogeneous parts of the electron density distribution,

$$E_{xc}^{GGA}[n_{\uparrow}, n_{\downarrow}] = \int d^3r \epsilon_{xc}^{GGA}(n_{\uparrow}(\mathbf{r}), n_{\downarrow}(\mathbf{r}), |\Delta n_{\uparrow}(\mathbf{r})|, |\Delta n_{\downarrow}(\mathbf{r})|) \quad (2.15)$$

There are many GGA functionals developed over years [30, 31, 32], among them Perdew, Burke and Ernzerhof (PBE) functional [33] has been used in this thesis. PBE has the advantages: in the lower limit  $t \rightarrow 0$  (slowly vary) Hamiltonian is given as the second-order gradient expansion, in the upper limit  $t \rightarrow \infty$  (rapidly vary) correlation vanishes, in the high density limit it cancels the logarithmic singularity of  $\epsilon_c^{LDA}$ .

## 2.2 The Projector Augmented Wave (PAW) method

Within the frozen core approximation that is assuming that atomic core states are mostly localized within so-called augmentation spheres and neglecting their adjustment during the formation of bonds in solids or molecules, wave functions in real materials have different characteristics in different region of space, when toward the nucleus (core states) wave functions oscillate rapidly due to the large attractive potential of the nucleus. So a large number of plane waves are needed to adequately describe the wavefunction and the nuclear potential, which leads to a numerical treatment of the core states problematic.

Pseudopotentials which was developed in the 1960s [34, 35, 36] as a way to solve Schrödinger equation for bulk crystals without knowing exactly the potential experienced by an electron in the lattice, where the nuclei and core electrons are described with a smoother effective potential. It is assumed that the core electrons are tightly bound to their nuclei, as the core electrons remain unchanged in most situations they can be replaced along with the nuclear potential to create a relatively weak pseudopotential, the valence and conduction band electrons outside of the core region, which are identical to the wavefunctions where all the electrons are taken into account are influenced only

by this potential. The pseudopotential method gives surprisingly accurate results considering the computing time and effort involved, while the drawback of this approach is that calculations are only done for the valence states and it is lack of the information on the Kohn-Sham wave functions even for the valence electrons near to the nuclei.

The projector augmented wave (PAW) method was firstly introduced by Blöchl in 1994 [37] and it is generalized in the way that partial-wave expansions are determined by the overlap with localized projector functions thus pseudopotential approach based on generalized separable pseudopotentials can be obtained by a simple approximation. The idea of PBE method is to divide the wave functions into two regions, namely, a region within an atom centered sphere  $a$  and a region outside this sphere, where a partial-wave expansion is used to describe the wave functions within  $a$  and envelope functions (plane waves or other convenient basis set) for the outside region, the two are matched with value and derivative at the sphere radius  $a$ . The setup has been implemented in GPAW code, the PAW approach combines the methods of both the pseudopotential method (computational efficiency) and the linear augmented-plane-wave method (accuracy).

The PAW method is a way to transform the wave functions that orthogonal to the core states which have strong oscillations into a new, so-called pseudo (PS) wave functions  $\tilde{\Psi}$  which are computationally convenient smooth functions, where the PS wave functions are represented with a tilde,

$$|\Psi(\mathbf{r})\rangle = \tilde{\tau}\tilde{\Psi}(\mathbf{r}) = \sum_i |\Phi_i(\mathbf{r})\rangle c_i \quad (2.16)$$

here  $\tilde{\Psi}$  are smooth auxiliary functions, which can be represented with a plane wave expansion.  $\Psi$  is the all-electron valence states,  $\tilde{\Psi}$  is the local basis set expansion,  $\tilde{\tau}$  is a transformation operator, which only operates on the functions that located in the augmentation region ( $< r_a$ ) while in the region outside  $r_a$ , all-electron (AE) and PS wave functions should be identical. For Eq. 2.16 to hold, some requirements are needed for this operator: it has to be a linear algebraic operator which is local in the sense that there are no interactions between atom-centered spheres. Then the partial wave functions  $\Phi_i$  inside the sphere can be transformed into numerically convenient auxiliary functions using,

$$\tilde{\tau} = 1 + \sum_{r_a} \sum_i |\Delta\Phi_i^a\rangle \langle \tilde{p}_i^a| \quad (2.17)$$



with  $\Delta\Phi_i^a = \Phi_i^a - \tilde{\Phi}_i^a$  within the sphere  $a$ , and  $\Phi_i^a = \tilde{\Phi}_i^a$  outside the sphere. Partial wave functions  $\Phi_i^a$  and  $\tilde{\Phi}_i^a$  are represented as radial functions. Each projector function  $\tilde{p}_i^a$  must be localized within an augmentation region and obey,

$$\langle \tilde{p}_i^a | \tilde{\Phi}_j^a \rangle = 1, \quad (2.18)$$

$$\langle \tilde{p}_i^a | \tilde{\Phi}_j^a \rangle = \delta_{i,j}, |\mathbf{r} - \mathbf{R}^a| < r_c^a \quad (2.19)$$

For obtaining physical quantities one needs to evaluate expectation values of an operator  $\hat{O}$ , in PAW formalism the expectation value can be expressed in terms of either the true or the auxiliary wavefunctions, for a local one-particle operator  $\langle A \rangle$  it is formulated as,

$$\begin{aligned} \langle A \rangle = \sum_n f_n \langle \Psi_n | A | \Psi_n \rangle &= \sum_n f_n \langle \tilde{\Psi}_n | A | \tilde{\Psi}_n \rangle + \sum_{i,j} D_{i,j} \langle \Phi_n^a | A | \Phi_n^a \rangle \\ &\quad - \sum_{i,j} D_{i,j} \langle \tilde{\Phi}_n^a | A | \tilde{\Phi}_n^a \rangle + \sum_n \langle \Psi_n^c | A | \Psi_n^c \rangle \end{aligned} \quad (2.20)$$

with

$$D_{i,j} = \sum_n \langle \tilde{p}_i | \tilde{\Psi}_n \rangle f_n \langle \tilde{\Psi}_n | \tilde{p}_j \rangle \quad (2.21)$$

where  $n$  is the band index and  $f_n$  the occupation of the state,  $D_{i,j}$  is the one-center density matrix, the indices  $i, j$  run over all valence states and only the indices on the same atom are summed over (on-site approximation). The second and third terms in Eq. 2.20 are neglected for operators such as the kinetic energy and the real space projection operator because they vanish for a sufficiently local operator \* as long as the partial is converged since the partial waves are pairwise identical outside the augmentation region, which produces the electron density. The last term  $\sum_n \langle \Psi_n^c | A | \Psi_n^c \rangle$  is the core contribution within the augmentation sphere.

**Electron Density** The electron density is defined by a plane wave part as well as two expansions in the form of radial functions times spherical harmonics as following the above scheme,

$$n(\mathbf{r}) = \sum_n f_n |\Psi_n|^2 = \tilde{n}(\mathbf{r}) + n^a(\mathbf{r}) - \tilde{n}^a(\mathbf{r}) \quad (2.22)$$

---

\*an operator which does not correlate separate parts of space, i.e.  $\langle \mathbf{r} | O | \mathbf{r}' \rangle = 0$  if  $\mathbf{r} \neq \mathbf{r}'$ .

with

$$\tilde{n}(\mathbf{r}) = \sum_n f_n \tilde{\Psi}_n^*(\mathbf{r}) \tilde{\Psi}_n(\mathbf{r}) + \tilde{n}^c(\mathbf{r}) \quad (2.23)$$

$$n^a(\mathbf{r}) = \sum_{i,j} \tilde{\Phi}_i^*(\mathbf{r}) D_{i,j} \tilde{\Phi}_j(\mathbf{r}) + n^c(\mathbf{r}) \quad (2.24)$$

$$\tilde{n}^a(\mathbf{r}) = \sum_{i,j} \tilde{\tilde{\Phi}}_i^*(\mathbf{r}) D_{i,j} \tilde{\tilde{\Phi}}_j(\mathbf{r}) + \tilde{n}^c(\mathbf{r}) \quad (2.25)$$

where  $\tilde{n}^c(\mathbf{r})$  is a smooth function for the description of the decay of the core density outside the augmentation spheres. An arbitrary operator  $\hat{B}$  which is purely localized within an atomic region is added to improve the convergence problem of the operator  $\hat{A}$ . One can use the identity between the auxiliary wavefunction of  $\hat{B}$  and its own partial wave expansion,

$$\langle \tilde{\Psi}_n | B | \tilde{\Psi}_n \rangle - \langle \tilde{\Psi}_n^a | B | \tilde{\Psi}_n^a \rangle = 0 \quad (2.26)$$

for the case where operator  $\hat{A}$  is not be well behaved the operator  $\hat{B}$  is added to the plane wave part and the matrix elements with its one-center expansions to improve the plane-wave convergence.

**Total Energy** Within PAW the total energy is calculated as the same of three contributions,

$$E = \tilde{E} + E^a - \tilde{E}^a \quad (2.27)$$

with

$$\begin{aligned} \tilde{E} = \sum_n f_n \langle \tilde{\Psi}_n | -\frac{1}{2} \nabla^2 | \tilde{\Psi}_n \rangle + E_H[\tilde{n}(\mathbf{r}) + \hat{n}(\mathbf{r})] + E_{xc}[\tilde{n}(\mathbf{r})] \\ + \int d^3r \bar{v}(\mathbf{r}) \tilde{n}(\mathbf{r}) \end{aligned} \quad (2.28)$$

$$E^a = \sum_n D_{i,j} \langle \tilde{\Phi}_i | -\frac{1}{2} \nabla^2 | \tilde{\Phi}_j \rangle + E_H[n^a(\mathbf{r}) + Z(\mathbf{r}) + E_{xc}[n^a(\mathbf{r})] \quad (2.29)$$

$$\begin{aligned} \tilde{E}^a = \sum_n D_{i,j} \langle \tilde{\tilde{\Phi}}_i | -\frac{1}{2} \nabla^2 | \tilde{\tilde{\Phi}}_j \rangle + E_H[\tilde{n}^a(\mathbf{r}) + \hat{n}(\mathbf{r})] + E_{xc}[\tilde{n}^a(\mathbf{r})] \\ + \int d^3r \bar{v}(\mathbf{r}) \tilde{n}^a(\mathbf{r}) \end{aligned} \quad (2.30)$$

In all three equations above, the respective first term corresponding to the kinetic energy, the second term to the Hartree energy, and the last term to the exchange and correlation energy. In Eq. 2.29,  $Z(\mathbf{r})$  accounts for the contribution of the charge density of the nucleus. An arbitrary potential  $\bar{v}(\mathbf{r})$  localized

in the augmentation region is added to the term  $\tilde{E}$  and  $\tilde{E}^a$ , with its contribution vanishing outside the augmentation region, it is used for the completeness of the partial wave expansion but does not have a physical meaning.

## CHAPTER 3

---

### Non-Equilibrium Green's Function (NEGF) Formalism

---

In this thesis the a Non-Equilibrium Green's function formalism [38] has been used, which is an approach for coherent electron tunneling and describes the response of a system to a perturbation, this is a numerically efficient way to evaluate the conductance for coherent electron tunneling through a nano-junction without having to calculate the scattering states explicitly within Landauer-Büttiker theory, the conductance  $G$  is defined as,

$$G = \mathcal{G}_0 \mathcal{T}(E) \quad (3.1)$$

where  $\mathcal{G}_0 = 2e^2/h$  is the quantum unit of the conductance and  $\mathcal{T}(E)$  is the transmission probability for incoming electrons moving through a junction in dependence on their kinetic energy  $E$ .

As the simplified example we consider a system with a single energy level  $\varepsilon$  contacted to source and drain electrodes. The number of electrons in this system depends on the equilibrium state to the Fermi level defined by the work functions of the two contacts, when a bias is applied, where we denote the respective Fermi levels for source and drain by  $\mu_L$  and  $\mu_R$  as depicted in figure 3.1, where  $\mu_L = E_f + qV/2$ ,  $\mu_R = E_f - qV/2$  and the current in the device is determined by the rate equations,

$$I_L = q\gamma_L/\hbar(f_L - N) \quad (3.2)$$

$$I_R = q\gamma_R/\hbar(N - f_R) \quad (3.3)$$

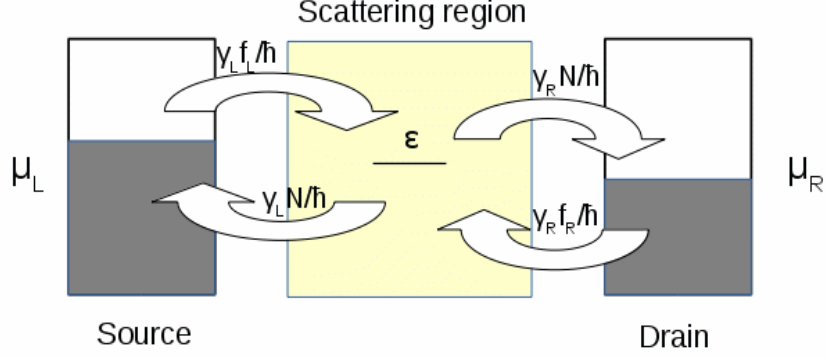


Figure 3.1: Flow of electrons in a single level picture derived from rate equations.

with  $\gamma_{L,R}/\hbar$  the rate constant and  $f_{L,R}$  the Fermi Dirac function.

$$f_{L/R}(E) = \frac{1}{\exp(\epsilon - \mu_{L,R})/k_B T + 1} \quad (3.4)$$

When  $I_L = I_R = I$ , namely no net current flow through the device, we can obtain the steady state electron occupation of the single level,

$$N = \frac{\gamma_L}{\gamma_L + \gamma_R} f_L(\epsilon) + \frac{\gamma_R}{\gamma_L + \gamma_R} f_R(\epsilon) \quad (3.5)$$

and the current,

$$I = \frac{q}{\hbar} \frac{\gamma_L \gamma_R}{\gamma_L + \gamma_R} [f_L(\epsilon) - f_R(\epsilon)] \quad (3.6)$$

where a factor 2 would need to be included in Eq. 3.6 to account for the spin degree of freedom. The equations illustrate that the flow through the level is proportional to the Fermi-Dirac functions  $f_{L/R}$ , and the level occupation  $N$  is dependent on the couplings  $\gamma_L$  and  $\gamma_R$  (Eq. 3.5). Current flows because of simultaneously equilibration with higher lying  $\mu_L$  and lower lying  $\mu_R$ , when the Fermi levels of source and drain equalize or molecular eigenstate  $\epsilon$  is outside the gap between  $\mu_L$  and  $\mu_R$ , the continuous flow of electrons stops. The couplings of the single molecular state to the two contacts lead to the broadening of the molecular level from a discrete level into a distribution,

$$D(E) = \frac{\gamma/2\pi}{(E - \epsilon)^2 + (\gamma/2)^2} \quad (3.7)$$

this broadening function is a Lorentzian distribution centered at  $\epsilon$ , where  $\gamma = \gamma_L + \gamma_R$ . Considering the broadening, Eqn. 3.5 and 3.6 need to be modified

as integration over the energy spectrum,

$$N = \int_{-\infty}^{\infty} dE D(E) \left[ \frac{\gamma_L}{\gamma_L + \gamma_R} f_L(\varepsilon) + \frac{\gamma_R}{\gamma_L + \gamma_R} f_R(\varepsilon) \right] \quad (3.8)$$

$$I = \frac{q}{\hbar} \int_{-\infty}^{\infty} dE D(E) \frac{\gamma_L \gamma_R}{\gamma_L + \gamma_R} [f_L(\varepsilon) - f_R(\varepsilon)] \quad (3.9)$$

### 3.1 Landauer Büttiker Theory

The essence of Landauer Büttiker theory is that one can define the conductance as the transmission probabilities of a tunneling barrier.

we firstly introduce the Green's function  $G(E)$ ,

$$G(E) = \frac{1}{E - \varepsilon + (i\eta)} \quad (3.10)$$

where  $i\eta$  is the imaginary part with an infinitesimal number  $\eta$  to avoid divergence of  $G(E)$  at the eigenvalues  $\varepsilon$ , and transmission function  $\mathcal{T}(E)$ ,

$$\mathcal{T}(E) = \gamma_L G(E) \gamma_R G^\dagger(E) \quad (3.11)$$

where  $G$  and  $G^\dagger$  are retarded and advanced Green's functions. In real system there are more molecular states, which would have more levels in the interacting energy range. Besides, we need to describe electronic structure with DFT method in atomic calculations where a localized basis set, linear combination of atomic basis set (LCAO) is used. With GPAW code the system can be described by a Hamiltonian matrix  $H$  which is presented with LCAO basis, the elements in this Hamiltonian can then be divided into left (L), central (C), and right region (R) as depicted in Fig. 3.2, the non-diagonal elements represent the coupling between the three regions.

$$\begin{pmatrix} H_L & V_L & 0 \\ V_L^\dagger & H_C & V_R^\dagger \\ 0 & V_R & H_R \end{pmatrix} \begin{pmatrix} |\Psi_L\rangle \\ |\Psi_C\rangle \\ |\Psi_R\rangle \end{pmatrix} = E \begin{pmatrix} |\Psi_L\rangle \\ |\Psi_C\rangle \\ |\Psi_R\rangle \end{pmatrix}$$

where  $V_{L,R}$  are the coupling matrices. Green's function is defined as,

$$(E - \mathbf{H})G(E) = \mathbf{I} \quad (3.12)$$

where  $I$  is an identity matrix. A more general definition is,

$$[(E + i\eta) - \mathbf{H}]G(E) = \mathbf{I} \quad (3.13)$$

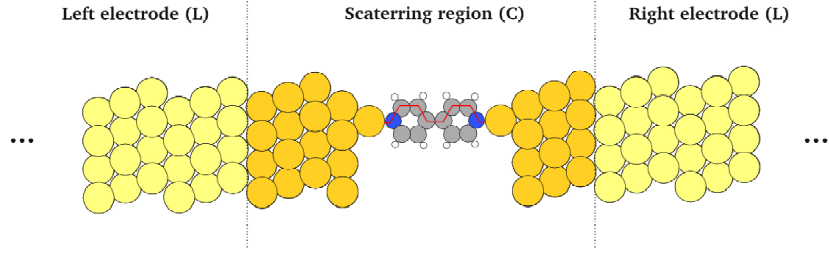


Figure 3.2: There is a central region (golden atoms plus a molecule) connected to two semi-infinite leads (light yellow atoms). The entire structure is periodic in the transverse direction ( $xy$  plane) for our GPAW calculations.

one could rewrite Eq. 3.12 in a matrix equation,

$$\begin{pmatrix} E - H_L & -V_{LC} & 0 \\ -V_{LC}^\dagger & E - H_C & -V_{RC}^\dagger \\ 0 & -V_{RC} & E - H_R \end{pmatrix} \begin{pmatrix} G_L & G_{LC} & 0 \\ G_{LC}^\dagger & G_C & G_{RC}^\dagger \\ 0 & G_{RC} & G_R \end{pmatrix} = \begin{pmatrix} I & 0 & 0 \\ 0 & I & 0 \\ 0 & 0 & I \end{pmatrix}$$

by taking out the equations involving the second column of the Green's function matrix, one gets,

$$(E - H_L)G_{LC} - V_{LC}G_C = 0 \quad (3.14)$$

$$-V_{LC}^\dagger G_{LC} + (E - H_C)G_C - V_{RC}^\dagger G_{RC} = I \quad (3.15)$$

$$-V_{RC}G_C + (E - H_R)G_{RC} = 0 \quad (3.16)$$

$$G_{LC} = g_L V_{LC} G_C \quad (3.17)$$

$$G_{RC} = g_R V_{RC} G_C \quad (3.18)$$

where  $g_{L,R} = (E - H_{L,R})^{-1}$ , substitute which into the Eq. 3.16, Green's function of the scattering region can be then derived,

$$G_C = [E\mathbf{I} - \mathbf{H} - \Sigma_L - \Sigma_R]^{-1} \quad (3.19)$$

where  $\Sigma_\alpha = V_{\alpha C}^\dagger g_\alpha V_{\alpha C}$  ( $\alpha = \{L, R\}$ ) is the self-energy, which is introduced for describing the broadening due to the couplings to the source and drain, and the transmission function as well as single-channel current can be written as,

$$\mathcal{T}(E) = \mathbf{Trace}[\Gamma_L G_C(E) \Gamma_R G_C^\dagger(E)] \quad (3.20)$$

$$\Gamma_{L,R} = i[\Sigma_{L,R} - \Sigma_{L,R}^\dagger] \quad (3.21)$$

$$\begin{aligned} I &= \frac{q}{\hbar} \int_{-\infty}^{\infty} dE \mathbf{Trace}[\Gamma_L G_C(E) \Gamma_R G_C^\dagger(E)] [f_L(\varepsilon) - f_R(\varepsilon)] \\ &= \frac{q}{\hbar} \int_{-\infty}^{\infty} dE \mathcal{T}(E) [f_L(\varepsilon) - f_R(\varepsilon)] \end{aligned}$$

and the conductance in Landauer formula becomes,

$$G = \frac{e}{\hbar^2} \mathcal{T}(E_F) \quad (3.22)$$

Eq. 3.22 indicates transmission probability of each channel contributes the conductance. The NEGF (implemented in GPAW) method presented here does not describe incoherent scattering, because electron-phonon couplings are disregarded. Incoherent scattering process becomes more significant when the junction length increases, which will be described in the chapter about hopping.





## CHAPTER 4

---

# Destructive Quantum Interference in Electron Transport

---

### 4.1 Motivation

Destructive quantum interference (DQI) effects are entirely defined by intrinsic molecular properties such as structure and symmetry. There are two simple models nowadays commonly used for interpreting the molecular properties in a single-molecule junction, one is a graphical scheme based on an atomic orbital (AO) representation, which determines DQI via a inspection of the connectivity of the atomic sites in conjugated  $\pi$  systems, the other is based on molecular orbital (MO) representation and uses the signs and amplitudes of the frontier orbitals for making the determination of DQI. The graphical scheme I will describe in more details in section [4.2.3](#). The MO representation is based on frontier orbitals (HOMO and LUMO, sometimes also includes HOMO-1 and LUMO+1) of  $\pi$  conjugated molecules, whose orbital phase and amplitude are important for determining the essential properties (e.g. conductance) of electron transport in single-molecule junctions.

In the work for paper I we clarified the relation between the two methods in terms of the zeroth order Green's function and compare their respective predictions for the occurrence of DQI. The purpose of this work is to reconcile the two schemes since the choice of an AO or MO representation should not make a difference for the properties of a topological molecular Hamiltonian as

long as all orbitals are properly considered, while in the literature disagreements have been reported. The representative testing systems we picked for this study are benzene, where it is well known that destructive quantum interference is observed in meta- connection while the ortho- and para- connections give a finite conductance at  $E_f$ ; Dinaphthylethene (DNE) and dithienylethene (DTE) both in open and closed configurations, where in both cases the closed isomer is much more conducting in the molecular junctions, hence this type of molecules constitute molecular switches, where the two isomers ("conducting" and "insulating") can be transformed into each other under the condition of highly reversible photochemical reactions; Azulene, a type of non-alternant hydrocarbons, so the Coulson-Rushbrooke (CR) pairing theorem which we will introduce in the following cannot be applied. All these systems in our study have been investigated theoretically and experimentally [39, 40, 41, 42, 43, 44, 45, 46, 47].

**Subdiagonalization** The transport Hamiltonian  $\mathbf{H}$  obtained from DFT calculation is described on a vector space defined by a localized atomic (LCAO) basis, while the transmission function is interpreted in terms of MOs within the interesting energy region close to the Fermi level, where the peak position corresponding to the eigenenergies of individual MO and the peak width reflects how strongly a particular MO is coupled to the electrodes. For the derivations of MO specific information from a diagonalization over the molecular subspace in the transport Hamiltonian is needed, which corresponds to a transformation into a molecular basis within the subspace. An unitary transformation on the scattering region is then performed,

$$\mathbf{H}_{sub} = \langle \mathbf{c} | \mathbf{H} | \mathbf{c} \rangle \quad (4.1)$$

where  $\mathbf{c}$  is the transformation matrix,  $\mathbf{H}$  is the full transport Hamiltonian, the transformation matrix contains the subspace (whose size is equal to the number of basis functions of the molecule) that needed to be rotated (diagonalized).  $\mathbf{H}_{sub}$  is the subdiagonalized Hamiltonian which now differs from  $\mathbf{H}$  in the molecular subspace. As a result of this subdiagonalization procedure, the energies of the molecular orbitals are obtained with reference to the Fermi level of the unit cell, which is mainly defined by the density of states (DOS) of the metallic bands. In addition, the non-diagonal elements in this molecular subspace undergo the same transformation and represent the electronic couplings of the MOs to the

electrodes [48, 49], which provides a convenient analysis perspective and will be frequently used in my thesis.

## 4.2 Pairing Theorem and Frontier Orbital Approximation

In order to interpret the transport characteristics one observes in a single molecule junction qualitatively, simple topological models are needed, in both of atomic and molecular orbitals representations, we can simplify Eq. 3.20 by assuming the central molecule is coupled to respective left (L) and right(R) electrodes via only a single atomic orbital (AO). Then each matrix  $\Sigma_{L,R}$  only contains one non-zero element  $\Sigma_{ll}$ ,  $\Sigma_{rr}$ , and the expression remaining in Eq. 3.20 is,

$$\mathcal{T}(E) = |G_{lr}^{mol}(E)|^2 \Gamma(E)_{ll} \Gamma(E)_{rr} \quad (4.2)$$

In order to obtain the molecular orbital spectrum of  $G_{lr}^{mol}$  in Eq. 4.2,  $\mathbf{H}_{mol}$  needs to be brought into its diagonalized form,  $\mathbf{H}_{mol} = \mathbf{C} \boldsymbol{\varepsilon}_m \mathbf{C}^\dagger$ , where  $\mathbf{C}$  is the coefficients matrix, coming from the linear combination of the AOs in a molecule,  $\boldsymbol{\varepsilon}_m$  is the diagonal matrix of the MO eigenenergies, by inserting  $\mathbf{H}_{mol}$  in the expression for the Green's function of the scattering region, a spectral representation of  $G_{lr}^{mol}$  can be written as,

$$G_{lr}^{mol}(E) = \sum_{m=1}^N \frac{C_{lm} C_{rm}^*}{E - \varepsilon_m + i\eta} \quad (4.3)$$

$C_{lm}$  are the coefficients of  $l(r)$  AO in the  $m$ -th MO, Eq. 4.3 runs over all  $N$  MOs (occupied and unoccupied). For the molecules with conjugated  $\pi$  system containing only alternant hydrocarbons (AHs), carbon atoms can be divided into two subsets, namely "starred" and "unstarred" according to the Coulson-Rushbrooke (CR) pairing theorem [50, 51] which states that the  $\pi$  electron energy levels are symmetrically distributed in this case and each occupied MO obtained from a subdiagonalization of the transport Hamiltonian  $\mathbf{H}_{mol}$  has a corresponding mirror term relative to the Fermi level in the unoccupied region and the shapes only differ in the sign of all AO coefficients. If we reform Eq. 4.3 by keeping this in mind and group up the pairs as the contributions from occupied MOs and the corresponding mirrored unoccupied MOs (i.e. HOMO,

LUMO; HOMO-1, LUMO+1;...) for the even numbers of MOs in a AH-type molecule we obtain,

$$G_{lr}^{mol}(E_f) = \sum_{k=0}^{N/2-1} \frac{C_{l,(H-k)}C_{l,(H-k)}^* - C_{r,(L+k)}C_{r,(L+k)}^*}{\varepsilon_k} \quad (4.4)$$

where the index  $k$  runs over such pairs. The CR pairing theorem states that when the same subset of carbon atoms are contacted to the two remaining electrodes sites on the left ( $l$ ) and right ( $r$ ), namely either both are "starred" or both are "unstarred", then  $C_{l,(H-k)} = C_{r,(L+k)}$  and  $C_{l,(H-k)}^* = C_{r,(L+k)}^*$  or  $C_{l,(H-k)} = -C_{r,(L+k)}$  and  $C_{l,(H-k)}^* = -C_{r,(L+k)}^*$ , consequently  $C_{l,(H-k)}C_{l,(H-k)}^* = C_{r,(L+k)}C_{r,(L+k)}^*$ , which means the terms in Eq. 4.4 vanish exactly at the Fermi level, and one can observe a DQI feature. On the other hand, if the two contact sites belong to different subsets,  $C_{l,(H-k)}C_{l,(H-k)}^* = -C_{r,(L+k)}C_{r,(L+k)}^*$ , which means the pairs add up constructively at  $E_f$ . However, what the CR pairing theorem does not address is how the individual pairs interact with each other, which means that the contribution of each pair could be positive or negative and it's possible that these contributions cancel each other out between pairs which can also lead to destructive quantum interference. Another limitation of the CR pairing theorem is that it is not applicable for non-alternant hydrocarbons and conjugated  $\pi$  systems containing hetero atoms. Yoshizawa and co-workers [52, 53, 54, 55, 56, 57] derived MO rules based on the phase and the amplitudes of molecular orbitals, where these rules link the DQI phenomenon and quantum chemical calculations in electron transport. These MO rules strictly focus on the contributions from frontier orbitals, namely the sign of the product of MO coefficients for the HOMO and LUMO which are considered to dominate the conductance at  $E_f$ , and the other states energetically further away from the Fermi level are neglected. This frontier orbital approximation results in correct conclusions only when the pairing theorem works, meaning, when the contacted sites are both starred or non-starred in junctions with alternant hydrocarbons, the cancellation of the contributions from the HOMO and LUMO is a reliable indicator for DQI because it also signifies the cancellation of the contributions from all the other CR pairs entering Eq. 4.4. This approximation doesn't consider the case where the contacted sites belong to different subsets, where the frontier orbitals constructively interfere, while the tails of lower lying occupied and higher lying unoccupied MOs might still cancel out with the MOs nearer to the Fermi level and cause DQI at  $E_f$ , i.e. due to the cancellation between pairs.

In the next step I will discuss Larsson's formula in a MO basis and clarify that for predicting DQI exactly within a MO representation, all MOs instead of only frontier orbitals need to be taken into account.

### 4.2.1 Larsson's Formula

is defined as,

$$\Gamma(E) = \sum_{m=1}^N \frac{\alpha_m \cdot \beta_m}{E - \varepsilon_m} \quad (4.5)$$

where  $\alpha_m, \beta_m$  are the couplings of the molecular state with eigenenergy  $\varepsilon_m$  to the respective left and right contact states. Larsson's formula was used to define the transfer integral mediated by selected MOs within Marcus theory for describing electron hopping [58, 59, 60], more recently it also has been used to define coherent tunneling approximately by  $\mathcal{T}(E) \sim \Gamma^2(E)$ . For the followings, two things need to be clarified, first the couplings  $\alpha_m, \beta_m$  describe the overlap of individual MOs and the contact AOs of the leads on each side. Since for all the systems for numerical studies the contact AO on each side is the same orbital, the couplings  $\alpha_m, \beta_m$  in Eq. 6.1 and the amplitudes of  $C_{l,MO}$  in Eq. 4.3 just differ by a same constant factor for all MOs, therefore the qualitative representation of transmission functions from 6.1 and 4.3 should be equivalent. The second issue is the normalization of the transmission function obtained by NEGF-TB. As we can see from the Larsson's formula the infinitesimal imaginary term  $i\eta$  has been taken out in the denominator, one could in principle repair this omission and divergence at eigenenergies of MOs by a normalization factor as derived by Sautet and Bocquet [61, 62]. This derivation was made under the assumption that the molecule and surface interact much stronger than the molecule and tip ( $\beta_m \ll \alpha_m$ ), while the couplings within the surface or within the tip are large than the couplings to the molecule. Then the expression for the transmission probability can be simplified to,

$$\mathcal{T}(E) = \Gamma^2(E)/Ah^2 \quad (4.6)$$

where  $A = \frac{x_{-1}^2 + 1 - qx_{-1}}{4 - q^2}$ , with  $q = (E_f - e)h^{-1}$  and  $x = h^{-1}[\sum_{m=1}^N \frac{\alpha_m^2}{E - \varepsilon_m}]$ , and  $e, h$  are the respective eigenenergies and couplings within the surface or within the tip. For general cases,

$$\mathcal{T}(E) = t_1 t_2 \quad (4.7)$$

with  $t_1 = \frac{4}{(Z + \frac{1}{Z})^2}$ ,  $t_2 = \frac{1}{(1 + \frac{X + q(W^2 - 1)}{W^4(4 - q^2)})}$  and  $W = Y \frac{(1 + Z^2)^{1/2}}{\sqrt{2}}$ ,  $Y = \alpha/h$  is the interaction to the left lead,  $X = (\omega - e)$  the energy difference between a single molecular state and the chain of leads, and  $Z = \beta/\alpha$  the asymmetry of the respective interaction to the left and right leads. For the general case where  $\beta_m$  is not much smaller than  $\alpha_m$ , the mathematical complexity of the given expression increases. Since the qualitative behavior of  $\Gamma^2(E)$  should not deviate from the transmission function obtained from NEGF-TB, we avoid the complication of this normalization procedure and plot  $\Gamma(E)^2$  in arbitrary units (the values of  $\Gamma(E)^2$  are divided by a scaling factor). For the systems investigated in paper I, we use a scaling factor of  $10^{-2}$  at the poles when applying Eq. 6.1 and only plot the relevant energy range for addressing the key points, the main conclusion in this chapter is that for the cases where pairing theorem and Frontier orbital approximation cannot predict DQI reliably, all MOs contributions need to be considered in order to get the appropriate exact cancellation in the transmission function at  $E_f$ . This is because as we mentioned above, the MOs energetically further away from the  $E_f$  also need to be accounted for in order to find DQI at  $E_f$  for these cases. The reasons are: i) even when the denominator that enters Eq. 6.1 is large, the numerator which is determined by the product of the couplings for individual MO to the leads can be so large that their contributions to  $\Gamma(E)$  in Eq. 6.1 is still significant; ii) the plot of transmission functions in a logarithmic scale magnifies the real value of  $\mathcal{T}(E)$ , which appears with a significant signal that cannot be treated as a total cancellation at  $E_f$ , i.e. the characteristic of DQI feature should be an exact cancellation (zero). Figure 4.1 shows the convergence for the number of CR pairs of MOs, one can see the oscillation of  $\Gamma^2(E)$  by increasing the number of pairs, we use DTE (open form without sulfur, Fig. 4.1 b)) as an example for the description of such a situation. Firstly only the frontier orbitals (HOMO and LUMO, curve label 1) are considered, then two more terms enter the summation (curve label 2) and progressively we increase the number of pairs (curves label 3, ..., label 5). When one includes 8 MOs (curve label 4) out of all 10 MOs,  $\Gamma^2(E)$  still doesn't vanish at  $E_f$ , while two minima appear close to  $E_f$  but not exactly at the Fermi level, and only the contributions from all MOs (curve label 5) lead to the exact cancellation at  $E_f$  and therefore DQI occurs in this case. The conclusion drawn from paper I is that the tails of MOs which are energetically far away from  $E_f$

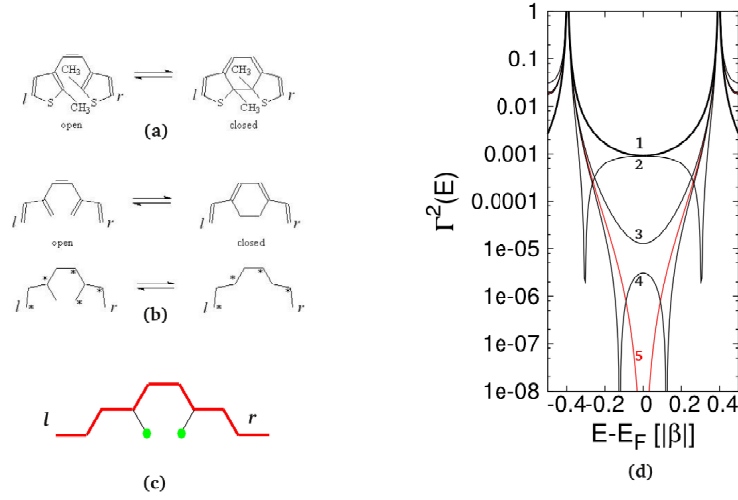


Figure 4.1: DTE a) Chemical structures; b) "starring" pattern according to the pairing theorem and c) graphical rules applied in the respective open and closed forms without sulfur atoms; d)  $\Gamma^2(E)$  with increasing accumulation of CR pairs for DTE (without sulfur). The labels indicate the number of pairs that are included, where 1 means HOMO and LUMO, 2 means HOMO, LUMO plus HOMO-1, LUMO+1 and so on, these three curves are marked as black. The curve from the first pair is marked with black bold, and the curve with contributions from all MO is marked with bold red.

can also influence the conductance at the Fermi level, hence DQI feature at  $E_f$  can also be induced by the contributions from all MO pairs canceling each other at  $E_f$ .

## 4.2.2 Numerical Studies

All the calculations in this section are performed by the Non Equilibrium Green's Function Tight Binding (NEGF-TB) method, where semi-infinite chains of single AOs are used as electrodes. In paper I we show numerical explanations in both AO and MO representations, where all onsite energies are set to zero in the TB Hamiltonian. The couplings of the respective MOs to the electrodes are



set to the resonance integral  $1 \beta$  (in eV) from Hückel theory, which also defines the units of our energy axis. In order to account for hetero atoms, we set the sulfur onsite energy to  $1.11 \beta$  and the couplings for C-S bonds to  $0.69 \beta$ . Our first simple but very illustrative example is butadiene, as depicted in Fig. 4.2 e). when the contact sites belong to the same subset (starred), as is the case for 1,3-, DQI occurs (red solid line) as predicted by the CR pairing theorem, while for the molecule contacted at different subsets (one starred, the other not starred) sites, as for the cases 1,2- 1,4- and 2,3-, in the two former cases a finite conductance is found at  $E_f$ , while for 2,3- connectivity (red dashed line) DQI occurs, where the pairing theorem cannot be applied for prediction. In the following, we focus on the graphical scheme based on atomic orbitals, which is more universal in its prediction of DQI than the pairing theorem.

### 4.2.3 Graphical Scheme

The Graphical AO scheme is derived for predicting the DQI effects in Refs. [63, 22], it can be formulated as the following rules: when there's no path traversed within a continuous line through contact site  $l$  to  $r$ , i.e. no continuous connection between contact sites  $l$  and  $r$  in a topological molecular scheme, DQI occurs at  $E = E_f$ . On the other hand, when there are continuous paths and not crossed AO can be grouped up as closed loops as shown in Fig. 4.2 b)) in the topology between two sites, one gets a finite zero bias conductance. This AO graphical scheme considered all orbitals in an AO representation of the carbon  $p_z$  orbitals as defined by the molecular topology. The Graphical AO scheme can be generally applied for conjugated  $\pi$  systems without hetero atoms, also for the cases where the CR pairing theorem cannot be used. This scheme is also more reliable than the frontier orbital approximation because it considers all orbitals, and not only the HOMO and the LUMO and does not disregard the contributions from the other MOs which are also significant for the prediction of the DQI occurrence at  $E_f$ . Here we use benzene and azulene to illustrate the application of the CR pairing theorem and graphical AO scheme, for comparison the transmission functions are also calculated with NEGF-TB simulations and by using the Larsson's formula. Both schemes can be applied successfully for benzene with three connections (m-,o-,p-) while for azulene the pairing theorem is not able to predict DQI as shown in Fig. 4.3. There are some extremes for the

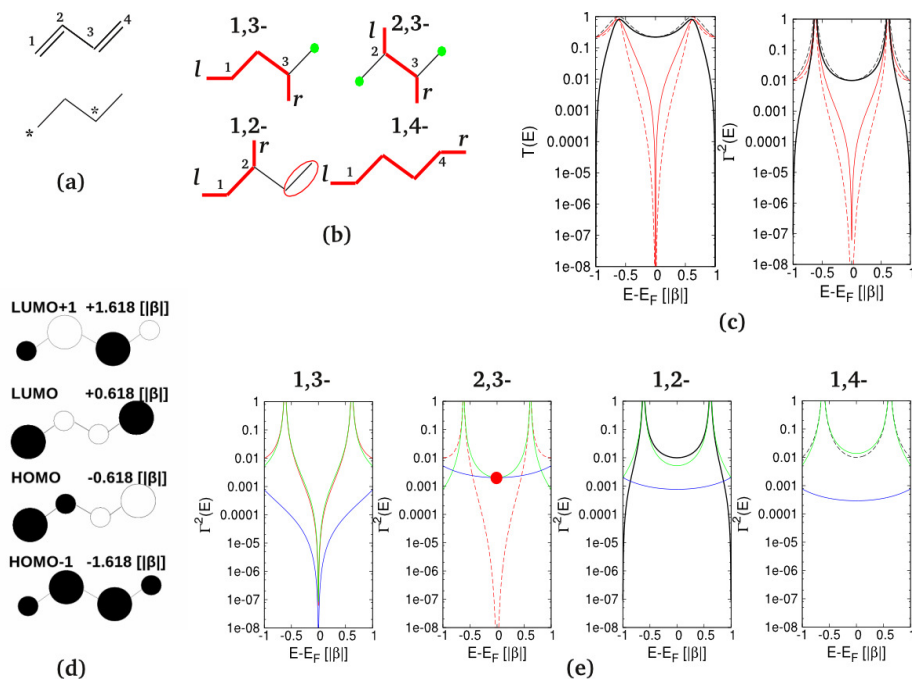


Figure 4.2: a) Chemical structure of butadiene where the pairing theorem is applied (“starring scheme”); b) graphical AO scheme; c) transmission functions from NEGF-TB calculations and  $\Gamma(E)^2$  from Larsson’s formula, with red lines for the cases where DQI occurs (solid line for 1,3- connectivity and dashed line for 2,3-) and black lines for the cases where no DQI occurs (solid line for 1,2- and dashed line for 1,4-); d) MO amplitudes, where the black and white fillings indicate the respective positive and negative signs of the wavefunctions; e) individual pair contributions (HOMO and LUMO, green line; HOMO-1 and LUMO+1, blue line), where a cross of the individual contribution was marked with a red dot for 2,3- connection case, and the color code of the curves is consistent with panel c).

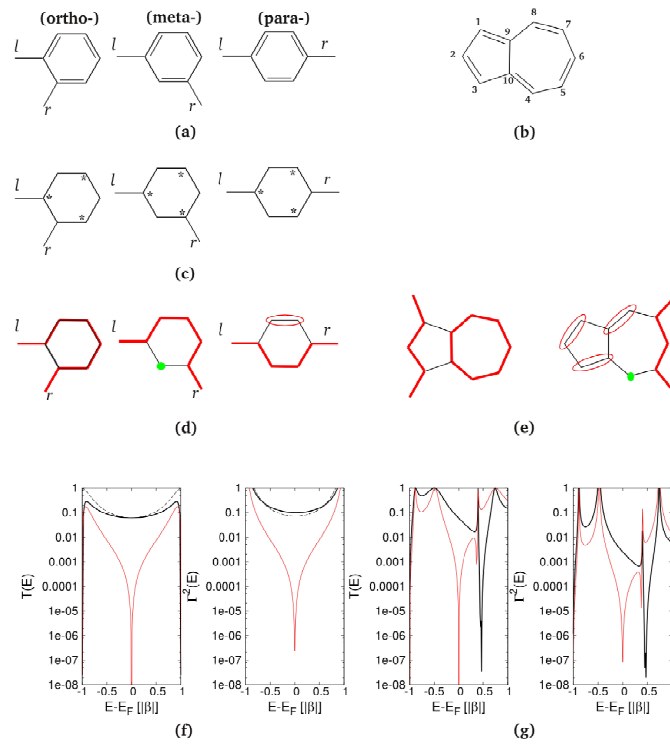


Figure 4.3: a) Benzene with o-, m- and p- connections; b) azulene with 1,3- and 5,7- contacted positions; c) pairing theorem application for benzene; graphical rules application for d) benzene and e) azulene; transmission functions calculated from NEGF-TB (left) and Larsson's formula (right) for f) benzene and g) azulene, respectively.

graphical scheme, e.g for hetero atoms, where one can vary the on-site energy for hetero atoms from zero at the cost of increasing mathematical complexity [64, 65]. The other assumption of the graphical scheme is that it only applies when  $E = E_f$  since for zero-bias transmission function, the conductance is defined at  $E_F$  and also the onsite energy of carbons in the conjugated systems are set to zero. However, this approximation does not limit the predictive capability of the method for most systems of interest, for molecules with hetero atoms as long as  $E_F$  is defined by the leads lies within the HOMO-LUMO gap of the molecule after Fermi level alignment.



## CHAPTER 5

---

# Quantum Interference for Branched Molecules Containing Ferrocene in the Junctions

---

### 5.1 Motivation

The ferrocene molecule we designed in Fig. 5.1 are with two objectives: i) ferrocene moieties can be oxidized, which can be used for implementing a switch with the two redox states for electron transport; ii) the two branches containing the two ferrocene moieties can be designed symmetrically or asymmetrically depending on whether one of the ferrocene is charged or not. For the asymmetric case destructive quantum interface might be induced. These ferrocene molecules are connected to electrodes with pyridyl anchors in meta- and para- positions, respectively. Single-branch and shorter-length structures without acetylenic spacers were also investigated for comparison. The acetylenic spacers have several effects: i) they stabilize the molecular structures via conjugated bonds; ii) the spacers enlarge the distance in the junction which reduces the through-space coupling between left and right leads and iii) separate the redox-active centers from the leads. In the neutral state of the molecule depicted in Fig. 5.1, constructive quantum interference (CQI) is expected in the coherent tunneling through it because electrons are passing through two identical branches. When we put a charge on one of the branches, this symmetry is broken and one would expect destructive quantum interface (DQI) to occur, where an OFF-state\*resulting from charging make this type of molecules potential redox switches. Pyridyl groups were chosen as anchors to the leads, because they provide peaks in the

transmission function, which are narrow enough to assume that a charge on the complex has an impact on the conductance but broad enough to avoid the Coulomb blockade regime [66, 67, 68].

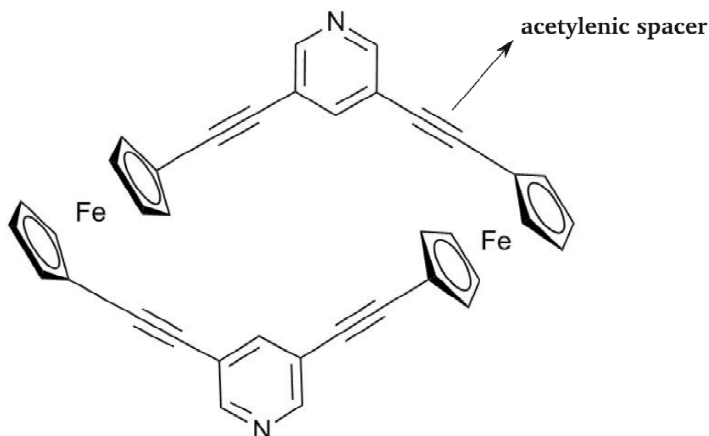


Figure 5.1: Branched molecule containing a ferrocene moiety in each branch, where two moieties have been separated from the pyridyl anchor groups by acetylenic spacer groups.

## 5.2 Theoretical/Computational methods

The transmission functions  $\mathcal{T}(E)$  for all junctions we obtained from NEGF-DFT calculations which were performed with the GPAW code [69, 70] using a linear combination of atomic orbitals (LCAO) [71] for the basis set on a double zeta level with polarization functions (DZP), a Perdew-Burke-Ernzerhof (PBE) parametrization for the exchange correlation (XC) functional [33] and a

---

\*a large ON/OFF ratio is the essential criteria for designing a switch and here we assume that the OFF-state due to the DQI will produce a large ON(symmetric case)/OFF(asymmetric case) ratio for this type of molecule.

grid spacing of 0.2 Å for the sampling of the potential in the Hamiltonian on a real space grid. In our transport calculations, the "extended molecule" defining the scattering region is formed by the respective metal organic compounds and three and four layers for the upper and lower fcc gold electrodes, respectively, in a (111) orientation and with a  $6 \times 6$  over-structure defining the periodically repeated unit cell, where the distance between the Au ad-atom attached to the lead surfaces and the N atom of the pyridyl anchor groups was chosen as 2.12 Å [72] and a  $k$  points sampling corresponding to a  $4 \times 4 \times 1$  Monkhorst Pack grid for evaluating  $\mathcal{T}(E)$ , where the  $z$ -coordinate is the direction of electron transport through the junction. For the charged systems we enlarged the size of the gold slabs in  $x$  direction in order to include a chlorine atom in the unit cell as shown in section 5.6 and reduce the gold slabs in the  $y$  direction in order to save computational cost.

**$\Delta$  SCF Method** The  $\Delta$  SCF method allows to define the occupation of particular electronic states of an atom, molecule or solid as a constrain to the self-consistent cycle. We used generalized  $\Delta$  SCF method for calculating the charging effect in section 5.6, where we put one electron on the chlorine  $p$  shell as proposed by Gavnholt *et al.* [73, 74]. In this scheme the excited electron can occupy any orbital which is a linear combination of empty Kohn-Sham (KS) orbitals,

$$\Psi^{res}(\mathbf{r}) = \sum_{i=n} c_i \psi_i(\mathbf{r}) \quad (5.1)$$

where  $n$  is the number of unoccupied orbitals and  $c_i$  are the expansion coefficients. The electron density then can be written as,

$$n(\mathbf{r}) = \sum_{i=1}^{N-1} \psi_i^*(\mathbf{r})\psi_i(\mathbf{r}) + \sum_{i,j=N}^M c_i^* c_j \psi_i^*(\mathbf{r})\psi_j(\mathbf{r}) \quad (5.2)$$

where  $N$  is the number of occupied KS orbitals and  $M$  is the total number of KS orbitals in the calculation, which means many-particle wave function now is a Slater determinant of  $N-1$  KS orbitals plus  $\Psi^{res}$ . The extra electron is usually taken from the molecule, in this way the molecule is charged and we keep the neutrality of the entire system.

In the case of molecules adsorbed to surface, a sufficient number of unoccupied KS orbitals has to be chosen for the expansion coefficients, which is consistent with a Newns and Anderson picture [75, 76].  $\Delta$  SCF is implemented



in GPAW, where the core electron density for the molecular orbital is calculated with the PAW method,

$$\Delta\tilde{n}(\mathbf{r}) = \sum_{i,j} c_i^* c_j \tilde{\psi}_m^*(\mathbf{r}) \tilde{\psi}_n(\mathbf{r}) \quad (5.3)$$

One of the methods in GPAW for obtaining the expansion coefficients is projector-pseudo-wavefunction overlap which is applied in this thesis for constraining an additional electron on the Cl counterion in order to calculate the transmission functions of the charged molecules in the junction, where the orbital to be occupied is chosen as an atomic orbital with a partial wave function inside the augmentation sphere  $|\Phi_i^a\rangle$ , the coefficients in Eq. 5.1 can be approximated as,

$$c_n = \langle \psi_n | \Phi_i^a \rangle = \langle \tilde{\psi}_n | \Phi_i^a \rangle + \sum_{a,i,j} \langle \tilde{\psi}_n | \tilde{p}_i^a \rangle \Delta S_{i,j}^a \langle \tilde{p}_j^a | \Phi_i^a \rangle \approx \langle \tilde{\psi}_n | \tilde{p}_i^a \rangle \quad (5.4)$$

where  $\Delta S_{i,j}^a$ , the overlap between atomic sites are neglected.

where  $\tilde{p}_i^a$  is the projector function according to Eq. 2.19. This projector overlap is calculated in each step of the self-consistency cycle, leading to a rather accurate way of acquiring the expansion coefficients  $c_i$ . The expansion for each  $k$ -point is calculated independently.

This approach is based on the generalized  $\Delta$  SCF method, and makes use of its flexibility to define the spatial expansion of an orbital forced to contain an electron as an arbitrary linear combination of Bloch states. In the charging sections for both cyclic ferrocene 5.6 and Ru/Os(PPh<sub>2</sub>)<sub>8</sub>(C<sub>2</sub>H<sub>4</sub>)<sub>4</sub> bis(pyridylacetylde) molecules 6.4, the constrained orbital of chlorine is localized on a single atomic site only, by extracting one electron from the system and inserting it into a predefined orbital in the beginning of every iteration step, the self-consistency cycle progresses as usual, but with the electron density of this particular orbital as a contribution to the external potential. In this way we can fix the electron occupation for the Cl manually <sup>†</sup>, which solves the self-interaction problem implicitly and makes this method ideal for charge localization.

---

<sup>†</sup>to ensure the charge neutrality in the unit cell of the system, which is necessary for a charged junction when applying periodic boundary conditions for electronic-structure calculations, the countercharge to the complex has to be an explicit part of the cell, where we use Cl<sup>-</sup> as a counterion. The counterion is added into the junction after the nuclear positions for the neutral complex without Cl is relaxed, then one supplementary electron is constrained to fill the Cl  $p$  shell.

### 5.3 QI Feature in Transmission Functions

First we look at the transmission function of the molecule in Figure 5.1 in its neutral and oxidized cases for comparison. As we can see in Fig. 5.2, this system

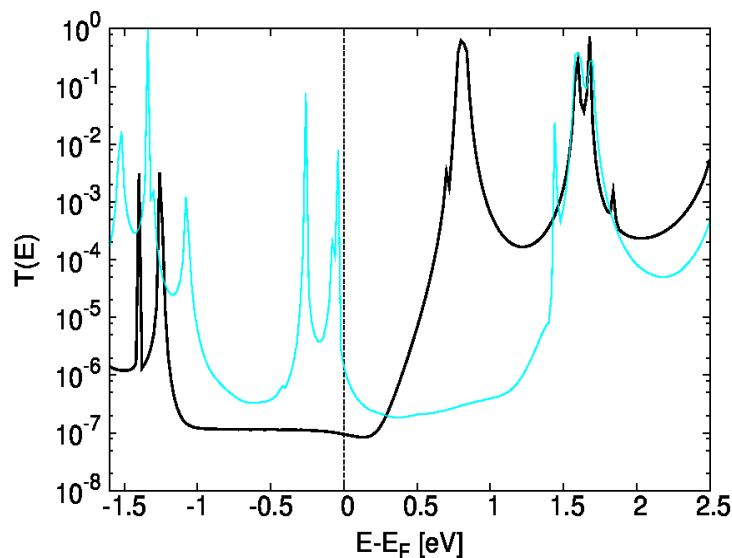


Figure 5.2: Transmission functions for  $m-d-l$  (black curve) and  $m-d-l(\text{Cl})$  (cyan curve).

in its neutral state gives a dip in the unoccupied region near to the Fermi level (black solid line), which deviates from the Lorentzian form of the LUMO peak and lowers the conductance. The flat characteristic in the transmission function within the HOMO-LUMO gap is just shifted towards the upper energy region for the charged state (red solid line). One can also observe that the different magnitude of the shift for the peaks in the respective occupied and unoccupied regions lead to the HOMO-LUMO gap narrowing slightly when compared with the corresponding uncharged transmission curve. The conductance of the neutral and charged states are  $0.95 \times 10^{-7}$  and  $1.41 \times 10^{-6}$ , respectively, with an ON/OFF ratio of  $\sim 15$  which is by far too small for an operative transistor. In order to learn more about the structural reasons for DQI in electron transport through the branched molecule, we further designed a series of molecules for comparison,  $m-d-s$ ,  $m-s-l$ ,  $m-s-s$ ,  $p-s-l$  and  $p-s-s$ , where  $m$  or  $p$  represents the connectivity of each anchor group and the ferrocene moiety,

namely meta- or para- connection;  $d$  or  $s$  is an abbreviation for double branches or single branch and  $l$  or  $s$  means the length of the molecule, namely longer with acetylenic spacers or shorter without spacers. By comparing  $m-d-l$  and  $m-d-s$  one could see the effect of the spacers, the comparison of  $m-d-l$  and  $m-s-l$  gives the consequence of the different number of branches, as does  $m-d-s$  versus  $m-s-s$ , while  $m-s-l$  versus  $p-s-l$  illustrates the impact of connectivity on the quantum interference feature. All the resulting junctions are shown in Fig. 5.3, For the ferrocene systems under investigation neither

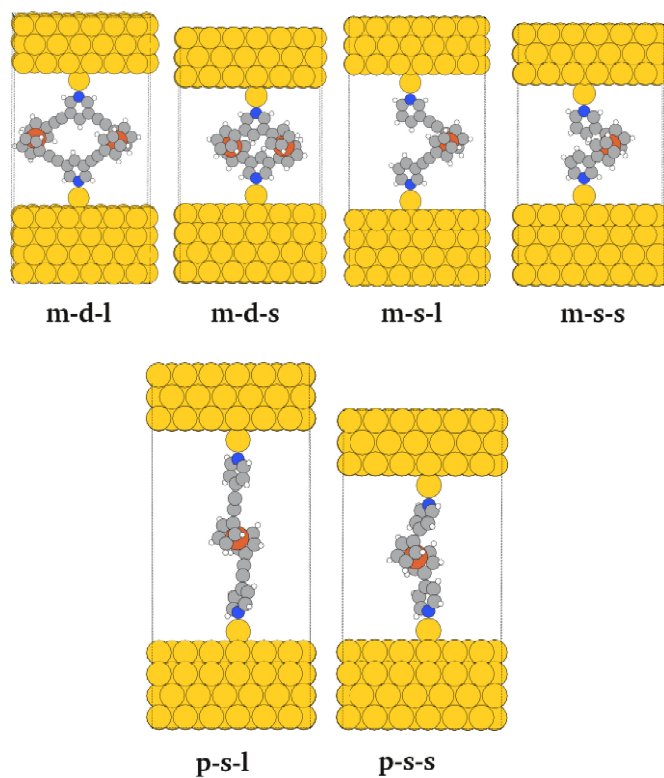


Figure 5.3: Junction geometries for the investigated ferrocene molecules.

the graphical rule nor the pairing theorem used for planar conjugated systems can be applied because both are applicable for planer hydrocarbons only. Thus in order to analyze the DQI feature and its main sources one needs to project a complex three dimensional molecular structure into deductive simplified models. For that purpose we first diagonalize the subspace of the molecule in the full

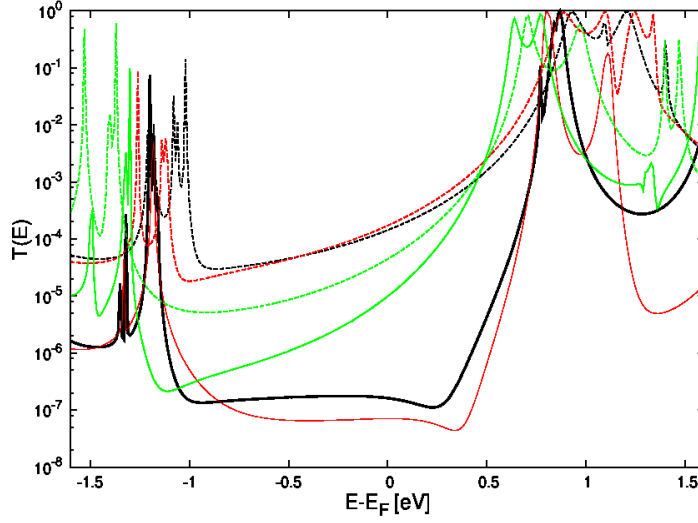


Figure 5.4: Transmission functions for the six ferrocene molecules, where the three solid lines denote  $m-d-l$  (black),  $m-s-l$  (red),  $p-s-l$  (green), and the three dashed lines are  $m-d-s$  (black),  $m-s-s$  (red),  $p-s-s$  (green).

transport Hamiltonian to get the molecular states and picked the interesting ones that close to the Fermi level. With NEGF-TB calculation we found that the number of molecular states needed to reproduce the main features in the DFT results is 10 for  $m-d-l$ , i.e. six occupied states and four unoccupied states. By looking at the molecular orbitals for these ferrocene molecules, we found that the relevant unoccupied states LUMO, ..., LUMO+3 are mostly delocalized on the two pyridyl groups, while the six occupied states HOMO, ..., HOMO-5 are localized on the two ferrocene moieties, which indicates that the DQI feature which appears below the LUMO is mainly determined by the four unoccupied states.

As we can see from Fig 5.5, the transmission function for  $m-d-l$  with six occupied states and four unoccupied states (green curve) contains all the main features as in the NEGF-DFT calculation. For obtaining the couplings of the MOs to the left and right electrodes, we use the atomic valence  $s$ -orbital of each gold add-atom on both sides, since around the Fermi level the density of states of a gold surface has dominantly  $s$ -character. The inclusion of four more unoccupied states (Fig. 5.5 blue curve) increases the conductance, while increasing the number of states (four more unoccupied states) even further

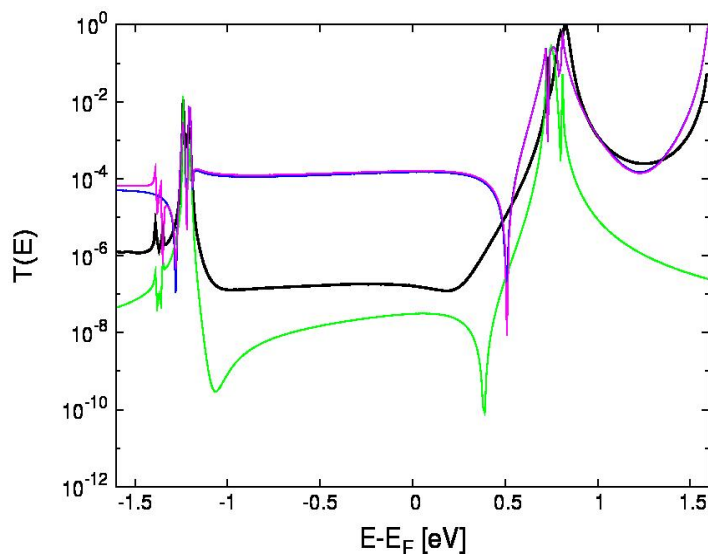


Figure 5.5: Transmission functions of  $m-d-l$  calculated with NEGF-DFT (black solid line) and NEGF-TB, where ten molecular states (six occupied plus four unoccupied states, green solid line), fourteen molecular states (six occupied plus eight unoccupied states, blue line) and eighteen molecular states (six occupied plus twelve unoccupied states, magenta line) are taken respectively.

doesn't improve the result any further qualitatively (Fig. 5.5 magenta curve), and compared the three transmission curves (green, blue and magenta) from NEGF-TB calculations one can draw the conclusion that by taking six occupied states and four unoccupied states for  $m-d-l$  molecule the main features in the transmission function are qualitatively reproduced compared with NEGF-DFT result (black curve). As for the  $m-d-l$  molecule, one can apply the same selection rule for MO states of  $m-s-l$  and  $m-d-s$ , namely by taking the three occupied states (HOMO, HOMO-1, HOMO-2) for molecules containing only one ferrocene branch, and six occupied states for double branched molecules, since the number of pyridyl groups is the same for all systems, four unoccupied states are used for all systems. NEGF-TB results for the system  $m-s-l$  are shown in Fig. 5.6, where one can see that the transmission functions calculated by NEGF-TB reproduce the main features as NEGF-DFT calculations in the energy range close to LUMO but not in the HOMO region. The DQI feature can be reproduced merely by the contributions from unoccupied states (LUMO, LUMO+1, LUMO+2, LUMO+3), while the feature in the HOMO region de-

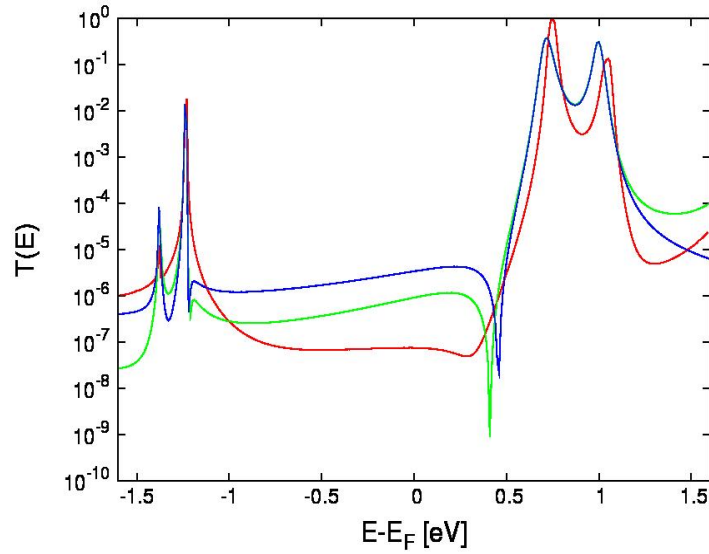


Figure 5.6: Transmission functions for  $m - s - l$  as calculated by DFT (red solid line) and NEGF-TB, where nine molecular states (three occupied plus six unoccupied states, green line), seven molecular states (three occupied plus four unoccupied states, blue line) were taken respectively.

viates from the DFT results with three occupied states (HOMO, HOMO-1, HOMO-2) included. We however want to have a model as simple as possible, what's more, the conductance is determined by the interplay of the unoccupied states exclusively for all the systems we investigated here, in the following section we focus on the localized basis presentation for interpreting the causes of DQI for some of these molecules.

## 5.4 Computational Tools Used for the Interpretation of Destructive Quantum Interference Effects

### 5.4.1 Localized Basis Representation

The electron transport regime is divided into three regions, the left electrode, the scattering (center) region and the right electrode, in order to separate each part of the setup the transport Hamiltonian needs to be defined on a localized basis set in order to describe each part of the system separately. In praxis, there are two potential candidates for such a localized basis set, namely, linear combination of atomic orbitals (LCAO) and wannier functions (WFs). With GPAW a LCAO mode is used, where the Kohn-Sham pseudo wave functions  $\tilde{\Psi}_n$  are expanded onto a set of atomic-like orbitals  $\Phi_{nlm}(\mathbf{r})$  following the approach of Sankey and Niklewski [77],

$$\tilde{\Psi}_n = \sum_{\mu} c_{\mu n} \Phi_{\mu}(\mathbf{r}) \quad (5.5)$$

where coefficients  $c_{\mu n}$  are variational parameters for minimizing the total energy, and the localized basis functions  $\Phi_{\mu}(\mathbf{r})$  are constructed as products of numerical radial functions and spherical harmonics. The Hamiltonian in a LCAO basis can then be defined as,

$$H_{\mu\nu} = T_{\mu\nu} + V_{\mu\nu} + \sum_{\mu\nu} P_{i\mu}^{a*} \Delta H_{i,j}^a P_{j\nu}^a \quad (5.6)$$

where  $T_{\mu\nu} = \langle \tilde{\Psi}_n | -\frac{1}{2} \nabla^2 | \tilde{\Psi}_n \rangle$  is the kinetic energy,  $V_{\mu\nu} = \int \Phi_{\mu}^*(\mathbf{r}) \tilde{v}(\mathbf{r}) \Psi_{\nu}(\mathbf{r}) d\mathbf{r}$  is the effective potential,  $\sum_{\mu\nu} P_{i\mu}^{a*} \Delta H_{i,j}^a P_{j\nu}^a$  are the atomic contributions inside the augmentation sphere, and the Kohn-Sham equation becomes,

$$\sum_{\nu} H_{\mu\nu} c_{\nu} = \sum_{\nu} S_{\mu\nu} c_{\nu} \epsilon_n \quad (5.7)$$

which can be solved by diagonalizing the Hamiltonian in the basis of the atomic orbitals.

**Wannier Functions (WFs)** A localized molecular orbital model has been used for understanding the interference effects in anthraquinone-based

molecules [78] by using the Wannier function (WF) concept [79]. For these investigated molecules, WFs have been used as "localized molecular orbitals" (LMOs) [80], the idea was to apply an unitary transformation for a few molecular eigenstates in the relevant energy range (close to the Fermi level) thus resulting in localized orbitals, which dominate the zero-bias conductance. Distinguishing between the branches in our set of molecules from the perspective of a MO basis set is challenging due to the fact that MOs in general are distributed over both branches. Wannier functions are involved for interpreting quantum interference features in terms of localized orbitals because they can be allocated to different parts of the molecules. Since WFs are obtained from an unitary transformation of the original MOs, electronic structures is remained, besides, the computational cost is comparable to TB method. The idea of the fragment orbitals representation where the localization is distinct from group to group is similar in the sense that the orbitals are localized on different groups based on the construction of a molecule, details about fragment orbital analysis are in the next section. When we try to transform few molecular orbitals within the physically relevant energy range (around the Fermi level) into localized WFs, where the spread of these localized molecular orbitals (LMOs) is minimized, i.e. they are maximally localized after the transformation, the mapping from the MO states onto LMO states is,

$$\Phi_n = \sum_m U_{mn} \Psi_m \quad (5.8)$$

where  $n$  is the number of eigenstates in the system, and  $m$  is the number of states transformed from MOs to the set of LMOs ‡.  $U$  is a unitary matrix designed to result in maximally localized orbitals, where in our cases we only take the MOs close to the Fermi level in the Hamiltonian,

$$H_{LMO} = U^T \text{diag}(\varepsilon_{H-i}, \dots, \varepsilon_H, \varepsilon_L, \dots, \varepsilon_{L+i}) U \quad (5.9)$$

$\varepsilon_{H-i}, \varepsilon_{L+i}$  represent the MO eigenstates in the respective occupied and unoccupied region, where the optimal number of MO states depends on the degree of localization of the resulting LMOs. Ideally one can sketch the transport pathways from left to right from these LMOs, and they can be in principal used for distinguishing geometric difference for the molecules we investigated here, since the difference of the couplings between LMOs should vary along the different

---

‡ $m$  in the original atomic Wannier function scheme is the number of states which has a energy below  $E_F$



molecule configurations. In practice the LMOs we obtained are delocalized over anchor and bridge groups, hence are not ideal for geometric distinction. One could in principle increase the localization by adding more MOs into the transformation (Eq. 5.8), which however, increased the complexity in our analysis as well, therefore we conclude that Wannier functions are not a good choice for our purpose.

### 5.4.2 Fragment Orbitals and Effective Coupling Model

The idea we pursued for our analysis of destructive quantum interference (DQI) is to derive a TB model, with a much smaller Hamiltonian containing only few anchor and bridge states. One can obtain such a model by diagonalizing the subspace of pyridyl, acetylenic and ferrocene groups one after the other from the original transport Hamiltonian and by picking the relevant states within each diagonalized subspace for building a smaller Hamiltonian in a fragment orbital (FO) basis. Our main goal is to distinguish the investigated systems with different geometries via a simple model where the differences are i) the number of branches, ii) the presence of acetylenic spacers, iii) the para- or meta- connections. From Fig. 5.7 and 5.8 we can see that the relevant

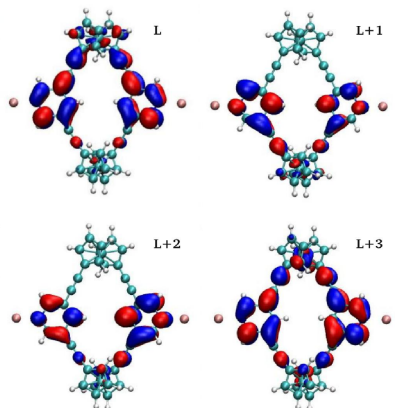


Figure 5.7: Four unoccupied molecular orbitals of the double-branched long molecule ( $m - d - l$ ) with ferrocene centers.

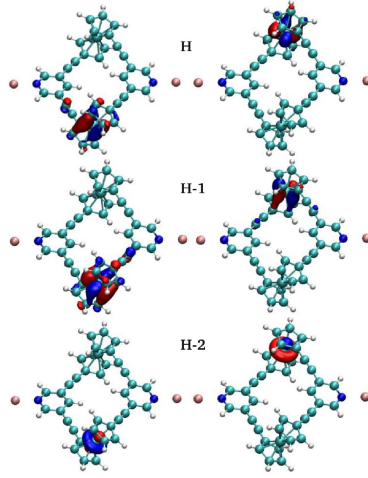


Figure 5.8: Six occupied molecular orbitals of  $m - d - l$ .

four unoccupied MOs are delocalized on both pyridyl and the six occupied MOs are mostly localized on ferrocene moieties, where we distinguish the lower branch on the left and upper branch on the right.  $L$  represents LUMO in Fig. 5.7 and  $H$  represents HOMO in Fig. 5.8, respectively. In Fig. 5.9  $Ac$ ,  $Py$  and  $Fc$  represent pyridyl, acetylenic and ferrocene states,  $A$  and  $B$  mean the upper and lower branches, the subscript  $L$ ,  $R$  mean left and right, respectively. The states we picked from each group are selected based on two criteria, namely their eigenenergies should be nearby the Fermi level and the size of the couplings between the neighboring fragments should be comparable large, resulting in two pyridyl states on each side, four acetylenic state on each branch and five ferrocene states on each branch are used in our analysis. The resulting transmission function as calculated by NEGF-TB is shown in Figure 5.10. Comparing the DFT result and these FO basis TB calculations we find that there are deviations in the conductance and in the DQI features. The reduction of the conductance in the blue curve can be attributed to the approximation we take regarding the number of FOs with only considering nearest couplings, while the other deviation is that there are more DQI features between HOMO-LUMO gap in the blue solid line compared with the black one. One could in principle improve the agreement of the two curves by including more states and couplings, this is however not in the spirit of our main idea of relating the sources of DQI to different geometries by a very simplified TB model. From

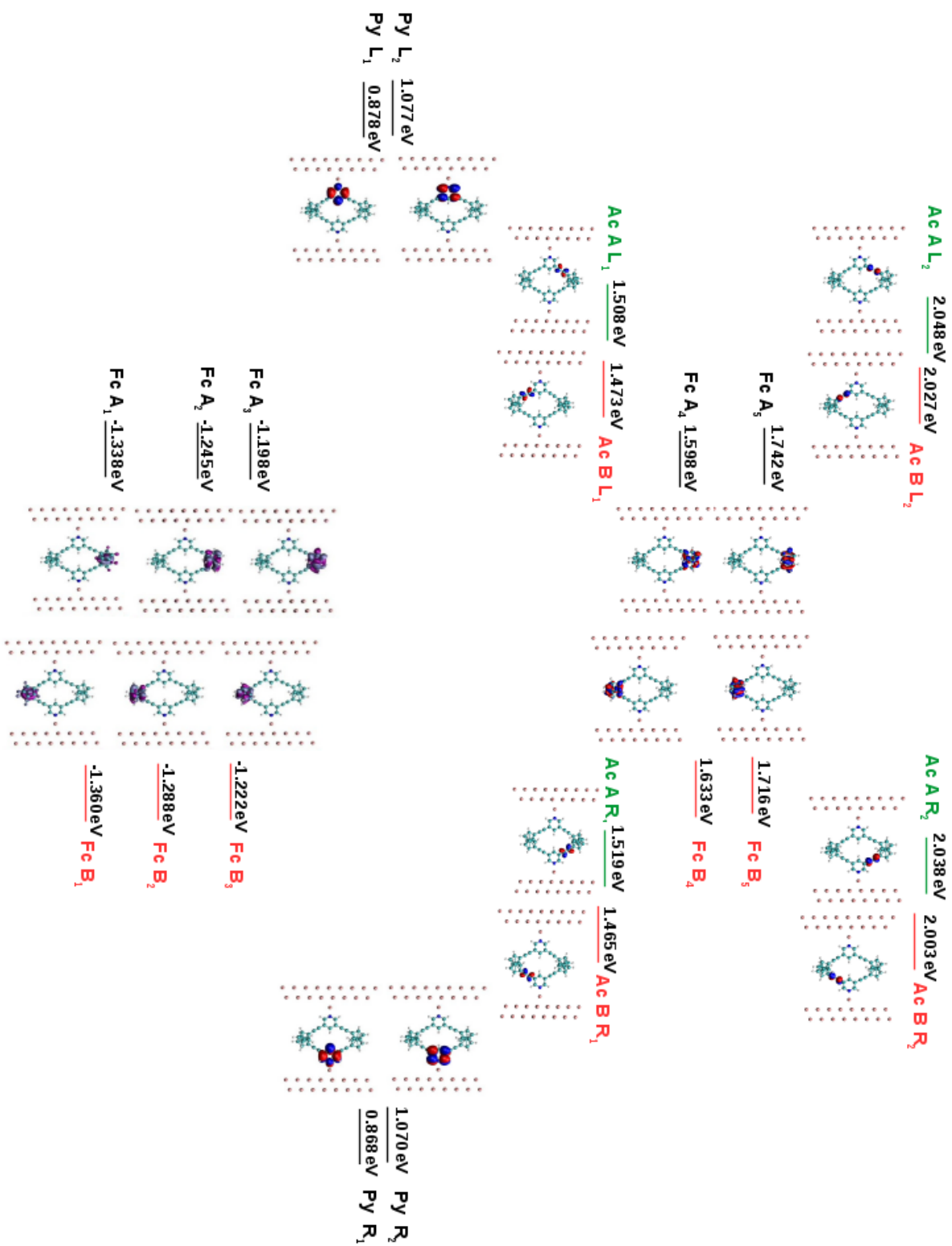


Figure 5.9: Relevant FOs and their corresponding energies for the m-d-l system.

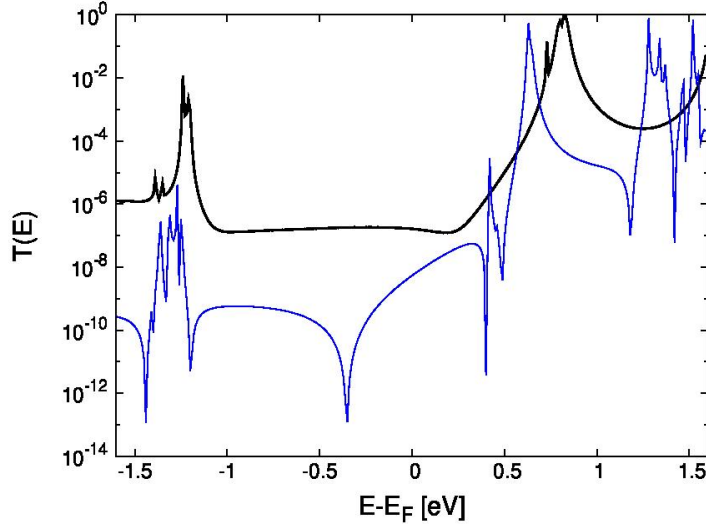


Figure 5.10: Transmission functions from respective full DFT (black solid line) and TB calculations of twenty two fragment orbitals (blue solid line) for the  $m - d - l$  system.

the transmission function (black solid line) in Figure 5.10, one can see that the peaks in the unoccupied region are broad and dominate the conductance. Hence we focus on the DQI feature in the upper board of the Fermi level which influences the conductance significantly. From a molecular orbitals analysis we know that four unoccupied states (Fig. 5.7) mainly contribute to the feature in the unoccupied region. From a FO perspective, we realize that the four MOs above the Fermi level are mostly localized on the two pyridyl fragment orbitals on each side where we show the orbital shapes as well as energies in Fig. 5.9. For all the molecules we designed, the two pyridyl groups remain the same, so the naive and simple assumption would be that if we replace the states in between the two pyridyl FOs with effective couplings, then only the sign and size of these effective couplings change for the different systems, and in this sense one could distinguish the geometrical differences through couplings in such a simple effective-coupling model.

**Effective Coupling model** We replace all the states for the acetylene and ferrocene fragments between pyridyl anchors by effective couplings, which include the direct couplings in between the pyridyl FOs as well as the

cumulative ferrocene or acetylenic FOs contributions which results in,

$$\Gamma = \gamma + \sum_i \frac{\alpha_i \cdot \beta_i}{\varepsilon - \omega_i} \quad (5.10)$$

Eq. 5.10 at the first glance is very similar to the Larsson's formula but there are actually some differences, because  $\gamma$  in Eq. 5.10 are the direct couplings for each pair of pyridyl states <sup>§</sup>, and  $\omega_i$  is the eigen energy of an individual acetylene or ferrocene state,  $\alpha_i, \beta_i$  are the couplings of the respective states to the left and right pyridyl states. The energy  $\varepsilon$  in Eq. 5.10 is obtained from the average value for the two involved pyridyl states on the left and right sides. If we mark the four pyridyl states we use here as 1, 2 on left side and 3, 4 on right side, there are then four combinations: 1 through the bridge to 3 or 4, and 2 through the bridge to 3 or 4. For the Hamiltonian in a subdiagonalized FO basis, states in the same subspace are orthogonal while the couplings between subspaces remain, which means couplings of the pyridyl FOs within the same pyridyl group are zero but the couplings of these pyridyl FOs to the other pyridyl groups or to the acetylenic and ferrocene FOs are not. In this way we can derive a model where only a few interesting FOs (in the energy range of 0.8 eV  $\sim$  2 eV ) remain so that the Hamiltonian we used for the analysis is dramatically reduced in size, but the states contributing to the four MOs in the unoccupied region are kept. Later on we derive effective coupling values by eq 5.10 between the 2 pairs of pyridyl FOs to replace bridge states, now only two pyridyl states on each side are kept (as shown in figure 5.11) resulting in a 4  $\times$  4 small Hamiltonian which should contain the relevant molecular information. In this way we obtained a rather small Hamiltonian which only contains pyridyl states with their respective onsite energy as well as effective couplings between them. By subdiagonalizing this smaller Hamiltonian, we get the transmission function  $\mathcal{T}(E)$  we obtained as a good approximation for the contributions from the four MOs in the region above the Fermi level with Larsson's formula. Fig. 5.12 shows that the two systems  $m - d - l$  and  $m - s - l$  with the DQI feature in the unoccupied region, which is close to the Fermi level are reproduced (in both solid black and red curves), while the other four systems correctly show no such dip. The next step is to look at the six small effective Hamiltonian and compare the signs and sizes of these effective couplings between the left and right pyridyl

---

<sup>§</sup>pairs are categorized by energy and orbital shape, namely the two pyridyl states with lower energy and the identical orbital shape on each side form one pair, and the other two form the other pair, as shown in figure 5.9.

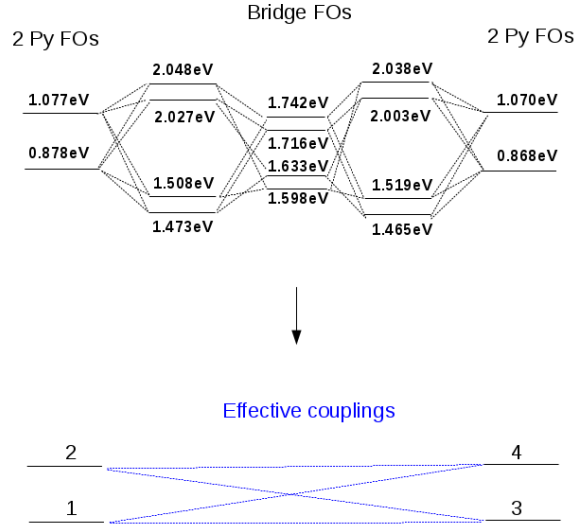


Figure 5.11: Effective coupling model of the  $m - d - l$  system in FO basis.

states. Unfortunately there are no distinguishable differences among the systems with DQI and no DQI regarding the four effective coupling values (Table 5.1), they are not distinguishable in the sense that the structure characteristics are not reflected directly apart from one fact that the shorter the length is the large the coupling value is. This is to say through the effective coupling values we cannot identify which structural features lead to the occurrence of destructive quantum interface.

Table 5.1: Effective coupling values for the model depicted in Fig. 5.11 for six ferrocene systems.

	$m - d - l$	$m - s - l$	$m - d - s$	$m - s - s$	$p - s - l$	$p - s - s$
$t_{13}$	-0.0015	-0.0014	-0.151	-0.0089	0.0059	0.031
$t_{14}$	0.00052	-0.00097	-0.016	0.248	0.0011	0.0081
$t_{23}$	0.00013	-4.1E-06	-0.0064	0.088	0.00027	-0.032
$t_{24}$	0.0014	-0.00029	-0.027	0.142	4.8E-05	0.0018

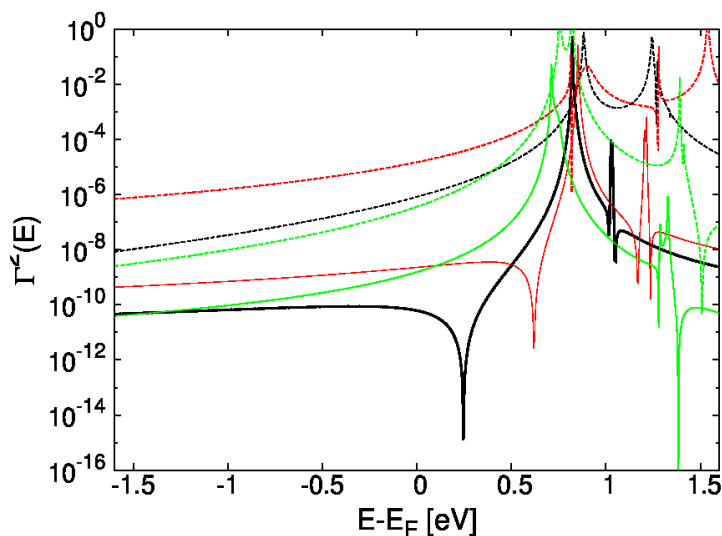


Figure 5.12: Transmission functions calculated from Larsson's formula of all investigated systems ( $m-d-l$ ,  $m-d-s$  are black solid and dashed lines,  $m-s-l$ ,  $m-s-s$  are red solid and dashed lines,  $p-s-l$  and  $p-s-s$  are green solid and dashed lines respectively) with the effective coupling model.

## 5.5 Atomic Orbital (AO) Analysis

Looking at the above models we discussed so far, there is one common approximation we take for the pyridyl groups, namely only the two pyridyl states on each side are considered out of the other states with higher or lower energies in our previous models. In fact, there are a few states in the higher or lower energy range with comparably large coupling values, where we know from the Larsson's formula that the large numerator value can compensate the decrease caused by a large denominator and hence the whole term is not negligible. Therefore it is indeed questionable to neglect these states with large couplings. In order to account for all the contributions of the two pyridyl groups, we derive another model based on an AO basis, where we take all  $p_\pi$  orbitals of the carbon or nitrogen atoms in pyridyl and acetylenic groups because  $p_\pi$  orbital contributions dominate the transmission probabilities in conjugated hydrocarbon molecules, while due to the complex nature of ferrocene moieties we still use FO basis for

ferrocene group.

As it is well known for conjugated hydrocarbon planar molecules, there are  $p_\pi$  orbitals occupied by valence electrons perpendicular to the planar backbone where the electrons can travel through MOs delocalized over the entire molecule. We treat the pyridyl and acetylenic groups as planar parts of the investigated molecules where only  $p_\pi$  orbitals contribute to the transmission function for single C or N atom, we do so by firstly subdiagonalizing the subspace of each carbon and nitrogen atom in the anchor groups, and then from the eigenenergy and orbital shape select the  $p_\pi$  states (as shown in figure 5.15 lower panel). Then we diagonalize stepwise the subspaces for two ferrocene groups in the full transport Hamiltonian and pick the relevant ferrocene states nearby the Fermi level, where only few FOs in the energy range of  $-2\text{eV} \sim 2\text{eV}$  are relevant. In this way we reduce the amount of states taken into consideration in a TB model meanwhile avoid an oversimplification regarding the anchor groups. Fig. 5.13 illustrates the Hückel model used for TB calculation with such a mixed atomic orbital (AO) and fragment orbital (FO) basis for the different compounds, In this simplified TB model, we define the anchors as pyridyl +

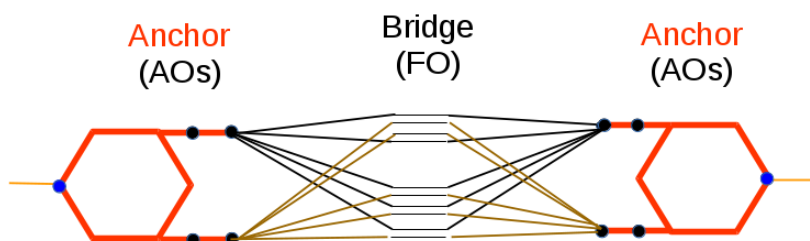


Figure 5.13: Tight binding model of  $m-s-l$ , where the different width of lines indicates the size of the couplings, upper and lower ferrocene groups are separated by different colors (black and brown).

acetylenic groups and the ferrocene groups as bridges, where only nearest couplings are considered. Another issue is the through space coupling between the anchor states on the respective left and right sides. One can easily build a TB model from molecular structures [81], and the coupling parameters between an-

<sup>¶</sup>in this context, this  $p_\pi$  type of orbital is the one perpendicular to the plane, i.e. also perpendicular to the transport direction  $z$ , I use  $\pi$  to avoid the confusion of coordinate  $z$ .



chor and bridge states for the model are taken from DFT calculations, which is in the range of  $0.1 \sim 0.2$  eV, the onsite energies for all AOs are set to be  $-2.5$  eV and the coupling values between AOs in the anchor groups are  $-3.0$  eV, where we show the result in Fig. 5.14. First of all, the HOMO-LUMO gap ranges

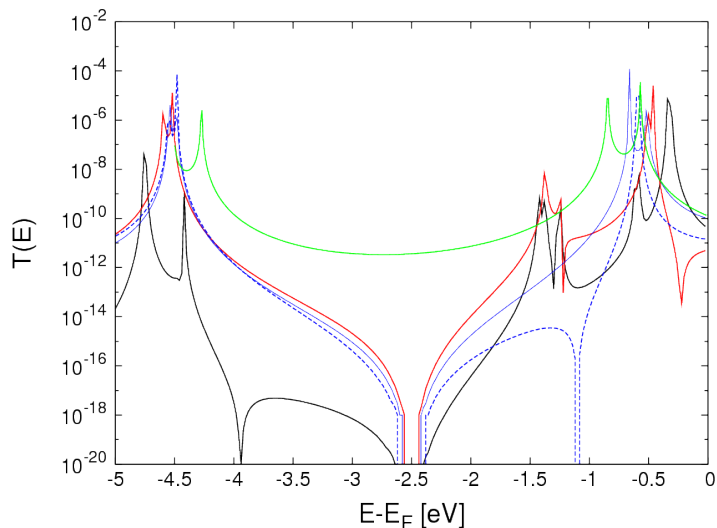


Figure 5.14: Transmission functions calculated from NEGF-TB for a  $m-d-l$  AO-FO model, where the black solid line represents calculations with all  $p_\pi$  AO of anchor states and ten relevant FO bridge states, the red solid line only contains contributions from one branch with five bridge states, the blue line shows the same single branch system but with only one FO bridge state, the green solid line shows a system with para- connectivity between anchor and one FO bridge state, the blue dashed line corresponds to the blue solid one but with through space coupling between acetylenic states on each side of the ferrocene.

from  $-4.5 \sim -1$ . eV for all curves, the deviation of this gap from that of DFT calculation is due to the approximations of the parameters (onsite energies and coupling values within anchor states) and the reduced number of bridge states. By considering also further reaching than only next nearest neighbor (NNN) couplings for the transmission function, they can be improved but at the cost of increasing the complexity of our TB model so we only consider the NNN couplings within the anchor states as well as between the anchor and bridge states. For the case where the two pyridyl groups are close to each other (for instance molecules  $m-d-s$  and  $m-s-s$ ) the through space coupling is comparable in size to NNN couplings thus also need to be taken into account. We

can see from Fig. 5.14 that there are more peaks in the HOMO region in the black curve due to a large number of localized ferrocene states for two branches compared with the red and blue curves which mimic the single branch system. Since we only consider the DQI feature in the LUMO region, we focus only on the ferrocene states in the unoccupied region, where one ferrocene FO which is strongly coupled to the anchors produces the blue solid curve. Compared with the red solid curve which contains five ferrocene states (two in the unoccupied region and three in the occupied region) the main (DQI) feature remains in the blue solid curve, which indicates that interference between multiple FO paths is not a decisive cause for DQI here. Switching on the through space (direct) coupling changes the feature in the HOMO-LUMO gap (blue solid line to dashed line), where for a detailed analysis we refer to the section 5.5.2. From this model, the potential causes for DQI we discussed above can be analyzed. For instance: how do the main features change when we switch off the couplings of one of the two branches, i.e. set all couplings of one branch to zero (the impact of the number of branches)? How does a meta- or para- connection influence the DQI feature? In order to obtain the model of Figure 5.13 we start from the full DFT transport Hamiltonian, and diagonalize the subspace containing anchor carbon or nitrogen atoms, we then select the  $p_\pi$  orbital. For the ferrocene bridge groups we keep the perspective of a FO basis. For the anchor  $p_\pi$  states only the nearest couplings are considered. We first consider all relevant bridge states, then reduce the states to a single state for each branch (in our cases this state is the ferrocene FO with the lowest energy in the unoccupied region). Then we add through space coupling for comparison. As one can see from Fig. 5.4, in the unoccupied region the double-branched molecules (black) and single branch analogs (red) have similar features apart from the number of peaks, since for double-branched molecules more states are coupled to the electrodes. while our attention is focused on when the DQI feature occurs independence on the different geometries, I use the three molecules  $m - s - l$ ,  $p - s - l$ ,  $m - s - s$  containing all the structural differences for illustration purpose <sup>¶</sup>. I show the three models for the three systems for comparison and their distinct behaviors in the transmission function. In Fig. 5.13 red, black and orange color codes distinguish the three types of couplings: couplings within the anchor states (red bold lines), couplings between anchor and bridge states (black) and couplings

---

<sup>¶</sup>the number of branches is verified that not a cause for the DQI effect by comparing  $m - d - l$  and  $m - s - l$  hence we focus one the single branch molecules.

of the anchor states to electrodes (orange thin lines), the red thin line between site 8 and 9 indicates the through space coupling. With this model we can analyze the consequence of geometrical differences: for instance by changing the connection from 3-, 7- and 10-, 11- to 4-, 7- and 10-, 16- one can mimic the frames formation from meta- to para- connectivity, when the sites 7, 8, 9, 10 are removed one moves to the non-spacers system  $m - s - s$ . In addition, the through space coupling can be adjusted from 0 (no through space coupling) to various values for different cases. Finally, one can by removing or adding states in this model easily investigate the role that multiple ferrocene states play. All the parameters we used are taken from DFT calculations, in this way we map the full Hamiltonian into a smaller TB Hamiltonian still containing the structural information causing the DQI in electron transport.

### 5.5.1 Identifying the Sources for Destructive Quantum Interference (DQI)

As one can see from the series of molecules we designed for the purpose of comparison (Fig. 5.3), there are two remaining possibilities which can be explored to explain the occurrence of DQI effects, i) the meta- connection of anchor groups to ferrocene; ii) multiple ferrocene FO paths, which interact with each other can also cause destructive quantum interference effects. The interaction of multiple FOs of the ferrocene moieties can be easily checked by taking few and single bridge states in this model respectively. Here I take all the AO  $p_\pi$  states of the anchor groups as well as bridge FOs with their number gradually reduced from five to one. Fig. 5.16 shows the DQI dip feature remains even for one bridge FO (black curve). In fact, the feature in the LUMO region remains the same for different number of bridge states apart from a peak shift, which means that multiple states do play a role but are not the fundamental reason to cause DQI. Comparing  $m - s - l$  and  $p - s - l$  for identifying the role of the meta- connection, we consider one bridge FO to obtain a model as simple as possible while keep the structural difference, i.e. meta or para- connectivity. Here, the difference is quite distinct, where in the interesting energy window  $m - s - l$  gives the DQI feature while  $p - s - l$  (green line) does not. We would like to know what is the essential difference between the two Hamiltonians. Since the two Hamiltonians still contain all AO states as well as one bridge states, we

need simplify the model further more.

### 5.5.2 Simplified Hamiltonian for Analyzing the Source of DQI from a Mathematical Point of View

If we look again the FO picture in Fig. 5.9, one would expect the pyridyl  $PyL_1/R_1$  states and acetylenic  $AcL_2/R_2$  states on each side have strong couplings to the ferrocene lowest unoccupied FO, since the hybridization of the orbitals depends highly on the overlap between them, i.e. the orbital shape and orientation. I subdiagonalize the subspace of the Hamiltonian for the anchor groups (pyridyl or pyridyl plus acetylenic) and pick the state\*\*that has the strongest couplings to ferrocene FO on each side for forming a  $3 \times 3$  small Hamiltonian †† which qualitatively reproduced the main features we are focusing on and the couplings between them are listed in Table 6.1.

Table 5.2: Couplings connecting the three FOs in Fig. 5.18 for three of the single branch systems, where all values are given in eV.

Coupling values			
	$m - s - l$	$p - s - l$	$m - s - s$
$t_L$	0.27	-0.23	-0.28
$t_R$	-0.22	0.25	0.22
$t_D$	-0.023	-0.0087	0.033

As a minimal model, where  $t_L$ ,  $t_R$  are the respective couplings of the left and right anchor states to the bridge state, and  $t_D$  is the through space coupling between the left and right anchor states. Now we compare the three parameters  $t_L$ ,  $t_R$  and  $t_D$  for the three single branch systems. As one can see from Table 6.1 there is not much difference IN  $t_{L/R}$  among the three Hamiltonians, but  $t_D$  differs from different cases. Since the through space coupling  $t_D$  seems to play a critical role, we need to generalize the  $3 \times 3$  Hamiltonian and

---

††in our case is the lowest unoccupied state.

††the three states are one anchor state on left/right side and one ferrocene lowest unoccupied FO.

see whether one could explain from a mathematical point of view by only using  $t_D$  as a variable. As we know  $\mathcal{T}(E)$  can be calculated as  $\mathcal{T}(E) \sim \Gamma^2(E)$ , where  $\Gamma^2(E)$  is obtained from the Larsson's formula (Eq. 6.1). One can define a DQI induced minimum at an energy  $E$  mathematically by,

$$\Gamma^2(E) = \left( \sum_{i=1}^N \frac{\alpha_i \cdot \beta_i}{E - \varepsilon_i} \right)^2 = 0 \quad (5.11)$$

Considering the three states in Fig. 5.18 that enter the  $3 \times 3$  Hamiltonian (FO basis) we obtain 3 MOs from subdiagonalizing this Hamiltonian, Eq. 5.11 can be written as,

$$\left( \frac{\gamma_1}{E - \varepsilon_1} + \frac{\gamma_2}{E - \varepsilon_2} + \frac{\gamma_3}{E - \varepsilon_3} \right)^2 = 0 \quad (5.12)$$

where  $\gamma_i$  is the product of the couplings of the MO states to the left and right electrodes ( $\alpha_i \cdot \beta_i$ ). From the MOs' eigen energies and eigen vectors in the subdiagonalized  $3 \times 3$  Hamiltonian, we found that MO<sub>1</sub> and MO<sub>2</sub> are mostly linear combinations of the 2 pyridyl FOs, while the coefficients for forming MO<sub>3</sub> are mostly from the ferrocene FO (almost 90 %). In addition we found that  $\gamma_1 + \gamma_2 + \gamma_3 = 0$  for the three systems due to specific symmetry properties of the  $3 \times 3$  Hamiltonian. We can obtain the DQI induced minimum position  $E_0$  ( $E_0 \neq \varepsilon_i$ ) from Eq. 5.12 as,

$$E_0 = \varepsilon_1 + \frac{1}{1 + \frac{\gamma_3(\varepsilon_2 - \varepsilon_3)}{\gamma_1(\varepsilon_1 - \varepsilon_2)}} (\varepsilon_3 - \varepsilon_1) = \varepsilon_1 + F_1 \cdot F_2 \quad (5.13)$$

We define two factors  $F_1 = 1/\{1 + (\gamma_3/\gamma_1) * [(\varepsilon_2 - \varepsilon_3)/(\varepsilon_1 - \varepsilon_2)]\}$  and  $F_2 = (\varepsilon_3 - \varepsilon_1)$ , where  $\varepsilon_i$  are sorted in energetic order, namely  $\varepsilon_1 < \varepsilon_2 < \varepsilon_3$ , so that  $F_2$  is always positive. We want to relate this minimum  $E_0$  to the energy  $\varepsilon_1$  where LUMO peak is, since only if the DQI feature is close to the LUMO peak the conductance will be influenced significantly. From Eq. 5.13 we notice that the sign of factor  $F_1$  plays a role on the position of the DQI minimum, if  $F_1 < 0$  and  $F_1 \cdot F_2 < 0$  the minimum lies above the  $\varepsilon_1$ , and if  $F_1 > 0$  it lies below the LUMO peak. I calculated the three transmission functions  $\mathcal{T}(E)$  by the Larsson's formula. As we can see from Figure 5.19, only  $m - s - l$  gives a minimum in the relevant energy region. For  $m - s - s$  there is a minimum appearing in the energy region above the LUMO+1, which is because for the former case,  $F_1$  has a negative value while for the latter case  $F_1$  is positive. In order to make a more general conclusion, we need to find out which factor is

Table 5.3: Explicit values for all parameters entering Equation 5.13 for the three MOs obtained by diagonalizing the  $3 \times 3$  Hamiltonian formed by the three FOs with  $\epsilon_L = \epsilon_R = 1.0$  eV,  $\epsilon_B = 1.6$  eV,  $t_L = 0.25$  eV,  $t_R = -0.25$  eV and with  $t_D$  as a variable. All values for  $t_D$  and  $E_0$  are given in eV, while the factors are dimensionless.

$t_D$	-0.12	-0.06	-0.03	0.03	0.06
$F_2$	0.93	0.89	0.91	0.95	0.97
$\gamma_3/\gamma_1$	-0.22	0.24	0.23	0.20	0.19
$F_{splitting}$	-11.75	-15.21	-7.32	-3.33	-2.54
$F_1$	0.28	-0.37	-1.48	3.02	1.92
$E_0$	1.12	0.56	-0.49	3.68	2.64

decisive for the sign of  $F_1$ . In order to simplify the mathematical explanation for the three Hamiltonians regarding the geometrical differences, we approximate all three systems with  $t_L = 0.25$ ,  $t_R = -0.25$ ,  $\epsilon_{L/R} = 1.0$  eV and the bridge state  $\epsilon_B = 1.6$  eV, while keep the individual different through-space coupling values for  $t_D$ . Then we take  $t_D$  as a variable and study how the position of the DQI minimum changes with varying  $t_D$ .

Now we decompose  $F_1$  into  $F_{ratio} = \gamma_3/\gamma_1$  and  $F_{splitting} = (\epsilon_2 - \epsilon_3)/(\epsilon_1 - \epsilon_2)$ , from Table 5.3 one can see that the factors  $F_2$  and ratio  $\gamma_3/\gamma_1$  are nearly the same for the testing systems with different  $t_D$  values while the factor  $F_{splitting}$  varies distinctly. We draw the conclusion that the energy dependent factor  $F_{splitting}$  plays the determining role for the DQI induced minimum positioning. We show the relation between  $t_D$  and the eigenenergies of 3 MOs obtained by diagonalizing the  $3 \times 3$  Hamiltonian within a FO basis, where  $\epsilon_L = \epsilon_R = 1.0$  eV,  $\epsilon_B = 1.6$  eV,  $t_L = 0.25$  eV,  $t_R = -0.25$  eV and  $t_D$  is a variable. As we can see from Fig. 5.21, the closer the vertical line to the crossing point ( $\sim -0.09$ eV) is, the closer the minimum to the LUMO peak will be. That is easy to explain when we look again at the Eq. 5.13, since  $F_2$  is always positive and the difference among systems is negligible, so  $F_1 = 1/(1 + (\gamma_3/\gamma_1) * F_{splitting})$  is decisive both in sign and size. There is only one way for  $E_0$  positioning below  $\epsilon_1$ , namely when  $F_1$  is negative. As we can see  $F_{splitting} = (\epsilon_2 - \epsilon_3)/(\epsilon_1 - \epsilon_2)$  is always negative, when  $F_{ratio}$  is positive,

meanwhile the product of  $F_{ratio}$  and  $F_{splitting}$  is smaller than -1 (i.e.  $< -1$ ), the whole denominator term  $(1 + (\gamma_3/\gamma_1) * F_{splitting})$  becomes negative. This means that  $F_{splitting}$  needs to be big enough in size to compensate the small  $F_{ratio}$  so that the product of these two is smaller than -1. For the cases when  $F_{ratio}$  is positive or the product of  $F_{ratio}$  and  $F_{splitting}$  is larger than -1 (i.e.  $> -1$ ) the minimum  $E_0$  will be above the LUMO peak ( $\varepsilon_1$ ). As we can see from Table 5.3, there is only one case where  $F_{ratio}$  is negative ( $t_D = -0.12$ ) resulting in  $F_1$  being positive and  $E_0$  is above the LUMO peak. For the two cases with  $t_D = 0.03$  and  $0.06$   $F_{splitting}$  is not small enough to produce a negative denominator of  $F_1$  hence the minimum  $E_0$  is above  $\varepsilon_1$ .

In summarizing this section, it is the splitting factor  $F_{splitting}$  due to the difference between the MO eigenenergies that causes the different positioning of the minimum. This factor  $F_{splitting}$  actually reflects the influence of the through-space coupling between the two FOs in Figure 5.18: Anchor-L and Anchor-R, since the three MOs are obtained by diagonalizing the Hamiltonian formed from three FOs. In the Hamiltonian with FO basis the only variable is  $t_D$ , hence the energetic difference among the three MOs obtained from the diagonalization must relate to the variable  $t_D$ . In this way we relate the geometrical differences of the ferrocene containing molecules and the position of the DQI minimum in the transmission function within a most simple topological model. In order to prove our argument, we illustrate this with more conventional Hückel models,

As one can see from Figure 5.22 by changing the through space coupling but keeping all the other parameters (meaning all anchor or bridge states onsite energies as well as couplings between anchor and bridge states are the same for all three configurations), the main difference is recovered, i.e. system  $m - s - l$  shows the DQI minimum in the energy region we are interested in while the other two systems don't show DQI in the interesting region. Due to the flat behavior of the transmission function in the HOMO-LUMO gap for  $m - d - l$  (which is caused by the narrowness of the HOMO peak and DQI nearby the LUMO peak), there would be almost no change in the conductance as a consequence of charging, while for  $m - d - s$  the conductance after charging might decrease due to the Lorentzian shape for the transmission curve in the HOMO-LUMO gap. These assumptions assumed a rigid shift of  $\mathcal{T}(E)$  and did

not foresee that the HOMO-LUMO gap is reduced in size by the charging where the tails of the HOMO peak now play a more active role for the definition of the conductance as can be seen from the NEGF-DFT calculations for the charged systems I discuss next ( 5.23 (b)). As we can see that all molecular states are shifted upwards in energy, where the shift for the branch closer to Cl is 1.12 eV, which is more than the shift of MOs on the other branch ( $\sim 0.9$  eV).

## 5.6 Charging effect

When we charge the double-branched ferrocene molecules, one would expect the different trend of conductance change due to the characteristic in HOMO-LUMO gap, namely conductance of  $m-d-l$  will not be influenced due to the flat feature in between HOMO-LUMO while  $m-d-s$  system the conductance changes substantially due to the sloped feature in HOMO-LUMO gap (as shown in figure 5.4), since the zero bias conductance is defined at the Fermi level. It can be seen that for  $m-d-s$  the transmission functions of the neutral and the charged system with  $d_{Cl-Fe} = 5.4 \text{ \AA}$  cross each other almost exactly at  $E_F$  resulting in almost equal conductance values, while the conductance is enhanced by the charging for  $m-d-l$  where the Fermi level is now at the shoulder of the HOMO peak for both charged setups with  $d_{Cl-Fe} = 5.7 \text{ \AA}$  and  $d_{Cl-Fe} = 4.3 \text{ \AA}$ . This latter charging effect on the conductance for  $m-d-l$ , however, would only result in an ON/OFF ratio of  $\sim 15-20$  which is by far too small for an operative transistor. Moreover, our initial idea that the charging might have an influence on the presence or absence of DQI effects is not supported by the changes in the transmission function, although the DQI induced flattening of the LUMO peak seems to be somewhat reduced for the asymmetrically charged setup <sup>‡‡</sup>. There is also a energy splitting (blue and cyan vertical lines in Fig. 5.23 lower panels) found in the occupied region for the charged systems compared with the corresponding neutral cases, which is caused by the different partial charge on two branches. In this study we investigated the potential use of branched molecules containing ferrocene centers in two branches as molecular transistors

---

<sup>‡‡</sup>asymmetrically charged setup refers to the shorter distance of  $d_{Cl-Fe} = 4.3 \text{ \AA}$  for the  $m-d-l$  molecule and  $d_{Cl-Fe} = 5.4 \text{ \AA}$  for the  $m-d-s$  molecule, respectively, while the longer distances  $d_{Cl-Fe} = 5.7 \text{ \AA}$  and  $d_{Cl-Fe} = 7.2 \text{ \AA}$  represent the symmetrically charged setups.



where the switching would be achieved by a redox process allowing to alternate between an ON and an OFF state and the latter might have a substantially reduced conductance due to DQI. We found such a DQI effect in the electron transmission for one of the branched molecules  $m - d - l$  but this effect is not altered significantly by charging for enabling a transistor functionality. Quite surprisingly, the appearance of the DQI effect was closely linked to the presence of acetylenic spacers between the ferrocene moieties and the pyridyl anchor groups. In an analysis where we mapped the essential orbital characteristics of the metal-organic compounds onto more and more simplified tight binding models in a systematic way, we could identify the structural sources for the unexpected finding: the direct through-space coupling between the anchor groups, which is determined in its size and sign by the detailed three-dimensional conformation of the respective molecule. This is fundamentally different from DQI as described for planar  $\pi$  conjugated hydrocarbons, where simple topological rules could be derived recently [82, 83] and geometrical details of the molecular structure beyond next-neighbor connectivity do not play an essential role. Our systematic analysis in this work can be applied to other metal-organic compounds exhibiting DQI effects which have an influence on their conductance and therefore provides an enabling tool for a rational design of molecular transistors.

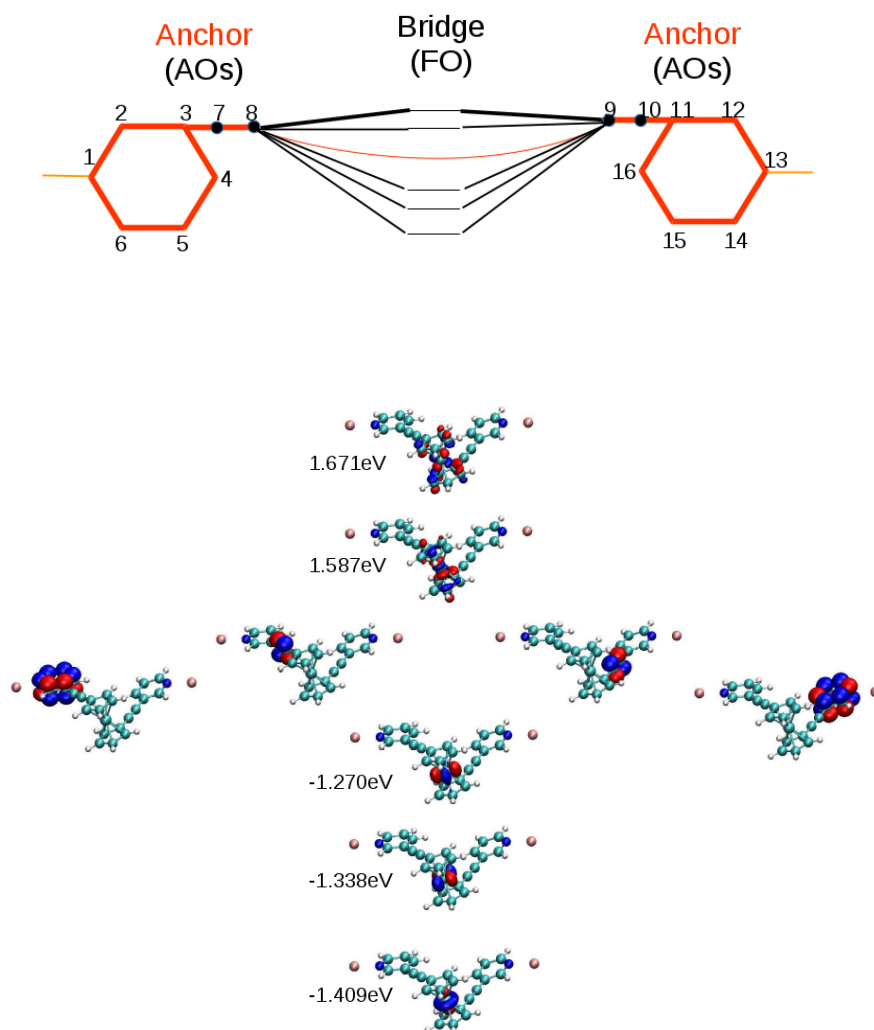


Figure 5.15: The Hückel model (upper panel) used for illustrating the geometrical differences and the direct coupling's role, the corresponding relevant FOs used in the TB model are depicted in the lower panel.

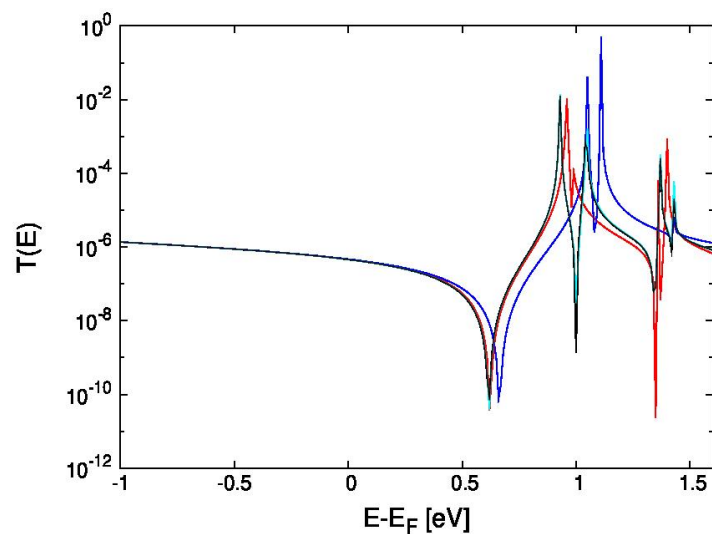


Figure 5.16: Transmission functions calculated from NEGF-TB for  $m - s - l$  with five bridge states (red line), three negative bridge states (blue line), two and single bridge FO states, respectively (cyan and black lines).

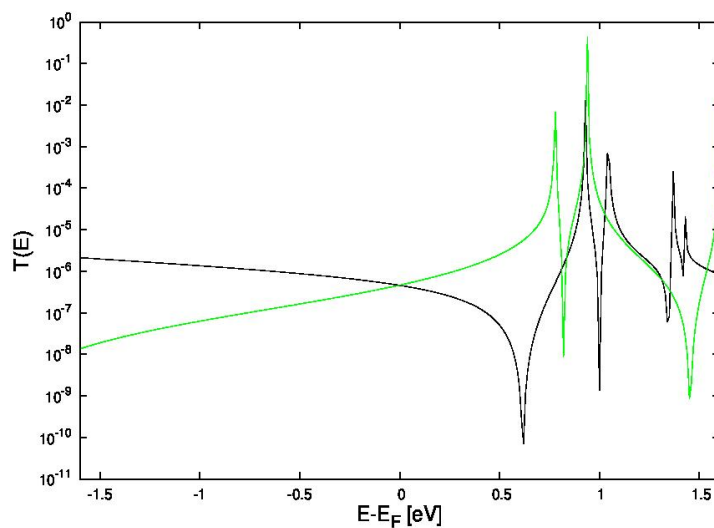


Figure 5.17: Transmission functions calculated from NEGF-TB of  $m - s - l$  (black line), and  $p - s - l$  (green line) respectively, with one bridge state for each case.

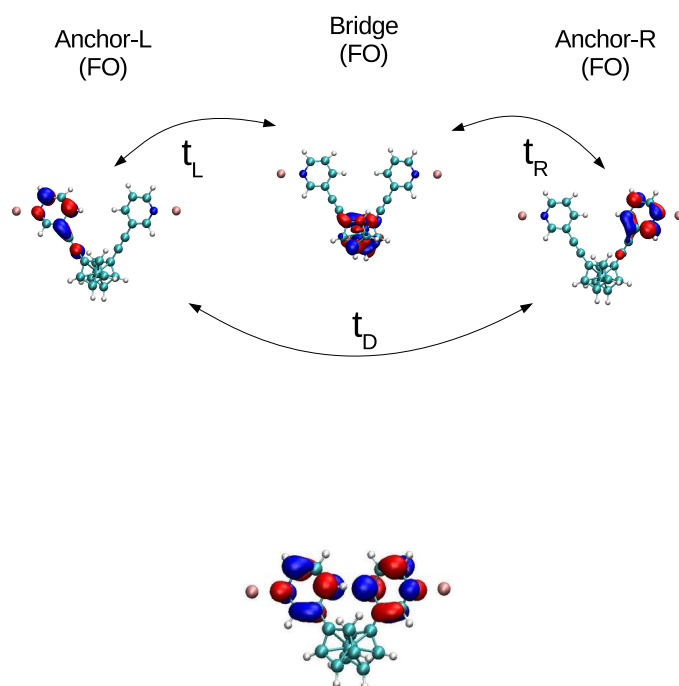


Figure 5.18: Three fragment orbitals in the upper panel for analysis; in the lower panel the two linker FOs for  $m - s - s$  to highlight the close distance between the linkers, i.e. the non-negligible through-space coupling.

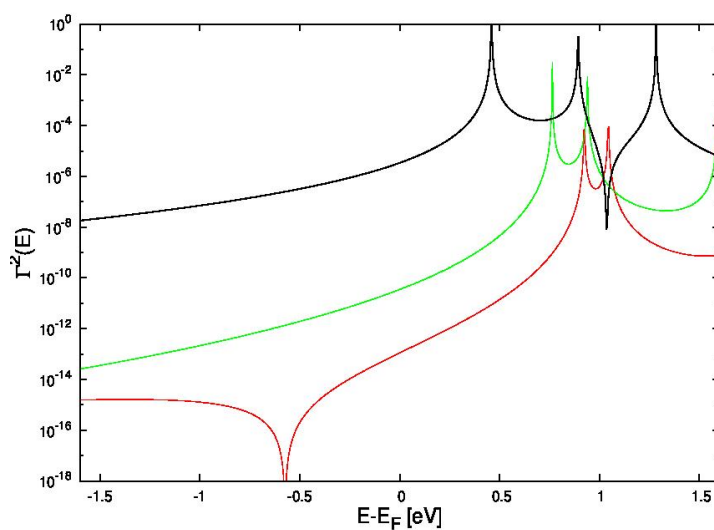


Figure 5.19: Transmission functions calculated from Larsson's formula of  $m-s-l$  (red solid line),  $m-s-s$  (black solid line) and  $p-s-l$  (green solid line), respectively.

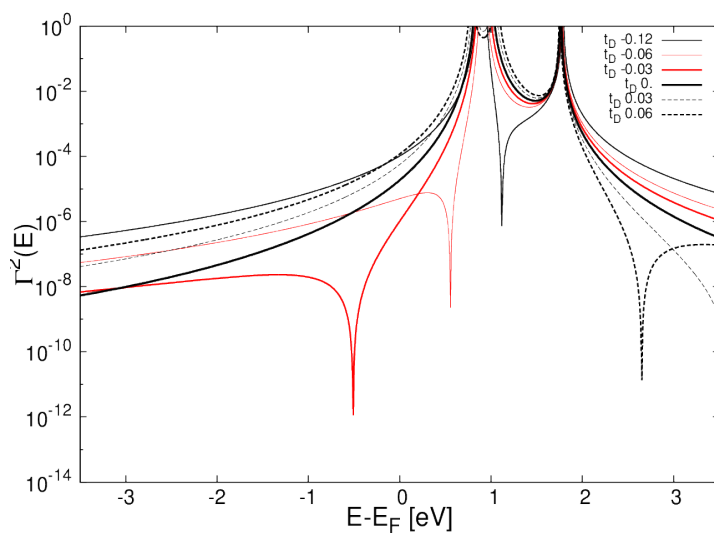


Figure 5.20: Transmission functions calculated from Larsson's formula with different direct coupling  $t_D$  values, where for the two solid red lines  $t_D$  are -0.06 eV (thin line) and -0.03 (bold line), two solid black lines are -0.12 (thin line) and 0.0 (bold line), for the two dashed black lines 0.03 eV (thin line) and 0.06 eV (bold line), respectively.

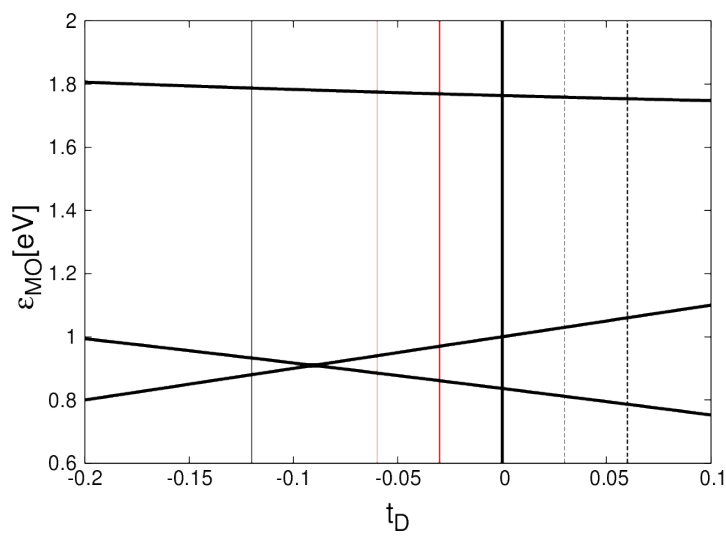


Figure 5.21: MO eigenenergies versus  $t_D$ , the color code is corresponding to the transmission curve in Fig. 5.20 where thin and bold vertical red lines are the ones with  $E_0$  positioning in the interesting region, thin and bold black lines illustrate that the further the distance of  $t_D$  to the crossing point (-0.09 eV), the further the minimum to  $\epsilon_1$  is in the transmission curve.

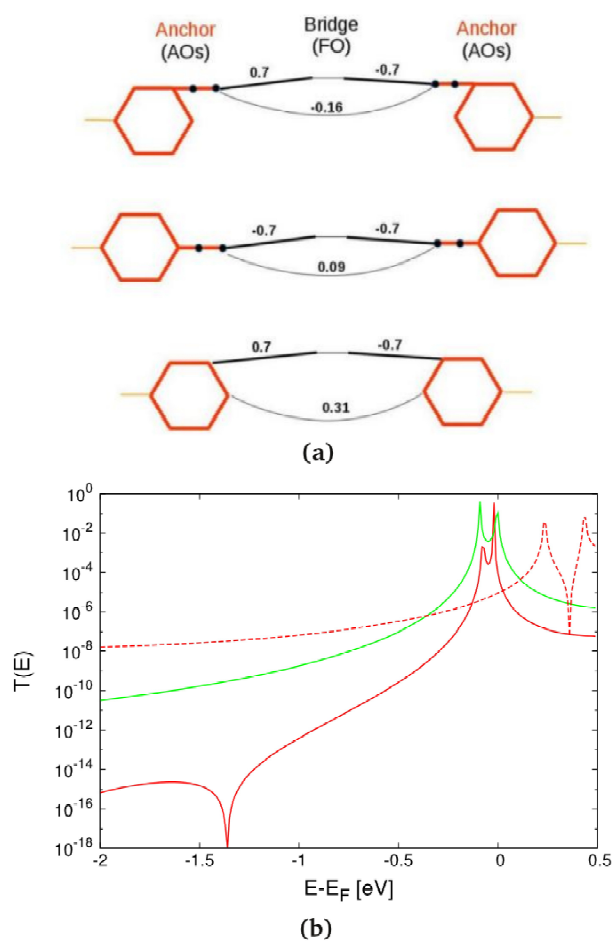


Figure 5.22: a) The topological model of  $m-s-l$ ,  $p-s-l$  and  $m-s-s$  with AO-FO-AO basis where all  $p_\pi$  anchor states and one bridge LUMO state are included; b) the corresponding transmission functions calculated from NEGF-TB for  $m-s-l$  (red solid line),  $p-s-l$  (green solid line) and  $m-s-s$  (red dashed line).

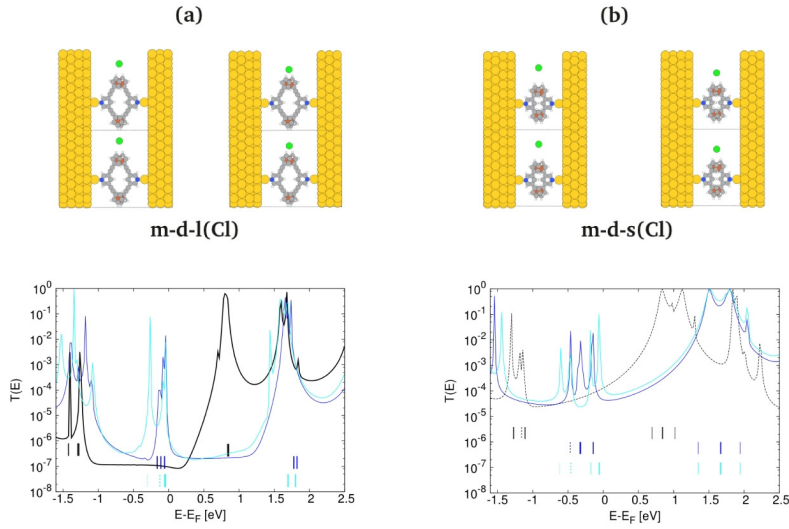


Figure 5.23: Junction geometries for two neighbouring cells in the periodic setup for the scattering region (upper panels) and  $\mathcal{T}(E)$  from NEGF-DFT calculations (lower panels) for the branched molecules a)  $m-d-l$  and b)  $m-d-s$  where the distance  $d_{Cl-Fe}$  between the Fe atom on one branch and the chlorine has been varied. For the transmission functions we calculated from NEGF-DFT, the curves for neutral systems are marked as solid black for  $m-d-l$  and solid dashed for  $m-d-s$ , while the cyan and blue curves mark  $\mathcal{T}(E)$  for the charged junctions for an asymmetric (right top panels) and symmetric (left top panels) placement of the chlorine between the two branches in neighbouring cells, respectively. The eigenenergies of the relevant MOs are also indicated in the lower panels, where the color code is corresponding to the one used for the transmission functions and the line type distinguishes the two branches.



CHAPTER 5. QUANTUM INTERFERENCE FOR BRANCHED MOLECULES  
CONTAINING FERROCENE IN THE JUNCTIONS

---

## CHAPTER 6

---

# Electron Transport Study in Coherent Tunneling Through Cyclic Ruthenium / Osmium Complexes

---

### 6.1 Motivation

Experimentally, the design and synthesis of branched compounds containing ferrocene moieties in each branch has been proposed [84] for the purpose of creating single molecule junctions, where the combination of quantum interference effects with redox gating for coherent electron tunneling as well as the electrostatic correlation between spatially distinct redox centers for electron hopping [85] can be explored. Theoretically a detailed analysis of branched compounds containing ferrocene centers has been published in our previous work [86]. In order to confirm the generality of this analysis we apply the same models and methods to cyclic Ru/Os(PPh<sub>2</sub>)<sub>8</sub>(C<sub>2</sub>H<sub>4</sub>)<sub>4</sub> bis(pyridylacetylde) molecules, where we use the notation of Ru/Os, Os/Os, Ru/Ru for the complexes containing symmetrical and asymmetrical branches. There are experimental and theoretical studies [85, 87] about coherent tunneling and electron hopping for Ru redox-active single-molecule junctions. Ref. [85] is focus on the comparison between coherent tunneling and hopping mechanisms in dependence of junction length for ruthenium bis(pyridylacetylde) complexes, and the work in [87] investigated the influence by the charge and spin states of redox-active metal centers on charge transport through single molecules in the transport pathway. The

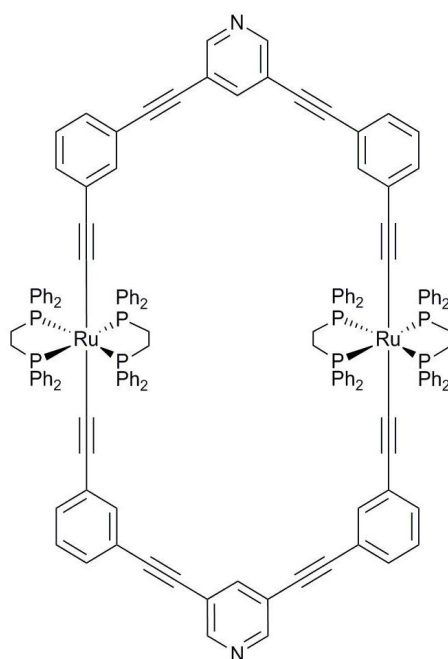


Figure 6.1: Chemical structure for cyclic  $\text{Ru}_2(\text{PPh}_2)_8(\text{C}_2\text{H}_4)_4$  bis(pyridylacetylide) complex .

simple but effective model we used for the work on branched ferrocene compounds is a combined atomic orbital (AO) fragment orbital (FO) tight-binding (TB) model where we keep only the  $p_\pi$  AO for each atom in both anchoring groups and one relevant bridge FO. For the molecule in Ref. [86] we found that the through-space coupling between the two anchor groups is the decisive parameter causing DQI effects in the interesting region, i.e. in the gap between the highest occupied molecular orbital (HOMO) and the lowest unoccupied molecular orbital (LUMO) and as close as possible to the Fermi level  $E_F$ . In Fig. 6.1 we show a type of molecule where one can create in-built asymmetry and by exchanging one of the redox centers Ru by Os. Due to the longer conjugated groups organic fragments are more decoupled from the pyridyl anchors than for the ferrocene compounds we studied in [86]. In this article, we want to address two issues: i) How do the models we used for the branched ferrocene molecules in Ref. [86] interpret coherent electron transport for this new type of molecules? ii) Will the decreased through-space couplings due to the longer molecular length have an impact on the occurrence of DQI?

## 6.2 Computational details for the NEGF-DFT calculations

We performed density functional theory (DFT) calculations with a PBE XC-functional within a non equilibrium Green's function (NEGF)-DFT framework [88, 89, 90, 91] using a linear combination of atomic orbitals (LCAO) [71] as basis set on a double zeta level with polarization functions (DZP) in the GPAW code [69, 70] for the computation of transmission probabilities,  $\mathcal{T}(E)$ , grid spacing of 0.2 Å for the sampling of the potential in the Hamiltonian on a real space grid is used. In our transport calculations, the scattering region is formed by the respective metal organic compounds and three and four layers for the upper and lower fcc gold electrodes, respectively, in a (111) orientation and with a  $6 \times 10$  gold surface defining the periodically repeated unit cell in the  $xy$  plane (transverse directions). The distance between the Au ad-atom attached to the electrodes surface and the N atom of the pyridyl anchor groups is 2.12 Å [72] and a  $k$  points sampling corresponding to a  $1 \times 2 \times 1$  Monkhorst Pack grid is used in scattering region for evaluating  $\mathcal{T}(E)$ , where the  $z$ -coordinate is the direction

of electron transport through the junction.

### 6.3 Results and discussion

In Fig. 6.2 we illustrate the molecular junctions derived from the compound in Fig. 6.1, where the two redox-center are Ru/Os, Os/Os and Ru/Ru, respectively. The transmission functions  $\mathcal{T}(E)$  for these junctions are shown in Fig. 6.3. In the resulting transmission functions in Fig. 6.3 the HOMO peaks are close to the Fermi level for all investigated systems, hence we expect the conductance to be dominated by the MOs below  $E_F$ . Our definition of DQI is that the transmission through a system with more than one MO around  $E_F$  is lower than the sum of the individual contributions of these MOs to  $\mathcal{T}(E)$  [92]. The exact energetic position of the Fermi energy within the HOMO-LUMO gap, which is also affected by the underestimation of this gap in our calculations due to the PBE parametrization of the XC functional, will have a crucial impact on the quantitative conductance but qualitatively DQI will always result in a significant conductance lowering for the structures where it occurs regardless of the details of the Fermi level alignment [82]. In order to clarify whether

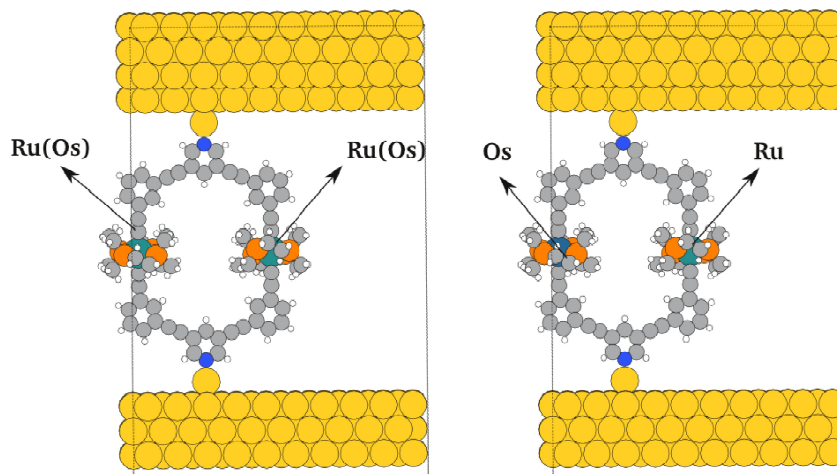


Figure 6.2: Junction structures for the Ru/Ru(Os) molecule.

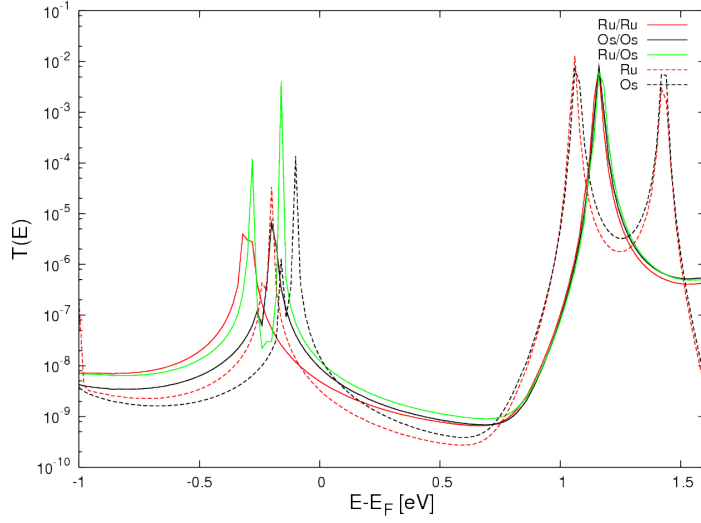


Figure 6.3: Transmission functions for double-branched molecules Ru/Ru (solid red line), Os/Os (solid black line), Ru/Os (green solid line), single branch Ru (dashed red line) and Os (dashed black line) in their neutral states, respectively.

there are DQI effects in the region of HOMO-LUMO gap, we focus on a simple TB model with a MO basis, where the eigenenergies of the molecular orbitals and their individual coupling values to the electrodes can be obtained by diagonalizing the subspace of the molecule in the we then use Larsson's formula Eq. 6.1 [93, 94, 95] to calculate the transmission properties  $\mathcal{T}(E)$ , where only frontier orbitals, namely HOMO and LUMO are included for the proof. As one can see from Fig. 6.4 the contributions from only frontier molecular orbitals HOMO and LUMO can produce the main features (blue curve) from the DFT result (red curve), From Fig. 6.4 we see that the contributions from the HOMO and LUMO together, i.e.  $(\text{HOMO} + \text{LUMO})^2$  (blue curve) are almost identical with the individual contributions  $(\text{HOMO}^2 + \text{LUMO}^2)$ , cyan curve) around  $E_F$ , which means no DQI between the two MOs is occurring for the system Ru/Ru, and for the other systems Ru/Os, Os/Os, single branch Ru and Os, the conclusion is the same, namely there is no DQI induced minimum in the energy region nearby the Fermi level. The transmission functions from NEGF-DFT for all investigated systems are shown in Fig. 6.3, where we note that for molecule Ru/Os the peak splitting (green curve) in the occupied region is distinct due to the intrinsic asymmetry by design of the two branches. Up to this point,

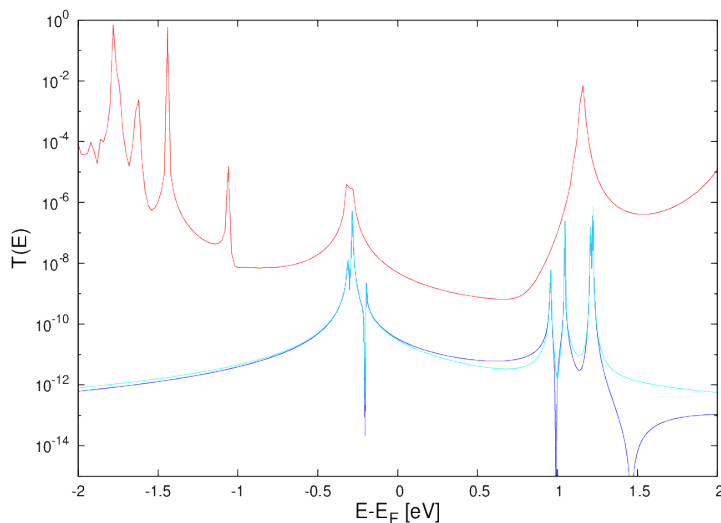


Figure 6.4: Transmission functions calculated from NEGF-DFT (red curve) and Larsson's formula (blue and cyan curves) for system Ru/Ru, where the blue curve denotes  $(\text{HOMO} + \text{LUMO})^2$  and the cyan curve  $\text{HOMO}^2 + \text{LUMO}^2$ .

we would expect that the charging induced upwards energy shift of the HOMO peak will cause conductance fluctuation in Fig 6.3.

We compare the transmission functions for single (red and black dashed lines) and double-branched (red and black solid lines) molecules to illustrate the impact of the number of branches. As we can see the conductance for the Ru (dashed red line) and Ru/Ru (solid red line) molecules are rather similar, and differ only by a factor of about 1.5. While the amount of peaks in the occupied region for the double-branched molecule is higher than the one in the single branch molecule as there are more molecular states coupled to the electrodes for the former. Comparing Os (dashed black line) and Os/Os (solid black line), the conductance for the double-branched molecule is lower by about a factor of 0.6 than for the single molecule.

The next question is then what is the reason for the absence of DQI in the HOMO-LUMO gap when these molecules share the similar design ideas with the ferrocene molecules we studied before? In order to address this question we move to the AO-FO model we previously used for ferrocene systems [86] and take the single branch Ru molecule as an example due to its representative

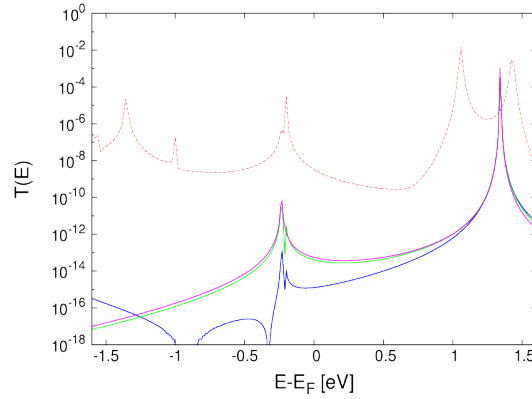


Figure 6.5: Transmission functions for single branch Ru molecule, where red dashed curve is from NEGF-DFT calculation, the three solid lines are obtained from NEGF-TB calculations with eight AO anchor states ( $p_\pi$  state of each carbon or nitrogen atom from subdiagonalization) and two bridge states (blue curve), two FOs on each side and two bridge states (green curve), one FO anchor state on each side and one bridge FO (magenta curve).

transmission function, which is very similar to those of the double-branched Ru/Ru, Os/Os and single branch Os molecules. In a first step we include all  $p_\pi$  AO states of the anchor groups (pyridyl plus the two acetylenic groups) by diagonalizing the subspace of each carbon or nitrogen on these groups and picking the  $p_\pi$  state. For the bridge group two relevant bridge (where we define Ru plus Phosphine ligands and conjugated spacers including acetylenic and benzene groups as the bridge group) FO in the occupied region are considered. Then we diagonalize the two anchor subspaces to get the relevant anchor FO states on both sides. By reducing the number of bridge FO states in the Hamiltonian we finally can minimize the Hamiltonian to the most simple one, which then only contains the three most relevant states, i.e. one FO on each anchor group and one bridge FO, which can be compared with the  $3 \times 3$  Hamiltonian for the ferrocene systems we discussed before [86].



Table 6.1: Parameters entering the  $3 \times 3$  Hamiltonian formed by three FOs ( Fig. 6.6) for three single branch systems, where all values are given in eV.

	Ru	Os	Fc
$t_L$	-0.026	-0.023	0.27
$t_R$	0.019	0.019	-0.22
$t_D$	5.7E-05	-5.1E-05	-0.023
$\Delta\varepsilon$	-1.5	-1.5	0.6

### 6.3.1 Comparison of a simplified $3 \times 3$ Hamiltonian for single branch Ferrocene, Ruthenium molecules

Based on the scheme we developed in Ref. [86] we use the simplified  $3 \times 3$  Hamiltonian for a mathematical perspective for explaining the role of the through-space coupling. The systems we investigated here have no DQI feature despite the number of branches even though they are designed similarly to the molecule Fc in [86], where the most distinct differences here are the molecular length and the type of metal centers. In our previous work [86] we found that in order to observe a DQI feature close to  $E_F$ , the through-space coupling value needs to be neither too small nor too big in size so that the DQI feature will not be pushed outside the interesting region as we illustrated in Ref. [86], where the  $t_D$  value for DQI occurring near to the position of LUMO peak is -0.023 eV. Now we ask for the Ru/Os(PPh<sub>2</sub>)<sub>8</sub>(C<sub>2</sub>H<sub>4</sub>)<sub>4</sub> bis(pyridylacetylde) molecules: is the length of the molecule causing the through-space coupling between left and right anchors vanish the only reason for the absence of near to the Fermi level? First of all we list the parameters that enter the  $3 \times 3$  Hamiltonian for the single systems Ru, Os and ferrocene (Fc).

$$H_{mol} = \begin{bmatrix} \varepsilon_L & t_L & t_D \\ t_L & \varepsilon_B & t_R \\ t_D & t_R & \varepsilon_R \end{bmatrix}$$

in Table 6.1 we can see the coupling values of  $t_L$ ,  $t_R$  and  $t_D$  connecting the three FOs (as shown in Fig. 6.6) for the three systems Ru, Os and Fc are distinct in the sense that: i) the size of the couplings between anchor and

bridge  $t_{L/R}$  are one magnitude smaller for Ru and Os than the ones in Fc; ii) the through-spacing coupling  $t_D$  for the Ru and Os molecules are negligible, iii) the bridge FO we used for the  $3 \times 3$  Hamiltonian is the highest-lying FO in the occupied region for Ru and Os and it was the the lowest-lying FO in the unoccupied region for Fc, which means the energy difference between anchor and bridge states  $\Delta\varepsilon$  are larger in size and the sign differs compared with the ferrocene molecule. Those differences can be interpreted in the perspective of fragment orbitals in Fig. 6.6, where the spatial localization on the anchors in Fig. 6.6(a) for the Ru molecule is rather similar to the one in ferrocene molecule (Fig. 6.6 b)), while  $t_{L/R}$ , the coupling between anchor where the spatial localization is mainly on pyridyl and the adjacent acetylenic group and bridge FOs where the localization is on the metal center and the neighboring acetylenic spacers are decreased markedly, because in between there is a benzene group separating them as shown in Fig. 6.6 a). In addition, the increased length also eliminates the direct coupling of the two anchor groups. The bridge state on the Ru molecule is now more delocalized because of the strong conjugation with the adjacent triple bonds, while for Fc the state is more localized on the ferrocene moiety.

Larsson's formula [93, 94, 95] has been used for approximating  $\mathcal{T}(E)$  as  $\mathcal{T}(E) \sim \Gamma^2(E)$  for coherent tunneling as we introduced in [86], where the resulting  $\mathcal{T}(E)$  can be normalized [96] and qualitatively reproduces the curves obtained from NEGF-TB [82]. From Larsson's formula,

$$\Gamma(E) = \sum_{m=1}^N \frac{\alpha_m \cdot \beta_m}{E - \varepsilon_m} \quad (6.1)$$

where  $\alpha_m, \beta_m$  are the couplings of the molecular state with eigenenergy  $\varepsilon_m$  to the respective left and right contact states, a simple mathematical condition can be defined for the energetic positions of DQI induced zeros in  $\mathcal{T}(E)$  (when  $\mathcal{T}(E) \sim \Gamma^2(E) = 0$ ), i.e.  $\Gamma(E) = \gamma_1/(E - \varepsilon_1) + \gamma_2/(E - \varepsilon_2) + \gamma_3/(E - \varepsilon_3)$  also must be zero, where  $\gamma_i = \alpha_i\beta_i$  for the three MOs resulting from the simple model. By making use of the specific symmetry properties of the  $3 \times 3$  Hamiltonian in the model, we can impose  $\gamma_1 + \gamma_2 + \gamma_3 = 0$  and obtain,

$$E_0 = \varepsilon_1 + \frac{1}{1 + \frac{\gamma_3(\varepsilon_3 - \varepsilon_2)}{\gamma_1(\varepsilon_1 - \varepsilon_2)}}(\varepsilon_3 - \varepsilon_1) \quad (6.2)$$

which should be the energy position of the DQI induced minimum  $E_0$ . Having now established that the parameters  $t_{L/R}$ ,  $t_D$  and  $\Delta\varepsilon$  distinguish the ferrocene

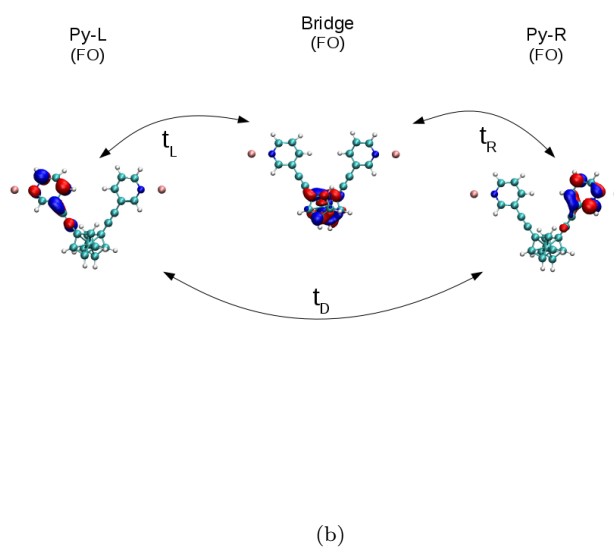
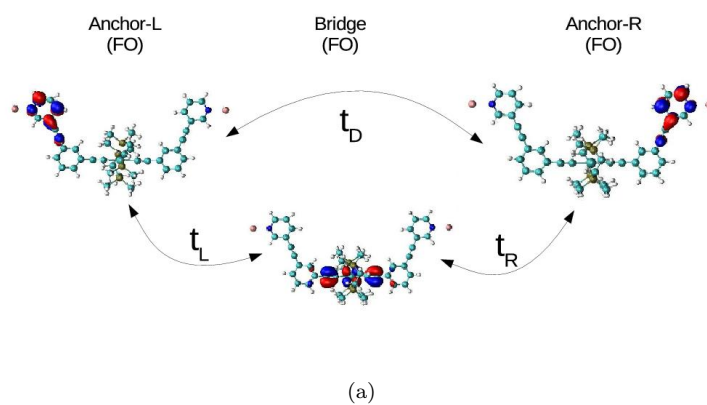


Figure 6.6: Spatial distributions of a) single branch Ru, the anchor FO on each side at 1.3 eV and the bridge FO at -0.2 eV; b) Fc, where the anchor FO on each side at 1.05 eV and the bridge FO at 1.66 eV [86].

Table 6.2: Three parameters defining the  $3 \times 3$  Hamiltonian which reproduces the transmission function for the single branch Ru and Fc systems, respectively.

	Ru	Fc
$\Delta\varepsilon$ (parameter 1)	-1.5	0.6
$t_{L/R}$ (parameter 2)	0.025	0.25
$t_D$ (parameter 3)	-5.0E-05	-0.023

molecule Fc with a DQI feature close to the LUMO from the single branch systems Ru and Os, we want to explore the mathematical reasons for the importance of these parameters, where we focus on the comparison of Ru and Fc regarding the three parameters entering the Hamiltonian. If we mark the three parameters for ferrocene molecule Fc as  $F_1, F_2, F_3$  and for Ru as  $R_1, R_2, R_3$ , there are six combinations for forming a  $3 \times 3$  Hamiltonian. From these Hamiltonians we calculate the transmission functions for each combination in order to identify the decisive parameter enabling DQI.

Now we approximate the coupling values  $t_{L/R}$  with 0.025 eV and 0.25 eV for Ru and Fc, respectively, and plot the transmission functions for the six resulting Hamiltonians based on the different combinations of the three parameters in Fig. 6.7. As one can see modifying any one of the three parameters in the Hamiltonian of Fc leads to the disappearance of the DQI feature in the interesting region, which indicates that all three parameters might have a fundamental influence on the DQI absence for Ru in the relevant energy region, meaning that the through-space coupling  $t_D$  seems to be no longer the only decisive parameter. We therefore keep two parameters and vary one in a systematic way to see the role each parameter plays. First of all we keep two parameters  $t_D, t_{L/R}$ , and vary  $\Delta\varepsilon$ , then plot  $E_0$  versus  $\Delta\varepsilon$ ; secondly we keep  $\Delta\varepsilon$  and  $t_D$ , vary  $t_{L/R}$  and plot  $E_0$  from Eq. 6.2 versus  $t_{L/R}$ ; finally we vary  $t_D$  while keep the other two parameters constant, and plot  $E_0$  versus  $t_D$ . The relation between  $E_0$  and each parameter is illustrated in Fig. 6.8. From panel (a) we can see that for the Ru system (black curves) where the  $t_D$  and  $t_{L/R}$  values are kept as in table 6.2,  $E_0$  is always above  $\sim 12$  eV not matter how  $\Delta\varepsilon$  varies, i.e. never in the interesting region, while for the Fc system (red curve) when variable  $\Delta\varepsilon$

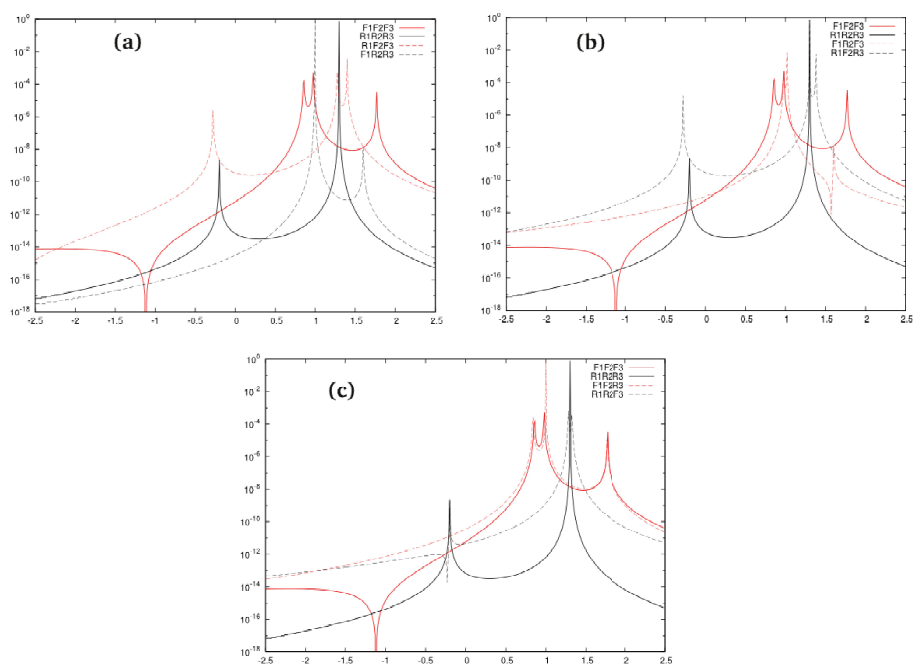


Figure 6.7: Transmission functions of the single branch Ru molecule (black solid line) and the single branch ferrocene molecule (red solid line) a)  $R_1F_2F_3$ , meaning replace parameter  $F_1$  by  $R_1$  (red dashed line), and  $F_1R_2R_3$  is obtained by replacing  $R_1$  with  $F_1$  (black dashed line); b)  $F_1R_2F_3$  (black dashed line) and  $R_1F_2R_3$  (red dashed line); c)  $F_1F_2R_3$  (black dashed line) and  $R_1R_2F_3$  (red dashed line), respectively.

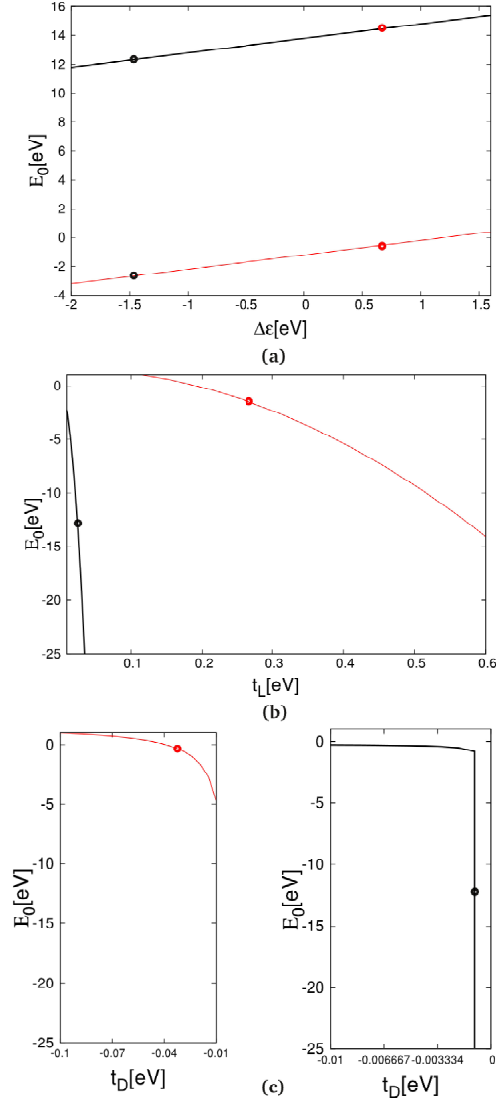


Figure 6.8:  $E_0$  versus a) the energy difference  $\Delta\epsilon$  between the anchor and bridge states; b) the coupling value  $t_{L/R}$  and c)  $t_D$  for Ru (black curve) and Fc (red curve), respectively. On each panel, the correct (real) parameter for each system is marked as black dot for Ru and red dot for Fc, i.e. in panel a) black dot ( $\Delta\epsilon = -1.5$ ,  $E_0 = 12.5$ ) and red dot ( $\Delta\epsilon = 0.6$ ,  $E_0 = -1.1$ ), in panel b) black dot ( $t_{L/R} = 0.025$ ,  $E_0 = -12.5$ ) and red dot ( $t_{L/R} = 0.25$ ,  $E_0 = -1.1$ ), in panel c) black dot ( $t_D = -0.00005$ ,  $E_0 = -12.5$ ) and red dot ( $t_D = -0.023$ ,  $E_0 = -1.1$ ), respectively.

reaches the real value of Fc, (i.e. 0.6 eV),  $E_0$  is around -1.1 eV, i.e. close to  $E_F$  as we also observed in Fig. 6.7 red solid curve. Besides, for Fc  $E_0$  covers the range of -3.0 — -1.0 eV along the variable  $\Delta\varepsilon$  changes from -2 — 1.5 eV, which means when keeping the  $t_D$  and  $t_{L/R}$  as in the Fc system, changing  $\Delta\varepsilon$  from 0.6 eV to -1.5 eV pushes the DQI minimum away from the Fermi level to  $\sim$  -3.0 eV. We also plot the relation between  $E_0$  and  $t_{L/R}$  where  $\Delta\varepsilon$  and  $t_D$  are kept as the values in the two respective real systems and show them in Fig. 6.8 b), and find that for system Ru (black curve)  $E_0$  decreases dramatically when variable  $t_{L/R}$  increases, at the real value point -0.00005 eV  $E_0$  is -12.5 eV, which is out of the interesting region, while for Fc (red curves) we can see the slope of the curve is comparably flat, meaning as long as  $t_{L/R}$  is in the range of 0.1 — 0.3 eV,  $E_0$  is located close to the Fermi level, while when  $t_{L/R}$  is smaller than 0.1 eV  $E_0$  locates above 1.5 eV, which is not within the interesting region anymore. Finally we plot the relation of  $t_D$  with  $E_0$  for the two systems, where we find that for Fc (red curves) the slope of the curve is rather flat compared with the black curve, namely in a rather wide range of variable  $t_D$  (-0.07 — -0.02 eV),  $E_0$  is located close to Fermi level, but when  $t_D$  is above -0.01 eV  $E_0$  decreases significantly (below -5.0 eV), which means even if one keeps the values of  $t_{L/R}$  and  $\Delta\varepsilon$  as in the Fc system, as long as  $t_D$  is above -0.01 eV, where we note that the negative sign is important and refer to our analysis in Ref. [86], DQI will never within a relevant energy window as is the case for Ru (where  $t_D \sim$  -0.00005 eV). While in Ru curve (black) when  $t_D$  reaches -0.023 eV (the real value as in Fc system)  $E_0$  locates around -0.023 eV which we also found in Fig. 6.7 c) black dashed curve, namely it is close to the Fermi level, however, as  $t_D$  is above -0.001 eV  $E_0$  decreases dramatically and always below -5.0 eV which is not in the relevant region anymore, that means in Ru system even the other two parameters  $\Delta\varepsilon$  and  $t_{L/R}$  are kept as they are, if  $t_D$  is in the region of -0.01 — -0.001 eV (where the curvature of black curve is rather flat)  $E_0$  will be close to the Fermi level and we can then observe DQI induced minimum, but when it is above the threshold -0.01 eV,  $E_0$  is pushed far below the Fermi level.

### 6.3.2 Conclusions from the TB analysis

The summary for this section is that molecules containing metal centers of Ru or Os differ distinctly from the ferrocene molecules we studied before in

the relation between molecular structures and the occurrence of DQI effects in electron transmission. Strikingly, the most important structural difference of these molecules from the ferrocene molecule Fc is that the length of the molecules we investigate here is larger resulting in the vanishing of through-space coupling, which plays a decisive role. From the plot 6.8 and the analysis above we conclude that: i) the energy difference between anchor and bridge states  $\Delta\varepsilon$  is not a decisive parameter, because as long as we keep the other two parameters ( $t_{L/R}$  and  $t_D$ ) for Ru we would never observe a DQI minimum in the interesting region ( $E_0$  is always above 12 eV); ii) the parameter  $t_{L/R}$  is also not a decisive parameter, since  $E_0$  will be always below -5 eV as long as we keep the other two parameters ( $\Delta\varepsilon$  and  $t_D$ ) for Ru; iii) the parameter  $t_D$  is a decisive parameter, because as long as  $t_D$  is below the threshold -0.001 eV ( $< -0.001$  eV) for Ru (i.e. keep the other two parameters as in Ru system), one would observe a DQI minimum close to the Fermi level as shown in Fig. 6.8 c) right panel.

## 6.4 Effect of Charging

We use the method as we did for the ferrocene systems in chapter 5 for the charging of the Ru/Os(PPh<sub>2</sub>)<sub>8</sub>(C<sub>2</sub>H<sub>4</sub>)<sub>4</sub> bis(pyridylacetylde) compounds with a chlorine atom in the cell close to the molecule which due to its higher electronegativity absorbs an electron from the junction while the overall neutrality of the device region is still maintained. As described in detail in Ref. [97] where the generalized  $\Delta$  self-consistent field ( $\Delta$  SCF) technique [73, 74] has to be applied in such a setup for ensuring that the self interaction problem of DFT is defied and the chloride ion is charged with one full electron while the resulting positive counter charge is distributed across the molecule and surfaces of the leads, the junction geometries are shown in Fig. 6.9.

Fig. 6.10, 6.11 and 6.12 show the transmission functions for each molecule in its neutral and charged states respectively, where we conducted spin polarized calculations. The spin-polarization resulting two effects in the transmission function: i) MOs move slightly downwards in the energy region, consequently the HOMO is further away from the Fermi level compared with the non-spinpolarized calculations; ii) the splitting of the occupied states nearby the Fermi level becomes more distinct. The dashed and dot dashed red curves



in each panel represent the spin low and high states for the charged system with a distance of  $5.2\text{\AA}$  between the metal center and Cl atom. As one can see the peak splitting for the two symmetrically built molecules Ru/Ru and Os/Os after charging is distinct as the amount of the charging induced peak shift for the two branches are different, where the branch closer to the chlorine atom have shifted more with respect to the Fermi level, while the MOs on the other branch almost have not been affected by the chlorine charging effect. For the asymmetrically built molecule Ru/Os, the peak splitting caused by charging is less distinct, where the peak splitting in the neutral case (black curve) is already rather distinct due to the in-built asymmetry, and charging does not seem to increase the splitting much further. As we can see from Fig. 6.11 and 6.12 the evolution from neutral states to the charged states, the HOMO-1 and HOMO-2 change the ordering sequence for Ru/Ru and Os/Os due to the degeneracy of HOMO, HOMO-1 and HOMO-2, HOMO-3 in the two symmetrically built systems. While that is not the case for Ru/Os, i.e. for Ru/Os the energetic ordering of HOMO, ... HOMO-3 remains the same as the corresponding neutral case after charging (as shown in Fig. 6.10).

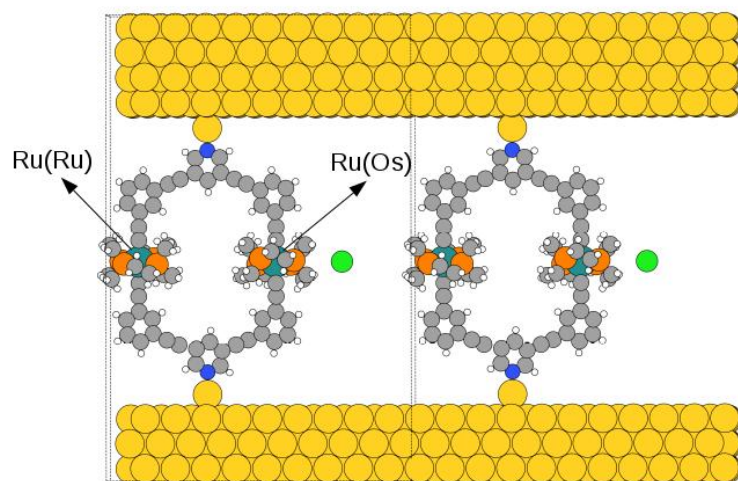


Figure 6.9: Junction geometries for two neighboring cells in the periodic setup for the scattering region of double branched Ru/Os (Cl) in a distance of  $5.2\text{\AA}$ .

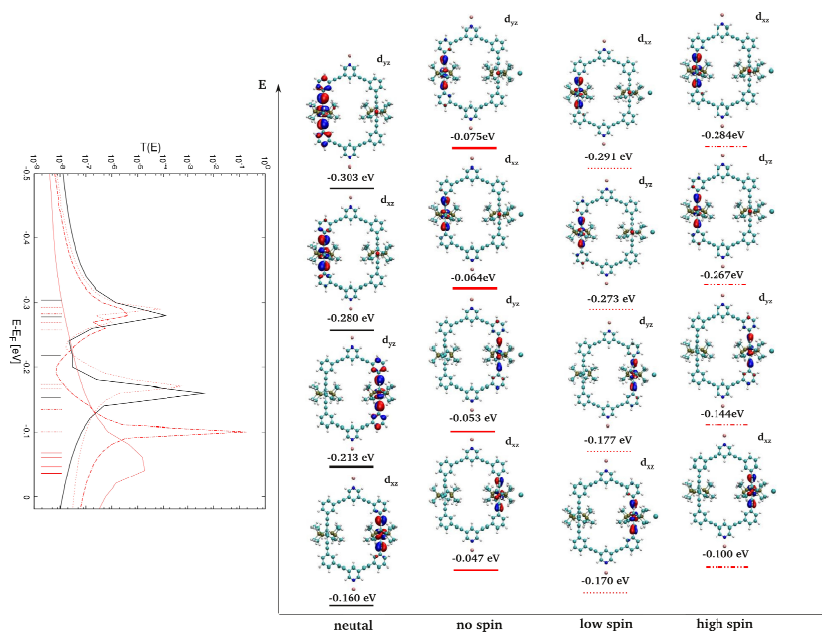


Figure 6.10: Four relevant occupied orbitals and transmission functions for Ru/Os(Cl) with spin and without spin-polarization in a distance of 5.2 Å, respectively. Where the black and red solid curves are the respective neutral and charged states, while the dashed and dot dashed curves in each panel mean spin low state and spin high state, respectively.

We list the conductance of the neutral and charged states for each system, as well as the partial charge on molecules where we intend to see the asymmetry induced by charging. As we can see from table 6.3 the asymmetry induced by Cl charging effect is quite distinct compared with the corresponding neutral molecules, while the conductance of the charged systems changes only slightly since the energy shifts of the peaks in the occupied region are small and the conductance is dominated by those peaks in the occupied region. We plot the spatial localization for the orbitals in the occupied region of both neutral and charged systems. As one can see from Fig. 6.10, 6.11 and 6.12 the  $d_{xz}$  and  $d_{yz}$  orbitals of the metal hybridize with the organic ligands resulting in the delocalization, which contributed to the conductance.

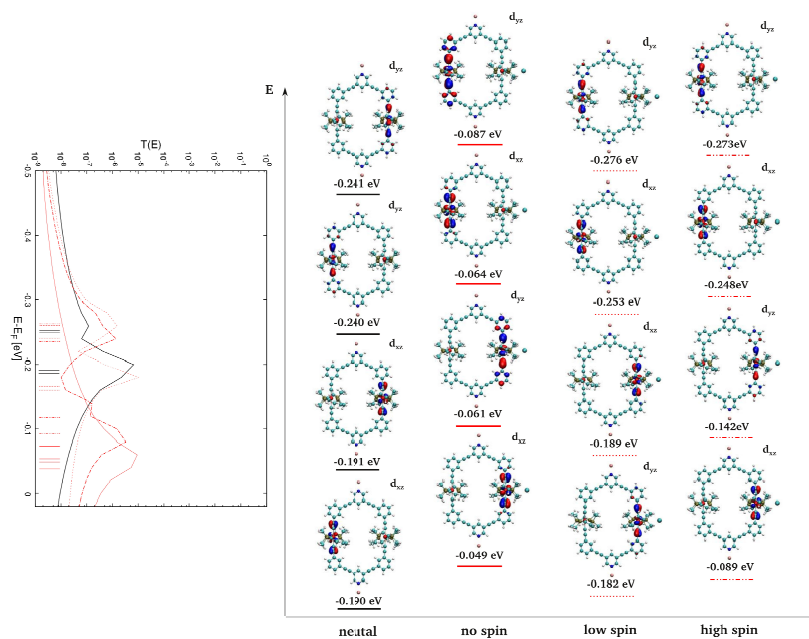


Figure 6.11: Four relevant occupied orbitals and transmission functions for Os/Os(Cl) with spin and without spin-polarization in a distance of 5.2 Å, respectively. Where the black and red solid curves are the respective neutral and charged states, while the dashed and dot dashed curves in each panel mean spin low state and spin high state, respectively.

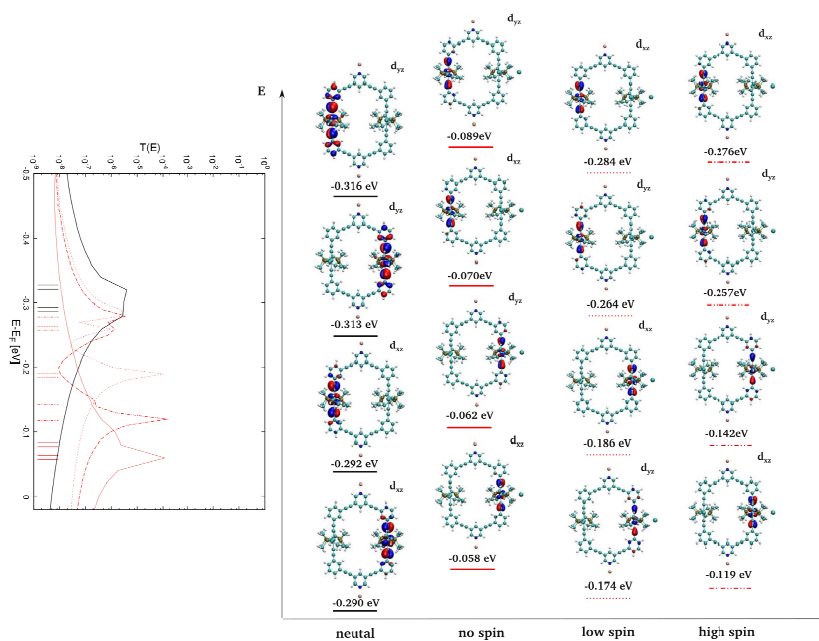


Figure 6.12: Four relevant occupied orbitals and transmission functions for Ru/Ru(Cl) with spin and without spin-polarization in a distance of 5.2 Å, respectively. Where the black and red solid curves are the respective neutral and charged states, while the dashed and dot dashed curves in each panel mean spin low state and spin high state, respectively.

Table 6.3: Partial charges in units of fractions of 1 e as obtained from a Bader analysis [98] for the neutral and charged molecules, where  $M_1$  and  $M_2$  denote the branch containing the metal center closer to and further away from the chloride ion, respectively. The conductance  $G$  for all molecules as defined by

$$\mathcal{T}(E_F) \text{ is given in units of } G_0.$$

	$M_1$	$M_2$	$G$
Ru/Os (neutral)	0.0345	0.0378	$4.57 \times 10^{-9}$
Ru/Os ( $d_{Cl-M}=5.2\text{\AA}$ )	-0.710	-0.173	$3.41 \times 10^{-9}$
Os/Os (neutral)	0.036	0.036	$4.61 \times 10^{-9}$
Os/Os ( $d_{Cl-M}=5.2\text{\AA}$ )	-0.230	-0.653	$1.84 \times 10^{-8}$
Ru/Ru (neutral)	0.038	0.037	$2.41 \times 10^{-9}$
Ru/Ru ( $d_{Cl-M}=5.2\text{\AA}$ )	-0.662	-0.208	$2.21 \times 10^{-8}$

## 6.5 Summary

In this study we investigated the potential use of branched molecules containing different metal centers in two branches as molecular transistors where the switching would be achieved by a redox process allowing to alternate between an ON and an OFF state. We did not find a DQI effect in electron transmission for these branched molecules, neither in their neutral nor in their charged states. By comparing our results with a previously studied ferrocene compound, we found that due to the increased molecular length, the decisive parameter over-space coupling  $t_D$  incapacitates the DQI induced minimum appear in the relevant energy region.

The charging effect on these cyclic molecules is not pronounced regarding the conductance change since from the transmission curves (Fig. 6.10, 6.11 and 6.12) the upward shift in energy induced by charging is small. The splitting peaks in the solid and dashed red curves in Fig. 6.11 and 6.12 indicate the charging effect on one branch (closer to Cl) is more significant than the other. Charging induced asymmetry for these cyclic molecules is rather distinct (see table 6.3), especially for the asymmetrically built molecule Ru/Os(Cl).

## CHAPTER 7

---

# Electron Hopping (Incoherent Electron Transport)

---

### 7.1 Motivation

Molecules incorporating metal complexes are of interest for molecular electronics since they can be oxidized and potentially lead to irregular I-V (current-voltage) characteristics and efficient charge conduction. Complexes containing transition metals like Iron, Ruthenium and Osmium (II/III) are investigated in this chapter due to the fact that they offer redox centers and spin states which are of importance in the experimental design for electronic devices like transistors [99]. When the Fermi level of one of the gold electrodes comes into resonance with a molecular level, charge injection into the molecule occurs.

One of the interesting topics for the double-branched systems we investigate in this chapter is that when there is already a charge on a molecule with two redox centers how would second charge hop through the system? The localization of a first charge be equally distributed on the left and right branch will if the symmetry is not broken. However in chlorine charged systems, asymmetry is manually induced by putting Cl closer to one of the branches, hence the partial charge on each branch is distinguishable.

In order to investigate the effect of the distribution of the first charge on the reorganization energy for the hopping of the second charge, the oxidation of the metal centers is induced by two ways in our work here: i) we add an external

positive charge at the beginning, and then relax the system for obtaining the equilibrium configuration of the charged molecule, so the final relaxed structure we obtained is a configuration with symmetrically distributed charge; ii) we put a chlorine near to one of the branches manually (the distance can be modified) and optimize the structure together with the Cl but fix the two atoms, i.e. the metal atom closer to the Cl and the Cl atom in order to keep the distance between them constant during the optimization process, this should result in an asymmetrical charge distribution where the external charge is mostly localized on one branch of the molecule.

## 7.2 Marcus-Hush Theory

Marcus theory was originally proposed by R. A. Marcus in 1956 [24] as a method for calculating the electron transfer (ET) rate between an electron donor (D) and an acceptor (A), where the first formulation of the ET theory only addressed the reorganization of solvation shell for the outer-sphere electron transfer reaction between Fe (II) and Fe (III). Marcus and Hush [25, 26] extended this formalism to include inner sphere ET contributions where a change of the atomic configuration for donor and acceptor moieties is also considered. This latter generalization also requires an explicit treatment of the reaction enthalpy (or driving force) as well as the overlap between the initial and final states of the electron-transfer reaction (usually is referred to as transfer integral). Marcus-Hush theory gives a unified treatment to homogeneous reactions where also electron transfer reactions at electrodes have been described.

Marcus-Hush theory has been extended to address a variety of applications such as electron transfer between inorganic, or organic molecules, in molecular crystals as well as bio- and electron-chemical cycles and proteins. The unanticipated and counter intuitive result of Marcus theory is the "inverted region" where electron transfer rates slow down with increasing exergonicity of the reaction, which was verified experimentally in 1984 [102]. The Nobel Prize in chemistry 1992 was awarded to R. A. Marcus for his contributions.

The three key parameters in the Marcus theory framework are i) the reorganization energy  $\lambda = \lambda_{in} + \lambda_{out}$ , where the inner reorganization energy

$\lambda_{in}$  is the energy gain due to the relaxation of the nuclei of the molecule as a consequence of charging, and the outer part  $\lambda_{out}$  is decomposed into Born and screening contributions where semiclassical models are involved for calculating this outer term, we discuss how they are calculated later; ii) the driving force  $\Delta G_0$ , which corresponds to the reaction enthalpy of the electron transfer reaction; iii) the transfer integral  $V_{DA}$ : which is the electronic coupling between the initial state and final state of the electron transfer reaction.

**Reorganization Energy** In the Marcus framework, potential energy wells are usually represented by parabolas as shown in 7.1 where the parabolic shape can be used to calculate reaction rates and the reaction coordinate represents all the nuclear coordinates involved in the reaction. The response of the polarized surrounding to the molecular charge is described by the linear response of a dielectric continuum, where the time scale of this response is separated into slow and fast parts. The reorganization energy  $\lambda$  is the energy required for the nuclei to reorganize nuclei enabling the electron transfer. It consists of an inner part and outer part, where the former ( $\lambda_{in}$ ) is the energy difference due to the relaxation of the nuclear positions of the donor and acceptor moieties from their neutral equilibrium state (initial state) to the oxidized state (final state). It is calculated by the total energy difference between the charged equilibrium configuration ( $q^f$ ) and its uncharged initial relaxed configuration ( $q^i$ ) of the central part of the electron transfer reaction following Gibbs parabola for the neutral state, or from the difference between its charged equilibrium initial configuration ( $q^i$ ) and uncharged relaxed configuration ( $q^f$ ) following the Gibbs parabola of the charged state. In our studies the electron transfer occurs between one of the electrodes and the central molecule in the junction, where the minimal structural rearrangement of the infinitely large metal electrodes is disregarded because its contribution to  $\lambda_{in}$  is insignificant. In Marcus theory, the curvature of the two Gibbs parabolas is identical, while in practical calculations they slightly differ so we take the average,

$$\lambda_{in} = \frac{\lambda_1 + \lambda_2}{2} = \frac{(|E_{f,eq}(q_{+1}) - E_{i,eq}(q_0)| + |E_{i,eq}(q_{+1}) - E_{f,eq}(q_0)|)}{2} \quad (7.1)$$

where  $q_0$  and  $q_{+1}$  are the respective neutral and charged equilibrium states, and  $E_i$  and  $E_f$  are the initial and final Gibbs energy functions.  $\lambda_{out}$  is the contribution of the surrounding medium to the reorganization energy which



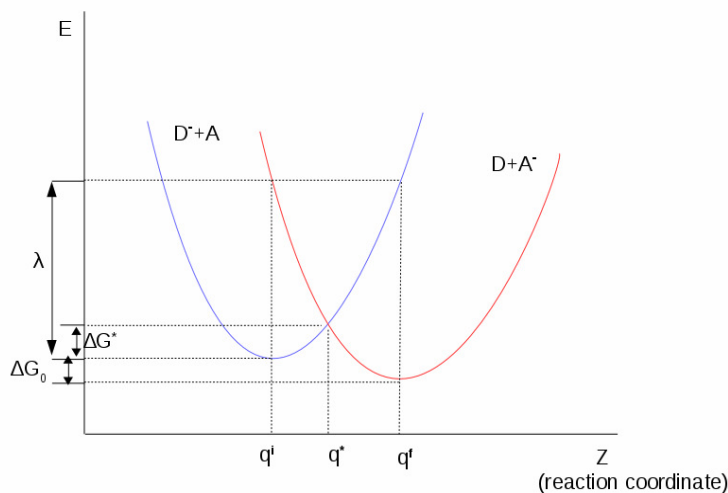


Figure 7.1: The two Marcus parabolas describing the free energy of the system as a function of the reaction coordinate in the dielectric solvent medium. The initial, final and transition state are marked as  $q^i$ ,  $q^f$  and  $q^*$ , respectively.

includes the response of a solvent and the screening effect caused by a charge near to a metal surface. Therefore  $\lambda_{out}$  can be decomposed into  $\lambda_{Born}$  and  $\lambda_{image}$ ,

$$\lambda_{out} = \lambda_{Born} + \lambda_{image} \quad (7.2)$$

where we calculate  $\lambda_{Born}$  with the generalized Born (GB) approach, which considers the solvent as a continuous medium which mimics real solvent properties in an averaged way. Such a model is computationally much more efficient than the alternative of molecular dynamics simulations in rather large cells. The total solvation free energy ( $G_{sol}$ ) within the GB framework is a sum over a solvent-solvent cavity term ( $G_{cav}$ ), a solvent-solute van der Waals term ( $G_{vdW}$ ) and a solvent-solute electrostatic polarization term ( $G_{pol}$ ),

$$G_{sol} = G_{cav} + G_{vdW} + G_{pol} \quad (7.3)$$

$G_{cav} + G_{vdW}$  in the GB model is computed by evaluating the solvent-accessible surface area, where this accessible area is computed numerically as,

$$G_{cav} + G_{vdW} = \sum_{i=1}^N \sigma_i SA_i \quad (7.4)$$

with  $\sigma$  an empirically determined atomic solvation parameter, and SA ( $\text{\AA}^2$ ) the solvent accessible surface area for atoms (that are taken into account). The method for calculating  $G_{pol}$  follows Di Qiu *et al* [103] with a generalized Born equation and was modified for irregularly shaped solutes. For systems with irregularly shapes, the Born radius  $a_i$  is complicated to calculate, since it is defined as the distance from the center of the ion to the boundary of the dielectric, and a reasonable accurate evaluation of  $a_i$  is the most time-consuming part of the GB model. The idea which improved the calculation of  $a_i$  is that it begins with the original Born expression for a monoatomic spherical ion surrounded by a continuum dielectric medium,

$$G_{pol} = -166.0 \left(1 - \frac{1}{\epsilon}\right) \frac{q^2}{a_i} \quad (7.5)$$

where  $\epsilon$  is the dielectric constant and  $q$  the charge. For the polyatomic solute, the distance from an atomic center to the molecular van der Waals surface varies. Di Qiu *et al* used an appropriate way to average the various distance and produce a single value of  $a$ , with corrections to the defects of this solvation model, generating a  $G'_{pol,i}$  as,

$$G'_{pol,i} = \frac{G_{pol,i}}{1 - \frac{1}{\epsilon}} = \frac{-166.0}{R_{vdW-i} + \phi + P_1} + \sum \frac{P_2 V_j}{r_{ij}^4} + \sum \frac{P_3 V_j}{r_{ij}^4} + \sum \frac{P_4 V_j CCF}{r_{ij}^4} \quad (7.6)$$

where  $G_{pol,i}$  is the polarization energy of atom  $i$ ,  $R_{vdW-i}$  ( $\text{\AA}$ ) is the van der Waals radius of atom  $i$ ,  $\phi$  is the dielectric offset ( $\text{\AA}$ ),  $r_{ij}$  ( $\text{\AA}$ ) is the distance between atom  $i$  and  $j$ ,  $V_j$  ( $\text{\AA}^3$ ) is the volume of atom  $j$ ,  $P_1, P_2, P_3$  and  $P_4$  are the empirical scaling factors,  $CCF$  is the close contact function for nonbonding interactions,

$$CCF = 1.0, \text{ if } \left(\frac{r_{ij}}{R_{vdW-i} + R_{vdW-j}}\right)^2 > \frac{1}{P_5} \quad (7.7)$$

where  $P_5$  is a soft cutoff parameter, otherwise,

$$CCF = 0.5 \left[1.0 - \cos\left(\frac{r_{ij}}{R_{vdW-i} + R_{vdW-j}}\right)^2 P_5 \pi\right]^2 \quad (7.8)$$

The Born radius can then be calculated as,

$$a_i = -\frac{-166.0}{G'_{pol,i}} \quad (7.9)$$

$$\lambda_{Born} = \left( \frac{1}{\epsilon_{\infty}} - \frac{1}{\epsilon_s} \right) \sum_{i=1}^N \sum_{j=1}^N \frac{\Delta q_i \Delta q_j}{f_{GB}} \quad (7.10)$$

with

$$f_{GB} = \sqrt{r_{ij}^2 + a_{ij}^2 \exp\left(-\frac{r_{ij}^2}{2a_{ij}^2}\right)} \quad (7.11)$$

where  $\epsilon_{\infty}$  and  $\epsilon_s$  are the solvent optical and static permittivities, respectively,  $\Delta q$  is the partial charge difference of an atom in its neutral and oxidized states in vacuum. The partial charge distribution we obtain from a Mulliken charge analysis [104] of a DFT calculation, and  $a_{ij} = \sqrt{a_i a_j}$  is van der Waals radii.

The image charge contribution originates from a charged molecule adsorbed close to a metal surface and  $\lambda_{image}$  is calculated from a model proposed by Thygesen *et al.* [105], [106], where one separates the two conducting surfaces with a distance  $L$  (junction length) in the transport direction  $z$  and obtains,

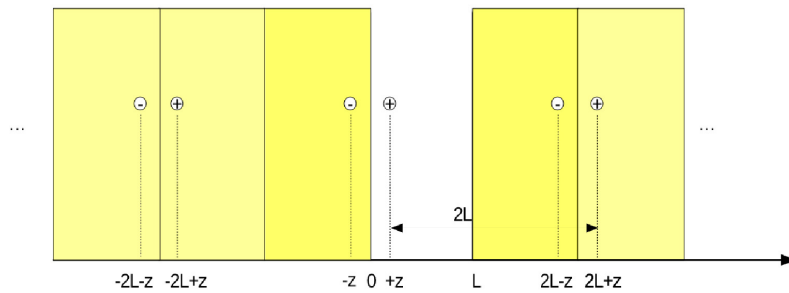


Figure 7.2: Schematic representation of the image charge model for a charge between two electrodes.

$$\lambda_{image} = -\frac{1}{2} \left( \frac{1}{\epsilon_{\infty}} - \frac{1}{\epsilon_s} \right) \sum_{i=1}^N \sum_{j=1}^N \Delta q_i \Delta q_j \times$$

$$\sum_{n=1}^{\infty} \left[ \frac{1}{\sqrt{(z_i + z_j - 2nL)^2 + R_{ij}^2}} + \frac{1}{\sqrt{(z_i + z_j - 2(n-1)L)^2 + R_{ij}^2}} \right. \\ \left. - \frac{1}{\sqrt{(z_i - z_j + 2nL)^2 + R_{ij}^2}} - \frac{1}{\sqrt{(z_i - z_j - 2nL)^2 + R_{ij}^2}} \right]$$

with  $R_{ij}^2 = (x_i - x_j)^2 + (y_i - y_j)^2$ . The image term contains the infinite sum of Coulomb interactions resulting from the partially charged molecule between two parallel electrodes, where an infinite number of mirror images are induced within an image potential framework for the screening.

**Driving Force** The driving force in Marcus theory is defined as the energy difference of the two parabolas' minima, which are the equilibrium states for the respective neutral and oxidized configurations in the reaction. We apply a method to calculate  $\Delta G_0$  for the junction setup by considering the Fermi level alignment and charge equilibration [107, 96, 108], meanwhile within a single particle picture which we also use for the description of coherent tunneling, in this way we can make a direct and meaningful comparison between the I-V curves for electron hopping and the transmission function for coherent tunneling. For a hole-transfer, the way we calculated the driving force for the junction setup is relating the HOMO position of the confined junction system to the Fermi level of the electrodes. The energy needed to transfer an electron from the HOMO to one of the electrodes within a single-particle picture can be expressed as,

$$\Delta G_0 = \varepsilon_{HOMO} - E_f \quad (7.12)$$

where  $\varepsilon_{HOMO}$  was obtained from subdiagonalizing the molecular sub space in the transport Hamiltonian from a NEGF-DFT calculation within this scheme. The relaxation of the other molecular eigenstates is neglected, and any energetic effect of the metal electrode is also ignored because of the large number of electronic bands near to Fermi level.

**Transfer Integral** The transfer integral  $V_{Au-mol}$  describes the electronic coupling between the molecule and the electrodes.  $V_{Au-mol}$  can be retrieved from the MO peak width in the transmission function calculated from

NEGF-DFT for coherent tunneling since on a single-particle level picture the two are related. Within this model  $V_{Au-mol}$  is obtained by a numerical fitting of a Lorentzian function in the form,

$$\mathcal{T}(E) = \frac{4V_{Au-mol}^2}{4V_{Au-mol}^2 + (E - \varepsilon_{MO})^2} \quad (7.13)$$

where  $MO$  is the involved molecular state (in our case the HOMO), and its energy  $\varepsilon_{MO}$  is obtained from NEGF-DFT calculation. We decoupled all the contributions of other molecular states to the electrodes, where  $\mathcal{T}_{HOMO}(E)$  and  $\epsilon_{HOMO}$  are known from NEGF-DFT, and the transfer integral can then be obtained by numerical fitting in the function 7.13.

**Hopping Conductance and Transfer Rates** The conductance in the hopping regime is calculated as [109, 85],

$$G_{hop} = \frac{e^2}{2k_bT} \frac{k_{ox}k_{red}}{k_{ox} + k_{red}} \quad (7.14)$$

where the  $k_{ox,red}$  are the transfer rate of the reduction and oxidation transfer reactions, which define the overall hopping process through the junction,

$$k_{ox} = \frac{2\pi}{\hbar} V^2 \frac{1}{\sqrt{4\pi\lambda k_B T}} \int_{-\infty}^{\infty} \exp\left(-\frac{(\lambda + \Delta G_0 + \epsilon)^2}{4\pi\lambda k_B T}\right) [1 - f(\epsilon)] d\epsilon \quad (7.15)$$

$$k_{red} = \frac{2\pi}{\hbar} V^2 \frac{1}{\sqrt{4\pi\lambda k_B T}} \int_{-\infty}^{\infty} \exp\left(-\frac{(\lambda - \Delta G_0 + \epsilon)^2}{4\pi\lambda k_B T}\right) f(\epsilon) d\epsilon \quad (7.16)$$

$f(\epsilon)$  is the Fermi Dirac function 3.4,

### 7.3 The Influence of Charging

When we consider the charged systems a single occupied molecular orbital (SOMO) is involved, if we apply a positive charge consequently  $\Delta G_0 = \varepsilon_{HOMO} - E_f$  will be zero. To avoid a zero value for the driving force spin-polarization needs to be applied, where spin-up and spin-down states of the corresponding MO can sit separately above and below the Fermi level thus  $\Delta G_0 = \varepsilon_{SOMO} - E_f$  is not a zero. We applied spin-polarization calculations for the partially occupied states of the double-branched charged systems. The spin-polarization calculations give two effects on the transmission functions: the MO states are shifted downwards for both spin-up and spin-down, and consequently the HOMO is

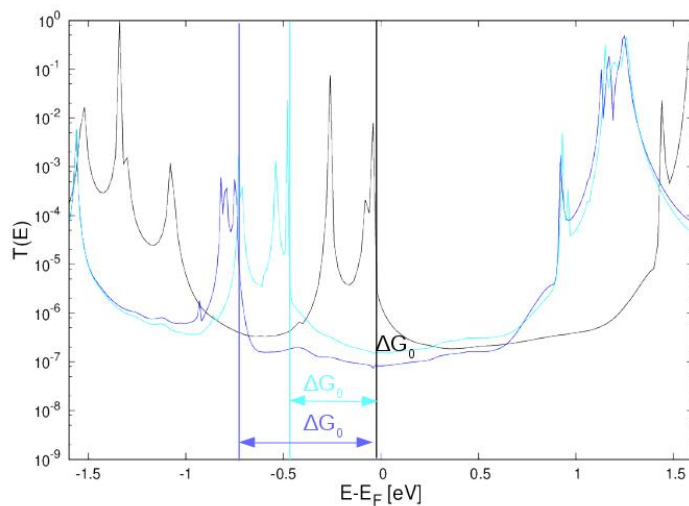


Figure 7.3: Transmission functions for system  $m - d - l$  (Cl) where the black curve is the calculation without applying spin-polarization, the blue and cyan curves are the results of respective spin-up and spin-down with spin-polarization.

distinctly further away from the Fermi level compared with the non-spin calculation results; Secondly, the splitting of the occupied states (due to the asymmetry induced by the Cl atom) near to the Fermi level is more distinct in the spin-polarized calculation results. The first effect leads to the driving force  $\Delta G_0$  in the hopping conductance calculation becoming nonzero in the oxidation process. Theoretically the peaks from respective spin-up and spin-down should sit below and above the Fermi level, while in practice as we can see from Fig. 7.3 the peaks of the two curves with spin-polarized calculations (blue and cyan) are below  $E_F$  and the HOMO peak in cyan curve is closer to  $E_F$  while it is supposed to be above the  $E_F$  theoretically, which remains an open question which needs to be solved in further investigations.

By comparing the inner reorganization energy for one-charge charged schemes as the energy difference of chlorine induced charged configuration and the neutral configuration, and an external charged configuration with the neutral configuration respectively, we found that for the chlorine-induced charged

scheme the inner reorganization energy is much larger than the external-charge charged scheme for all investigated systems because the initial configuration goes through dramatic changes in the former case to final configuration.

Table 7.1: Inner reorganization energy for all investigated systems.

	external +1	Cl induced +1	external +2
$m - d - l$ ( $d_{Cl-Fe}=4.3\text{\AA}$ )	0.033	1.107	0.056
$m - d - s$ ( $d_{Cl-Fe}=5.4\text{\AA}$ )	0.084	1.496	0.077
$Ru/Os$ ( $d_{Cl-M_1}=5.2\text{\AA}$ )	0.035	0.476	0.035
$Os/Os$ ( $d_{Cl-M_1}=5.2\text{\AA}$ )	0.039	0.511	0.041
$Ru/Ru$ ( $d_{Cl-M_1}=5.2\text{\AA}$ )	0.038	0.433	0.036

One can in principle compare the geometrical variation movie in each iteration from the two schemes to capture the most obvious movements of each atom. We observed that for the ferrocene double-branched systems in the chlorine charged configuration atoms move more violently due to the attractive interactions between the branches and Cl. Especially the atoms closer to Cl move towards it (apart from the fixed iron), while in the external-charge charged scheme where the external charge is equally distributed on both branches. The movements of two branches are symmetric, but is also repulsion between the two branches while the difference between initial and final configurations is comparably small. For the big cyclic molecules because of the large size of the molecules, there are more degree of freedom for the movement of the atoms when an external charge is applied. So the difference between initial and final configurations are overall smaller than ones for the ferrocene molecules. However, in the chlorine-induced charged scheme the reorganization energy is still big due to the interaction between the branches and Cl. Table 7.2 gives the charge distributions respectively on the two branches for all charged systems we investigated. As we can see from the partial charge values for the two branches, the Cl-induced charged scheme does bring in pronounced asymmetry compared with the external-charge charged scheme.

For the hopping topic, I would need to do more analysis on the driving force issue with spin-polarized calculations and try to understand the large

Table 7.2: Charge distribution for the charged systems of the two schemes.

	external +1		Cl induced +1	
	branch M <sub>1</sub>	branch M <sub>2</sub>	branch M <sub>1</sub>	branch M <sub>2</sub>
$m - d - l$ ( $d_{Cl-Fe}=4.3\text{\AA}$ )	0.345	0.342	0.673	0.092
$m - d - s$ ( $d_{Cl-Fe}=5.4\text{\AA}$ )	0.450	0.440	0.677	0.283
$Ru/Os$ ( $d_{Cl-M_1}=5.2\text{\AA}$ )	0.399	0.448	0.710	0.173
$Os/Os$ ( $d_{Cl-M_1}=5.2\text{\AA}$ )	0.394	0.460	0.653	0.230
$Ru/Ru$ ( $d_{Cl-M_1}=5.2\text{\AA}$ )	0.443	0.406	0.662	0.208

reorganization energies for the Cl-induced charged systems as shown in Table 7.1. The calculation of the hopping conductance and transfer rates needs three parameters, i.e. reorganization energy, driving force and transfer integral, where I would need to do more calculations in order to draw a conclusion about the question we came up with in the motivation section: "while the first charge hopping through one branch is oxidized, then when a second charge is applied the hopping process will be under the local electric field of the oxidized branch, how does the presence of a temporarily oxidized metal center  $M_1^*$  affect the redox properties of the other center  $M_2$ ?"

---

\*M<sub>1</sub> is the metal center closer to the Cl atom in the junction.





## CHAPTER 8

---

# Configuration Prediction for Ferrocene Compounds with Different Anchor Groups in Single-Molecule Junctions

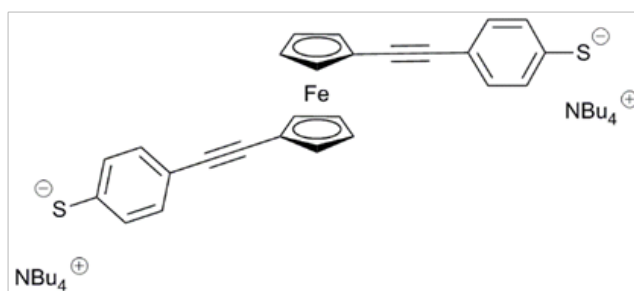
---

### 8.1 Motivation

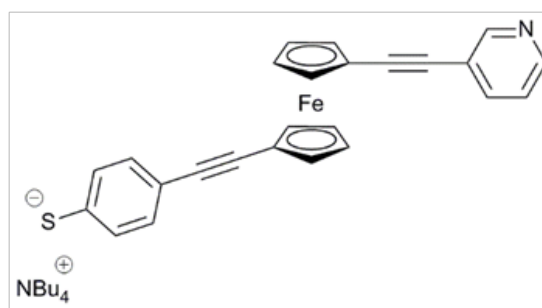
Molecules can self-organize when adsorbed to electrodes, which is an essential advantage for overcoming technological difficulties. For making single-molecule junctions applicable as molecular devices, they need to be operable at room temperature. Experimentally, these ambient conditions can be achieved with an electrochemical scanning tunneling microscopy (E-STM) [110, 99, 111, 112]. In such experiments, the target molecules are adsorbed on the metal surface of the working electrode. When a STM tip is brought to the solution containing target molecules and withdrawing after that, in some cases the molecule is trapped by the tip and the contacted metal surface and thereby a junction is formed. During the approaching and withdrawing process different geometrical contacts can be accessed, which increases the difficulty for the quantitative description in theoretical simulations. The synthesis is done [113] while efforts for measurements of such ferrocene compounds are on the way, our theoretical work hence can be used as a predicting tool for the experimental results. For a theoretical description of electron-transport in a single molecule junction a non-equilibrium Green's function formalism (NEGF) [114] combined with density functional theory (DFT) is used. The simulations of molecular electron trans-

CHAPTER 8. CONFIGURATION PREDICTION FOR FERROCENE  
COMPOUNDS WITH DIFFERENT ANCHOR GROUPS IN SINGLE-MOLECULE  
JUNCTIONS

port properties enables a clearer understanding of the conductance dependence on the molecular structures and help the design of logical gates [22], transistors [99] in single molecule electronics as well as the implementation of thermoelectric devices [100, 101]. We investigate the electrical transport properties of



(a)



(b)

Figure 8.1: a) s-FDT with thiol on each side; b) s-FPT one side with pyridyl and the other side thiol.

two type of molecular wires containing a ferrocene moiety with the same and different anchoring groups, as shown in Fig. 8.1. Where s-FDT is the notation of 1,1'-bis(thiophenol-4-ethynyl)ferrocene: with thiol group on both terminals of the chain and s-FPT, 1-(3-pyridylethynyl)-1'-(thiophenol-4-ethynyl)ferrocene where one of the anchor group at the end of the chain is pyridyl. The novelties of these molecules here are: i) ferrocene moiety can be oxidized and in electron transport play a role as a switch between two redox states (Fe II/ Fe III), with an oxidation state which can be regulated via gating [110], ii) it is interesting to see what is the influence on conductance when different anchoring sites adsorbed to STM-tip and surface forming a junction compared with the case where the same anchoring sites adsorbed to tip and surface. The molecular backbone is the same for both cases while the end of the chain is connected with thiol or

pyridyl group on the two sides, and the different conductance behavior for the two type of molecules due to the difference in anchoring sites is a focus on our studies.

In the molecular design the acetylenic spacers are added to increase the molecule distance between the two electrodes for the prevention of through-vacuum tunneling and for the separation of the redox-active centers from the leads. The pyridyl anchor group is chosen because they can provide the best junction formation and conductance properties in recent experimental [115] and theoretical [72, 116, 92, 97] studies. They also provide peaks in the transmission function, which are narrow enough to assume that a charge on the complex has an impact on the conductance but not narrow enough for Coulomb blockade, Thiolate type anchor groups on the other hand are also popular because they have been found to reduce contact resistance [117, 118, 119], and they provide broad peaks compared with pyridyl anchor groups due to the stronger couplings to the electrodes.

## 8.2 Geometry Adoption/Choice of geometries

The measurements in the experiment are operated under ambient conditions, which means it is unavoidable for the thiolates to be saturated with hydrogen atoms. Another aspect for us to consider the anchoring groups thiolates are saturated with hydrogen atoms and form the thiol-Au bond instead of dissociating hydrogen atoms when adsorbed to gold electrodes is that the thiol-Au structure is energetically preferable than thiolate-Au type as the literature [120], [121] pointed out, DFT calculations also proved that [122], [123] recently. Hence it is rational to use the thiol-Au bond in our simulations. During the approaching and withdrawing process of the tip in E-STM experiments, different geometries for the established contact can occur even if there is one type of molecule in the solution which bonds to the gold surface acting as the working electrode in the setup. In principle, one could imagine three possible sources for the variation of the conductance in dependence of the junction structure for any particular molecule: i) inner (e.g. conformational) degrees of freedom for the molecular structure, ii) variations in the surface or tip structure occurring during the repeated measurement process or iii) differences in the adsorption geometry of

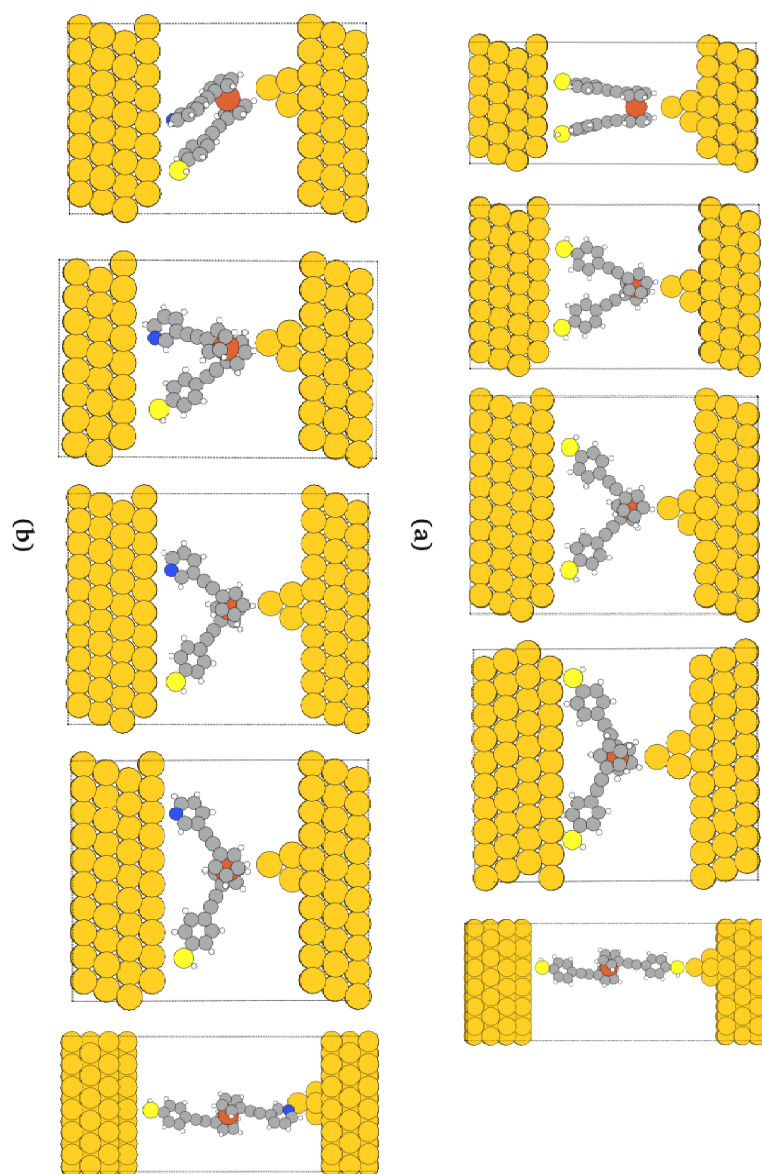


Figure 8.2: The selected junction geometries for a) s-FDT and b) s-FPT.

the molecules in the junction. While variations in the surface structure of the working electrode itself are likely to occur while conductance data is recorded, there is no indication that such gradual variations would result in distinct peaks in histograms. The inner degrees of freedom of the molecule itself, most notably the rotational angle related to the two anchor groups attached to the Ferrocene (Fc) moiety, on the other hand cannot be identified with distinct local minima in the corresponding total energies where the two cyclopenta-dienyl (Cp) rings are known to rotate quite freely with energy barriers of only a few kJ/mol. So we assume that the defining element for the likelihood of particular junction geometries to be formed lies in the commensurability of the rotation angle between the anchor groups of the molecule with the sequence of potential on-top gold positions defined by the fcc (111) surface structure. This selection criterion leaves only few potential adsorption geometries for both s-FDT and s-FPT, where one is linear in the sense that one of the anchor groups is attached to the surface and the other one to the tip, while for the others both anchor groups bond to the surface but the rotation angle varies within the lower limit of being zero and the upper limit of the Fc moiety touching the surface, where the Fc is contacted directly by the tip in this setup. All selected junction geometries are shown in Fig. 8.2.

In this section we provide further details on the step-wise structure optimization process we adopted for the definition of all the relevant degrees of freedom including the distances between the respective molecules and the tip and surface. For the linear structures with one anchor group attached to the substrate and the other one to the tip, we assumed a rotation angle of  $180^\circ$  and the sulfur or nitrogen atom of the contact site on the molecule to be adsorbed on top to a respective gold position. For the structures with both anchor groups adsorbed on the surface and the tip directly contacting the Ferrocene (Fc) moiety, the rotation angle was defined by the criterion that the sulfur or nitrogen contact atoms of both anchor groups needed to be on-top of two gold atoms of the surface, without the Fc moiety touching the surface, this criterion gives two types of potential Au contact positions, i.e. the anchoring atoms are either adsorbed to the same fcc sublattice or different sublattice as shown in Fig. 8.3, where the number of Au atoms in between the two contacted sites are zero (Fig. 8.3 a,d)), one (Fig. 8.3 b,e)) or two (Fig. 8.3 c,f)) on a line.

For obtaining stable junction geometries from the NEGF-DFT calculations,

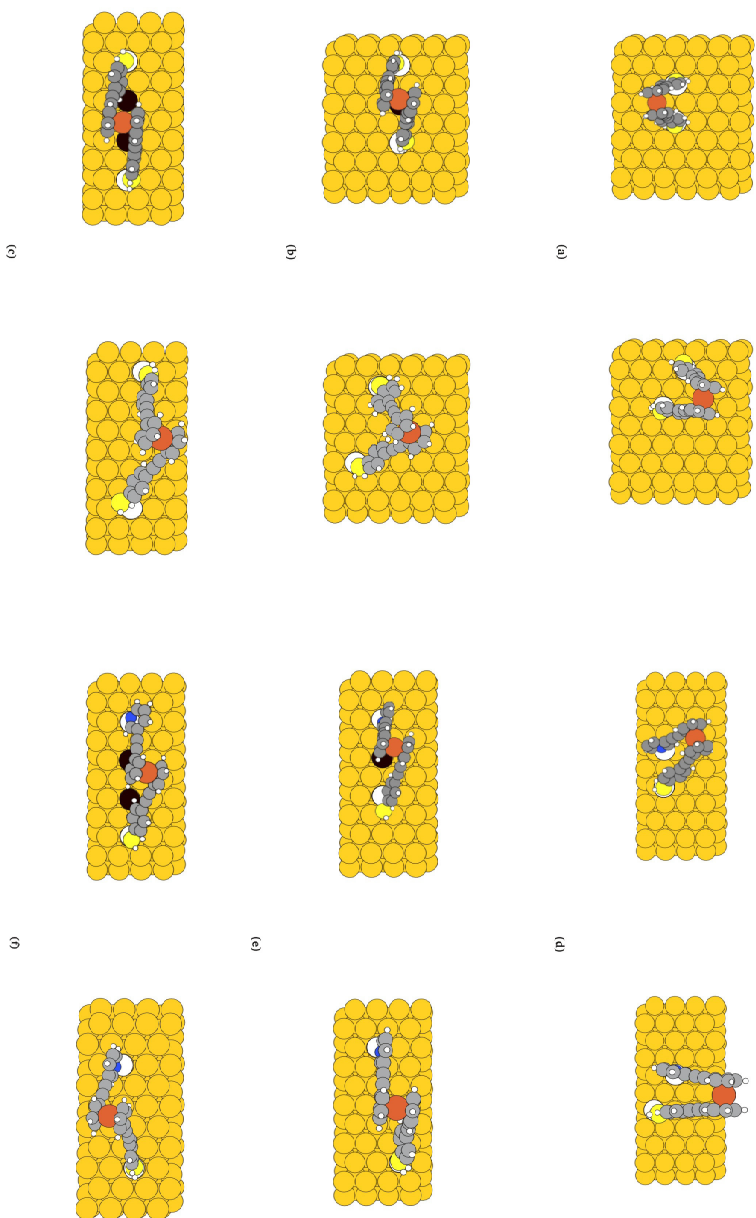


Figure 8.3: Adsorption geometries for same sublattice adsorption (left) and different sublattice adsorption (right) for the molecules s-FDT (a-c) and s-FPT (d-f), where the distances  $d(\text{Au-S})$  between the respective sulfur and gold sites resulting from on-top adsorption of both anchor groups are a) 3.32 (left), b) 3.17 (left), c) 3.18 (left)  $\text{\AA}$  and a) 3.32 (right), b) 3.17 (right), c) 3.18 (right) for s-FDT, while for the asymmetric s-FPT  $d(\text{Au-S})/d(\text{Au-N})$  were found to be d) 3.30/2.76 (left), e) 3.60/3.01 (left), f) 3.55/2.74 (left)  $\text{\AA}$  and d) 3.11/3.14 (right), e) 3.70/3.13 (right), f) 3.55/2.85 (left)  $\text{\AA}$  by our optimization procedure. The contacted gold positions on the surface for each adsorption geometry are marked in white, while the Au atoms on the same fcc sublattice in between these positions are marked in black.

CHAPTER 8. CONFIGURATION PREDICTION FOR FERROCENE  
 COMPOUNDS WITH DIFFERENT ANCHOR GROUPS IN SINGLE-MOLECULE  
 JUNCTIONS

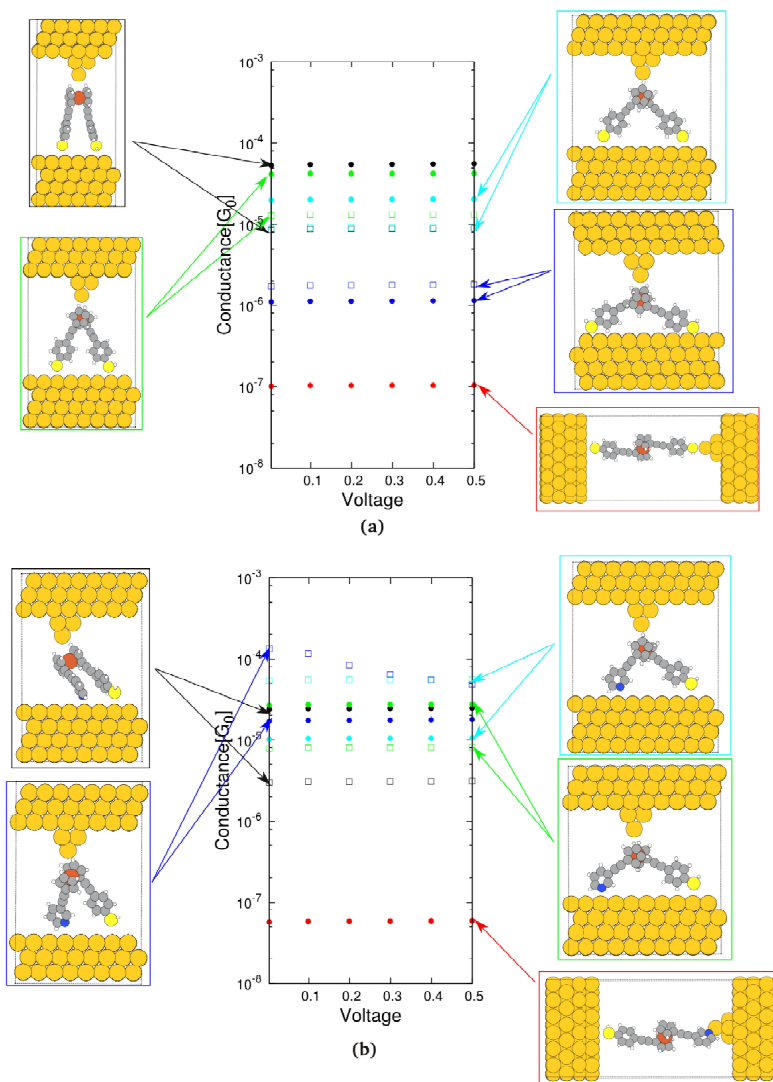


Figure 8.4: The selected junction geometries for a) s-FDT, black color for molecule with  $0^\circ$ , green with  $54^\circ$ , cyan with  $89^\circ$ , blue with  $125^\circ$  and red with  $180^\circ$ ; b) s-FPT, black color for molecule with  $0^\circ$ , blue with degree 50, cyan with degree 92, green with  $117^\circ$  and red with  $180^\circ$ , as well as the resulting conductance in dependence on the voltage from NEGF-DFT calculations with (middle panels) and without (right panels) SO corrections, where dots in each panel represent the anchoring sites of molecules adsorbed on the same sublattice on surface, the squares represent the adsorbed sites on surface for anchoring sites on different sublattice.



we i) relaxed all nuclear positions on the molecules in a linear conformation by means of DFT based total energy minimization, ii) adjusted the rotation angle between anchor groups manually so that it fit the commensurability requirement with the surface illustrated in Fig. 8.3, iii) relaxed all nuclear positions on the molecule again, and then iv) optimized the distances between the respective contact atoms on the electrodes and on the molecules. This distance optimization resulted in  $d_{Au-Fe} = 4.45 \text{ \AA}$  for the contact of the Fc moiety to the lowest atom on the tip for all adsorption geometries depicted in Fig. 8.2, while  $d_{Au-S}$  and  $d_{Au-N}$  for the respective contacts of the anchor groups to the substrate varied more widely for each configuration and the values we obtained are explicitly given in the caption of Fig. 8.3. The respective linear adsorption geometries for both molecules have one anchor group contacting the substrate with  $d_{Au-S} = 3.08 \text{ \AA}$  for s-FDT and  $3.12 \text{ \AA}$  for s-FPT, and the other anchor group contacting the tip with  $d_{Au-S} = 2.61 \text{ \AA}$  for s-FDT and  $d_{Au-N} = 2.21 \text{ \AA}$  for s-FPT.

### 8.3 Theoretical/Computational methods

We performed density functional theory (DFT) calculations with a PBE XC-functional within a Non Equilibrium Green's Function (NEGF)-DFT framework [88, 89, 90] using the GPAW code [69, 70] to compute transmission probabilities  $\mathcal{T}(E)$ . In order to account for self-interaction errors and image charge effects present in DFT with local XC-functionals we applied a scissor operator (SO) correction according to Quek et al. [124]. This ad hoc correction is only applicable for rather weakly coupled molecules, a condition which is fulfilled for dithiols but not dithiolates adsorbed on gold surfaces [125]. In Ref. [125] it was demonstrated that the dissociative adsorption of dithiols on Au substrates is energetically highly unfavourable and that for adsorbed dithiols a good agreement with experimental data for the conductance can be achieved when the values calculated from NEGF-DFT are corrected with a SO approach [105], which is described in details in section 8.5. All DFT calculations were carried out without treating spin polarization as a degree of freedom because previous tests on similar Ferrocene complexes [86] revealed the low spin configuration to be the ground state. The I-V curves we simulated for the geometries of each molecule

(as shown in Fig. 8.2) are obtained from the transmission functions  $\mathcal{T}(E)$  in a rigid band approximation where the bias dependence of  $\mathcal{T}(E)$  is disregarded. This means that the current is determined within the linear response regime as the following integration over the zero bias transmission function,

$$I(V) = (2e/h) \int_{-\infty}^{\infty} \mathcal{T}(E)[f_L(E) - f_R(E)]dE = G_0 \int_{-V/2}^{V/2} \mathcal{T}(E)dE \quad (8.1)$$

where  $f_{L,R}(E)$  is the Fermi Dirac function of the left and right electrode, respectively. and the conductance is calculated as,

$$G(V) = I(V)/V \quad (8.2)$$

## 8.4 Voltage and structure dependence of the conductance

In Fig. 8.4 we show the voltage dependence of the conductance for all junction structures for both s-FDT and s-FPT, where we can identify the following trends i) the conductance varies only within a range of two orders of magnitude for the bended structures of both molecules as shown in Fig. 8.4, the quantitative values for both molecules are rather similar, and there is a pattern for each case with a set of higher conductance values and a single lower value (red dots), where in our calculations the lower value is identified as the linear junction geometry and the higher ones are bended configurations, i.e adsorption structures with both anchor groups attached to the substrate; ii) the conductance for all bended configurations increases with an increase in length for s-FDT and oscillates for s-FPT, which is counter intuitive in coherent transport regime where the tunnel current is expected to increase with a decrease of the junction length; iii) the conductance dependence on the voltage (V) is not very significant, i.e. the conductance does not change very much with V as shown in Fig. 8.4 the flat trend for most of the dots in panel a) and b).

The SO correction opens up the HOMO-LUMO gap for all geometries, thereby reducing the conductance values quite substantially but it should not change the fundamental reasons for the conductance trend that we observed in the transmission curves. We calculate conductance (G) dependent of Voltage (V) as  $I(V)/V$ , this just means that  $I(V)$  is a linear function with a slope of

CHAPTER 8. CONFIGURATION PREDICTION FOR FERROCENE COMPOUNDS WITH DIFFERENT ANCHOR GROUPS IN SINGLE-MOLECULE JUNCTIONS

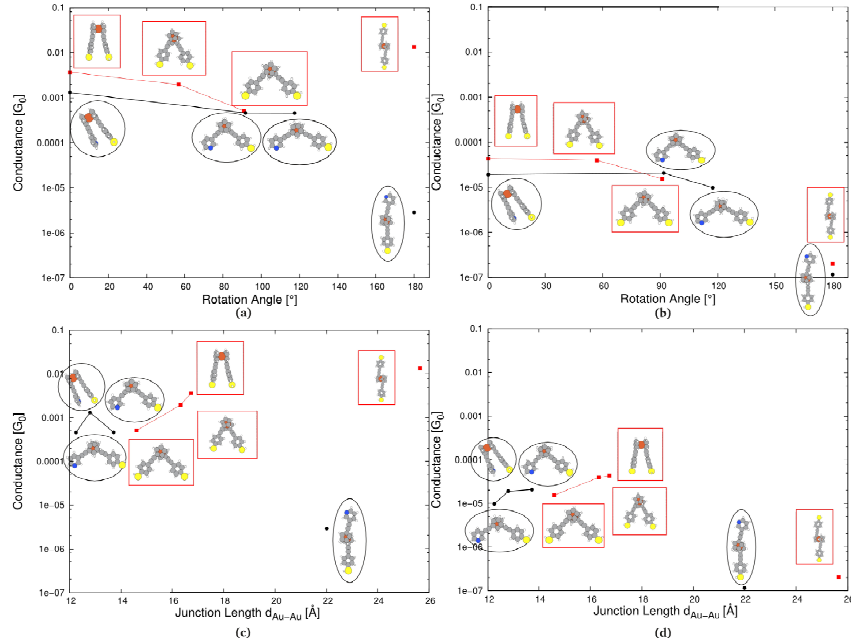


Figure 8.5: Zero-bias conductance as calculated from  $\mathcal{T}(E_F)$  with NEGF-DFT a),c) without and b),d) with SO corrections in dependence on a),b) the rotation angle between anchor groups and c),d) the junction length defined as the distance between the surface plane of the substrate and the contact Au atom on the tip.

roughly one in the voltage range considered since the conductance varies only little with the voltage. In Fig. 8.5 we selected some bended configurations with both anchor groups bonded to Au atoms with the same fcc sublattice and focus on exploring the reason behind the observed conductance trend. We plot the zero bias conductance we obtain directly in  $\mathcal{T}(E_F)$  from NEGF-DFT calculations in dependence on the rotation angle between the anchor groups attached to the Fc moiety as well as on the junction length which we define as the distance between the surface plane of the substrate and the position of the tip atom contacting the molecule from above. While usually the conductance decreases with the junction length for electron transport in the coherent tunneling regime, we find that for the conductance without SO corrections that it even increases in our calculations for s-FDT and oscillates for s-FPT when both anchor groups are attached to the substrate as shown in Fig. 8.5. The conductance without SO corrections directly correlates with the energetic positions of

the HOMO (Fig. 8.6), which is defined by a delicate angle dependent Fermi level alignment, where both the component of the molecular dipole moment in the transport direction and differences in zero bias charge transfer play decisive roles. A detailed analysis of the structure dependent interplay of the two effects is provided in section 8.4.1.

### 8.4.1 Analysis of the Dependence of the Conductance on the Junction Length in Terms of Fermi Level Alignment

The SO correction should not change the trend of the conductance dependence of the junction length, which is counter intuitive in the sense that usually the conductance decreases with an increase in length in the coherent tunneling regime, while in our cases it increases for both type of molecules as one can see from Table 8.1. We plotted the dependence of the conductance on the junction length for the selected geometries with both anchors adsorbed on the substrate as representatives (they are also discussed in connection to Fig. 8.5, conductance versus molecular angle), where we focus on the NEGF-DFT calculations without SO corrections because here the physical effects determining the conductance can be distinguished unambiguously. A comparison with the energetic position of the HOMO as obtained from a diagonalization of the subspace of molecular region (subdiagonalization) in the transport Hamiltonian (the solid lines in 8.7 b)) shows that the closer the  $\varepsilon_{HOMO}$  is to the Fermi Level  $E_F$ , the higher the conductance becomes. The only exception from that trend is the slightly tilted cis-configuration of s-FPT where a distinctly broadened peak in the corresponding transmission function (Fig. 8.6 a), black curve) indicates an overall increased electron coupling of the HOMO to the leads in this particular configuration. This means that any analysis of the conductance trends must focus on the sources of Fermi level alignment (FLA) of MOs obtained from a subdiagonalization in general and the HOMO in particular. These sources can be divided into properties of the separate components of the junction and the charge rearrangement when these components are combined to form the junction. The former consist mostly of the permanent dipole of the free molecule in the transport direction which has a strong dependence on the contact angle but also the dipole moment of the metallic slab which is caused by the asym-

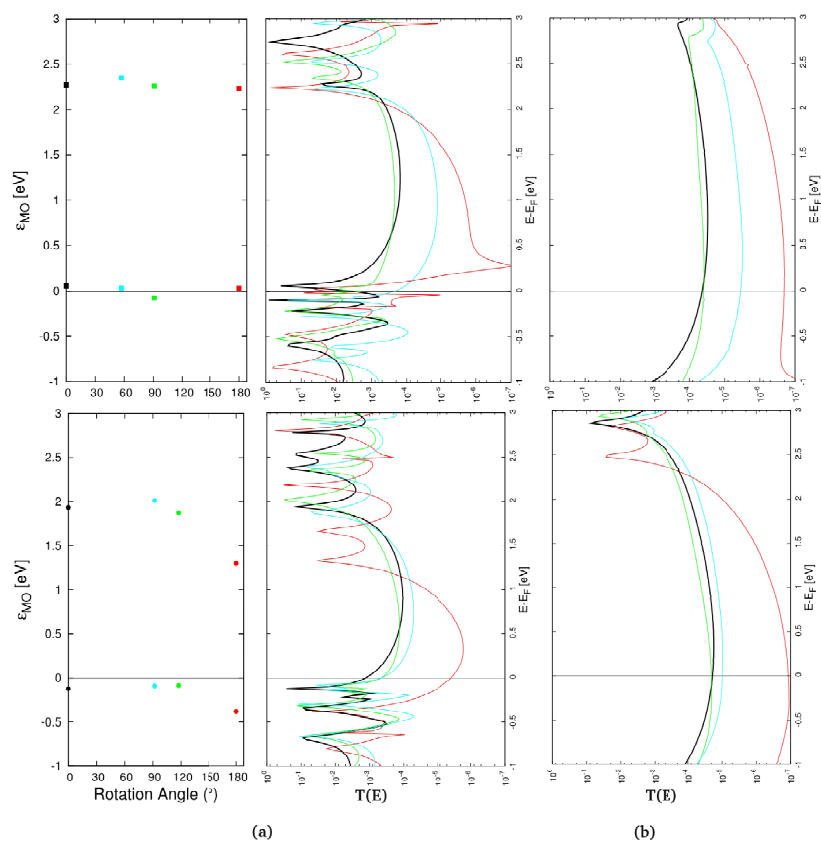
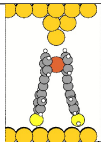
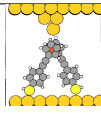

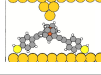
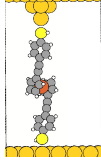
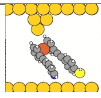
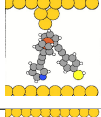

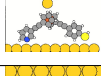
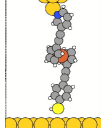


Figure 8.6: Eigenenergies of the HOMO and LUMO from a subdiagonalization of the molecular part of the transport Hamiltonian in the respective junction setups ((a) left panels), transmission functions  $\mathcal{T}(E)$  without ((a) right panels) and with SO corrections (panel b)), where the upper panels are for s-FDT and the lower panels for s-FPT. The colors attributed to the respective four junction geometries are the same as those chosen for Fig. 8.4.

CHAPTER 8. CONFIGURATION PREDICTION FOR FERROCENE  
COMPOUNDS WITH DIFFERENT ANCHOR GROUPS IN SINGLE-MOLECULE  
JUNCTIONS

---

Table 8.1: Conductance (in units of  $G_0$ ) with scissor operator corrections dependence of the junction configurations (junction length  $\text{\AA}$ ) for molecules s-FDT and s-FPT, respectively.

	Length	Conductance
	14.794	$1.72 \times 10^{-5}$
	16.329	$4.14 \times 10^{-5}$
	14.593	$1.54 \times 10^{-5}$
	12.411	$2.23 \times 10^{-6}$
	25.649	$2.04 \times 10^{-7}$
	12.791	$1.90 \times 10^{-5}$
	14.720	$8.64 \times 10^{-5}$
	13.708	$2.06 \times 10^{-5}$
	12.246	$0.98 \times 10^{-5}$
	22.002	$1.15 \times 10^{-7}$

CHAPTER 8. CONFIGURATION PREDICTION FOR FERROCENE  
 COMPOUNDS WITH DIFFERENT ANCHOR GROUPS IN SINGLE-MOLECULE  
 JUNCTIONS

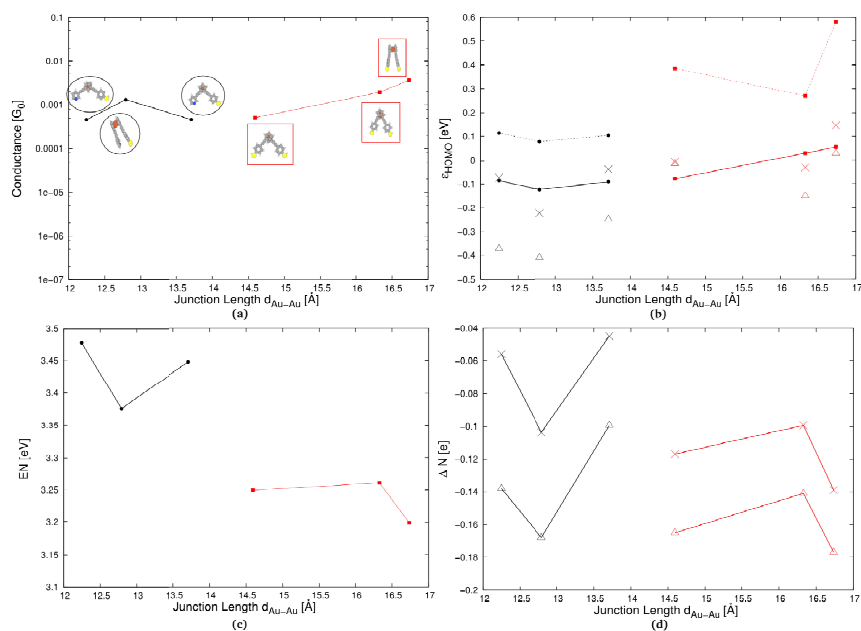


Figure 8.7: Junction length dependence of a) the conductance without SO corrections, b) the eigenenergy of the HOMO from a subdiagonalization of the molecular part of transport Hamiltonian of the junction (solid) and Vacuum level alignment (dotted), where for the latter shifted values taking into account the contribution from partial charging are also shown as crosses (Bader analysis) and triangles (integration over electron  $e$ ), c) Electronegativities of the free molecules in dependence on the rotation angle and d) partial charges on the molecules in the junction from a Bader analysis (crosses) as well as from integration over  $\Delta n(z)$  in the molecular region (triangles) in units of electrons. For all panels symbols and lines are shown in black for s-FPT and in red for s-FDT.

metry that arises from the fact that there is a tip on one side but a surface substrate on the other and the variation of the vacuum level positioning with the length of the gap between tip and substrate. These effects result in the dotted lines in Fig. 8.7 b), which were obtained from vacuum level alignment from independent DFT calculations for the free molecule and the metal slabs without the molecule, where the vacuum level is calculated as the electrostatic potential in the vacuum region for both separate systems and the HOMO of the molecule and  $E_F$  of the metal slab put in reference to this vacuum level are assumed to be the same for both when the junction is formed. The values for  $\epsilon_{HOMO}$  obtained from this procedure are all substantially higher in energy than those obtained from the subdiagonalization of the transport Hamiltonian of the junction (8.7 b)) but show very similar qualitative trends for s-FPT (black lines) and somewhat different behavior for s-FDT (red lines). These differences are due to the neglect so far of the effect of charge rearrangements when the components of the junction are brought together. There are different views in the literature of how best to describe this effect, where some authors prefer a description in terms of interface or bonding dipoles [126] and one of us has written a series of papers where they are discussed in terms of partial charges on the molecule [107, 127, 128, 129]. Both views agree in attributing the charge rearrangement at the interface to Pauli repulsion, but while the interface dipole approach does not allow for a quantitative analysis of the resulting energy shifts of MOs [126], these can be reproduced to a high level of accuracy from vacuum level aligned eigenenergies from free molecule calculations where the partial charge the molecule also has in the junction because of its interaction with the leads is added [107, 127, 128, 129]. This is because in case of a positive charge the remaining electrons are bound more tightly to the respective nuclei in the molecule leading to more negative MO eigenenergies, in case of a negative charge the opposite behavior with a rise in MO energies is encountered [107]. For such a description it is not relevant whether the partial charge comes from the emptying or filling of a molecular level or from Pauli repulsion effects at the interface, where a clear distinction of both in any case is not rigorously possible in the junction setup where the MOs and the surface states of the leads form hybrid orbitals. The only source of accuracy in this partial charge perspective is the definition of this charge in its technical practicality, where the various options, such as a Mulliken analysis [104], a Bader analysis [98] or an integration over  $\Delta n(z)$ , i.e. the difference of the electron density between the junction



CHAPTER 8. CONFIGURATION PREDICTION FOR FERROCENE  
 COMPOUNDS WITH DIFFERENT ANCHOR GROUPS IN SINGLE-MOLECULE  
 JUNCTIONS

and its two components in the transport direction and averaged over the surface plane in the molecular region [107, 127]. Since we are interested in the electrostatic effect of the charge on the MOs, a Mulliken analysis where electrons are attributed to atoms in terms of the LCAO basis sets is not a good option. The Bader analysis which uses zero flux surfaces to divide atoms or the integration over  $\Delta n(z)$  where the borders on  $z$  for the definition of the molecular region are put at the mid-point between the  $z$ -coordinates of the molecular and metallic contact atoms provide much more useful molecular partial charge values  $\Delta N$  for this purpose. In Fig. 8.7 c) we plot the electronegativities  $EN$  of the free molecules according to Mulliken's definition of  $EN = (IP+EA)/2$  [104] where the ionization potential  $IP$  and the electron affinities  $EA$  have been calculated from the DFT total energies of charged and neutral molecules as  $IP=E(N-1)-E(N)$  and  $EA = E(N)-E(N+1)$ , respectively, where  $N$  is the number of electrons in the neutral molecules. The junction length dependence of  $EN$  in Fig. 8.7 c) corresponds qualitatively with that of the molecular partial charges  $\Delta N$  in Fig. 8.7 d), which were obtained from a Bader Analysis (crosses) and by integrating over  $\Delta n(z)$  (triangles), where stronger negative values mean that larger fractions of an electron have been subtracted from the molecule due to the formation of the junction. These values of  $\Delta N$ , where the results from the Bader analysis and from the integration disagree quantitatively in the sense that the Bader charges are smaller, have also been used for the vacuum level alignment with partially charged molecules in Fig. 8.7 b), where the Bader shifted energies seem to show better agreement with  $\varepsilon_{HOMO}$  obtained from a subdiagonalization of the transport Hamiltonian of the junctions. For s-FPT both  $EN$  and  $\Delta N$  follow the same trend as the vacuum level aligned  $\varepsilon_{HOMO}$  without the consideration of partial charges, while for s-FDT the second point whose value is the lowest one in the vacuum level alignment of the neutral molecules but the trends from  $EN$  and  $\Delta N$  are in the opposite direction, thereby flattening the qualitative trends in the length dependence of the final  $\varepsilon_{HOMO}$  and the conductance in Fig. 8.7 b).

Because the values for  $\varepsilon_{HOMO}$  in Fig. 8.7 b) are quite close to  $E_F$ , the question arises whether Fermi level pinning plays a role, i.e. whether the energetic distance of  $\varepsilon_{HOMO}$  to  $E_F$  can be tuned by variations in  $EN$  or will be pinned at the electrodes Fermi level regardless of  $EN$ . In Ref. [130] a test for the occurrence or absence of Fermi level pinning was proposed by conducting

cluster calculations, where the respective molecule is just attached to single gold atoms at each contact point with electrodes. For the molecules in our study this would mean that the linear structures where one anchor group is bonded to the surface and one to the tip there would be two gold atoms in the cluster calculations, namely one at each anchor group, while the junction geometries with both anchors adsorbed on the surface would in addition have a third gold atom, where the Fc moiety is contacted by the tip. They proposed that in these cluster calculations with molecule and the single contact Au atoms when the HOMO is a metal-induced gap state (MIG), i.e. it is mostly localized on the gold atoms, any Fermi level pinning effect is annihilated and the energetic position of the HOMO level is determined by the respective electronegativity of the molecule. In Fig. 8.8 we plot the HOMOs from cluster calculations for all the junction geometries we investigate in this article. Since for all cases the HOMO has MIG character (as shown in Fig. 8.8), Fermi level pinning can be clearly disregarded as a factor in the observed FLA trends. In Ref. [126], where the coverage dependence of FLA for biphenyl-dithiolate monolayers on Au(111) was studied, it was found that the tilt-angle dependence of Pauli repulsion at the interface played a crucial role. In order to investigate whether this is also the case for our molecules we plot electron density  $\Delta n$  in the transport direction and the running integral over its molecular part for all junction geometries in our study in Fig. 8.9, where no big differences between these functions for different rotation angles can be identified at the interfaces. This finding further confirms the conclusions from the FLA analysis we presented so far, namely that the level alignment determining the conductance trends in dependence on rotation angle (or junction length) in our article does not rely on interface effects but is defined by the accumulative effects of the respective molecular dipole moments and the partial charging driven by the respective molecular electronegativities, which result in the observed energetic positions of the HOMO.

## 8.5 Summary

In this study we investigated the potential use of molecular wires containing ferrocene centers with the same and different anchoring groups on each side. We found that the conductance of the proposed set of configurations for molecules

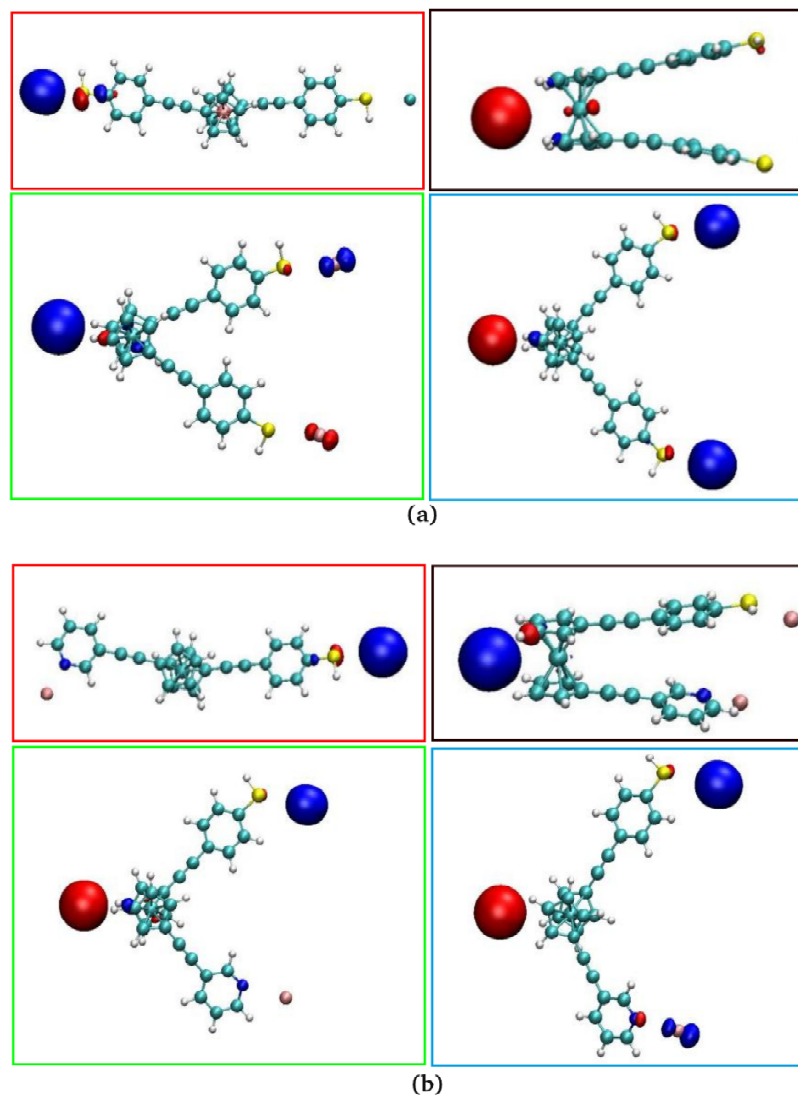


Figure 8.8: Localization patterns for the HOMO from cluster calculations containing the free molecule and the two or three Au contact atoms defined by the respective junction geometries for a) s-FDT and b) s-FPT.

CHAPTER 8. CONFIGURATION PREDICTION FOR FERROCENE  
COMPOUNDS WITH DIFFERENT ANCHOR GROUPS IN SINGLE-MOLECULE  
JUNCTIONS

---

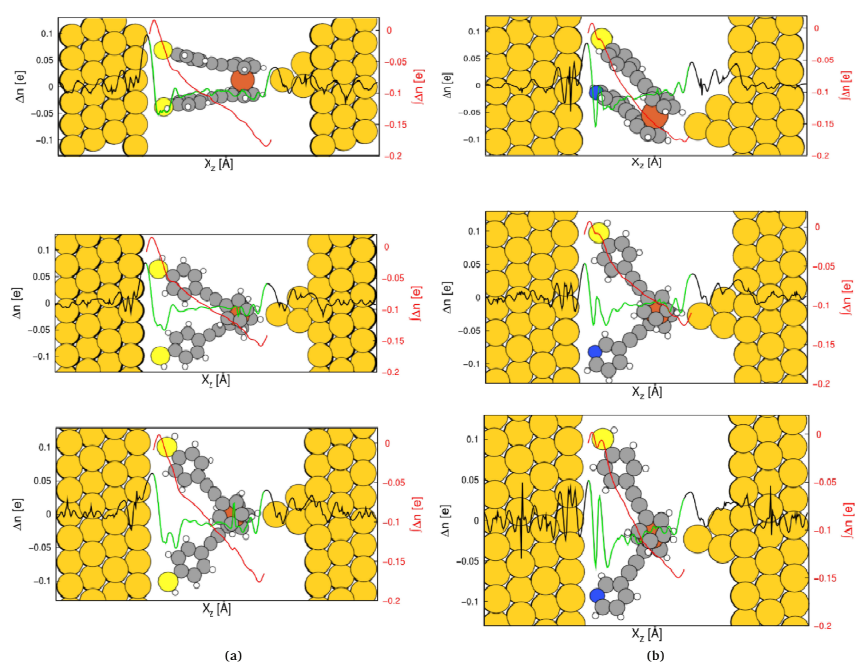


Figure 8.9: Electron density difference  $\Delta n$  between the junctions density and that of its two components (black lines), where the functions attributed to the molecular region are highlighted in green and the running integral over this molecular part is plotted in red for a) s-FDT and b) s-FPT.

CHAPTER 8. CONFIGURATION PREDICTION FOR FERROCENE  
 COMPOUNDS WITH DIFFERENT ANCHOR GROUPS IN SINGLE-MOLECULE  
 JUNCTIONS

s-FDT and s-FPT formed in the junction with two anchoring atoms adsorbed to the surface vary in general only within a rather small region in dependence on the rotation angles or type of molecule. The counter intuitive phenomenon that the conductance does not increase while the junction length decreases is explained by Fermi level alignment where we found that the HOMO position for the bended configurations is close to the Fermi level and dominate the conductance.

We found that for the two types of molecule the set of conductance have similar values and patterns, which is that the set of conductance from the junctions where molecules are adsorbed with both anchoring sites on the surface have higher conductance values ( $10^{-4}$  –  $10^{-5}$ ) while a significantly lower conductance value ( $\sim 10^{-7}$ ) is found for the junction geometry formed by a molecule linearly attached to one side tip and the other side substrate. In addition, the conductance dependence on the voltage (V) is not very significant. Our study allows experimentalists to relate their measurement data on similar systems to the relative abundance of potentially junction geometries.

**Scissor Operator corrections** In order to compare the conductance with experimental results, we need to account for self-interaction errors and image charge effects in DFT calculations with semi-local XC-functionals. We applied a so-called scissor operator (SO) correction according Quek et al [124], where we manually open the single particle HOMO-LUMO gap in order to account for many body contributions. For a molecule adsorbed to the metal surface, the SO is  $\Sigma_0 - \Delta\Sigma_0$ , where  $\Sigma_0$  is calculated for the highest occupied molecular orbital (HOMO) as follows,

$$\Sigma_0^o = -(\varepsilon_{HOMO} + I_0). \quad (8.3)$$

$$IP_0 = E_{q(1)} - E_{q(0)} \quad (8.4)$$

where  $IP_0$  and  $\varepsilon_{HOMO}$  are the first ionization energy and the HOMO energy with respect to vacuum potential for the isolated molecule,  $E_{q(1)}$  and  $E_{q(0)}$  are the respective total energies for the molecule with one positive charge and the neutral case. For the lowest unoccupied MO (LUMO)  $\Sigma_0^u$  is calculated as,

$$\Sigma_0^u = -(\varepsilon_{LUMO} + E_{ea}). \quad (8.5)$$

where  $E_{ea}$  is electron affinity energy of isolated molecule,

$$E_{ea} = E_{q(0)} - E_{q(-1)} \quad (8.6)$$

$\Delta\Sigma_0$  accounts for the image charge effect when a molecule is adsorbed near to a metal surface, and we calculate it following the recipe by Thygesen et al [105]. This part actually corrects the polarization between the molecular subsystem and metal electrodes, and moves the shifted occupied/unoccupied states slightly back respect to the Fermi level. The molecular states obtained by a subdiagonalization of the transport Hamiltonian are then adjusted by  $\Sigma_0^o - \Delta\Sigma_0^o$  for all occupied states and  $\Sigma_0^u - \Delta\Sigma_0^u$  for unoccupied states. In this way the molecular HOMO-LUMO gap is enlarged by pushing occupied states down and unoccupied states up.

**Vacuum Level Alignment** The alignment of the vacuum level is about setting the same reference for molecular eigenenergies and the Fermi level of metallic electrodes in order to relate MOs to  $E_F$ . This can be done in DFT calculations according to the following scheme:

i) In order to obtain the molecular eigenenergies with respect to the vacuum potential, a calculation of the isolated molecule in the same unit cell as the junction structure needs to be performed, where the obtained MOs energies are defined as:

$$\varepsilon_{i,vac} = \varepsilon_{i,DFT} - V_{mol,vac} \quad (8.7)$$

$\varepsilon_{i,DFT}$  are the molecular eigenvalues from DFT static calculation and  $V_{mol,vac}$  is obtained by averaging the potential of the vacuum area as illustrated in Fig. 8.10.

ii) For the calculation of the metal Fermi energy relative to the vacuum potential, one needs to perform a DFT calculation of the metal electrodes without the molecule in the same unit cell as the junction structure. The vacuum potential can then be determined as the electrostatic potential from that calculation in the gap between the two surfaces. The Fermi level can now be determined relative to this vacuum level as,

$$\varepsilon_{le,vac} = \varepsilon_{le,DFT} - V_{le,vac} \quad (8.8)$$

iii) Now we align the MOs to this defined metal Fermi level as,

$$\varepsilon_{i,le} = (\varepsilon_{i,DFT} - V_{mol,vac}) - (\varepsilon_{le,DFT} - V_{le,vac}) \quad (8.9)$$

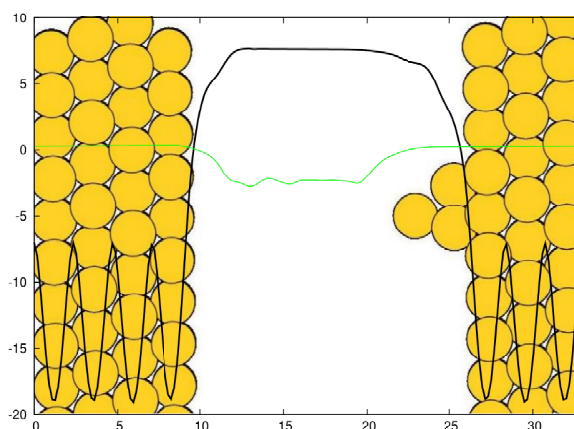


Figure 8.10: The setup of a scattering region in a NEGF-DFT transport calculation, the black curve is the electron potential in transport direction for the empty junction without molecule in the unit cell, the green curve is the electron potential for molecule, where the vacuum potential is averaged in the region of 7.5 Å —20 Å for the empty junction and in the region below 8.5 Å and above 25 Å for molecule, respectively.

The origin of the Fermi level pinning effect can be attributed into intrinsic dipole (molecular dipole) and interface dipole which also involves charge distribution between molecule and metal surface, the latter is closely related to the Pauli repulsion due to the overlap of molecule and the surface. From the charge distribution we find that the molecules lose partial electron when they interact (absorbed to) with the electrode.

---

## Bibliography

---

- [1] F.Q. Xie, L. Nittler, Ch. Obermair, Th. Schimmel, *Phys. Rev. Lett.*, **93**, 128303 (2004).
- [2] F. Reif, *Am. J. Phys.*, **50**, 1048 (1982).
- [3] M. Magoga and C. Joachim, *Phys. Rev. B*, **59**, 16011 (1999).
- [4] C. Joachim, *Nat. Nanotech.*, **7**, 620 (2012).
- [5] H. Vazquez, R. Skouta, S. Schneebeli, M. Kamenetska, R. Breslow, L. Venkataraman and M.S. Hybertsen, *Nat. Nanotech.*, **7**, 663 (2012).
- [6] A. Aviram and M.A. Ratner, *Chem. Phys. Lett.*, **29**, 277 (1974).
- [7] N. Agrait, A.L. Yeyati and J.M. van Ruitenbeek, *Phys. Rep.*, **377**, 81 (2003).
- [8] A. Nitzan and M.A. Ratner, *Science*, **300**, 1384 (2003).
- [9] B. Xu and N.J. Tao, *Science*, **301**, 1221 (2003).
- [10] D.M. Eigler, C.P. Lutz and W.E. Rudge, *Nature*, **352**, 600 (1991).
- [11] X. Xiao, B. Xu and N.J. Tao, *Nano. Lett.*, **4**, 267 (2004).
- [12] S.Y. Quek, M. Kamenetska, M.L. Steigerwald, H.J. Choi, S.G. Louie, M.S. Hybertsen, J.B. Neaton and L. Venkataraman, *Nat. Nanotechnol.*, **4**, 230 (2009).
- [13] J. Moreland and J.M. Ekin, *J. Appl. Phys.*, **58**, 3888 (1985)
- [14] C.J. Muller, J.M van Ruitenbeek and L.J. de Jongh, *Physica, C: Superconductivity*, **191**, 485 (1992).



## BIBLIOGRAPHY

---

- [15] M.A. Reed, C. Zhou, C.J. Muller, T.P. Burgin and J.M. Tour, *Science*, **278**, 252 (1997).
- [16] M. Tsutsui, Y. Teramae, S. Kurokawa and A. Sakai, *Appl. Phys. Lett.*, **89**, 163111 (2006).
- [17] M.T. González, S. Wu, R. Huber, S.J. van der Molen, C. Schönenberger and M. Calame, *Nano Lett.*, **6**, 2238 (2006).
- [18] R.B. Pontes, F.D. Novaes, A. Fazzio and A.J.R. Silva, *J. Am. Chem. Soc.*, **128**, 8996 (2006).
- [19] W.R. French, C.R. Iacovella, I. Rungger, A.M. Souza, S. Sanvito and P.T. Cummings, *J. Phys. Chem. Lett.*, **4**, 887 (2003).
- [20] T. Markussen, R. Stadler, K.S. Thygesen, *Nano Lett.*, **10**, 4260 (2010).
- [21] R. Stadler, *Nano Lett.*, **15**, 7175 (2015).
- [22] R. Stadler, S. Ami, M. Forshaw and C. Joachim, *Nanotechnology*, **15**, S115 (2004).
- [23] R. Stadler, M. Forshaw and C. Joachim, *Nanotechnology*, **14**, 138 (2003).
- [24] R. A. Marcus, *J. Chem. Phys.*, **24**, 966 (1956).
- [25] N. S. Hush, *Trans. Faraday Soc.*, **57**, 557 (1961).
- [26] R. A. Marcus, *J. Chem. Phys.*, **43**, 679 (1965).
- [27] W. Kohn and L.J. Sham, *Phys. Rev.*, **140**, A1133 (1965).
- [28] J.C. Slater, *Phys. Rev.*, **81**, 385 (1951).
- [29] P. A. M. Dirac, *Proc. Cambridge Phil. Roy. Soc.*, **26**, 376 (1930).
- [30] A.D. Becke, *Phys. Rev. A*, **38**, 3098(1988).
- [31] C. Lee, W. Yang and R.G. Parr, *Phys. Rev. B*, **37** 785 (1988).
- [32] J.P. Perdew, *Electronic structure of solids 1991*, **11** (1991).
- [33] J.P. Perdew, K. Burke, M. Ernzerhof, *Phys. Rev. Lett.*, **77**, 3865 (1996).
- [34] J.C. Phillips, *Phys. Rev.*, **112**, 685 (1958).
- [35] J.C. Phillips and L. Kleinman, *Phys. Rev.*, **116**, 287 (1959).

- 
- [36] L. Kleinman and J.C. Phillips, *Phys. Rev.*, **118**, 1153 (1960).
- [37] P.E. Blöchl, *Phys. Rev. B*, **50**(24), 17953 (1994).
- [38] M. Strange, I. S. Kristensen, K. S. Thygesen, and K. W. Jacobsen, *J. Chem. Phys.*, **128**, 114714 (2008).
- [39] P. Sautet and C. Joachim, *Chem. Phys. Lett.*, **153**, 511 (1988).
- [40] C. Patoux, C. Coudret, J.P. Launary, C. Joachim and A. Gourdon, *Inorg. Chem.*, **36**, 5037(1997).
- [41] M. Mayor, H.B. Weber, J. Reichert, M. Elbing, C. von Hänisch, D. Beckmann and M. Fischer, *Angew. Chem. Int. Ed.*, **42**, 5834 (2003).
- [42] S.J. van der Molen and P. Liljeroth, *J. Phys.: Condens. Matter*. **22**, 133001 (2010).
- [43] M. Irie, *Chem. Rev.*, **100**, 1685 (2000).
- [44] K. Matsuda and M. Irie, *J. Am. Chem. Soc.*, **122**, 7195 (2000).
- [45] S. Fraysse, C. Coudret and J.P. Launary, *Eur. J. Inorg. Chem.*, **7**, 1581 (2000).
- [46] D. Dulić, S.J. van der Molen, T. Kudernac, H.L. Jonkman, J.J.D. de Jong, T.N. Bowden, J. van Esch, B.L. Feringa and B.J. van Wees, *Phys. Rev. Lett.*, **91**, 207402 (2003).
- [47] C. van Dyck, V. Geskin, A.J. Kronemeijer, D.M. de Leeuw and J. Cornil, *Phys. Chem. Chem. Phys.*, **15**, 4392 (2013).
- [48] L.-hua Wang, Y. Sun, Z.-zhen Zhang, B.-jun Ding, and Y. Guo, *Phys. Lett. A*, **378**, 646 (2014).
- [49] H. Liu, H. Wang, J. Zhao, and M. Kiguchi, *J. Comput. Chem.*, **34**, 360 (2013).
- [50] C. A. Coulson and G. S. Rushbrooke, *Math. proc. Cambridge Philos. Soc.*, **36**, 193 (1940).
- [51] I. Gutman and O. E. Polansky, *Mathematical Concepts in Organic Chemistry* (Springer, 1986), **57**, ISBN: 978-3-642-70984-5.

## BIBLIOGRAPHY

---

- [52] K. Yoshizawa, T. Tada and A. Staykov, *J. Am. Chem. Soc.*, **130**, 9406 (2008).
- [53] Y. Tsuji, A. Staykov and K. Yoshizawa, *Thin Solid Films*, **518**, 444 (2009).
- [54] Y. Tsuji, A. Staykov and K. Yoshizawa, *J. Phys. Chem. C*, **113**, 21477 (2009).
- [55] X. Li, A. Staykov and K. Yoshizawa, *J. Phys. Chem. C*, **114**, 9997 (2010).
- [56] Y. Tsuji, A. Staykov and K. Yoshizawa, *J. Am. Chem. Soc.*, **133**, 5955 (2011).
- [57] K. Yoshizawa, *Acc. Chem. Res.*, **45**, 1612 (2012).
- [58] S. Larsson, *J. Am. Chem. Soc.*, **103**, 4034 (1981).
- [59] M. A. Ratner, *J. Phys. Chem.*, **94**, 4877 (1990).
- [60] G. Kastlunger and R. Stadler, *Phys. Rev. B*, **89**, 115412 (2014).
- [61] P. Sautet and M. -L. Bocquet, *Phys. Rev. B*, **53**, 4910 (1996).
- [62] P. Sautet and C. Joachim, *Phys. Rev. B*, **38**, 12238 (1988).
- [63] T. Markussen, R. Stadler and K. S. Thygesen, *Phys. Chem. Chem. Phys.*, **13**, 14311 (2011).
- [64] T. Markussen R. Stadler and K.S. Thygesen, *Phys. Chem. Chem. Phys.*, **13**, 14311 (2011).
- [65] M.H. Garner, G.C. Solomon and M. Strange, *J. Phys. Chem. C*, **120**, 9097 (2016).
- [66] R. Stadler, K. S. Thygesen, and K. W. Jacobsen, *Nanotechnology*, **16**, S155 (2005).
- [67] R. Stadler, K. S. Thygesen, and K. W. Jacobsen, *Phys. Rev. B*, **72**, 241401(R) (2005).
- [68] R. Stadler, *Phys. Rev. B*, **80**, 125401 (2009).
- [69] J. J. Mortensen, L. B. Hansen, K. W. Jacobsen, *Phys. Rev. B*, **71**, 035109 (2005).

- 
- [70] J. Enkovaara, C. Rostgaard, J.J. Mortensen, J. Chen, M. Dulak, L. Ferrighi, J. Gavnholt, C. Glinsvad, V. Haikola, H.A. Hansen, H. Kistoffersen, M. Kuisma, A.H. Larsen, L.J. Lehtovaara, *Phys.: Conf. Ser.*, **22**, 253202 (2010).
- [71] A.H. Larsen, M. Vanin, J.J. Mortensen, K.S. Thygesen and K.W. Jacobsen, *Phys. Rev. B*, **80**, 195112 (2009).
- [72] R. Stadler, K. S. Thygesen and K. W. Jacobsen, *Phys. Rev. B*, **72**, 241401(R) (2005).
- [73] J. Gavnholt, T. Olsen, M. Engelund and J. Schiøtz, *Phys. Rev. B*, **78**, 075441 (2008).
- [74] T. Olsen, J. Gavnholt and J. Schiøtz, *Phys. Rev. B*, **79**, 035403 (2009).
- [75] D.M. Newns, *Phys. Rev.*, **178**, 1123 (1969).
- [76] P.W. Anderson, *Phys. Rev.*, **124**, 41 (1961).
- [77] O. F. Sankey and D. J. Niklewski, *Phys. Rev. B*, **40**, 3979 (1989).
- [78] T. Markussen, J. Schiøtz and K.S. Thygesen, *J. Chem. Phys.* **132**, 224104 (2010).
- [79] G.H Wannier, *Phys. Rev.*, **52**, 191 (1937).
- [80] C. Edmiston and K. Ruedenberg, *Rev. Mod. Phys.*, **32**, 457 (1963).
- [81] <https://quantumgraphs.com/>.
- [82] X. Zhao, V. Geskin and R. Stadler, *J. Chem. Phys.*, **146**, 092308 (2017).
- [83] D. Z. Manrique, C. Huang, M. Baghernejad, X. Zhao, O.A. Al-Owaedi, H. Sadeghi, V. Kaliginedi, W. Hong, M. Gulcur, T. Wandlowski, M. R. Bryce and C. J. Lambert, *Nat. Commun.*, **6**, 6389 (2015).
- [84] M. S. Inkpen, T. Albrecht and N. J. Long, *Organometallics*, **32**, 6053 (2013).
- [85] G. Kastlunger and R. Stadler, *Phys. Rev. B*, **91**, 125410 (2015).
- [86] X. Zhao, G. Kastlunger, and R. Stadler, *Phys. Rev. B*, **96**, 085421 (2017).
- [87] F. Schwarz, G. Kastlunger, F. Lissel, H. Riel, K. Venkatesan, H. Berke, R. Stadler and E. Lörtscher, *Nat Nanotechnol*, **11**, 170 (2016).

## BIBLIOGRAPHY

---

- [88] M. Brandbyge, J.-L. Mozos, J. Taylor, K. Stokbro, *Phys. Rev. B*, **65**, 165401 (2002).
- [89] Y. Xue, S. Datta, M. A. Ratner, *Chem. Phys.*, **281**, 151 (2002).
- [90] A.R. Rocha, V.M. Garcia-Suarez, S.W. Bailey, C.J. Lambert, J. Ferrer, S. Sanvito, *Nat. Mater.*, **4**, 335 (2005).
- [91] K. S. Thygesen and K. W. Jacobsen, *Chem. Phys.*, **319**, 111 (2005).
- [92] R. Stadler, *Phys. Rev. B*, **80**, 125401 (2009).
- [93] P. O. Löwdin, *J. Chem. Phys.* **18**, 365 (1950). S. Larsson, *J. Am. Chem. Soc.*, **103**, 4034 (1981).
- [94] M. A. Ratner, *J. Phys. Chem.*, **94**, 4877 (1990).
- [95] G. Kastlunger and R. Stadler, *Phys. Rev. B*, **89**, 115412 (2014).
- [96] P. Sautet and M.-L. Bocquet, *Phys. Rev. B*, **53**, 4910 (1996).
- [97] G. Kastlunger and R. Stadler, *Phys. Rev. B*, **88**, 035418 (2013).
- [98] W. Tang, E. Sanville and G. Henkelman, *J. Phys. Condens. Matter*, **21**, 084204 (2009).
- [99] T. Albrecht, A. Guckian, J. Ulstrup and J.G. Vos, *Nano Lett.*, **5**, 1451 (2005).
- [100] R. Stadler and T. Markussen, *J. Chem. Phys.*, **135**, 154109 (2011).
- [101] C.M. Finch, V.M. Garcia-Suarez and C.J. Lambert, *Phys. Rev. B*, **79**, 033405 (2009).
- [102] J.R. Miller, L.T. Calcaterra and G.L. Closs, *J. Am. Chem. Soc.*, **106**, 3047 (1984).
- [103] D. Qiu, P. S. Shenkin, F. P. Hollinger, and W. C. Still, *J. Phys. Chem. A*, **101**, 3005 (1997).
- [104] R. S. Mulliken, *J. Chem. Phys.*, **23**, 1833 (1955).
- [105] D. J. Mowbray, G. Jones and K. S. Thygesen, *J. Chem. Phys.*, **128**, 111103 (2008).

- 
- [106] T. Markussen, C. Jin, and K. S. Thygesen, *Phys. Status Solidi B*, **250**, 2394 (2013).
- [107] R. Stadler, K.W. Jacobsen, *Phys. Rev. B*, **74**, 161405(R) (2006).
- [108] R. Stadler, *Phys. Rev. B*, **81**, 165429 (2010).
- [109] A. Migliore, P. Schiff and A. Nitzan, *Phys. Chem. Chem. Phys.*, **14**, 13746 (2012).
- [110] T. Albrecht, K. Moth-Poulsen, J.B. Christensen, A. Guckian, T. Bjø, J.G. Vos, and J. Ulstrup, *Faraday Discuss.*, **131**, 265 (2006).
- [111] W. Haiss, H. van Zalinge, S.J. Higgins, D. Bethell, H. Höbenreich, D.J. Schiffrin, and R.J. Nichols, *J. Am. Chem. Soc.*, **125**, 15294 (2003).
- [112] A.M. Ricci, E.J. Calvo, S. Martin, and R.J. Nichols, *J. Am. Chem. Soc.*, **132**, 2494 (2010).
- [113] M.S. Inkpen, T. Albrecht, and N.J. Long, *Organometallics*, **32** 6053 (2013).
- [114] Y. Meir and N. S. Wingreen, *Phys. Rev. Lett.*, **68**, 2512 (1992).
- [115] W. Hong, D. Z. Manrique, P. Moreno-García, M. Gulcur, A. Mishchenko, C. J. Lambert, M. R. Bryce and T. Wandlowski, *J. Am. Chem. Soc.*, **134**, 2292 (2012).
- [116] R. Stadler, *J. Phys.: Conf. Ser.*, **61**, 1097 (2007).
- [117] B.-S. Kim, J.M. Beebe, Y. Jun, X.-Y. Zhu and C.D. Frisbie, *J. Am. Chem. Soc.*, **128**, 4970 (2006).
- [118] J.M. Beebe, V.B. Engelkes, L.L. Miller and C.D. Frisbie, *J. Am. Chem. Soc.*, **124**, 11268 (2002).
- [119] L. Luo, A. Benameur, P. Brignou, S.H. Choi, S. Rigaut and C.D. Frisbie, *J. Phys. Chem. C*, **115**, 19955 (2011).
- [120] R.B. Pontes, F.D. Novaes, A. Fazzio and A.J.R. Silva, *J. Am. Chem. Soc.*, **128**, 8996 (2006).
- [121] W. R. French, C. R. Iacovella, I. Rungger, A. M. Souza, S. Sanvito and P. T. Cummings, *J. Phys. Chem. Lett.*, **4**, 887 (2013).

## BIBLIOGRAPHY

---

- [122] J. Nara, S.Higai, Y. Morikawa and T. Ohno, *J. Chem. Phys.*, **122**, 6705 (2004).
- [123] Z. Ning, W. Ji and H. Guo, *arXiv:cond-mat/arXiv:0907.4674* (2010).
- [124] S.Y. Quek, J.B. Neaton, M.S. Hybertsen, L. Venkataraman, C.H. Choi, S.G. Louie, *Nano Lett.*, **7**, 3477 (2007).
- [125] A. de Melo Souza, I. Rungger, R. B. Pontes, A. R. Rocha, A. J. R da Silva, U. Schwingenschlöegl, S. Sanvito, *Nanoscale*, **6**, 14495 (2014).
- [126] E. Verwüster, O.T. Hofmann, D.A. Egger, E. Zojer, *J. Phys. Chem. C*, **119**, 7817 (2015).
- [127] R. Stadler, *J. Phys.: Conf. Ser.*, **61**, 1097 (2007).
- [128] R. Stadler, *Phys. Rev. B*, **81**, 165429 (2010).
- [129] G. Kastlunger, R. Stadler, *Phys. Rev. B*, **88**, 035418 (2013).
- [130] C. Van Dyck, V. Geskin, J. Cornil, *Adv. Funct. Mater.*, **24**, 6154 (2014).

# Destructive quantum interference in electron transport: A reconciliation of the molecular orbital and the atomic orbital perspective

Xin Zhao, Victor Geskin, and Robert Stadler

Citation: *J. Chem. Phys.* **146**, 092308 (2017); doi: 10.1063/1.4972572

View online: <http://dx.doi.org/10.1063/1.4972572>

View Table of Contents: <http://aip.scitation.org/toc/jcp/146/9>

Published by the [American Institute of Physics](#)

---

## Articles you may be interested in

[Nonequilibrium diagrammatic technique for Hubbard Green functions](#)

*J. Chem. Phys.* **146**, 092301 (2016); 10.1063/1.4965825

[Enhancing the conductivity of molecular electronic devices](#)

*J. Chem. Phys.* **146**, 092310 (2016); 10.1063/1.4972992

[Effects of vibrational anharmonicity on molecular electronic conduction and thermoelectric efficiency](#)

*J. Chem. Phys.* **146**, 092303 (2016); 10.1063/1.4965824

[Electronic friction near metal surfaces: A case where molecule-metal couplings depend on nuclear coordinates](#)

*J. Chem. Phys.* **146**, 092304 (2016); 10.1063/1.4965823

---



# Destructive quantum interference in electron transport: A reconciliation of the molecular orbital and the atomic orbital perspective

Xin Zhao,<sup>a)</sup> Victor Geskin,<sup>a),b)</sup> and Robert Stadler<sup>a)</sup>

Institute for Theoretical Physics, TU Wien - Vienna University of Technology, Wiedner Hauptstrasse 8-10, A-1040 Vienna, Austria

(Received 13 September 2016; accepted 6 December 2016; published online 23 December 2016)

Destructive quantum interference (DQI) in single molecule electronics is a purely quantum mechanical effect and is entirely defined by the inherent properties of the molecule in the junction such as its structure and symmetry. This definition of DQI by molecular properties alone suggests its relation to other more general concepts in chemistry as well as the possibility of deriving simple models for its understanding and molecular device design. Recently, two such models have gained a wide spread attention, where one was a graphical scheme based on visually inspecting the connectivity of the carbon sites in conjugated  $\pi$  systems in an atomic orbital (AO) basis and the other one puts the emphasis on the amplitudes and signs of the frontier molecular orbitals (MOs). There have been discussions on the range of applicability for these schemes, but ultimately conclusions from topological molecular Hamiltonians should not depend on whether they are drawn from an AO or a MO representation, as long as all the orbitals are taken into account. In this article, we clarify the relation between both models in terms of the zeroth order Green's function and compare their predictions for a variety of systems. From this comparison, we conclude that for a correct description of DQI from a MO perspective, it is necessary to include the contributions from all MOs rather than just those from the frontier orbitals. The cases where DQI effects can be successfully predicted within a frontier orbital approximation we show them to be limited to alternant even-membered hydrocarbons, as a direct consequence of the Coulson-Rushbrooke pairing theorem in quantum chemistry. *Published by AIP Publishing.* [<http://dx.doi.org/10.1063/1.4972572>]

*".. you have a program, for God's sake use it, play with it, do a calculation on any small problem related to your problem. Let the calculations teach you. They are so easy! Shall we stop teasing one another about MO and VB?"*

*"... quantum chemistry has given us two wonderful tools to reason about chemistry, and denying any one of them would impoverish our ability to reason."<sup>1</sup>*

## I. INTRODUCTION

First experimental studies of electron transport through single molecules attached to metal contacts by using a scanning tunnelling microscope (STM) or mechanically controlled break junction techniques,<sup>2-5</sup> also triggered considerable theoretical activity in this field since the beginning of the new millennium. The theoretical framework most widely used in this context is a Non-Equilibrium Green's Function (NEGF) formalism,<sup>6</sup> where coherent electron transmission according to Landauer's theory is assumed.

The conductance of a molecular junction can then be described in dependence on the incoming electron's energy  $E$  in terms of the transmission probability  $T(E)$ , which within NEGF is defined as

$$T(E) = \text{Tr}[G^r(E)\mathbf{\Gamma}_L(E)G^a(E)\mathbf{\Gamma}_R(E)], \quad (1)$$

<sup>a)</sup>Email: victor.geskin@mail.be and robert.stadler@tuwien.ac.at

<sup>b)</sup>Permanent address: 11, rue de la Limerie, B-7000 Mons, Belgium.

where the self energy matrices  $\mathbf{\Gamma}_L$  and  $\mathbf{\Gamma}_R$  contain the coupling of the molecule to the left and right electrodes and  $G^r$  and  $G^a$  are the retarded and advanced Green's functions (GFs) of the (extended) molecule.

The NEGF formalism has been implemented in a variety of codes, where in combination with density functional theory (DFT) it allows for a first principles treatment of the conductance of single molecule junctions.<sup>7-10</sup> The usefulness of such calculations, however, still relies on simple models for interpreting them in terms of quantum chemical concepts such as atomic orbitals (AOs) or molecular orbitals (MOs) in order to achieve a qualitative understanding of the observed electron transport characteristics in the context of our general knowledge of the electronic properties of molecules or what is regarded as chemical intuition.

In principle, electron transmission can be viewed as a particular manifestation of the more general phenomenon of electronic communication through a molecule, where a Green's function describes the propagation of a perturbation and is a measure of the connected paths made available by the bonding pattern of the molecule.<sup>11</sup>

The zeroth Green's function  $G_{lr}^{mol}$  can be used to rewrite the expression for  $T(E)$  given in Eq. (1) under the assumption that the central molecule is coupled to both metal contacts only via a single AO labeled  $l$  and  $r$  on the respective side because then each matrix  $\mathbf{\Gamma}$  contains only one non-zero element,  $\Gamma_{ll}$  and  $\Gamma_{rr}$ , respectively, and therefore a single term remains from

the trace resulting in

$$T(E) = |G_{lr}^{mol}(E)|^2 \Gamma_{ll}(E) \Gamma_{rr}(E). \quad (2)$$

By evaluating the relevant matrix elements of  $G_{lr}^{mol}$ , chemical understanding of the general properties of molecules can arguably be complemented by studying their transmission properties. For example, the low-bias conductance through benzene is orders of magnitude lower when it is contacted at positions which are meta (*m*) with respect to each other when compared with ortho (*o*) or para (*p*).<sup>12–14</sup>

This result comes as no surprise for a chemist even without any prior exposure to the theory of molecular conductivity, who knows that the influence of a substituent in a benzene ring is “felt,” in both electrophilic and nucleophilic substitution reactions, in *o*- and *p*-position to it, while *m*-positions “do not communicate.”

This knowledge might be referred to as chemical intuition but is actually based on the rules stemming from resonance theory within the Valence Bond (VB) framework, where the relation of electronic communication to the topology of MOs is not self-evident but should be contained in  $G_{lr}^{mol}$ . In their classical 1947–1950 series of papers, Coulson and co-workers attempted to put the one-electron Green’s function (without using the term at the time) at the heart of chemical theory.<sup>15–20</sup>

They demonstrated how starting from a Hückel Hamiltonian in an AO representation, basic molecular characteristics such as MO energies, atomic charges, bond orders, and response coefficients can be derived directly from the secular determinant without referring to explicit MO vectors, where the relation of this work to electron transport phenomena has been commented on very recently.<sup>21–24</sup>

Although it was correctly claimed by Datta<sup>25</sup> amongst others that in a single molecule junction the conductance is defined not only by the central molecule but rather by the entire system including the metal contacts, the individual contributions of the components are separable in Eq. (1). Therefore, for the purpose of device design, the molecular contribution can be optimized independently from the coupling to the metal contacts, a notion which has been recently confirmed in a joint theoretical and experimental work by Manrique *et al.*<sup>26</sup> In this study it was shown that molecules and even their fragments contribute well defined and transferable factors to electron transport as a crucial observation for the investigation of destructive quantum interference (DQI) effects, a phenomenon which has been the topic of a tremendous number of recent articles, where for a rather complete bibliography we refer to Ref. 27.

Such DQI effects when occurring in the transmission close to the Fermi energy  $E_F$  can be used for data storage,<sup>28</sup> inducing thermoelectricity<sup>29</sup> or the design of logic circuits.<sup>30</sup> Simple models have been proposed for their analysis, which were derived from tight-binding (TB) or topological Hückel theory and validated by DFT calculations: One of them which we refer to as “the graphical AO scheme” in the following has been derived specifically for the prediction of DQI and is based on a graphical analysis of the connectivity matrix of atomic orbitals (AOs),<sup>30–34</sup> while the other interprets the efficiency of transmission in a broader sense in terms of the signs and amplitudes of the molecular orbitals on the atomic

sites directly connected to the electrodes,<sup>35–40</sup> and the analysis is sometimes limited to a “frontier orbital approximation” where only the highest occupied MO (HOMO) and the lowest unoccupied MO (LUMO) are taken into account.

The aim of this article is to reconcile the predictions from these two conceptually different approaches for an interpretation and analysis of the molecular Green’s function. It is expected that by focusing on either an AO or a MO representation of the same quantum-mechanical problem, one should obtain the same results. Their reconciliation is akin to that of the VB and MO theories in the earlier days of quantum chemistry by Van Vleck and Sherman in 1935.<sup>41</sup>

But while VB and MO approaches become variationally equivalent for the ground state only in the limit of full configuration interaction, for electron transport within a single particle framework the representations of the molecular Green’s function in the AO and MO bases are already strictly equivalent on a single determinant level. From Eq. (2) it can be seen that it is both necessary and sufficient to evaluate the purely molecular quantity  $G_{lr}^{mol}$  for estimating whether the transmission will be finite or zero at any given energy  $E$ .

The derivation of both “the graphical AO scheme” and the MO based scheme mentioned above starts from this observation. Within a frontier orbital approximation, however, only the HOMO and LUMO are taken into account instead of all MOs contained in  $G_{lr}^{mol}$  and this approximation then limits the range of applicability of the MO based scheme to that of the Coulson–Rushbrooke pairing theorem<sup>42,43</sup> as we explain in detail in Sec. II.

If the contributions of all MOs and not only the frontier orbitals to  $G_{lr}^{mol}$  in Eq. (2) are correctly accounted for on a quantitative level, however, DQI can be analyzed from a MO perspective leading to equivalent results as the graphical AO scheme from Refs. 30–34 for all conjugated  $\pi$  systems both alternant and non-alternant, with and without hetero-atoms and regardless of which subset of sites the contact atoms belong to, which is the main message of our article.

The paper is organized as follows: In Sec. II we shortly review the graphical AO scheme and highlight its relation to Eq. (2). Here we also explain on the basis of the pairing theorem that DQI effects entering  $G_{lr}^{mol}$  can in general only be quantitatively described and understood in terms of the onsite energies of all MOs and their respective amplitudes at the contacted atomic sites. Furthermore, we clarify the connection of such a MO centered analysis scheme to Larsson’s formula, which has been originally proposed for the definition of an effective coupling from the MO contributions to the transfer integral in a Marcus theory description of electron hopping<sup>44–46</sup> but later on also used for the analysis of coherent electron transport in single molecule junctions.<sup>47,48</sup>

In Sec. III we provide computational studies for a variety of test systems in order to substantiate our claim that it is possible to gain understanding of the DQI effects in accurate terms for any conjugated  $\pi$  system without the limitations of applicability facing the original frontier MO rules.

For all the molecular systems in our article, numerical calculations on a DFT level exist in the literature and most of them have also been studied experimentally. Since the focus of our work is on the topological properties of  $G_{lr}^{mol}$ , for the

calculations we present here the topological Hückel Hamiltonians that are used in combination with NEGF. In this numerical chapter, we also present the respective predictions from the graphical AO scheme for all systems as a reference and demonstrate their equivalence to the results obtained from an analysis of MO contributions, where the convergence with respect to the number of MOs included plays a prominent role. In the final chapter we provide a summary.

## II. THEORETICAL DISCUSSION OF DQI PREDICTION AND ANALYSIS IN AO AND MO REPRESENTATIONS

The zeroth Green's function  $G_{lr}^{mol}$  in Eq. (2) describes the propagation of a tunnelling charge between the atomic sites  $l$  and  $r$  mediated by all molecular orbitals (MOs) which in the weak coupling limit can be formulated as<sup>31</sup>

$$G_{lr}^{mol}(E) = [(E \pm i\eta)\mathbf{I} - \mathbf{H}_{mol}]^{-1}, \quad (3)$$

where  $\mathbf{H}_{mol}$  is the molecular Hamiltonian,  $\mathbf{I}$  a unity matrix, and  $i\eta$  an infinitesimal imaginary term introduced in order to avoid the divergence of  $G_{lr}^{mol}$  at the eigenvalues of  $\mathbf{H}_{mol}$ .

### A. Graphical AO scheme

Since  $G_{lr}^{mol}$  is obtained from the inversion of the Hamiltonian matrix  $\mathbf{H}_{mol}$ , which is defined in an AO representation, one can analyze the properties of  $G_{lr}^{mol}$  from the ratio of one of the minors of  $\mathbf{H}_{mol}$  and its determinant<sup>30-34</sup> where  $G_{lr}^{mol}$  is only equal to zero when the respective minor, as defined by the connection of the leads to two particular atomic sites  $l$  and  $r$  on the molecule, is also zero.

In this way, the graphical AO scheme for the prediction of DQI effects was derived, which has been formulated as the following set of rules: DQI occurs at  $E = E_F$  if it is impossible to connect the two atomic sites  $l$  and  $r$  in a molecular topology, i.e., the only two sites with a direct coupling to the leads, by a continuous chain of paths, and at the same time fulfill the conditions (i) two sites can be connected by a path if they are nearest neighbors and (ii) at all atomic sites in the molecule other than  $l$  and  $r$ , there is one incoming and one outgoing path.

In other words, for a finite zero-bias conductance all AOs of the molecular topology have to be either traversed within a continuous chain of paths from  $l$  to  $r$  or be part of a closed loop in the topology, where the latter can be a double line due to the pairing of connected orbitals or a triangle or any larger loop.<sup>30,31,33</sup> We will demonstrate in Sec. III B how to apply these rules for any given molecular topology in praxis. In a later extension of this scheme, it has been clarified that such defined paths can also cancel each other out in special cases and that therefore a sign has to be attributed to them.<sup>34</sup> It has to be noted that these "paths" are just mathematical terms obtained from forming the minor of  $\mathbf{H}_{mol}$  and should not be interpreted as the physical path of an electron moving through the molecule.

This graphical AO scheme has the advantage that it allows for the prediction of DQI without any numerical calculations being required simply by a visual assessment of the chemical structure of the central molecule in the junction. The scheme

has been designed for the molecules with a conjugated  $\pi$  system because it is only  $\pi$  electrons which are taken into account in the topological Hückel Hamiltonian it was derived from. In praxis this is not really a limitation, since potential functional molecules of interest are usually conjugated systems, where  $\pi$ -transmission is dominant. In order to allow for a simple analytical treatment, the derivation of the scheme also originally assumed sites with identical onsite energies and couplings to each other.<sup>30,31</sup>

This assumption was later lifted in an attempt to generalize the method now also allowing for hetero atoms in the molecular structure but this came at the price of increased mathematical complexity.<sup>32,49</sup> Another assumption was that the only energy  $E$ , where  $T(E)$  is of interest, is the Fermi energy because it defines the zero-bias conductance and therefore the rules only apply at  $E = E_F$ . This latter assumption is rather delicate considering that in the model Hamiltonian the graphical rules were derived from the onsite energy of carbon sites and were artificially set to  $E_F$ . Quite surprisingly, it was found in praxis that this rather crude approximation did not seem to limit the predictive qualities of the model even for the cases where hetero atoms such as oxygen were involved in the molecular structures under investigation<sup>32</sup> as long as the Fermi energy defined by the metal leads lies within the HOMO-LUMO gap of the molecule when energy levels are aligned.<sup>50</sup>

### B. Pairing theorem and frontier orbital approximation

In order to gain a MO perspective of  $G_{lr}^{mol}$  instead of an AO one,  $\mathbf{H}_{mol}$  has to be looked at in its diagonalized form as  $\mathbf{H}_{mol} = \mathbf{C}\epsilon_{MO}\mathbf{C}^\dagger$ , where  $\epsilon_{MO}$  is the diagonal matrix of MO eigenenergies and  $\mathbf{C}$  is the matrix of the coefficients for the expansion of all MOs as a linear combination of all AOs in the molecule. Inserting this definition of  $\mathbf{H}_{mol}$  into Eq. (3) gives

$$G_{lr}^{mol}(E) = \sum_{m=1}^N \frac{C_{lm}C_{rm}^*}{E - \epsilon_m \pm i\eta}, \quad (4)$$

which is the spectral representation of  $G_{lr}^{mol}$  in a Hückel AO basis with  $C_{l(r)m}$  the coefficient of the  $l(r)$ -th AO in the  $m$ -th MO in a sum that runs over all  $N$  occupied and unoccupied MOs, which result from the coupling of the AOs defining the basis vectors for  $\mathbf{H}_{mol}$ .

It should be stressed that Eq. (4) is exact for any Hamiltonian with an orthogonal AO basis and that this spectral representation of  $G_{lr}^{mol}$  served as the starting point for the formulation of the molecular orbital rules for efficient transmission by Yoshizawa and co-workers.<sup>35-40</sup>

For the special case of alternant hydrocarbons (AHs), which are molecules with a conjugated  $\pi$  system where carbon atoms can be divided into two subsets, "starred and unstarred," such that the atoms of one subset are bonded only to those from the other, the Coulson-Rushbrooke pairing theorem<sup>42,43</sup> applies which states that (i) the  $\pi$  electron energy levels are symmetrically distributed about the zero energy level (which is assumed to be  $E_F$  in single molecule junctions) and (ii) that each occupied MO obtained from diagonalizing the corresponding Hamiltonian in an orthogonal AO basis with an energy  $-\epsilon_{MO}$  has its mirror image in the unoccupied region



with the energy  $+\epsilon_{MO}$ , which regarding its shape differs only in the sign of all AO coefficients of one subset.

In the following, we focus on the molecules with an even number of MOs, which we can then group in Eq. (4) into pairs of the contributions from the MOs whose energies are linked by the symmetry relation it defines, i.e.,  $(H,L)$ ,  $(H-1,L+1)$ ,  $\dots$ ,  $(H-(N/2-1), (L+(N/2-1)))$  with  $H = \text{HOMO}$ ,  $L = \text{LUMO}$ , and  $-\epsilon_{H-k} = \epsilon_{L+k} = \epsilon_k$ . We can then redefine  $G_{lr}^{mol}(E_F)$  as the sum of these pairs, which in the following we will refer to as Coulson-Rushbrooke or CR pairs

$$G_{lr}^{mol}(E_F) = \sum_{k=0}^{N/2-1} \frac{C_{l,(H-k)} C_{r,(H-k)}^* - C_{l,(L+k)} C_{r,(L+k)}^*}{\epsilon_k}. \quad (5)$$

The pairing theorem now predicts for AOs  $l$  and  $r$  on the carbon atoms of the same subset that  $C_{l,(H-k)} C_{r,(H-k)}^* = C_{l,(L+k)} C_{r,(L+k)}^*$  because either  $C_{l,(H-k)} = -C_{l,(L+k)}$  and simultaneously  $C_{r,(H-k)}^* = -C_{r,(L+k)}^*$  or  $C_{l,(H-k)} = C_{l,(L+k)}$  and simultaneously  $C_{r,(H-k)}^* = C_{r,(L+k)}^*$ , as all the coefficients in only one subset change their sign when comparing an occupied with its mirrored unoccupied level. Therefore, the terms in every CR pair of Eq. (5) cancel exactly at  $E_F$  for this case and DQI occurs as a result as has also been observed in Refs. 51 and 52.

If on the other hand, the contact AOs  $l$  and  $r$  belong to the carbon atoms from different subsets, then  $C_{l,(H-k)} C_{r,(H-k)}^* = -C_{l,(L+k)} C_{r,(L+k)}^*$  because either  $C_{l,(H-k)} = -C_{l,(L+k)}$  and  $C_{r,(H-k)}^* = C_{r,(L+k)}^*$  or  $C_{l,(H-k)} = C_{l,(L+k)}$  and  $C_{r,(H-k)}^* = -C_{r,(L+k)}^*$ . For this case, the contributions coming from the two individual parts of each CR pair of MOs ( $H-k$ ,  $L+k$ ) including the HOMO and the LUMO always add up constructively at  $E_F$  in Eq. (5).

Although any individual CR pair contribution is therefore nonvanishing, it is important to stress that destructive interference is still possible between CR pairs, as each of them can contribute either a positive or a negative term to  $G_{lr}^{mol}$ . The pairing theorem, however, does not provide the means for an assessment of prediction of such inter-pair interference.

The general conclusion from the pairing theorem is therefore that DQI will always occur for the electron transport through the junctions containing alternant hydrocarbons when the carbon atoms of the same subset are contacted, which is already sufficient to account for the low conductance of a variety of systems such as polyenes with contact atoms of the same parity, meta-contacted benzene or generic cross-conjugated molecules, where these cases can readily be identified from their chemical structure without any deeper analysis of the shapes and signs of their frontier MOs.

On the other hand, for alternant hydrocarbons contacted on the carbons belonging to different subsets, i.e., where one contact atom is starred and the other one unstarred or for non-alternant hydrocarbons or for conjugated  $\pi$  systems containing hetero atoms, the pairing theorem can neither predict nor rule out DQI. In the literature, these two cases are sometimes distinguished in terms of “easy zeros” (the same subset contacted) and “hard zeros” (different subsets contacted)<sup>53</sup> or linked to the occurrence of an odd or even number of zeroes in  $T(E)$ .<sup>51,52</sup> But for the purpose of our article the important distinction is that for even-membered alternant hydrocarbons contacted at sites

of the same subset DQI will always occur, while for all other cases DQI cannot be predicted without numerical calculations from a MO perspective.

We note that our discussion above only refers to the alternant hydrocarbons with an even number of MOs and therefore also an even number of carbon sites. This is the general case for stable alternant hydrocarbons. When the total number of MOs is odd, which implies the existence of a non-bonding MO at the Fermi energy with non-vanishing contributions from only one subset follows from the pairing theorem, which then allows for a conduction peak instead of a DQI induced minimum at  $E_F$  when the contacted atoms belong to the subset contributing to this non-bonding MO.

We now turn our attention to the molecular orbital rules derived by Yoshizawa and co-workers,<sup>35–40</sup> where the starting point was also the spectral representation of  $G_{lr}^{mol}$  given in Eq. (4). These rules are amongst the earliest formulated providing a link between the complex phenomenon of DQI in electron transmission and the standard output of quantum chemical calculations, in this case the sign of the amplitudes of MOs. Within a frontier orbital approximation they also become particularly simple to apply because then the entire sum in Eq. (5) is dominated by only one CR pair, namely the contribution to  $G_{lr}^{mol}(E_F)$  coming from the HOMO and the LUMO, and then the remaining pairs can all be neglected because their large energetic distance  $\epsilon_k$  to  $E_F$  results in large denominators in the respective terms, thereby making them numerically negligible.

From this assumption, it can be concluded that the transport through a single molecule would be effective, i.e., DQI would be absent, when on the two contact atoms to the two leads (i) the sign of the product of the MO expansion coefficients in the HOMO ( $C_{l,H} C_{r,H}^*$ ) is different from that in the LUMO ( $C_{l,L} C_{r,L}^*$ ) and (ii) all four involved amplitudes  $C_{l,H}$ ,  $C_{r,H}^*$ ,  $C_{l,L}$ , and  $C_{r,L}^*$  are of significant magnitude. If these conditions are not fulfilled, then “inefficient” transmission due to at least a partial cancellation of the contributions from the HOMO and LUMO was predicted which was not formulated as necessarily the zero transmission which is typical for DQI in a rigid sense.

Such a frontier orbital approximation, however, only delivers correct results for the prediction of DQI where the CR pairing theorem<sup>42,43</sup> is applicable. If the atoms contacted by the two electrodes belong to the same subset (either starred or unstarred) of carbon atoms in an even-membered AH, the cancellation of the contributions from the HOMO and the LUMO to  $G_{lr}^{mol}(E_F)$  is a reliable indicator of DQI not necessarily because they are dominant, but because it also represents the cancellation of the contributions within all other CR pairs entering Eq. (5). This is the reason why DQI can be understood in this case in terms of the frontier orbitals alone.

For all other cases, all MOs in the system need to be considered. If an alternant hydrocarbon is contacted at atomic sites belonging to different subsets, i.e., one being starred and one being unstarred according to the CR framework, then although the contributions from the HOMO and LUMO can only interfere constructively, the tails related to lower lying occupied and higher lying unoccupied MOs might still cancel out with those of the frontier orbitals at  $E_F$  and cause DQI. For the

non-alternant hydrocarbons and organic molecules containing hetero atoms, it turns out to be equally insufficient to limit the analysis to just one or even two CR pairs of MO contributions. In Sec. III C we will provide a range of numerical examples justifying this assertion.

### C. Larsson's formula for a MO based analysis

A somewhat simplified form of Eq. (4) has been known for decades as Larsson's formula in a different but related context, where it was used for the definition of the transfer integral mediated by a selected set of MOs in a Marcus theory description of electron hopping.<sup>44–46</sup> More recently, it has been realized<sup>47,48</sup> that the same formula can be also employed to define an approximation for  $T(E)$  in coherent electron tunnelling as  $T(E) \sim \Gamma^2(E)$  with  $\Gamma(E)$  being an energy dependent effective coupling containing the contributions from all MOs of a molecular bridge and defined by

$$\Gamma(E) = \sum_{m=1}^N \frac{\alpha_m \beta_m}{E - \epsilon_m}. \quad (6)$$

Here  $\epsilon_m$ ,  $\alpha_m$ , and  $\beta_m$  are the eigenenergy and the respective couplings to the left and right contact of the  $m$ th MO, and  $E$  is the kinetic energy of a transferred electron. It is easy to see by direct comparison that the effective coupling  $\Gamma(E)$  in Eq. (6) is very much related to the zeroth Green's function in Eq. (4). There are only two differences between the two equations. First, the MO amplitudes  $C_{l(r)m}$  have been replaced by the couplings  $\alpha_m$  and  $\beta_m$ , which describe the overlap of each MO with a respective contact AO on the two leads. Since in the NEGF-TB description we employ for our numerical studies in Sec. III, the contact AO on the leads is always the same orbital, this difference amounts to just the same constant factor for all the MO terms of the sum in Eq. (6) and is therefore irrelevant for our study where we just set this value to 1.

The second difference between the two expressions, namely the dropping of the infinitesimal term  $i\eta$  just means that  $\Gamma(E)$  diverges at the eigenenergies of all MOs. In principle this deficiency can be repaired by introducing an energy dependent normalisation factor as has been derived from the more general theory in Ref. 54 by Sautet and Bocquet<sup>47</sup> under the very limiting condition of  $\alpha_m \gg \beta_m$ , which is relevant when the focus is on the analysis of STM measurements. Since the qualitative behaviour of  $\Gamma^2(E)$  does not deviate from that of  $T(E)$  obtained from NEGF-TB in all systems investigated in this article, we avoid such a normalisation factor as an unnecessary complication. In Sec. III we just truncate  $\Gamma^2(E)$  as obtained from Eq. (6) at the poles and scale it with the arbitrary constant of  $10^{-2}$  for the purpose of its graphical presentation in the related figures.

While the poles of  $G_{lr}^{mol}(E_F)$  in Eq. (4) or  $\Gamma(E)$  in Eq. (6) define the peaks in  $T(E)$  when these quantities are squared and each of these peaks can be identified with the electron transmission through one individual MO in the absence of degeneracies, the non-resonant transmission for energies between the peaks contains the contributions from all MOs  $m$  with the respective couplings  $\alpha_m$  and  $\beta_m$  and these contributions can interfere constructively or destructively in dependence on the energy  $E$ .

In the sums of Eqs. (4) and (6), the sign of the contribution from any MO is determined by (i) the numerator of its corresponding term in the summation as defined by the product of amplitudes at the contact site or product of couplings to the metal leads and (ii) its denominator which depends on whether the energy  $E$  for which  $T(E)$  is evaluated lies below or above the onsite energy of the MO in question. For AHs contacted via carbon atoms belonging to the same subset, DQI at the center of the HOMO-LUMO gap can be directly concluded from the CR pairing theorem by using Eq. (5).

For all other cases, neither the pairing theorem applies nor can reliable predictions on DQI be obtained within a frontier orbital approximation because the occurrence or absence of DQI for any given value of  $E$  seems to depend on a fine balance of cumulative contributions with different signs from all MOs, where a quantitative description of the decay of their respective tails is crucial as we will demonstrate in Sec. III.

## III. NUMERICAL CASE STUDIES

### A. Computational details

All the case studies in this article are based on simple models both in AO and MO representations as derived from the topological properties of the molecular Hamiltonian  $\mathbf{H}_{mol}$  in a tight binding approximation with all onsite energies for the carbon AOs contributing to the  $\pi$  system set to zero, i.e., to the origin of energy assumed to represent  $E_F$ , and the couplings between them to the resonance integral  $\beta$  from the Hückel theory which also defines the unit of the energy axis.

As an appropriate numerical benchmark for our conclusions, we therefore present the NEGF-TB calculations which have been conducted within the Atomic Simulation Environment (ASE)<sup>55,56</sup> with a coupling of  $\beta$  between the molecular topology and the semi infinite carbon chains used for the electrodes.

Sulfur atoms have been given an onsite energy of 1.11  $\beta$  and C–S bonds a coupling value of 0.69  $\beta$ <sup>57</sup> in order to account for the effect of the hetero atom. Since the molecules we investigate here all have been chosen due to the recent interest they attracted, we also refer to the relevant literature for each system in order to show that our conclusions harmonize with the results from the more realistic NEGF-DFT calculations or experimental conductance measurements.

### B. Butadiene as the simplest illustrative example

As a first example for our arguments in Sec. II A, we consider butadiene contacted at different sites (Fig. 1). Since this molecule with a conjugated  $\pi$  system is an even-membered AH, its even- and odd-numbered atoms belong to different starred/unstarred subsets and therefore DQI can be predicted for the (1,3-) connection within a frontier orbital approximation in agreement with the pairing theorem as outlined in Section II B because carbon sites belonging to the same subset are contacted (Fig. 1(a)). For all other possible connections, sites belonging to different subsets are contacted, and therefore constructive interference of the contributions from the HOMO and LUMO alone is found according to the pairing theorem.

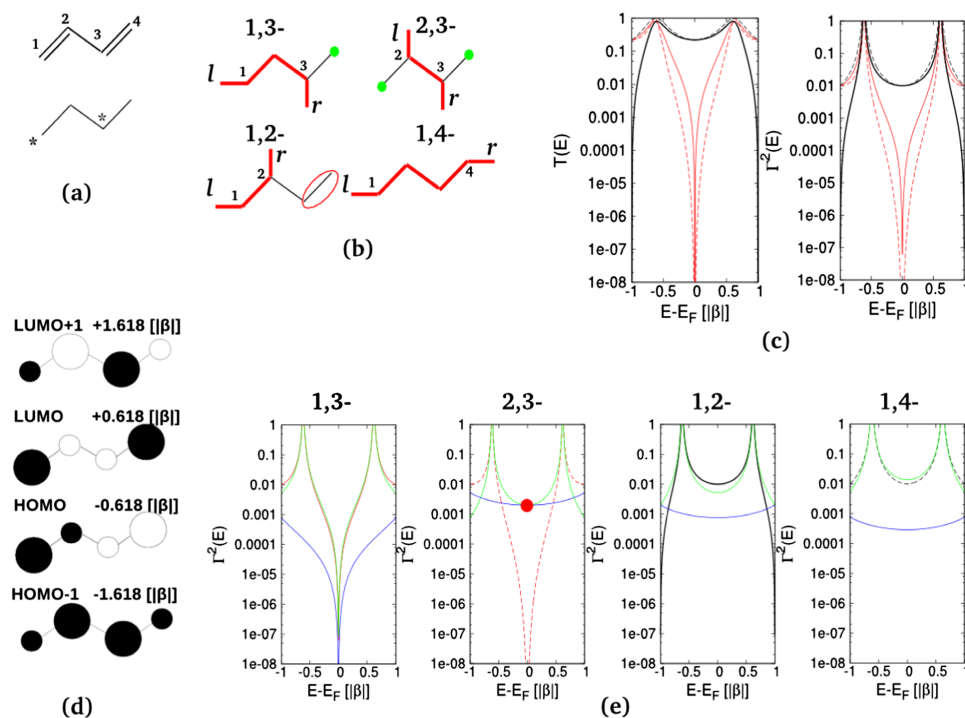


FIG. 1. Butadiene contacted to two electrodes with all possible combinations of contact sites: (a) chemical structure and “starring scheme,” (b) application of the graphical AO scheme (for details we refer to the caption of Fig. 4), (c)  $T(E)$  (in units of the conductance quantum  $G_0$ ) from NEGF-TB compared with  $\Gamma^2(E)$  (in arbitrary units) from Eq. (6) with red lines where DQI occurs (solid for 1,3- and dashed for 2,3-) and black lines where it does not (solid for 1,2- and dashed for 1,4-), (d) amplitudes (indicated as the size of spheres at each atomic size with black and white fillings distinguishing between a positive or negative sign of the wavefunction, respectively) and energies of all  $\pi$ -MOs, (e) individual contributions from the (HOMO + LUMO) (green line) and (HOMO - 1 + LUMO + 1) (blue line) to  $\Gamma^2(E)$  (where the crossing point of the two curves is marked with a red dot for the 2,3-connection) which is contrasted with the total  $\Gamma^2(E)$  from (c) in the respective color code used there.

The graphical AO scheme (Fig. 1(b)) as well as NEGF-TB calculations for  $T(E)$  and their estimates as  $\Gamma^2(E)$  from Eq. (6) after a diagonalisation of  $\mathbf{H}_{mol}$  where for both all four MOs have been properly accounted for (Fig. 1(c)) finding DQI not only for the 1,3-connection but also for the 2,3-connection. Within the graphical AO scheme DQI is predicted if it is not possible to form a continuous line between the two contact sites and have all AOs which are not on this line grouped up in pairs or as part of a closed loop. The single sites which are not crossed or grouped up are marked by green dots for the sake of clarity, which also allows for the simple correspondence that DQI occurs where green dots are unavoidable.

The MO based scheme within a frontier orbital approximation on the other side also correctly predicts DQI for 1,3-positioning of the contacts, but not for the 2,3-connection. While the amplitudes of both the HOMO and LUMO are low on sites 2 and 3 (Fig. 1(d)), this justifies a reduced conductance but not a cancelling out to zero which is a characteristic for DQI and is found for the 2,3-connection for  $T(E)$ .

In Fig. 1(e) we plot  $\Gamma^2(E)$  when only the contributions from the HOMO and the LUMO enter the expression for  $\Gamma(E)$  in Eq. (6) (green lines). There it can be seen that indeed zero transmission is found also considering only the two frontier orbitals for the 1,3-connection in agreement with the predictions from the pairing theorem, while the 2,3-case shows a reduced but finite conductance when compared to 1,2- and 1,4-positions of the contacts.

We also plot  $\Gamma^2(E)$  from the contributions of the HOMO - 1 and LUMO + 1 alone (blue lines) and find that only for the (2,3-) connection they cross those of the frontier orbitals at  $E_F$ . Since the corresponding sum of terms entering Eq. (6) for the two pairs has different signs at their crossing point, they cancel each other out and lead to zero transmission. This is probably the simplest example to contrast a case of DQI,

which can be predicted within a frontier orbital approximation with one that is beyond its range of applicability.

### C. Other representative molecular structures

In Figure 2 we show the other molecular systems which we investigate as case studies in this article and also the corresponding TB next neighbor connectivity, which provides the basis for all our NEGF-TB computations as well as the application of the pairing theorem and the graphical AO scheme in the following. We note that only unsaturated carbon atoms are part of the  $\pi$  system and that it is only those which need to be considered in a TB framework.

For benzene (Fig. 2(a)), it is established knowledge<sup>12-14</sup> that the conductance is finite for an o- or p-connected pair of contacts but DQI occurs at  $E_F$  for a m-connection, which is also consistent with the chemical understanding of communication through an aromatic ring. In Figure 2(a) we illustrate that these findings can be also understood in the context of the pairing theorem (Fig. 2(b)) because only for the m-connection two “starred” carbon sites are contacted in this example of an even-membered AH meaning that each CR pair will provide a contribution of exactly zero in Eq. (5).

Another type of systems where DQI plays an important role is molecular switches<sup>58</sup> based on “conducting” and “insulating” isomers that can be transformed into each other in a highly reversible photochemical reaction. We will consider here one family of such switches, namely diarylethenes,<sup>59</sup> and in particular the homocyclic dinaphthylethene (DNE) (Fig. 2(b)) and the heterocyclic dithienylethene (DTE) (Fig. 2(c)). For both systems, the closed isomer is much better conducting than the open isomer in a molecular junction which has been demonstrated experimentally<sup>58-62</sup> and confirmed theoretically,<sup>36,63</sup> where the formation (or breaking) of a single bond distinguishes one from the other in structural terms.

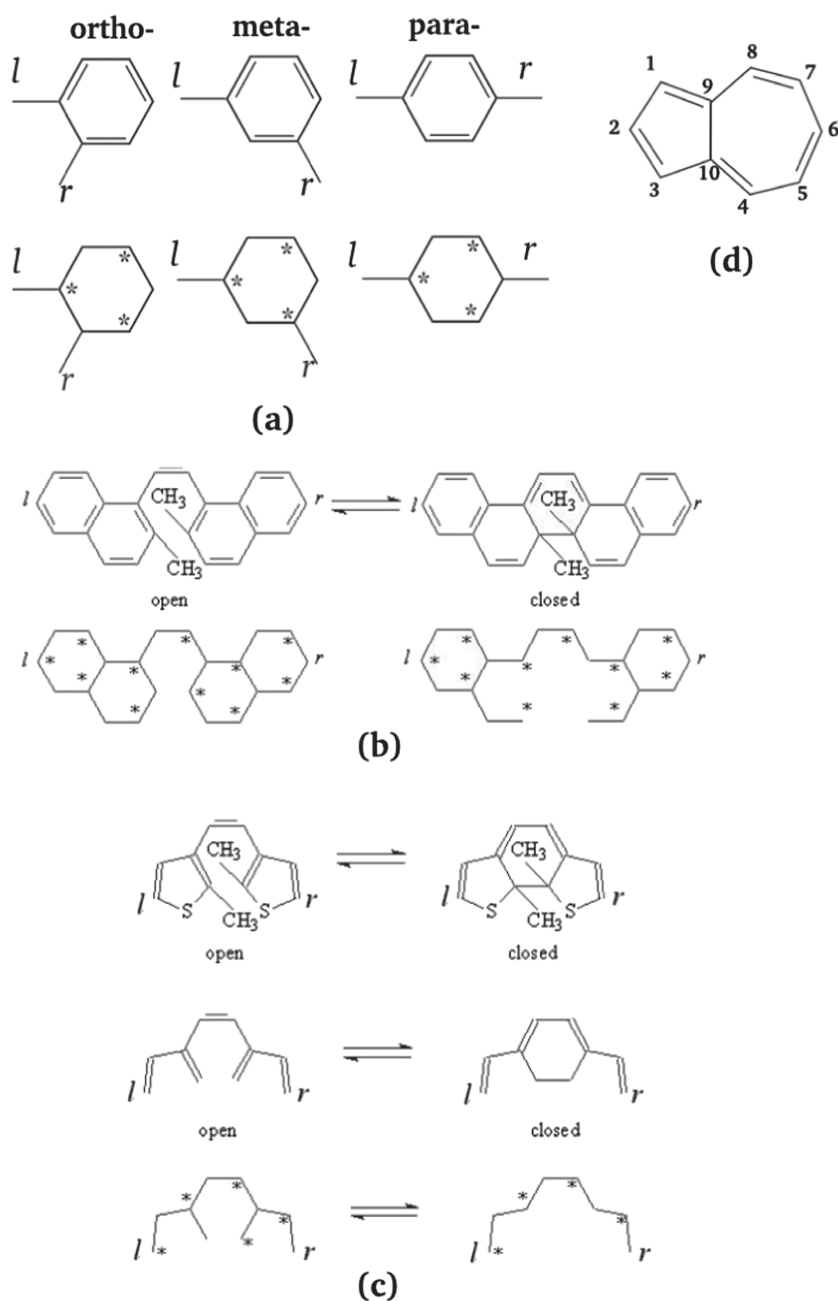


FIG. 2. Chemical structures and corresponding TB next neighbor connectivity with the positions of the contacts to the electrodes marked as  $l$  and  $r$  and with “stars” related to the pairing theorem and involving only the  $\pi$  electrons for (a) benzene connected in ortho- ( $o$ -), meta- ( $m$ -), and para- ( $p$ -) positions, (b) dinaphthylethene (DNE), and (c) dithienylethene (DTE) in their open and closed forms, respectively, where for the latter also the alternant hydrocarbon analogs obtained by removing the S sites are shown. In (d) the chemical structure of azulene is shown and the positions for connecting metal contacts are numbered for making reference to them in the text.

NEGF-DFT calculations can be found, e.g., in Refs. 36 and 63 for DNE and DTE, respectively. The molecular orbital rules by Yoshizawa and co-workers have also been applied for both systems, where although their application in a narrow sense would have suggested constructive interference for the “closed” (conducting) and “open” (insulating) form for DNE, the differences in conductance between the two forms found with NEGF-DFT have been attributed to the larger orbital amplitudes for the “closed” form.<sup>36</sup> As for the butadiene example we discussed above, this argument explains quantitative differences in the conductance but not the qualitative difference defined by the occurrence or absence of an interference minimum.

For DTE on the other side, the contributions from the HOMO  $- 1$  and LUMO  $+ 1$  had to be added to those from the frontier orbitals in order to reach a better agreement with

the experimental findings.<sup>64</sup> As can be seen from their respective TB next neighbor connectivity in Figs. 2(b) and 2(c), the electrodes are attached to the carbon atoms which belong to different subsets of the starring scheme for the open forms of both DNE and DTE. As a consequence of the MO symmetry properties following from the pairing theorem therefore constructive QI has to be found within all CR pairs of MOs defined by Eq. (5) including the HOMO and the LUMO, and hence DQI can only occur due to cancellation of the terms between different CR pairs which cannot be assessed by using a frontier orbital approximation, and this is the reason why we included these systems in the present study.

DTE is heterocyclic, which means that we need to include an onsite energy for the sulfur atoms differing from those of the carbon sites and also a value for the C–S coupling in the NEGF-TB calculations in the following as specified in the



computational details. In order to have a reference point for the application of the graphical AO scheme also for DTE, we also introduce a structure with the S atoms of DTE deleted in Fig. 2(c), which transforms it into an even-membered AH, where in Sec. III D we will compare the transmission functions of both DTE forms with and without sulfur sites.

As the final system for our study, we chose azulene (Fig. 2(d)), which is a non-alternant hydrocarbon and therefore it is not possible to divide its carbon sites into “starred” and “unstarred” subsets in relation to the pairing theorem or derive any conclusions regarding destructive or constructive QI within a frontier orbital approximation. This system is also of interest because it has been wrongly claimed in a joint experimental and theoretical study that for azulene the graphical AO scheme also fails in its predictions at least when the electrodes contact the sites 1 and 3 in Fig. 2(d).<sup>65</sup>

This claim has later been refuted,<sup>33</sup> where it was shown that the predictions of the graphical AO scheme were also correct for azulene with 1,3-contacts when closed loops of AOs and not only pairs of them are considered which always has been a central aspect of the scheme.<sup>30,31</sup> NEGF-DFT calculations for azulene containing compounds with different electrode contact sites including the 1,3- and 5,7-cases can be, e.g., found in Refs. 65 and 66.

#### D. DQI predictions from NEGF-TB, Larsson’s formula, and the graphical AO scheme

In Fig. 3,  $T(E)$  as calculated from NEGF-TB for all systems introduced in Fig. 2 is shown in the left panels for each label and compared with  $\Gamma^2(E)$  in the right panels, which was obtained from Eq. (6) with MO onsite energies and amplitudes resulting from a diagonalisation of  $\mathbf{H}_{mol}$  in the same TB setup, where for both quantities the curves for the systems exhibiting DQI at  $E_F$  are shown in red and the others in black.

Apart from the units, which are in multiples of the conductance quantum  $G_0$  for  $T(E)$  and chosen arbitrarily for  $\Gamma^2(E)$  the agreement in all cases is excellent, which fully justifies to investigate the absence or occurrence of DQI solely in terms of the contributions entering Eq. (6).

From both  $T(E)$  and  $\Gamma^2(E)$ , the m-connection is correctly identified as the only one with DQI for benzene (Fig. 3(a)) and zero conductance found only for the open form of DNE (Fig. 3(b)), a result which needs the inclusion of all MOs and not just the frontier orbitals<sup>36</sup> as we will further argue below.

Also for DTE (Fig. 3(c)), only the open form exhibits a transmission zero at  $E_F$  for the analog alternant hydrocarbons (right two panels), which is shifted to higher energies if the S atoms are included in the calculations (left two panels) but still lowers the conductance at the Fermi energy in its vicinity quite substantially even then.

For azulene (Fig. 3(d)) there are QI minima across the energy spectrum for the two investigated junctions which differ in their respective contact sites. But while contacts in the 5, 7-positions (red lines) result in zero conductance, the minima for the 1, 3-connected system are not only lying above  $E_F$  but are also so narrow that they do not seem to have an impact on  $T(E_F)$ .

We note that all these features we summarized here are in good qualitative agreement with the respective NEGF-DFT

calculations in the literature we referred to in Sec. III C when introducing the respective molecular structures above.

In Fig. 4 we demonstrate the application of the graphical AO scheme<sup>30,31</sup> for all the systems in Fig. 2 without hetero atoms and its predictions for DQI identify the cases with  $T(E_F) = 0$  in the calculations shown in Fig. 3 without a single failure, regardless of whether the molecular topology belongs to an alternant or non-alternant hydrocarbon or which subset of carbon atoms in relation to the “starring” scheme the electrodes are connected to.

In principle, it would also be possible to account for the presence of hetero atoms within the scheme as it has been done elsewhere<sup>32,49</sup> for a treatment of DTE containing its sulfur sites but this would come at the price of diminishing the scheme’s simplicity and would not provide any important arguments for the present discussion.

This AO scheme considers all orbitals in an AO representation and relies on the structure of the entire Hamiltonian thereby strongly reflecting the respective molecular topology. This is in contrast to any frontier orbital approximation within a MO based scheme where by definition all but two MOs are disregarded. The pairing theorem justifies this omission for the specific case, where each CR pair defined by the respective equal distance of its parts to  $E_F$  cancels out individually for symmetry reasons. For the other cases where interference is constructive within each pair, DQI can still occur due to cancellation between pairs. This is why all MO contributions are significant in this latter case as we will further explore below.

#### E. Convergence with respect to the number of included CR pairs of MOs

Independently of the frontier orbital approximation as we discuss it in this article, there is the common conception in the studies of the conductance of single molecule junctions that  $T(E_F)$  is dominated by the MOs close to  $E_F$  since the tails of the peaks further apart decay rapidly and their contributions can therefore safely be disregarded.<sup>48,67</sup>

This assumption is also motivated by the fact that the respective distance of each MO to the Fermi energy enters its respective term in Eqs. (4) and (6) explicitly in the denominator and its increase can therefore be expected to reduce the terms significance.

There are two reasons why such preconceptions should be questioned regarding their validity in general: (i) While it is true that the denominator of a term in Eqs. (4) and (6) increases for high values of  $\epsilon_m$ , this effect might be outweighed by large couplings or large MO amplitudes at the contact sites; (ii) the distinction between the occurrence and absence of DQI is often one between an exact value of zero (at least in the framework of TB where only  $\pi$  electrons are considered) and a rather small number which appears to be bigger than it actually is due to the logarithmic plotting of  $T(E)$ .

In Fig. 5 we increase the number of CR pairs of MOs included in the sum of Eq. (6) for the calculation of  $\Gamma^2(E)$  stepwise for the systems in Fig. 2 which exhibit DQI close to the Fermi level but where this cannot be predicted within a frontier orbital approximation. Here we first consider only the HOMO and the LUMO (label 1), then the HOMO, the LUMO, the HOMO – 1 and the LUMO + 1 (label 2), and so



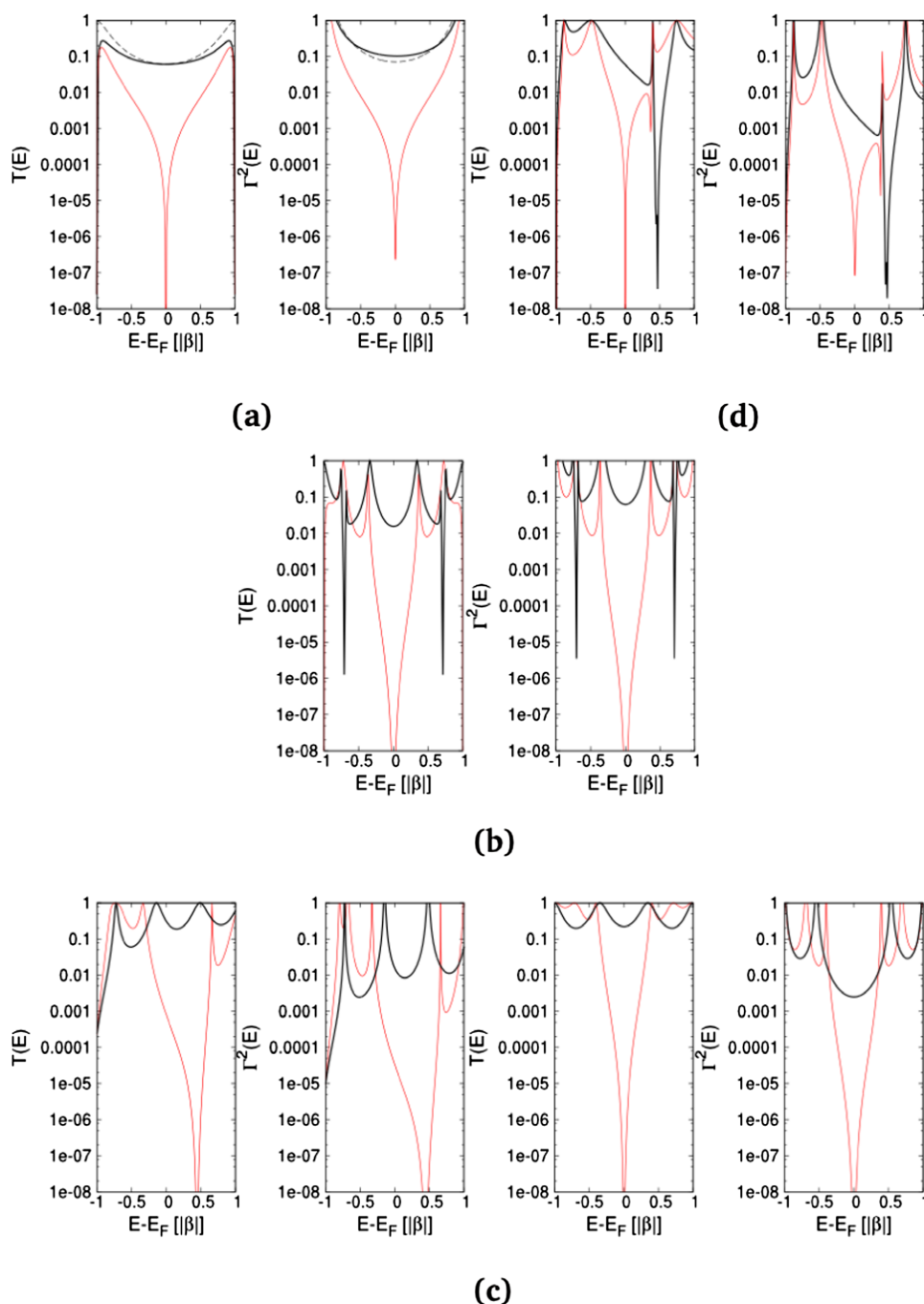


FIG. 3.  $T(E)$  from NEGF-TB calculations (in units of  $G_0$ ) is contrasted with  $\Gamma^2(E)$  as obtained from Eq. (6) (in arbitrary units) for (a) benzene connected in *o*- (solid black), *m*- (solid red), and *p*- (dashed black) positions, (b) DNE and (c) DTE in their open (solid red) and closed (solid black) forms, respectively, where for the latter also curves for the AH analog of DTE with S atoms removed are shown in the two panels at the right side and (d) azulene contacted in 1, 3 (solid black) and 5, 7 (solid red) positions.

on where only the red curve with the highest label includes the contributions from all CR pairs of MOs corresponding to the respective molecular topology.

Quite contrarily to what might be expected, for the open forms of DNE (Fig. 5(a)) and DTE (Figs. 5(b) and 5(c)) the convergence of  $\Gamma^2(E)$  with the number of included pairs is not smooth but oscillating because the contributions of CR pairs of MOs enter with alternating signs. Even for the label with only the CR pair with the energies most remote from  $E_F$  missing, i.e., the labels 10, 4, and 5 for DNE, DTE without and with S, respectively, the conductance is still far from zero on a logarithmic scale. For the label 3 with the three CR pairs of MOs closest to the Fermi energy included it even has a magnitude comparable to that of the conducting closed form of the respective switch, where for DTE the convergence behavior

seems to be rather unaffected by the presence or absence of the S atoms.

This analysis strongly indicates that in order to capture DQI effects for a particular molecular topology correctly really all MOs belonging to its  $\pi$  system need to be properly accounted for in order to achieve a reliable theoretical description. Even for the non-alternant hydrocarbon azulene contacted in (5,7-) positions (Fig. 5(d)), where no destructive but also no constructive interference within each pair can be indicated directly from the pairing theorem, the contributions from the frontier orbitals, i.e., the HOMO and LUMO, alone (label 1) do not result in any DQI feature close to  $E_F$ . The inclusion of the second CR pair of MOs (label 2) produces this feature but it then again needs the contributions from all CR pairs to position it energetically exactly at  $E_F$ .

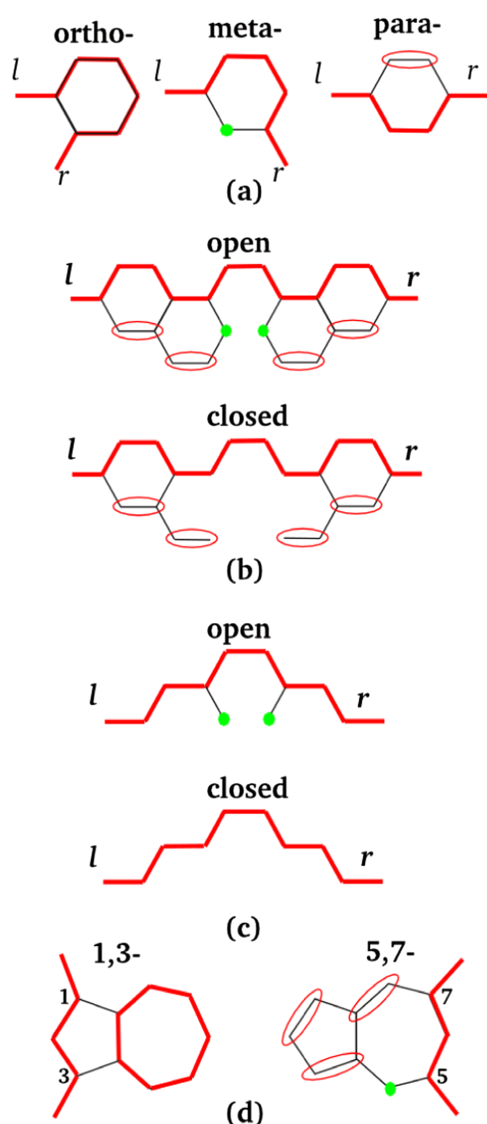


FIG. 4. Application of the graphical AO scheme<sup>30,31</sup> for (a) benzene connected in o-, m-, and p-positions, (b) DNE and (c) DTE (with S atoms removed) in their open and closed forms, respectively, and (d) azulene contacted in 1,3- and 5,7-positions. DQI is predicted if it is not possible to form a continuous line between the two contact sites and have all AOs which are not on this line grouped up in pairs or as part of a closed loop. The single sites which are not crossed or grouped up are marked by green dots for the sake of clarity.

Another property that arises from the pairing theorem is that in the case of DQI for even-membered AHs connected at sites belonging to different subsets, the contributions from all occupied and all unoccupied MOs to  $\Gamma(E)$  in Eq. (6) must each cancel out individually at  $E_F$ . This is because in those cases the contribution from each half of a CR pair is equal to the other half in both sign and magnitude at  $E_F$ , which means that it is then sufficient to consider either all occupied or all unoccupied MOs alone.

Making use of this knowledge, in Fig. 6 we plot  $\Gamma^2(E)$  from the sum over the occupied states in Eq. (6), where we compare taking all the five occupied MOs for the open form of the AH analog of DTE with the S atoms removed (blue curve) with the case where the lowest lying two MOs have been excluded from the summation (magenta curve). As can be seen from the figure, cutting out the lowest lying two MOs does not

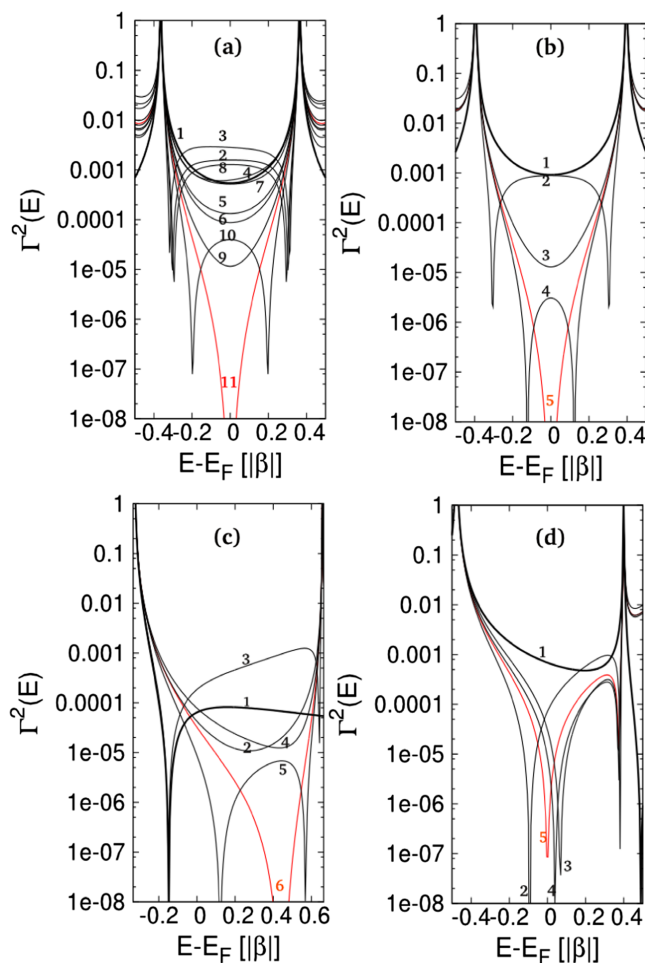


FIG. 5.  $\Gamma^2(E)$  (in arbitrary units) with an increasing number of CR pairs included in Eq. (6) for (a) DNE in its open form, DTE in its open form: (b) without S, (c) with S, and (d) azulene contacted in (5,7-) positions. The label 1 means that only the HOMO and the LUMO enter Eq. (6), for 2 it is the HOMO, the LUMO, the HOMO - 1 and the LUMO + 1, and so on for higher labels up to where all CR pairs are included for the respective highest label. Only the lines with all CR pairs accounted for are shown in red, all other lines are in black.

make any difference in the energy regions of the peaks of the three higher lying MOs because the transmission in the vicinity of a peak is always largely dominated by the contribution of the one MO it is related to, but crucially decides whether DQI occurs at the Fermi level or not.

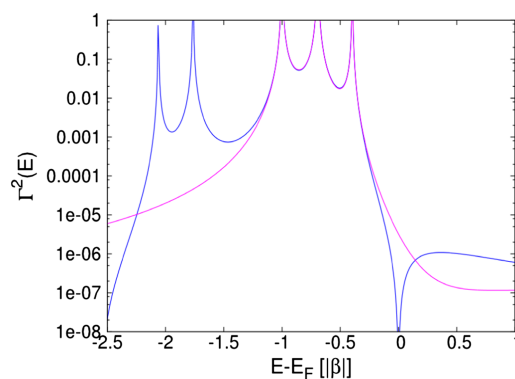


FIG. 6.  $\Gamma^2(E)$ , where  $\Gamma(E)$  is taken as the sum over all the five occupied (blue curve) or only the three occupied MOs closest to  $E_F$  (magenta curve) in Eq. (6) for the open form of the AH analog of DTE with the S atoms removed.

This enforces the main message of our article that in order to identify DQI reliably from a MO perspective, the contribution of all MOs needs to be taken into account and not just a selected few of them. This finding has also high importance for the analysis of NEGF-DFT results, where a cut coupling approach is routinely used to describe DQI in terms of a few MOs close to  $E_F$  only.<sup>48,67</sup>

#### IV. CONCLUSIONS

In summary, we showed that DQI in the electron transport of single molecule junctions can be reliably discussed from a MO perspective if the contributions from all MOs are accounted for and not only those from MOs close to the Fermi level. This applies in general and not only for even-membered alternant hydrocarbons contacted at carbon sites of the same subset as it is the case for predictions within a frontier orbital approximation.

This MO perspective, however, does not in general allow for the prediction of DQI without prior numerical calculations within a TB framework which puts it into contrast to a recently proposed graphical AO scheme<sup>30,31</sup> where such predictions are indeed possible. On the other hand such a MO based analysis is not limited to the prediction of the zero-bias conductance defined by the transmission at the Fermi level and can thus provide essential input for the interpretation of computationally more demanding NEGF-DFT results as well as reconcile findings from single molecule electronics with more traditional concepts from quantum chemistry.

#### ACKNOWLEDGMENTS

X.Z. and R.S. are currently supported by the Austrian Science Fund FWF, Project No. P27272.

- <sup>1</sup>S. Shaik, H. S. Rzepa, and R. Hoffmann, *Angew. Chem., Int. Ed.* **52**, 3020 (2013).
- <sup>2</sup>C. Joachim, J. K. Gimzewski, R. R. Schittler, and C. Chavy, *Phys. Rev. Lett.* **74**, 2102 (1995).
- <sup>3</sup>M. A. Reed, C. Zhou, C. J. Muller, T. P. Burgin, and J. M. Tour, *Science* **278**, 252 (1997).
- <sup>4</sup>J. Reichert, R. Ochs, D. Beckman, H. B. Weber, M. Mayor, and H. v. Lohneysen, *Phys. Rev. Lett.* **88**, 176804 (2002).
- <sup>5</sup>R. H. M. Smit, Y. Noat, C. Untiedt, N. D. Lang, M. C. van Hemert, and J. M. van Ruitenbeek, *Nature* **419**, 906 (2002).
- <sup>6</sup>Y. Meir and N. S. Wingreen, *Phys. Rev. Lett.* **68**, 2512 (1992).
- <sup>7</sup>M. Brandbyge, J. L. Mozos, P. Ordejon, J. Taylor, and K. Stokbro, *Phys. Rev. B* **65**, 165401 (2002).
- <sup>8</sup>Y. Xue, S. Datta, and M. A. Ratner, *Chem. Phys.* **281**, 151 (2002).
- <sup>9</sup>A. R. Rocha, V. M. Garcia-Suarez, S. W. Baily, C. J. Lambert, J. Ferrer, and S. Sanvito, *Nat. Mater.* **4**, 335 (2005).
- <sup>10</sup>K. S. Thygesen and K. W. Jacobsen, *Chem. Phys.* **319**, 111 (2005).
- <sup>11</sup>Y. Öhrn and J. Linderberg, *Phys. Rev.* **139**, A1063 (1965).
- <sup>12</sup>P. Sautet and C. Joachim, *Chem. Phys. Lett.* **153**, 511 (1988).
- <sup>13</sup>C. Patoux, C. Coudret, J. P. Launay, C. Joachim, and A. Gourdon, *Inorg. Chem.* **36**, 5037 (1997).
- <sup>14</sup>M. Mayor, H. B. Weber, J. Reichert, M. Elbing, C. von Hänisch, D. Beckmann, and M. Fischer, *Angew. Chem., Int. Ed.* **42**, 5834 (2003).
- <sup>15</sup>C. A. Coulson and H. C. Longuet-Higgins, *Proc. R. Soc. A* **191**, 39 (1947).
- <sup>16</sup>C. A. Coulson and H. C. Longuet-Higgins, *Proc. R. Soc. A* **192**, 16 (1947).
- <sup>17</sup>C. A. Coulson and H. C. Longuet-Higgins, *Proc. R. Soc. A* **193**, 447 (1948).
- <sup>18</sup>C. A. Coulson and H. C. Longuet-Higgins, *Proc. R. Soc. A* **195**, 188 (1948).
- <sup>19</sup>B. H. Chirgwin and C. A. Coulson, *Proc. R. Soc. A* **201**, 196 (1950).
- <sup>20</sup>B. T. Pickup, *Philos. Mag. B* **69**, 799 (1994).
- <sup>21</sup>T. Stuyver, S. Fias, F. De Proft, P. W. Fowler, and P. Geerlings, *J. Chem. Phys.* **142**, 094103 (2015).
- <sup>22</sup>T. Stuyver, S. Fias, F. De Proft, and P. Geerlings, *Chem. Phys. Lett.* **630**, 51 (2015).
- <sup>23</sup>T. Stuyver, S. Fias, F. De Proft, and P. Geerlings, *J. Phys. Chem. C* **119**, 26390 (2015).
- <sup>24</sup>Y. Tsuji, R. Hoffmann, M. Strange, and G. C. Solomon, *Proc. Natl. Acad. Sci. U. S. A.* **113**, E413 (2016).
- <sup>25</sup>S. Datta, *Electronic Transport in Mesoscopic Systems* (Cambridge University Press, Cambridge, UK, 1995).
- <sup>26</sup>D. Z. Manrique, C. Huang, M. Baghernejad, X. Zhao, O. A. Al-Owaedi, H. Sadeghi, V. Kaliginedi, W. Hong, M. Gulcur, T. Wandlowski, M. R. Bryce, and C. J. Lambert, *Nat. Commun.* **6**, 6389 (2015).
- <sup>27</sup>M. G. Reuter and T. Hansen, *J. Chem. Phys.* **141**, 181103 (2014).
- <sup>28</sup>R. Stadler, M. Forshaw, and C. Joachim, *Nanotechnology* **14**, 138 (2003).
- <sup>29</sup>R. Stadler and T. Markussen, *J. Chem. Phys.* **135**, 154109 (2011).
- <sup>30</sup>R. Stadler, S. Ami, M. Forshaw, and C. Joachim, *Nanotechnology* **15**, S115 (2004).
- <sup>31</sup>T. Markussen, R. Stadler, and K. S. Thygesen, *Nano Lett.* **10**, 4260 (2010).
- <sup>32</sup>T. Markussen, R. Stadler, and K. S. Thygesen, *Phys. Chem. Chem. Phys.* **13**, 14311 (2011).
- <sup>33</sup>R. Stadler, *Nano Lett.* **15**, 7175 (2015).
- <sup>34</sup>K. G. L. Pedersen, A. Borges, P. Hedegård, G. C. Solomon, and M. Strange, *J. Phys. Chem. C* **119**, 26919 (2015).
- <sup>35</sup>K. Yoshizawa, T. Tada, and A. Staykov, *J. Am. Chem. Soc.* **130**, 9406 (2008).
- <sup>36</sup>Y. Tsuji, A. Staykov, and K. Yoshizawa, *Thin Solid Films* **518**, 444 (2009).
- <sup>37</sup>Y. Tsuji, A. Staykov, and K. Yoshizawa, *J. Phys. Chem. C* **113**, 21477 (2009).
- <sup>38</sup>X. Li, A. Staykov, and K. Yoshizawa, *J. Phys. Chem. C* **114**, 9997 (2010).
- <sup>39</sup>Y. Tsuji, A. Staykov, and K. Yoshizawa, *J. Am. Chem. Soc.* **133**, 5955 (2011).
- <sup>40</sup>K. Yoshizawa, *Acc. Chem. Res.* **45**, 1612 (2012).
- <sup>41</sup>J. H. Van Vleck and A. Sherman, *Rev. Mod. Phys.* **7**, 167 (1935).
- <sup>42</sup>C. A. Coulson and G. S. Rushbrooke, *Math. Proc. Cambridge Philos. Soc.* **36**, 193 (1940).
- <sup>43</sup>I. Gutman and O. E. Polansky, *Mathematical Concepts in Organic Chemistry* (Springer, 1986), pp. 57–58, ISBN: 978-3-642-70984-5.
- <sup>44</sup>S. Larsson, *J. Am. Chem. Soc.* **103**, 4034 (1981).
- <sup>45</sup>M. A. Ratner, *J. Phys. Chem.* **94**, 4877 (1990).
- <sup>46</sup>G. Kastlunger and R. Stadler, *Phys. Rev. B* **89**, 115412 (2014).
- <sup>47</sup>P. Sautet and M.-L. Bocquet, *Phys. Rev. B* **53**, 4910 (1996).
- <sup>48</sup>R. Stadler, *Phys. Rev. B* **80**, 125401 (2009).
- <sup>49</sup>M. H. Garner, G. C. Solomon, and M. Strange, *J. Phys. Chem. C* **120**, 9097 (2016).
- <sup>50</sup>R. Stadler, *J. Phys.: Conf. Ser.* **61**, 1097 (2007).
- <sup>51</sup>K. G. L. Pedersen, M. Strange, M. C. Leijnse, P. Hedegård, G. C. Solomon, and J. Paaske, *Phys. Rev. B* **90**, 125413 (2014).
- <sup>52</sup>M. Strange, J. S. Seldenthuis, C. J. O. Verzijl, J. M. Thijssen, and G. C. Solomon, *J. Chem. Phys.* **142**, 084703 (2015).
- <sup>53</sup>Y. Tsuji, R. Hoffmann, R. Movassagh, and S. Datta, *J. Chem. Phys.* **141**, 224311 (2014).
- <sup>54</sup>P. Sautet and C. Joachim, *Phys. Rev. B* **38**, 12238 (1988).
- <sup>55</sup>S. R. Bahn and K. W. Jacobsen, *Comput. Sci. Eng.* **4**, 56 (2002).
- <sup>56</sup>See <https://wiki.fysik.dtu.dk/gpaw/exercises/transport/transport.html> for a description of electron transport within ASE.
- <sup>57</sup>See <http://www.hulis.free.fr/> for obtaining MO energies and amplitudes from topological models.
- <sup>58</sup>S. J. van der Molen and P. Liljeroth, *J. Phys.: Condens. Matter* **22**, 133001 (2010).
- <sup>59</sup>M. Irie, *Chem. Rev.* **100**, 1685 (2000).
- <sup>60</sup>K. Matsuda and M. Irie, *J. Am. Chem. Soc.* **122**, 7195 (2000).
- <sup>61</sup>S. Frayssé, C. Coudret, and J. P. Launay, *Eur. J. Inorg. Chem.* **2000**, 1581.
- <sup>62</sup>D. Dulić, S. J. van der Molen, T. Kudernac, H. T. Jonkman, J. J. D. de Jong, T. N. Bowden, J. van Esch, B. L. Feringa, and B. J. van Wees, *Phys. Rev. Lett.* **91**, 207402 (2003).
- <sup>63</sup>C. Van Dyck, V. Geskin, A. J. Kronemeijer, D. M. de Leeuw, and J. Cornil, *Phys. Chem. Chem. Phys.* **15**, 4392 (2013).
- <sup>64</sup>Y. Tsuji and R. Hoffmann, *Angew. Chem., Int. Ed.* **53**, 4093 (2014).
- <sup>65</sup>J. Xia, B. Capozzi, S. Wei, M. Strange, A. Batra, J. R. Moreno, R. J. Amir, E. Amir, G. C. Solomon, L. Venkataraman, and L. M. Campos, *Nano Lett.* **14**, 2941 (2014).
- <sup>66</sup>F. Schwarz, M. Koch, G. Kastlunger, K. Venkatesan, H. Berke, R. Stadler, and E. Lörtscher, *Angew. Chem., Int. Ed.* **55**, 11781 (2016).
- <sup>67</sup>C. M. Gudon, H. Valkenier, T. Markussen, K. S. Thygesen, J. C. Hummelen, and S. J. van der Molen, *Nat. Nanotechnol.* **7**, 305 (2012).

## Quantum interference in coherent tunneling through branched molecular junctions containing ferrocene centers

Xin Zhao,<sup>1</sup> Georg Kastlunger,<sup>1,2</sup> and Robert Stadler<sup>1,\*</sup>

<sup>1</sup>*Institute for Theoretical Physics, TU Wien—Vienna University of Technology, Wiedner Hauptstrasse 8-10, A-1040 Vienna, Austria*

<sup>2</sup>*School of Engineering, Brown University, Providence, Rhode Island 02912, USA*

(Received 20 March 2017; revised manuscript received 9 June 2017; published 15 August 2017)

In our theoretical study where we combine a nonequilibrium Green's function approach with density functional theory we investigate branched compounds containing ferrocene moieties in both branches which, due to their metal centers, are designed to allow for asymmetry induced by local charging. In these compounds the ferrocene moieties are connected to pyridyl anchor groups either directly or via acetylenic spacers in a metaconnection, where we also compare our results with those obtained for the respective single-branched molecules with both meta- and paraconnections between the metal center and the anchors. We find a destructive quantum interference (DQI) feature in the transmission function slightly below the lowest unoccupied molecular orbital, which dominates the conductance even for the uncharged branched compound with spacer groups inserted. In an analysis based on mapping the structural characteristics of the range of molecules in our article onto tight-binding models, we identify the structural source of the DQI minimum as the through-space coupling between the pyridyl anchor groups. We also find that local charging in one of the branches changes the conductance only by about one order of magnitude, which we explain in terms of the spatial distributions of the relevant molecular orbitals for the branched compounds.

DOI: [10.1103/PhysRevB.96.085421](https://doi.org/10.1103/PhysRevB.96.085421)

### I. INTRODUCTION

Molecular electronics has become an active field of research in recent decades, since it holds the promise of maintaining continuous progress in the miniaturization of digital devices, thereby overcoming the limitations of semiconductor technology [1,2]. One enabling tool for this purpose can be found in destructive quantum interference (DQI) effects [3,4], which can significantly reduce the conductance in some conjugated  $\pi$  systems, where this purely electronic effect has also been shown to be robustly observable at room temperature [5]. For such hydrocarbon molecules a graphical atomic orbital (AO) scheme [6–10] as well as molecular orbital (MO)-based rules [11–16] could be derived to predict the occurrence of DQI from the molecular structure, where the relation between the two schemes has been clarified recently [17]. Such simplified schemes allow for the design of logical gates [6] and memory cells [18] in single-molecule electronics as well as the implementation of thermoelectric devices [19,20].

Also, the constructive quantum interference (CQI) expected in electron transport through branched molecular compounds has gained attention, where a deviation from the classical Kirchhoff's law was first predicted theoretically [21] and then confirmed experimentally [22,23] for junctions containing molecules providing symmetrically equivalent pathways through two of their branches. Recently, the design and synthesis of branched compounds containing ferrocene moieties in each branch have been presented [24] for the purpose of creating single-molecule junctions, where the combination of QI effects with redox gating for coherent electron tunneling as well as the electrostatic correlation between spatially distinct redox centers for electron hopping [25] can be explored.

The latter electrostatic interactions between multiple ferrocene-based redox centers within the same compound have been observed in an unrelated study [26]. Ferrocene moieties in junctions with linear molecules [27] have also been used for the design of molecular diodes [28–30], highly conducting molecular wires [31], and redox-gated molecular switches [32], where the switching between a low-conductance reduced state and a high-conductance oxidized state was due to stochastic fluctuations between these two redox states induced by the gate. The details of the mechanism for this type of switching have recently been explored in joint experimental and theoretical studies on a Mo compound [33,34] and azulene [35], where the  $I/V$  curves measured in a mechanically controlled break junction setup were also reproduced by simulations based on density functional theory (DFT).

The novelty of the molecular design in Ref. [24] lies in bringing all these structural aspects together in a single molecule, which could, in principle, allow to combine redox-gated fluctuations of the electron population at ferrocene moieties as a switching mechanism between two redox states, where DQI effects would guarantee a very low conductance for one of them, and their absence a significantly higher conductance for the other one. A similar idea for a redox-gated switch, where one state of the redox pair was designed to exhibit DQI effects, has recently been pursued with anthraquinone derivatives but the on/off ratios were found to be rather modest, since DQI occurred rather far in energy from the Fermi level ( $E_F$ ) in the transmission function [36]. Although the synthesis part in Ref. [24] focused on branched compounds where both branches were to be attached on a substrate separately and only connected intramolecularly by a pyridyl anchor group on the end to be contacted by the tip of a scanning tunneling microscope, the authors stated in their conclusions that efforts towards cyclic analogs of these molecules such as the one shown in Fig. 1 were under way.

\*robert.stadler@tuwien.ac.at



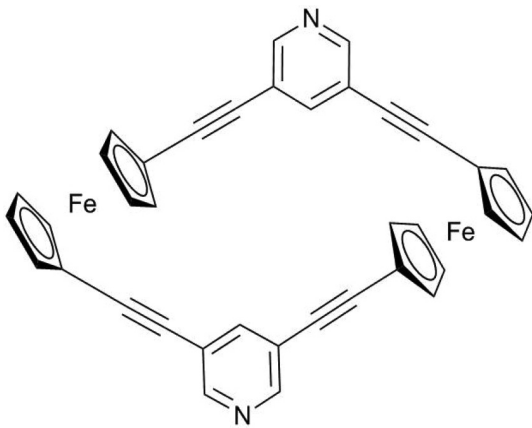


FIG. 1. Cyclic molecule containing a ferrocene moiety in each of its two branches, where they have been separated from the pyridyl anchor groups by acetylenic spacer groups.

Such cyclic analogs are of particular interest in the context described above, since as pointed out in Ref. [22], QI effects can only be expected to play a dominant role for electron transport if both sides of a branched molecule are connected to electrodes by a common intramolecular node. For the molecule in Fig. 1 in its neutral state the transmission through both branches is expected to interfere constructively, because the branches are symmetry equivalent [21–23]. If one of the two ferrocene moieties is oxidized, however, this symmetry will be broken thereby possibly enabling a DQI-induced suppression of the conductance. In that case the compound in Fig. 1 could be used as a molecular redox switch with very high on/off ratios. In the molecular design the acetylenic spacers are meant to make the molecular structure more rigid and to increase the distance between the two electrodes for the prevention of through-vacuum tunneling and for the separation of the redox-active centers from the leads. The pyridyl anchor groups were chosen because they were found to provide the best junction formation and conductance properties in recent experimental [37] and theoretical [38–41] studies.

In our article we investigate the coherent electron transport through the molecule in Fig. 1 by means of DFT calculations in combination with a nonequilibrium Green’s function (NEGF) formalism [42], where we put an emphasis on DQI effects in neutral and charged compounds. Because of the presence of the ferrocene moieties in the compound neither the graphical AO scheme nor the MO rules mentioned above can be applied for this purpose, since both have been designed exclusively for the study of  $\pi$  conjugated hydrocarbons [17], which is also true for the quantum circuit rules derived in Ref. [43]. In the present case, however, DQI can arise (i) from the metaconnection [44–46] of the branches to the pyridyl anchor group, although it has recently been demonstrated that for meta-connected bipyridine DQI in the  $\pi$ -electron contribution can be masked by the conductance mediated by  $\sigma$  electrons [47]; (ii) from interference between transmission through the two branches, which is expected to be constructive for the neutral molecule but might be destructive if the redox-active center on only one of the branches is oxidized; and (iii) from multiple paths provided by nearly degenerate orbitals on the

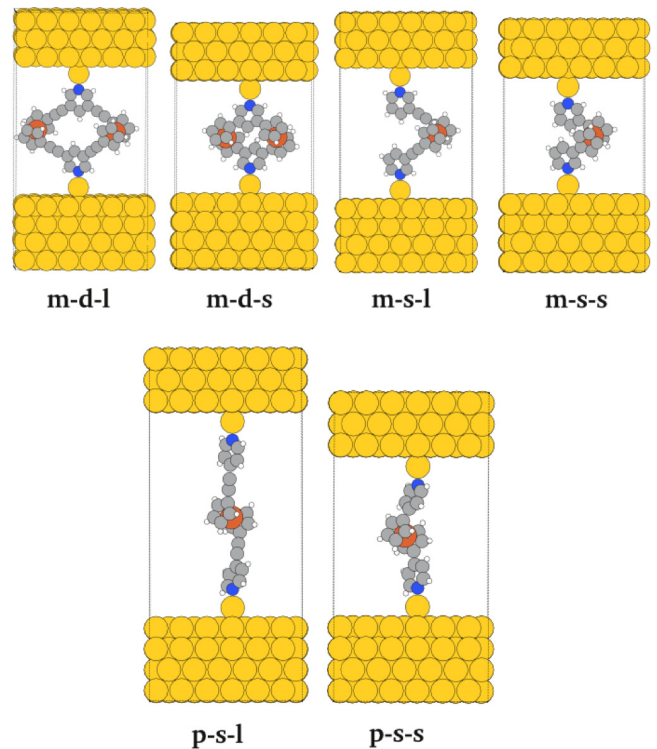


FIG. 2. Junction geometries for the compounds we investigate in this article. m-d-l (meta-double-long) denotes the molecule in Fig. 1; m-d-s (meta-double-short), the same molecule without the acetylenic spacer groups; m-s-l (meta-single-long) and m-s-s (meta-single-short), the corresponding single-branched compounds; and p-s-l (para-single-long) and p-s-s (para-single-short), their respective counterparts with a para-connection to the pyridyl anchor groups. All molecules have been connected to fcc Au electrodes on (111) surfaces with an adatom on each lead.

ferrocene moieties. In order to be able to distinguish these effects we extend our study to the range of molecular junctions illustrated in Fig. 2, where, derived from the compound in Fig. 1, we also chose molecules without acetylenic spacers, with only one branch between the pyridyl anchor groups and with paraconnections for the single-branched systems.

The paper is organized as follows: In the next section we present transmission functions from NEGF-DFT [48–51] calculations for all junctions in Fig. 2 and discuss their characteristic features. There we find that DQI occurs for neutral compounds in the energy region of the lowest unoccupied MO (LUMO) close to the Fermi level, with a strong impact on the conductance only for molecules with branches connected in metaconnections at the pyridyl anchors with respect to their N atom and containing acetylenic spacers regardless of the number of branches, i.e., for the compounds we refer to as m-d-l and m-s-l in the caption to Fig. 2. In Sec. III we derive topological tight-binding (TB) models from the DFT calculations and identify the through-space coupling between the pyridyl anchor groups, which depends on both the meta-versus paraconnectivity and the presence or absence of spacer groups as the defining quantity for the DQI effects we observe. In Sec. IV we assess the usefulness of the double-branched systems m-d-l and m-d-s in Fig. 2 as molecular switches

by explicitly putting a positive charge on one of the two branches in our NEGF-DFT calculations and comparing the resulting conductance with that of the respective neutral compound. We conclude with a brief summary of our results in Sec. V.

## II. DFT-BASED ELECTRON TRANSPORT CALCULATIONS AND MOLECULAR ORBITALS FOR NEUTRAL COMPLEXES

### A. Computational details for NEGF-DFT calculations

We obtained the transmission functions  $T(E)$  for all junctions in Fig. 2 from NEGF-DFT calculations performed with the GPAW code [52,53] using a linear combination of atomic orbitals (LCAO) [54] for the basis set on a double-zeta level with polarization functions (DZP), a Perdew-Burke-Ernzerhof (PBE) parametrization for the exchange correlation (XC) functional [55], and a grid spacing of 0.2 Å for the sampling of the potential in the Hamiltonian on a real-space grid. In our transport calculations, the “extended molecule” defining the scattering region is formed by the respective metal organic compounds and three and four layers for the upper and lower fcc gold electrodes, respectively, in a (111) orientation and with a  $6 \times 6$  overstructure defining the periodically repeated unit cell, where the distance between the Au adatom attached to the lead surfaces and the N atom of the pyridyl anchor groups was chosen as 2.12 Å [38] and a  $k$ -point sampling corresponding to a  $4 \times 4 \times 1$  Monkhorst Pack grid for evaluating  $T(E)$ , where

the  $z$  coordinate is the direction of electron transport through the junction.

### B. Transmission functions from NEGF-DFT and the observation of DQI

In the resulting transmission functions in Fig. 3 the peaks in the LUMO region are much broader than those in the HOMO region for all systems, and hence we expect the conductance to be dominated by the MOs above the Fermi level. DQI-induced minima in the energy region at the upper border of the HOMO-LUMO gap can be observed only for metaconnected molecules with acetylenic spacers regardless of the number of branches but this feature disappears when the spacers are removed or when the connection of the ferrocene moieties to the pyridyl anchors is in a para position. We note that these minima in  $T(E)$  in the LUMO region for the compounds m-d-l and m-s-l do not result in zero conductance accompanied by the typical DQI shape known from topological models [17] but rather in a distinct deviation from Lorentzian decay around the LUMO peaks, which lowers the conductance significantly and has been encountered in molecules with metaconnected pyridyl anchors also in Ref. [43].

These less distinctly visible manifestations of DQI can occur in DFT calculations for real systems, because DQI is linked to the symmetry properties of  $\pi$  electrons of a conjugated system, where  $\sigma$  electrons are not necessarily affected [47]. Our definition of DQI is that the transmission through a system with more than one MO around  $E_F$  is lower

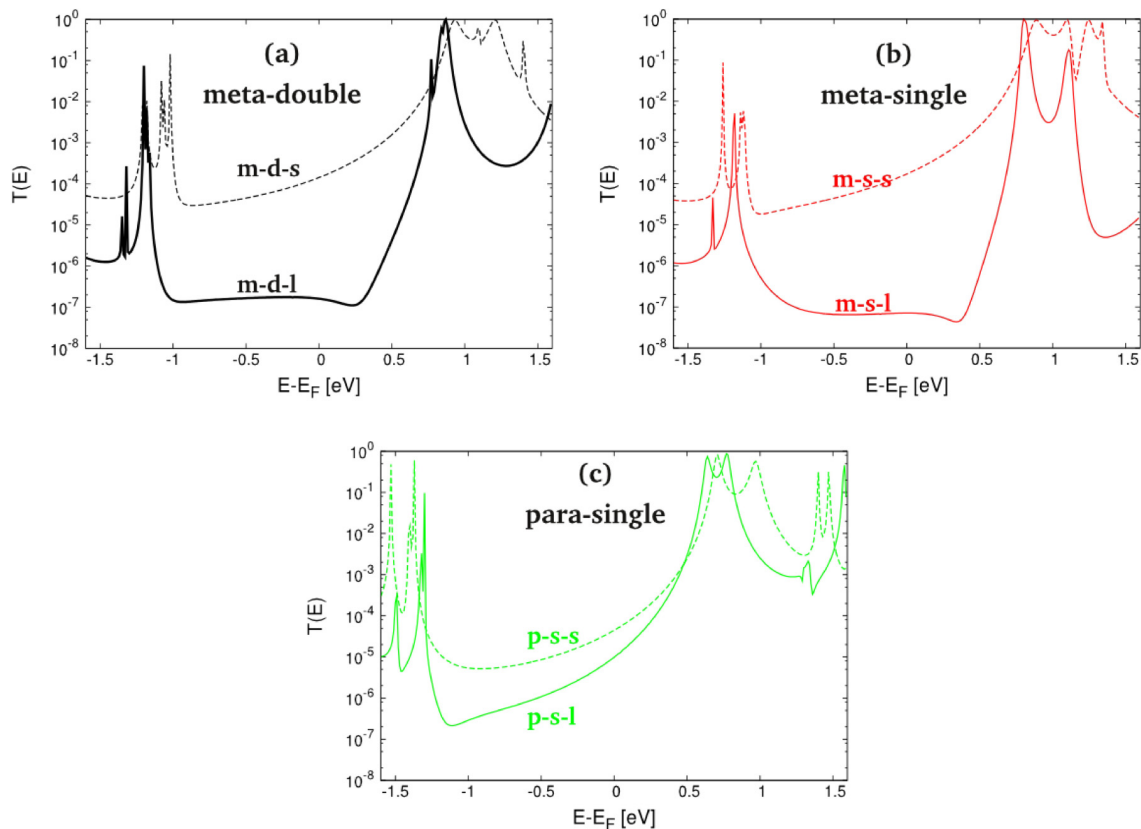


FIG. 3. Transmission functions calculated from the NEGF-DFT for the six junctions in Fig. 1. (a) m-d-l, solid black line; m-d-s, dashed black line. (b) m-s-l, solid red line; m-s-s, dashed red line. (c) p-s-l, solid green line; p-s-s, dashed green line.

than the sum of the individual contributions of these MOs to  $T(E)$  [40]. The exact energetic position of the Fermi energy within the HOMO-LUMO gap, which is also affected by the underestimation of this gap in our calculations due to the PBE parametrization of the XC functional, will have a crucial impact on the quantitative conductance, but qualitatively DQI will always result in a significant conductance lowering for the structures where it occurs regardless of the details of the Fermi level alignment [17].

### C. General remark on CQI for the branched molecules

From the circuit laws derived for branched molecules with two equivalent branches [21,22], one would expect that due to constructive QI the conductance of the molecules would be roughly four times as large as the respective value for the single-branched analog. While for molecules containing acetylenic spacers we indeed find a ratio greater than 2 between the respective transmission functions of m-d-l and m-s-l at  $E_F$  in Fig. 3, this is distinctly not the case for m-d-s and m-s-s, where the conductance of the single-branched system is even slightly higher than that found for the double-branched compound. In Refs. [4,21] it was pointed out that the circuit laws for CQI only apply when the branches are rather weakly coupled to the nodal point in comparison with the nodal point's electronic connection to the electrodes. In our case, however, the coupling between the ferrocene moieties and the pyridyl anchors is larger than the coupling between the anchors and the leads. In the experimental evaluation of the circuit laws for CQI in Ref. [23] it was also found that the observability of these laws strongly depends on the chemical nature of both the anchors and the branches as well as on the atomistic details of the surface structure the respective compounds are attached to.

### D. Molecular orbital analysis

In Figs. 4 and 5 we plot the spatial distributions of the MOs for the double-branched compounds directly above (Fig. 4) and directly below (Fig. 5) the Fermi energy, which we obtain from a subdiagonalization of the molecular part of the transport Hamiltonian [41]. In Table I the corresponding eigenenergies are listed for all six junctions in Fig. 2, where the lists are complete for the energy range  $-2 \text{ eV} < E_F < 1.5 \text{ eV}$  and the shapes of MOs for the single-branched systems share

TABLE I. Eigenenergies  $\epsilon_{\text{MO}}$  (in eV) for the four MOs above  $E_F$  (LUMO,...,LUMO + 3) for all compounds in Fig. 3 and the three MOs below  $E_F$  (HOMO,...,HOMO - 2) for one of the two branches. For m-d-l and m-d-s the values for the respective second branch are given in parentheses.

	m-d-l	m-d-s	m-s-l	m-s-s	p-s-l	p-s-s
L + 3	0.85	1.39	1.08	1.33	1.32	1.46
L + 2	0.81	1.17	1.06	1.21	1.28	1.39
L + 1	0.79	1.09	0.78	1.07	0.70	0.91
L	0.76	0.86	0.76	0.81	0.57	0.64
H	-1.16 (-1.20)	-1.02 (-1.06)	-1.18	-1.12	-1.30	-1.37
H - 1	-1.18 (-1.21)	-1.02 (-1.08)	-1.19	-1.14	-1.32	-1.41
H - 2	-1.32 (-1.35)	-1.18 (-1.21)	-1.33	-1.26	-1.49	-1.53

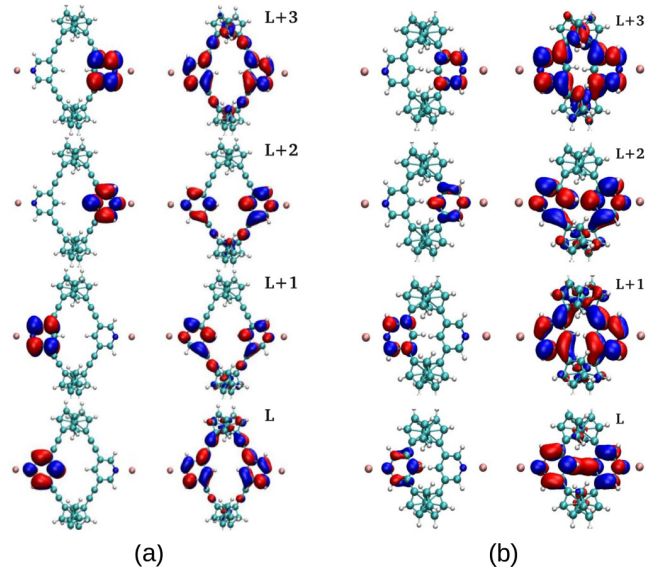


FIG. 4. Spatial distributions of the four MOs directly above  $E_F$  (LUMO,...,LUMO + 3) for the branched compounds (a) m-d-l and (b) m-d-s; the two FOs on each pyridyl anchor defining them are shown in the left columns, and the four MOs themselves in the right columns.

the same localization patterns with those plotted for the double-branched molecules in Figs. 4 and 5. For the LUMO region all four MOs are mostly localized on the pyridyl anchor groups (Fig. 4), which explains the broad peaks found for all junctions in  $T(E)$  above  $E_F$  (Fig. 3). Furthermore, visual inspection allows us to identify these four MOs as bonding or antibonding pairs resulting from the hybridization of just two pyridyl fragment orbitals (FOs), which were again obtained from a subdiagonalization of the respective transport Hamiltonian, but in this case limited to the basis functions centered on the pyridyl groups.

The MOs below  $E_F$  on the other side (Fig. 5) are all mostly localized on the ferrocene moieties as hybrids of Fe d states

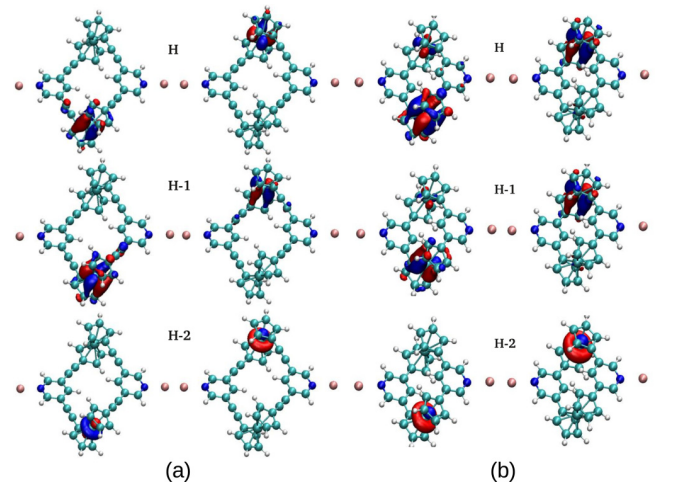


FIG. 5. Spatial distributions of the six MOs directly below  $E_F$  (HOMO,...,HOMO - 5) for the branched compounds (a) m-d-l and (b) m-d-s; the notation we use here (H,...,H - 2) refers to each branch individually.



and the  $\pi$  system of their cyclopentadienyl rings. As a result we observe rather narrow peaks of  $T(E)$  in the HOMO region (Fig. 3) at all junctions. For the double-branched compounds, these six MOs can be clearly separated into three on each branch, suggesting that our initial concept of introducing a positive charge at one ferrocene center for the creation of an asymmetry resulting in DQI might work for  $T(E)$  in the HOMO region. It is, however, not likely to be applicable in the LUMO region since the localization patterns in the pyridyl anchors cannot be expected to be affected in an asymmetric way by the charging of one ferrocene moiety. In order to evaluate the validity of this first assessment further, NEGF-DFT calculations with explicitly charged ferrocene centers are presented in Sec. IV.

Since both the shapes and the eigenenergies (as listed in Table I) of all MOs are quite similar for the six junctions in Fig. 2, it cannot be directly derived from these properties why a DQI feature occurs in  $T(E)$  in the LUMO region for compounds m-s-l and d-s-l but not for the other four molecules in Fig. 3. It might be expected that the number of branches does not make a difference here because the existence of the second branch should induce CQI but not DQI without the charging of a ferrocene center [21–23]. It also seems intuitive that molecules, where ferrocene is connected to the pyridyl anchors in metaconnections exhibit DQI, while the para-analog does not but this intuition is only based on the observations made for planar  $\pi$ -conjugated hydrocarbons [44,45], while the six compounds in Fig. 2 are not planar and contain ferrocene moieties. Most strikingly, there is no easy explanation for the dependence of the DQI feature on the absence or presence of acetylenic spacers. In order to investigate these questions further, we project the data we can derive from NEGF-DFT calculations onto topological TB models in Sec. III.

### III. INVESTIGATION OF THE STRUCTURAL SOURCES OF DQI WITH TB MODELS

All conventional topological TB models and the various sets of QI or quantum circuit rules derived from such models have been developed for planar  $\pi$ -conjugated hydrocarbons. Also, the simple assertion that metaconnected junctions exhibit DQI, while paraconnected ones do not, can be considered to be a simple case of a QI rule derived from a conventional topological TB model. In such models the molecular structure is replaced by a connectivity matrix where each carbon position is represented by a single AO (presumably the  $p_z$  orbital perpendicular to the plane), where all AOs have the same on-site energy and only next-neighbor couplings are considered. The ferrocene makes both assumptions ambiguous. It cannot be represented by carbon  $p_z$  AOs alone but has degenerate FOs at different energies instead. Additionally, it enforces molecular structures in three dimensions in deviation from planarity, where parts of the molecule not directly bonded to each other can come close to each other in the third dimension and QI can no longer be understood in terms of next-neighbor connectivity alone. As conventional TB models are not applicable for the structures we investigate, we have to derive our own models, which must fulfill two requirements: (i) the qualitative structure dependence of the transmission functions from our DFT calculations needs to be reproduced,

and (ii) the number of orbitals involved at the end needs to be minimal in order to make the key structural source of DQI in our systems discernible. This step-by-step model development is introduced in this section and the applicability of the procedure is not limited to the particular six molecules we investigate but is also given for similar systems.

For double-branched molecules the transmission functions in Fig. 3 have a shape very similar to that of their respective single-branched analogs in the LUMO region in metaconnected cases, and the acetylenic spacers do not seem to have a significant impact on paraconnected anchors other than the well-known decrease in conductance with molecular length. Therefore, we focus our analysis of the relationship between structural features and  $T(E)$  in this section on an evaluation of the differences between compounds m-s-l, m-s-s, and p-s-l.

#### A. Definition of the electrodes for all NEGF-TB calculations

We calculate transmission functions from NEGF-TB with a one-dimensional chain of AOs acting as electrodes, where all inner-electrode on-site energies have been set to 0.83 eV and all inner-electrode couplings to  $-5.67$  eV. This particular choice for the latter two parameters has been identified as optimal for reproducing NEGF-DFT results for  $T(E)$  with fcc Au (111) electrodes in Ref. [40] and is used for all NEGF-TB calculations in the current article. The couplings between the contact atoms of these artificial electrodes and the  $p_z$  orbitals within the pyridyl anchors have been derived by a subdiagonalization of the part of the transport Hamiltonian from the NEGF-DFT calculations describing the gold adatoms on top of the surfaces (see Fig. 2) and taking only the couplings of the valence  $s$  state of this atom to the pyridyl  $p_z$  states because the density of states of the gold surface has a predominantly  $s$  character around  $E_F$ .

#### B. Selection of AOs in the anchor groups and FOs in the ferrocene for reproducing the DFT results

In the first part of this analysis we try to map the structural characteristics of these three molecules onto a topological TB model, with the aim of matching the  $T(E)$  from NEGF-DFT as closely as possible but at the same time minimize the number of involved orbitals. For the pyridyl anchors and acetylenic spacers it can be safely assumed that transport near the HOMO-LUMO gap is dominated by the  $p_z$  AOs at the C and N sites [40]. The DZP-LCAO basis set of the NEGF-DFT calculations, however, does not provide physically meaningful AOs, in particular, atoms in the environment of all neighboring atoms. Hence, we obtained the basis which we need to apply in our TB models by subsequent subdiagonalizations and basis set rotations of the transport Hamiltonian for each C and N atom individually. [47] Additionally, orthogonality between AOs on neighboring atoms was ensured by applying a Löwdin transformation [56]. As it has been demonstrated in the supporting information in Ref. [47] that not only first- but also second- and third-nearest-neighbor couplings within a pyridyl group are crucial for defining the energetic position of a DQI minimum, we include all three categories in our model. For the ferrocene part of the molecules we perform a subdiagonalization of the part of the Hamiltonian covering the



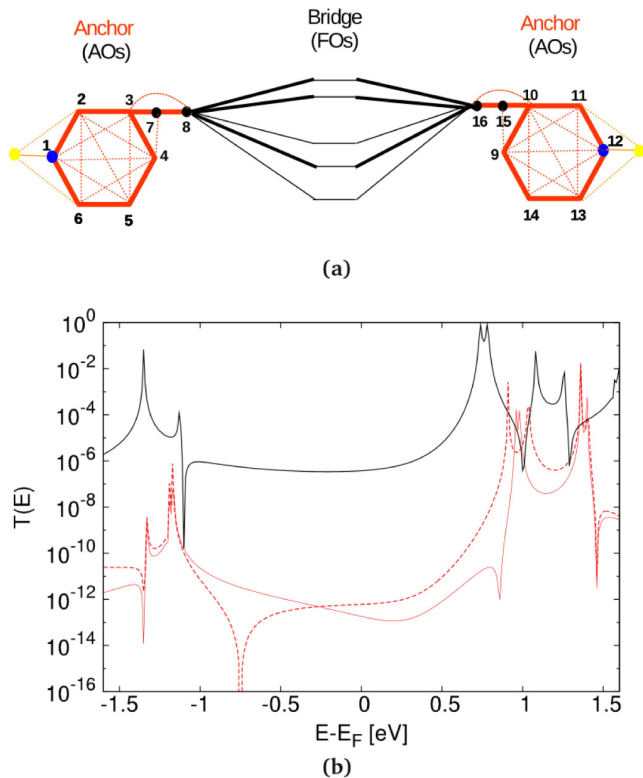


FIG. 6. (a) TB model derived from the NEGF-DFT as exemplified for compound *m-s-l*, where the line colors distinguish between couplings within anchors and spacers (red) and couplings to ferrocene FOs (black) or the gold leads (yellow), respectively, while the line thickness illustrates the hierarchy of the respective coupling strengths. (b)  $T(E)$  from the TB model for *m-s-l*, with (dashed red curve) and without (solid red curve) an artificially high value for the direct coupling, and for *m-s-s* (solid black curve).

whole moiety, which results in just five FOs in the relevant energy range around the HOMO-LUMO gap, namely, three FOs with energies from  $-1.55$  to  $-1.20$  eV in the HOMO region and two FOs with energies from  $1.35$  to  $1.55$  eV in the LUMO region for all three compounds.

In Fig. 6(a) we illustrate this TB model schematically for molecule *m-s-l*; direct couplings between the  $p_z$  orbitals of anchor and spacer groups left and right of the ferrocene are not drawn for the sake of simplicity but still considered in the model.

### C. Identification of the through-space coupling between anchor groups as the structural source of DQI

Since we know that the most distinct structural difference between the *m-s-l* and the *m-s-s* molecules lies in their respective molecular lengths, as brought about by the presence or absence of acetylenic spacers, we show in Fig. 6(b) the  $T(E)$  from NEGF-TB for *m-s-l* in the original parametrization as derived from DFT (solid red line) and with just one parameter changed to the higher value we obtain for *m-s-s* (dashed red line), namely, the direct coupling between AO 4 and AO 9 in Fig. 6(a). Of course, this “artificial” parametrization, which is meant to mimic a key structural aspect of *m-s-s* does not

reproduce the high conductance found for this system in Fig. 3 but it can be clearly seen that just changing this one parameter from the value it has in *m-s-l* to the one it has in *m-s-s* seems to be sufficient to shift the DQI feature so far down in energy that it is no longer observable in the LUMO region. In Fig. 6(b) we also plot the transmission function we obtain from the parameters and topology of compound *m-s-s* (solid black line), which, just like the one for *m-s-l* (solid red line), perfectly reproduces all characteristics found from NEGF-DFT in Fig. 3. The model, however, needs to be simplified further in order to pin down and separate the effects of the most important structural differences between the single-branched molecules.

For that purpose we perform another subdiagonalization of the transport Hamiltonian in the subspace of the eight  $p_z$  AOs on the pyridyl anchors and acetylenic spacers in Fig. 6(a) on each side of the ferrocene center. This results in the FO-TB model in Fig. 7(a), where the five FOs on the ferrocene moiety are the same as in Fig. 6(a) and two FOs on each anchor can be roughly identified by their shape with those shown in Fig. 4(a), albeit they now show some localization on the spacer groups too due to the manner of their definition. From the size of the couplings of the five bridge FOs to these two anchor FOs we can identify the three bridge FOs most relevant for the *m-s-l* molecule, namely, one in the HOMO region and two in the LUMO region as indicated in Fig. 7(a), while for *p-s-l* only the bridge FO lowest in energy in the LUMO region and only the lower lying of the two FOs on the anchors plays a role for the transmission.

Molecules *m-s-l* and *p-s-l* now differ in the FO-TB model in two ways, namely, in the number of FOs on each of the three fragments connected by sizable couplings and in the detailed values for these couplings. Therefore, the question arises whether DQI in  $T(E)$  would still be found for compound *m-s-l* if only the one FO on each fragment also relevant for the *p-s-l* system but with the parameters for *m-s-l* (Fig. 7b) is selected for NEGF-TB calculations with a minimal number of FOs. In Figs. 7(c) and 7(d), we present the results of such calculations. Figure 7(c) shows the  $T(E)$  for molecule *m-s-l* with two anchor FOs on each side and five (solid line), three (dashed line), and one (dotted line) FO on the ferrocene, respectively, and it can be seen that the DQI feature is shifted to the HOMO region if the quality of the FO model is reduced but remains observable. In Fig. 7(d) we choose the same single FO on each fragment setup for compounds *m-s-l* (red curve) and *p-s-l* (green curve) as illustrated in Fig. 7(b), where we come to the somewhat surprising conclusion that DQI is still observed for *m-s-l* but not for *p-s-l*, although the models for the two systems now differ only in the detailed parameters for the couplings between three FOs which have very similar spatial distributions and on-site energies in both cases.

### D. Analysis of the mathematical reasons for the decisive influence of the through-space coupling with a simplified $3 \times 3$ Hamiltonian

In Table II we list the coupling values for  $t_L$ ,  $t_R$ , and  $t_D$  connecting the three FOs in Fig. 7(b) for all three junctions, where the first two parameters do not vary with the molecular structure significantly but the third one does. Having now established that the direct coupling between the two anchor

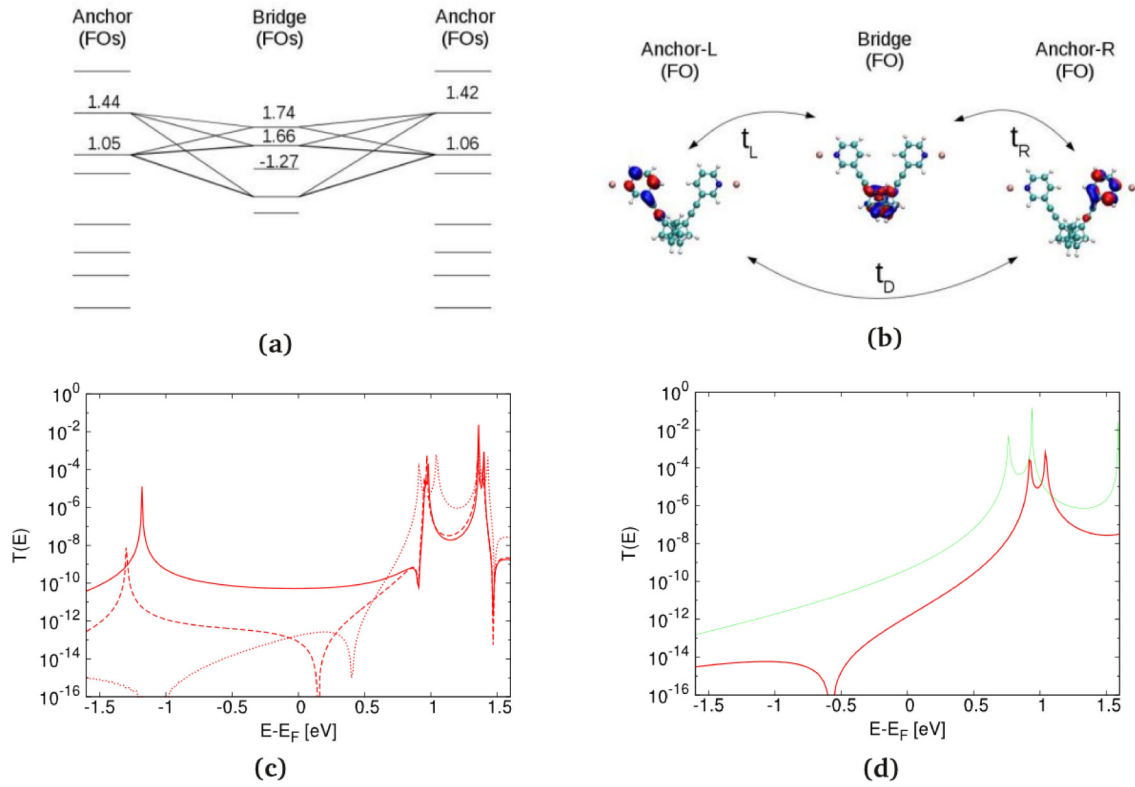


FIG. 7. (a) FO-TB model for molecule m-s-l as described in the text, where the relevant couplings between anchor and bridge states which are all in the range of 0.1–0.2 eV are indicated by lines. (b) Spatial distributions of the anchor FO on each side at 1.05 eV and the ferrocene FO at 1.66 eV. (c)  $T(E)$  as calculated from the NEGF-TB for this model are shown as red lines for two anchor FOs [as marked in (a)] and all five bridge FOs (solid red line), only three bridge FOs [as marked in (a); dashed red line], and only the one bridge FO at 1.66 eV (dotted). (d)  $T(E)$  or compound m-s-l (red line) and p-s-l (green line) for only the one anchor FO on each side and one bridge FO in the middle as plotted in (b).

groups distinguishes the only single-branched system with a DQI feature close to the LUMO, namely, molecule m-s-l, from both compound m-s-s and compound p-s-l, we want to explore the mathematical reasons for the importance of this parameter. We therefore diagonalized a  $3 \times 3$  Hamiltonian with fixed parameters for the three FOs in Fig. 7(b) and plotted the evolution of the resulting three MOs in dependence on  $t_D$  in Fig. 8(a). In Fig. 8(b) we show the transmission functions for selected values of  $t_D$ , which we obtained by making use of Larsson's formula [57],

$$\Gamma(E) = \sum_i \frac{\alpha_i \cdot \beta_i}{E - \varepsilon_i}, \quad (1)$$

where  $\varepsilon_i$  is the eigenenergy of each MO, and  $\alpha_i$  and  $\beta_i$  are its respective couplings to the left and right electrodes.

TABLE II. Couplings connecting the three FOs in Fig. 7(b) for three of the single-branched systems; all values are eV.

	Coupling		
	m-s-l	p-s-l	m-s-s
$t_L$	0.27	-0.23	-0.28
$t_R$	-0.22	0.25	0.22
$t_D$	-0.023	-0.0087	0.033

Larsson's formula was originally introduced for the definition of the transfer integral in the context of Marcus theory for the description of electron hopping [57–59], but recently it has been shown that it can also be used to approximate  $T(E)$  as  $T(E) \sim \Gamma^2(E)$  for coherent tunneling [40,60], where the resulting  $T(E)$  can be normalized [60] and qualitatively reproduces the curves obtained from NEGF-TB [17].

Equation (1) has the additional advantage that a simple mathematical condition can be defined for the energetic positions of DQI-induced zeros in  $T(E)$ , because at the same energies the effective coupling  $\Gamma(E) = \gamma_1/(E - \varepsilon_1) + \gamma_2/(E - \varepsilon_2) + \gamma_3/(E - \varepsilon_3)$  with  $\gamma_i = \alpha_i \beta_i$  for the three MOs resulting from the simple model in Fig. 8 must also be 0. By making use of the specific symmetry properties of the  $3 \times 3$  Hamiltonian in the model, we can impose  $\gamma_1 + \gamma_2 + \gamma_3 = 0$  and obtain

$$E_0 = \varepsilon_1 + \frac{1}{1 + \frac{\gamma_3(\varepsilon_3 - \varepsilon_2)}{\gamma_1(\varepsilon_1 - \varepsilon_2)}}(\varepsilon_3 - \varepsilon_1) = \varepsilon_1 + F_1 F_2 \quad (2)$$

for the energy of the DQI-induced minimum, i.e., the energy  $E_0$  defined by the condition  $T(E_0) = 0$  in our model.

In Eq. (2) the factor  $F_2 = \varepsilon_3 - \varepsilon_1$  is always positive by definition since the indices order the MOs in the sequence of their respective eigenenergies. Therefore, it is the sign of the other factor in the product, namely,  $F_1 = 1/(1 + (\gamma_3/\gamma_1) \cdot ((\varepsilon_3 - \varepsilon_2)/(\varepsilon_1 - \varepsilon_2)))$ , which decides whether the minimum

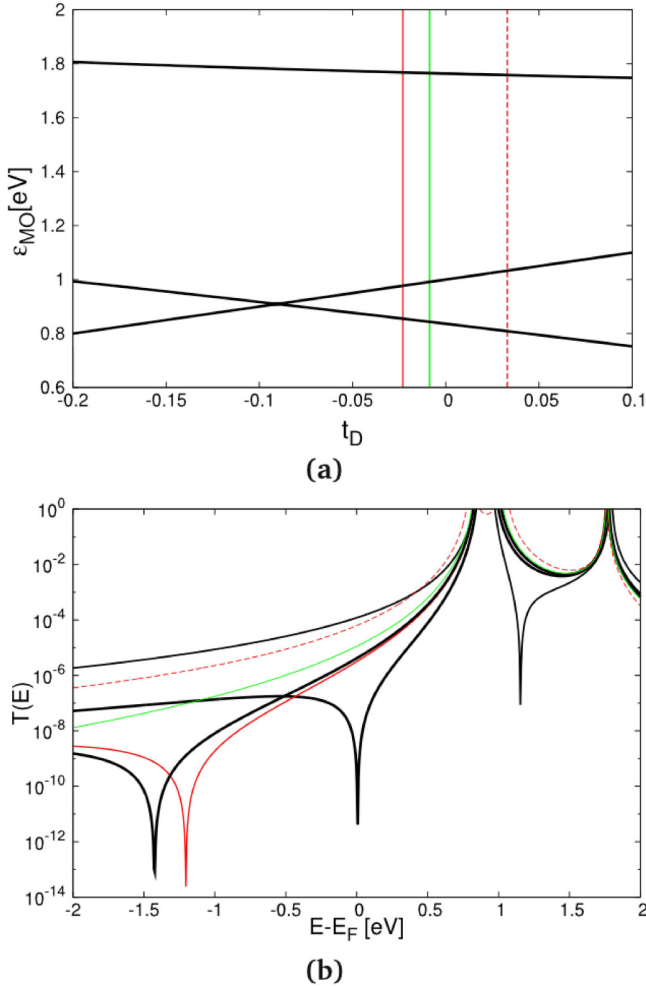


FIG. 8. (a) MO eigenenergies obtained by diagonalizing the  $3 \times 3$  Hamiltonian formed by the three FOs in Fig. 7(b) with  $\epsilon_L = \epsilon_R = 1.0$  eV,  $\epsilon_B = 1.6$  eV,  $t_L = 0.25$  eV,  $t_R = -0.25$ , and  $t_D$  as a variable, where the three vertical lines mark the respective  $t_D$  values of compounds m-s-l (solid red line), p-s-l (solid green line), and m-s-s (dashed red line). (b) Transmission functions calculated from  $\Gamma^2(E)$  for the resulting three MOs for the  $t_D$  values of the three molecules explicitly listed in Table II and highlighted in the colors corresponding to (a) and shown as black lines for  $t_D = -0.14$ ,  $-0.04$ , and  $-0.02$  eV, respectively.

$E_0$  lies to the left or to the right of the LUMO's energy  $\epsilon_1$  on the energy axis. All three compounds discussed in this section have  $t_D$  values to the right of the crossing point between the lower two MO energies in Fig. 8(a), i.e., higher than  $t_D = -0.09$  eV, which we obtain from Table II and list again in Table III. Within this range of  $t_D$ ,  $\gamma_3/\gamma_1$  is always positive and  $F_{\text{splitting}} = (\epsilon_3 - \epsilon_2)/(\epsilon_1 - \epsilon_2)$  always negative, and therefore the product of the latter two factors must always be negative. Hence, the sign of  $F_1$  is determined by whether this product is larger or smaller than 1; we can see from Table III that  $\gamma_3/\gamma_1$  is fairly system independent, while  $F_{\text{splitting}}$  varies widely.

For molecules m-s-l and p-s-l, where  $E_0$ , as a consequence of the negative  $F_1$ , lies to the left of the LUMO peak, the size of  $F_{\text{splitting}}$  also determines how close in energy  $E_0$  and this peak are, since  $F_1$  scales inversely with  $F_{\text{splitting}}$ . The dependence

TABLE III. Explicit values for all parameters entering Eq. (2) for the three MOs obtained by diagonalizing the  $3 \times 3$  Hamiltonian formed by the three FOs in Fig. 7(b) with  $\epsilon_L = \epsilon_R = 1.0$  eV,  $\epsilon_B = 1.6$  eV,  $t_L = 0.25$  eV,  $t_R = -0.25$  eV, and  $t_D$  as a variable. All values for  $t_D$  and  $E_0$  are eV, while the factors are dimensionless.

	m-s-l	p-s-l	m-s-s
$t_D$	-0.023	-0.0087	0.033
$E_0$	-1.12	-5.58	3.49
$\gamma_3/\gamma_1$	0.225	0.218	0.20
$F_{\text{splitting}}$	-6.49	-5.24	-3.24
$F_1$	-2.16	-6.97	2.83
$F_2$	0.91	0.92	0.95

of  $F_{\text{splitting}}$  on  $t_D$  can be directly read from Fig. 8(a), where it can be seen that  $F_{\text{splitting}}$  increases when the crossing point at  $-0.09$  eV is approached from either side of the  $t_D$  axis. We further illustrate this point in Fig. 8(b), where we plot  $\Gamma^2(E)$  in dependence on  $t_D$  and find that  $T(E)$  is reproduced for the particular values for the three single-branched molecules. In addition, we also pick two characteristic values to the right of the crossing point, where it can be seen that the one approaching it more closely, at  $-0.04$  eV, results in a DQI closer to the LUMO peak than the one farther away, at  $-0.02$  eV, or the value for compound m-s-l ( $-0.023$  eV). With the  $t_D$  value left from the crossing point at  $-0.14$  eV we demonstrate that in this range  $\gamma_3/\gamma_1$  becomes negative, which means that  $F_1$  is always positive, thereby moving the DQI feature to energies higher than the LUMO peak, while  $F_{\text{splitting}}$  then merely determines the energetic distance between the minimum and the peak.

### E. Introducing the through-space coupling as an *ad hoc* parameter into conventional topological TB models

Now armed with the knowledge that the direct coupling  $t_D$  for the FO model in Fig. 7(b) reflects the structural differences most relevant for the occurrence or absence of the DQI feature below the LUMO peak for the range of molecules we investigate in this article, we return to the topological TB model we started from in Fig. 6(a) and simplify it accordingly by removing all second- and third-nearest-neighbor couplings within the anchor groups and all but one of the ferrocene FOs. In the resulting minimal topological TB model [Fig. 9(a)] we set all C and N sites at the same on-site energies for all compounds as well as using the same value for the next-nearest-neighbor couplings within all anchor groups. The single remaining ferrocene FO has an on-site energy higher than those of the AOs but also here the same value is chosen for all three systems. They now differ only in the direct coupling between the AOs in the anchor groups on opposite sides of the ferrocene closest to each other, and meta and para are also distinct in the signs of the couplings of these AOs to the bridge FO. These minimal structural differences in the model already fully reproduce the characteristic features of  $T(E)$  for all molecules as can be verified from the NEGF-TB calculations presented in Fig. 9(b).

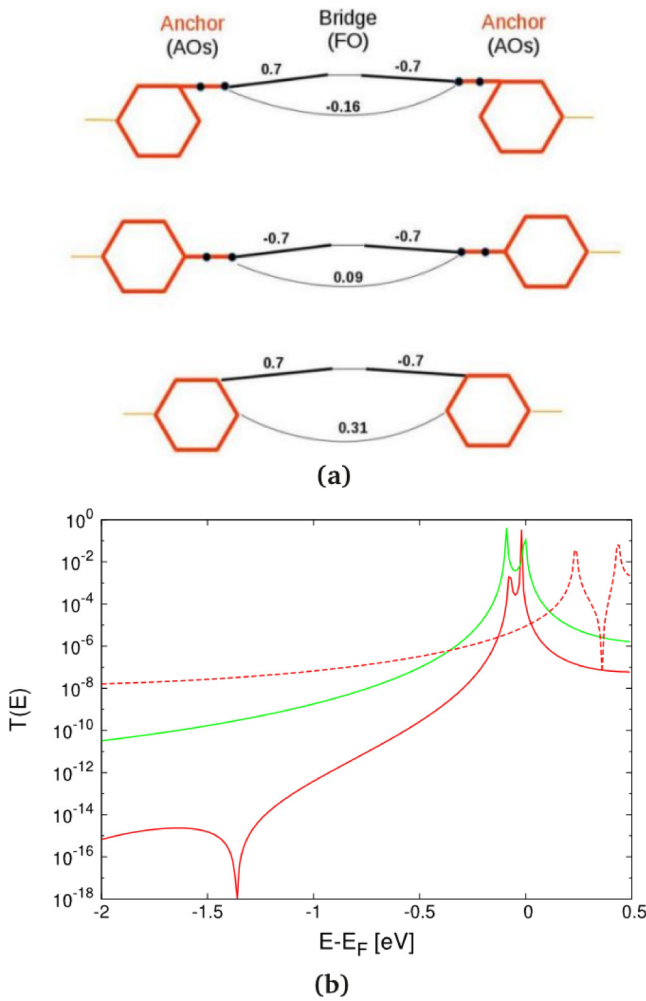


FIG. 9. (a) Conventional topological TB models for compounds m-s-l, p-s-l, and m-s-s, where only next-neighbor couplings have been considered within the pyridyl groups and acetylenic spacers, which are all set to  $-3.0$  eV, while the coupling of the contact atom to the leads is taken to be  $-0.2$  eV. For the on-site energies all AOs representing C and N sites are at  $-2.5$  eV, while the single ferrocene FO is positioned at  $1.7$  eV for all three molecules, where only the sign of the couplings of this FO to the AOs nearest to it differs between meta and para and the value for the direct through-space coupling between anchor FOs (both given explicitly in the figure) is different for all three structures. (b) NEGF-TB calculations for the models in (a) for m-s-l (solid red line), p-s-l, (solid green line), and m-s-s (dashed red line).

**F. Conclusions from the TB analysis**

In summarizing this section, it can be said that molecules containing ferrocene moieties differ distinctly from planar conjugated hydrocarbons in the correspondence between molecular structure and DQI effects in electron transmission, where general rules derived from simplified topological assumptions for the latter [17,43] are not applicable to the former. Strikingly, the most important structural difference between the molecules in this study is not defined by either the meta- or the paraconnection of their respective components, the availability of almost-degenerate orbitals on

the ferrocene, or the number of branches connecting the two anchor groups, although all of these aspects play a certain role in the exact energetic positioning of the DQI minimum. It is rather the direct through-space coupling between the anchor groups defined by the three-dimensional conformation of the respective compound and widely adjustable by spacer groups that determines the observability of DQI in  $T(E)$  in a delicate way.

**IV. EFFECT OF CHARGING OF THE BRANCHED COMPOUNDS**

**A. Methodology for the charging of the molecule in the junction**

In this section we address the effect of the selective charging of the ferrocene center on one of the two branches in the two double-branched molecules, m-d-l and m-d-s, on the conductance in order to assess their usefulness as molecular switches along the lines suggested in Sec. I. While in experiments one of the two ferrocene moieties has to be marked by a substituent in order to achieve the asymmetry allowing for redox splitting [24], in our theoretical calculations we can achieve the same effect by making use of an idea introduced in Ref. [61], where the electronic structure of a benzene molecule was distorted in an asymmetric fashion by the strategic placement of a potassium point charge. In our work we use a method for the charging of the branched compounds with a chlorine atom in the cell close to the molecule which, due to its higher electronegativity, absorbs an electron from the junction while oxidizing it in the process [41]; the overall neutrality of the device region is still maintained. As we describe in detail in Ref. [41], where we introduced this approach for the oxidation of another organometallic complex, the generalized  $\Delta$  self-consistent field technique [62,63] has to be applied in such a setup to ensure that the self-interaction problem of DFT is defied and the chloride ion is charged with one full electron while the resulting positive countercharge is distributed across the molecule and surfaces of the leads.

Following the concepts in Ref. [61] we built unit cells for the device region with a  $4 \times 8$  overstructure in the surface plane in order to create some space to vary the position of the chloride ion in one direction but, with the reduction of the unit cell length along the other lattice vector, keep the computational costs at a reasonable level. Since the position of the chloride anion in the unit cell has a marked influence on the distribution of the positive charge on the molecule and surface due to electrostatic attraction [41], we vary the distance of the ion to one of the two ferrocene centers as  $d_{Cl-Fc}$  (Fig. 10) in order to create asymmetry; in the following we denote the closer one Fc 1 and the one farther away Fc 2. Because of the different sizes of molecules m-d-l and m-d-s, the detailed values of  $d_{Cl-Fc}$  also differ in the two cases, with values of  $5.7$  and  $7.2$  Å for the symmetric setup where the ion has an equal distance to both Fe atoms and of  $4.3$  and  $5.4$  Å where it is markedly closer to Fc 1.

**B. Partial charge distributions**

In Table IV we list the resulting partial charges in Fc 1 and Fc 2 as obtained from a Bader analysis [64]; it can be seen that already in the neutral cases without the presence of



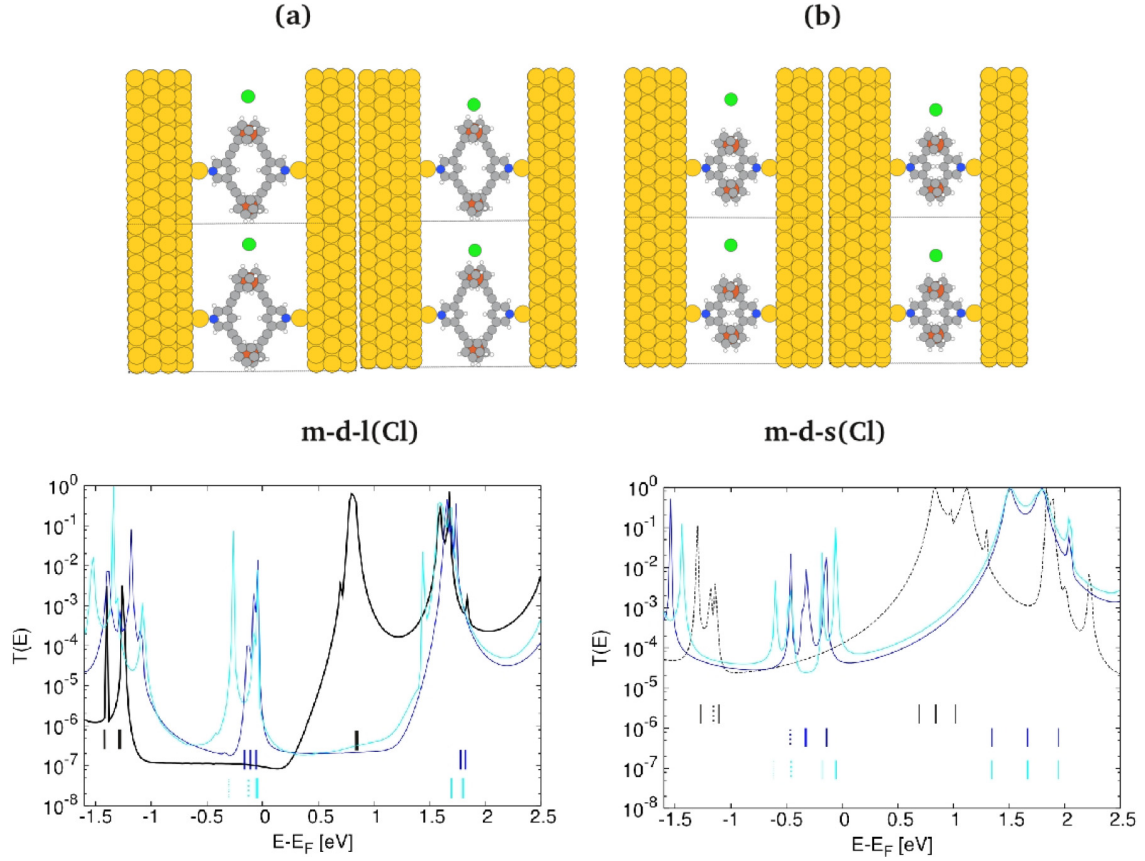


FIG. 10. Junction geometries for two neighboring cells in the periodic setup for the scattering region (upper panels) and  $T(E)$  from NEGF-DFT calculations (lower panels) for the branched molecules (a) m-d-l and (b) m-d-s, where the distance  $d_{\text{Cl-Fe}}$  between the Fe atom on one branch and the chloride counterion stabilizing the positive charge on the respective junction has been varied. For the transmission functions in the lower panels, which we calculated from NEGF-DFT, the neutral reference systems in the absence of charging or chlorine are represented as in Fig. 3, i.e., solid black curve for m-d-l and dashed black curve for m-d-s, while the cyan and blue curves show the  $T(E)$  values for charged junctions, for asymmetric (top right panels) and symmetric (top left panels) placement of the chloride ions between the two branches in neighboring cells, respectively. The eigenenergies of the relevant MOs are also indicated in the lower panels, where the color code reflects the one used for the transmission functions and the line type distinguishes between the two branches.

the chlorine the molecules have some positive partial charges since they lose fractions of electrons to the anchor groups and the gold surfaces. When the chloride ion is introduced into the

TABLE IV. Partial charges in units of fractions of 1 e as obtained from a Bader analysis [64] for the neutral and charged junctions defined in Fig. 10, where Fc 1 and Fc 2 denote the ferrocene closer to and farther away from the chloride ion, respectively. The conductance  $G$  for all junctions as defined by  $T(E_F)$  in Fig. 10 is given in units of  $G_0$ .

	Fc 1	Fc 2	$G$
m-d-l			
Neutral	-0.41	-0.44	$0.95 \times 10^{-7}$
$d_{\text{Cl-Fe}} = 5.7 \text{ \AA}$	-0.61	-0.64	$1.89 \times 10^{-6}$
$d_{\text{Cl-Fe}} = 4.3 \text{ \AA}$	-0.71	-0.55	$1.41 \times 10^{-6}$
m-d-s			
Neutral	-0.17	-0.17	$1.28 \times 10^{-4}$
$d_{\text{Cl-Fe}} = 7.2 \text{ \AA}$	-0.28	-0.23	$4.50 \times 10^{-5}$
$d_{\text{Cl-Fe}} = 5.4 \text{ \AA}$	-0.36	-0.18	$1.57 \times 10^{-4}$

cell and a negative partial charge corresponding to one electron is enforced on it, only fractions of the resulting positive countercharge reside in the ferrocene moieties, while the partial charge on the surface changes from negative to positive (not shown here), an effect which has been discussed in terms of the respective electronegativities for another metal-organic complex in Ref. [41]. We find also a substantial accumulation of negative partial charges on the acetylenic spacers, which explains why both charges on the ferrocene groups of molecule m-d-l are consistently more than twice as large as those found for m-d-s with and without charging via the chlorine atom.

For both compounds, however, the partial charge is distinctly higher on Fc 1 than on Fc 2 in the asymmetric setup, which is also reflected by the differences in peak shifts in the respective transmission functions in Fig. 10. While the peaks in the LUMO region are almost rigidly shifted to higher energies as a consequence of the charging for both molecules, regardless of whether the ion is placed symmetrically or asymmetrically with respect to the Fe positions, there are distinct differences in the HOMO region where the asymmetry induces peak

splitting, which could be expected from the discussion in Sec. II, where we note that the HOMOs are mostly localized in the ferrocene moieties and the LUMOs in the pyridyl anchors.

### C. Transmission functions and DQI for the charged compounds

Our expectation from the  $T(E)$  for the neutral molecules in Sec. II was that, due to the flat behavior of the function in the HOMO-LUMO gap induced by the narrowness of the HOMO peak and DQI close to the LUMO peak, there would be almost no change in the conductance as a consequence of charging for system m-d-l, while the Lorentzian decay of the LUMO peak for m-d-s might give rise to charge-induced conductance changes since the Fermi level would move down the tail of the peak. These assumptions assumed a rigid shift of  $T(E)$  and did not foresee that the HOMO-LUMO gap is reduced in size by the charging, where the tails of the HOMO peak now play a more active role in the definition of the conductance as can be seen from the NEGF-DFT calculations for the charged systems in Fig. 10, where we also list the corresponding values for  $G$  in Table IV.

It can be seen that for m-d-s the transmission functions of the neutral and the asymmetrically charged system cross each other almost exactly at  $E_F$ , resulting in almost-equal conductance values, while the conductance is enhanced by the charging for m-d-l, where the Fermi level is now at the shoulder of the HOMO peak for both the symmetric and the asymmetric setups. The latter charging effect on the conductance for m-d-l, however, would result in an on/off ratio of only  $\sim 15$ – $20$ , which is by far too low for an operative transistor. Moreover, our initial idea that the charging might have an influence on the presence or absence of DQI effects is not supported by the changes in the transmission function, although the DQI-induced flattening of the LUMO peak seems to be somewhat reduced for m-d-l in the cyan curve in Fig. 10 for the asymmetrically charged setup, where there is also a corresponding energy splitting found for the LUMO and LUMO+1, which are almost degenerate in the neutral system.

## V. SUMMARY

In this study we have investigated the potential use of branched molecules containing ferrocene centers in two branches as molecular transistors, where the switching would be achieved by a redox process allowing us to alternate between an on and an off state and the latter might have a substantially reduced conductance due to DQI. We found such a DQI effect in the electron transmission for one of the branched molecules we studied in its neutral state, but this effect was not altered significantly enough by charging to enable a transistor functionality with this particular system. Quite surprisingly, the appearance of the effect was closely linked to the presence of acetylenic spacers between the ferrocene moieties and the pyridyl anchor groups. In an analysis where we mapped the essential orbital characteristics of the metal-organic compounds under investigation onto more and more simplified tight-binding models in a systematic way, we could identify the structural sources for this unexpected finding. The key quantity turned out to be the direct through-space coupling between the anchor groups, which is determined in its size and sign by the detailed three-dimensional conformation of the respective molecule. This is fundamentally different from DQI as described for planar  $\pi$ -conjugated hydrocarbons, where simple topological rules were derived recently and where geometrical details of the molecular structure beyond next-neighbor connectivity do not play an essential role. The systematics of our analysis in this work can be applied to other metal-organic compounds exhibiting DQI effects with an influence on their conductance and therefore provides an enabling tool for the rational design of molecular transistors.

## ACKNOWLEDGMENTS

We gratefully acknowledge helpful discussions with Tim Albrecht and Michael Inkpen. All authors were supported by the Austrian Science Fund FWF (Project No. P27272). We are indebted to the Vienna Scientific Cluster, whose computing facilities were used to perform all calculations presented in this paper (Project No. 70671).

- 
- [1] M. Ratner, *Nat. Nanotechnol.* **8**, 378 (2013).
  - [2] E. Lörtscher, *Nat. Nanotechnol.* **8**, 381 (2013).
  - [3] M. Mayor, H. B. Weber, J. Reichert, M. Elbing, C. von Hänisch, D. Beckmann, and M. Fischer, *Angew. Chem. Int. Ed.* **42**, 5834 (2003).
  - [4] C. J. Lambert, *Chem. Soc. Rev.* **44**, 875 (2015).
  - [5] C. M. Guedon, H. Valkenier, T. Markussen, K. S. Thygesen, J. C. Hummelen, and S. J. van der Molen, *Nat. Nanotechnol.* **7**, 305 (2012).
  - [6] R. Stadler, S. Ami, M. Forshaw, and C. Joachim, *Nanotechnology* **15**, S115 (2004).
  - [7] T. Markussen, R. Stadler, and K. S. Thygesen, *Nano Lett.* **10**, 4260 (2010).
  - [8] T. Markussen, R. Stadler, and K. S. Thygesen, *Phys. Chem. Chem. Phys.* **13**, 14311 (2011).
  - [9] R. Stadler, *Nano Lett.* **15**, 7175 (2015).
  - [10] K. G. L. Pedersen, A. Borges, P. Hedegård, G. C. Solomon, and M. Strange, *J. Phys. Chem. C* **119**, 26919 (2015).
  - [11] K. Yoshizawa, T. Tada, and A. Staykov, *J. Am. Chem. Soc.* **130**, 9406 (2008).
  - [12] Y. Tsuji, A. Staykov, and K. Yoshizawa, *Thin Solid Films* **518**, 444 (2009).
  - [13] Y. Tsuji, A. Staykov, and K. Yoshizawa, *J. Phys. Chem. C* **113**, 21477 (2009).
  - [14] X. Li, A. Staykov, and K. Yoshizawa, *J. Phys. Chem. C* **114**, 9997 (2010).
  - [15] Y. Tsuji, A. Staykov, and K. Yoshizawa, *J. Am. Chem. Soc.* **133**, 5955 (2011).
  - [16] K. Yoshizawa, *Acc. Chem. Res.* **45**, 1612 (2012).
  - [17] X. Zhao, V. Geskin, and R. Stadler, *J. Chem. Phys.* **146**, 092308 (2017).

- [18] R. Stadler, M. Forshaw, and C. Joachim, *Nanotechnology* **14**, 138 (2003).
- [19] R. Stadler and T. Markussen, *J. Chem. Phys.* **135**, 154109 (2011).
- [20] C. M. Finch, V. M. Garcia-Suarez, and C. J. Lambert, *Phys. Rev. B* **79**, 033405 (2009).
- [21] M. Magoga and C. Joachim, *Phys. Rev. B* **59**, 16011 (1999).
- [22] C. Joachim, *Nat. Nanotechnol.* **7**, 620 (2012).
- [23] H. Vazquez, R. Skouta, S. Schneebeli, M. Kamenetska, R. Breslow, L. Venkataraman, and M. S. Hybertsen, *Nat. Nanotechnol.* **7**, 663 (2012).
- [24] M. S. Inkpen, T. Albrecht, and N. J. Long, *Organometallics* **32**, 6053 (2013).
- [25] G. Kastlunger and R. Stadler, *Phys. Rev. B* **91**, 125410 (2015).
- [26] A. Tárraga, P. Molina, D. Curiel, and M. D. Velasco, *Organometallics* **20**, 2145 (2001).
- [27] K. Kanthasamy, M. Ring, D. Nettelroth, C. Tegenkamp, H. Butenschön, F. Pauly, and H. Pfnür, *Small* **12**, 4849 (2016).
- [28] C. Engtrakul and L. R. Sita, *Nano Lett.* **1**, 541 (2001).
- [29] C. A. Nijhuis, W. F. Reus, and G. M. Whitesides, *J. Am. Chem. Soc.* **132**, 18386 (2010).
- [30] F. Ding, S. Chen, and H. Wang, *Materials* **3**, 2668 (2010).
- [31] S. A. Getty, C. Engtrakul, L. Wang, R. Liu, S. H. Ke, H. U. Baranger, W. Yang, M. S. Fuhrer, and L. R. Sita, *Phys. Rev. B* **71**, 241401 (2005).
- [32] X. Xiao, D. Brune, J. He, S. Lindsay, C. B. Gorman, and N. Tao, *Chem. Phys.* **326**, 138 (2006).
- [33] F. Schwarz, G. Kastlunger, F. Lissel, C. Egler-Lucas, S. Semenov, K. Venkatesan, H. Berke, R. Stadler, and E. Lörtscher, *Nat. Nanotechnol.* **11**, 170 (2016).
- [34] G. Kastlunger and R. Stadler, *Monatsh. Chem.* **147**, 1675 (2016).
- [35] F. Schwarz, M. Koch, G. Kastlunger, K. Venkatesan, H. Berke, R. Stadler, and E. Lörtscher, *Angew. Chem. Int. Ed.* **55**, 11781 (2016).
- [36] M. Baghernejad *et al.*, *J. Am. Chem. Soc.* **136**, 17922 (2014).
- [37] W. Hong, D. Z. Manrique, P. Moreno-García, M. Gulcur, A. Mishchenko, C. J. Lambert, M. R. Bryce, and T. Wandlowski, *J. Am. Chem. Soc.* **134**, 2292 (2012).
- [38] R. Stadler, K. S. Thygesen, and K. W. Jacobsen, *Phys. Rev. B* **72**, 241401(R) (2005).
- [39] R. Stadler, *J. Phys.: Conf. Ser.* **61**, 1097 (2007).
- [40] R. Stadler, *Phys. Rev. B* **80**, 125401 (2009).
- [41] G. Kastlunger and R. Stadler, *Phys. Rev. B* **88**, 035418 (2013).
- [42] Y. Meir and N. S. Wingreen, *Phys. Rev. Lett.* **68**, 2512 (1992).
- [43] D. Z. Manrique, C. Huang, M. Baghernejad, X. Zhao, O. A. Al-Owaedi, H. Sadeghi, V. Kaliginedi, W. Hong, M. Gulcur, T. Wandlowski, M. R. Bryce, and C. J. Lambert, *Nat. Commun.* **6**, 6389 (2015).
- [44] P. Sautet and C. Joachim, *Chem. Phys. Lett.* **153**, 511 (1988).
- [45] C. R. Arroyo, S. Tarkuc, R. Frisenda, J. S. Seldenthuis, C. H. M. Woerde, R. Eelkema, F. C. Grozema, and H. S. J. van der Zant, *Angew. Chem. Int. Ed.* **52**, 3152 (2013).
- [46] C. Patoux, C. Coudret, J.-P. Launay, C. Joachim, and A. Gourdon, *Inorg. Chem.* **36**, 5037 (1997).
- [47] A. Borges, E.-D. Fung, F. Ng, L. Venkataraman, and G. C. Solomon, *J. Phys. Chem. Lett.* **7**, 4825 (2016).
- [48] M. Brandbyge, J. L. Mozos, P. Ordejon, J. Taylor, and K. Stokbro, *Phys. Rev. B* **65**, 165401 (2002).
- [49] Y. Xue, S. Datta, and M. A. Ratner, *Chem. Phys.* **281**, 151 (2002).
- [50] A. R. Rocha, V. M. Garcia-Suarez, S. W. Baily, C. J. Lambert, J. Ferrer, and S. Sanvito, *Nat. Mater.* **4**, 335 (2005).
- [51] K. S. Thygesen and K. W. Jacobsen, *Chem. Phys.* **319**, 111 (2005).
- [52] J. J. Mortensen, L. B. Hansen, and K. W. Jacobsen, *Phys. Rev. B* **71**, 035109 (2005).
- [53] J. Enkovaara *et al.*, *J. Phys. Condens. Matter* **22**, 253202 (2010).
- [54] A. H. Larsen, M. Vanin, J. J. Mortensen, K. S. Thygesen, and K. W. Jacobsen, *Phys. Rev. B* **80**, 195112 (2009).
- [55] J. P. Perdew, K. Burke, and M. Ernzerhof, *Phys. Rev. Lett.* **77**, 3865 (1996).
- [56] P. O. Löwdin, *J. Chem. Phys.* **18**, 365 (1950).
- [57] S. Larsson, *J. Am. Chem. Soc.* **103**, 4034 (1981).
- [58] M. A. Ratner, *J. Phys. Chem.* **94**, 4877 (1990).
- [59] G. Kastlunger and R. Stadler, *Phys. Rev. B* **89**, 115412 (2014).
- [60] P. Sautet and M.-L. Bocquet, *Phys. Rev. B* **53**, 4910 (1996).
- [61] R. E. Sparks, V. M. García-Suárez, D. Zs. Manrique, and C. J. Lambert, *Phys. Rev. B* **83**, 075437 (2011).
- [62] J. Gavnholt, T. Olsen, M. Engelund, and J. Schiøtz, *Phys. Rev. B* **78**, 075441 (2008).
- [63] T. Olsen, J. Gavnholt, and J. Schiøtz, *Phys. Rev. B* **79**, 035403 (2009).
- [64] W. Tang, E. Sanville, and G. Henkelman, *J. Phys. Condens. Matter* **21**, 084204 (2009).





## Conferences / Workshops

### “Many Paths to Interference”

Dresden, Germany, the conference is focus on the specific field of electron transport (poster contribution).

### “8th International Conference on Molecular Electronics”

Paris, France, a big International conference assembled both theoreticians and experimentalists (poster contribution).

### “Section Spectroscopy and Theory of the Council for Chemical Science (CW)” (Theoretical Chemistry and Spectroscopy Graduate Course)

Han-sur-Lesse, Belgium, a one-week school experience focus on the theoretical knowledge.

## Publications

### “Quantum interference in coherent tunneling through branched molecular junctions containing ferrocene centers”

Xin Zhao, Georg Kastlunger and Robert Stadler, Physical Review B 96, 085421 (2017).

### “Destructive quantum interference in electron transport: A reconciliation of the molecular orbital and the atomic orbital perspective”

Xin Zhao, Victor Geskin and Robert Stadler, The Journal of Chemical Physics, 146, 092308 (2017).

### “Crystal orbital study on the double walls made of nanotubes encapsulated inside zigzag carbon nanotubes”

Xin Zhao, Weiye Qiao, Yuliang Li and Yuanhe Huang, Journal of Solid State Chemistry, 221, 102-108 (2015).

### “Adsorption configuration prediction for Ferrocene compounds with different anchor groups in single-molecule junctions”

Xin Zhao, Robert Stadler, in submission (2018).

### “Electron transport study in coherent tunneling through cyclic Ru/Os(PPh<sub>2</sub>)<sub>8</sub>(C<sub>2</sub>H<sub>4</sub>)<sub>4</sub> bis(pyridylacetylide) complexes”

Xin Zhao, Robert Stadler, in preparation (2018).